UNIVERSIDAD MIGUEL HERNÁNDEZ DE ELCHE
INSTITUTO DE BIOINGENIERÍA
Área de Química Orgánica

TESIS DOCTORAL

Síntesis de derivados de ftalocianina, su estudio como materiales transportadores de huecos y agentes de reconocimiento de cuadruplejos

MEMORIA PARA OPTAR AL GRADO DE DOCTOR PRESENTADA POR:

Adrián Hernández García

Bajo la dirección de:
Prof. Dra. Ángela Sastre Santos
Y la codirección de:
Prof. Dr. Juan Javier Ortiz Carricondo

Programa de Doctorado en Bioingeniería

Elche, 2023

UNIVERSITAS
Miguel Hernández

La presente Tesis Doctoral, titulada "Síntesis de derivados de ftalocianina, su estudio como materiales transportadores de huecos y agentes de reconocimiento de cuadruplejos", realizada por D. Adrián Hernández García, bajo la dirección de la Prof. Ángela Sastre Santos y la codirección del Prof. Juan Javier Ortiz Carricondo, se presenta bajo la modalidad de Tesis por compendio de las siguientes publicaciones con los siguientes indicios de calidad según el área de la ANEP de Química y subárea Química Orgánica.

Publicaciones Científicas:

P. Huang, A. Hernández, S. Kazim, J. Ortiz, Á. Sastre-Santos, S. Ahmad, **Molecularly engineered thienyl-triphenylamine substituted zinc phthalocyanine as dopant free hole transporting materials in perovskite solar cells**, *Sustain. Energy Fuels*, **2020**, *4*, 6188−6195. DOI: 10.1039/d0se01215g. Factor de Impacto: 6.367. Área de conocimiento: Materials Science, Multidisciplinary. Puesto que ocupa/total de revistas en el área: 82/334. (Q1).

P. Huang, A. Hernández, S. Kazim, J. Follana-Berná, J. Ortiz, L. Lezama, Á. Sastre-Santos, S. Ahmad, **Asymmetrically Substituted Phthalocyanines as Dopant-Free Hole Selective Layers for Reliability in Perovskite Solar Cell**s, *ACS Appl. Energy Mater.*, **2021**, *4*, 9, 10124–10135. DOI: 10.1021/acsaem.1c02039. Factor de Impacto: 6.959. Área de conocimiento: Materials Science, Multidisciplinary. Puesto que ocupa/total de revistas en el área: 86/345 (Q1).

A. Hernández, N. Harindu Hemasiri, S. Kazim, J. Ortiz, S. Ahmad, Á. Sastre-Santos, **Fluorinated- and non-fluorinated-diarylamine-Zn(II) and Cu(II) Phthalocyanines as Symmetrical vs Asymmetrical Hole Selective Materials**, *J. Mater. Chem. C*, **2023**, DOI: 10.1039/D3TC00254C. Factor de Impacto: 8.067. Área de conocimiento: Materials Science, Multidisciplinary. Puesto que ocupa/total de revistas en el área: 71/345. (Q1).

La Dra. Dña. Piedad Nieves de Aza Moya, Coordinadora de la Comisión Académica del Programa de Doctorado en Bioingeniería de la Universidad Miguel Hernández de Elche por Resolución Rectoral 3120/19, de 09 de diciembre de 2019,

INFORMA

Que la tesis doctoral titulada "Síntesis de derivados de ftalocianina, su estudio como materiales transportadores de huecos y agentes de reconocimiento de cuadruplejos", ha sido realizada por D. Adrián Hernández García, bajo la dirección la Prof. Dra. Ángela Sastre Santos y la codirección del Prof. Dr. Juan Javier Ortiz Carricondo, da su conformidad para que sea presentada a la Comisión de Doctorado de la Universidad Miguel Hernández.

Y para que así conste, y a los efectos oportunos, firma el presente documento en Elche, a __ de _____ de 2023.

Fdo.: Prof. Dra. Piedad Nieves de Aza Moya

Coordinadora del Programa de Doctorado en Bioingeniería

La Dra. Dña. Ángela Sastre Santos, directora, y el Dr. D. Juan Javier Ortiz Carricondo, codirector,

CERTIFICAN

Que el presente trabajo titulado “Síntesis de derivados de ftalocianina, su estudio como materiales transportadores de huecos y agentes de reconocimiento de cuadruplejos”, el cual constituye la memoria que presenta el graduado ADRIÁN HERNÁNDEZ GARCÍA para optar al Grado de Doctor por la Universidad Miguel Hernández de Elche, ha sido realizado bajo su dirección en el Instituto de Bioingeniería, cumpliendo todos los requisitos necesarios y dan su conformidad a la lectura de la tesis doctoral, conforme a los términos y condiciones definidos en su Plan de Investigación y de acuerdo al Código de Buenas Prácticas de la Universidad Miguel Hernández de Elche.

Y para que conste, expiden y firman el presente certificado en Elche, a __ de _____ de 2023

Fdo.: Prof. Dra. Ángela Sastre Santos

Fdo. Prof. Dr. Juan Javier Ortiz Carricondo

El trabajo realizado a lo largo de la tesis doctoral ha sido posible gracias a la financiación de:

- Proyecto de investigación “Hacia la Síntesis de Moléculas Avanzadas para la Generación de Energía” (referencia: CTQ2017-87102-R AEI/FEDER) financiado por el Ministerio de Economía y Competitividad y por la Unión Europea a través del Fondo Social Europeo de Desarrollo Regional- FEDER- “Una manera de hacer Europa”. Responsable: Prof. Dra. Ángela Sastre Santos.

- Proyecto de investigación “Síntesis y Organización Supramolecular de Sistemas Electroactivos basados en Ftalocianinas y Dicetopirrolopirroles para Fotovoltaica Molecular y Tratamiento contra el Cáncer (SioSi)” (referencia: PID2020-117855RB-I00) financiado por el Ministerio de Economía y Competitividad y por la Unión Europea a través del Fondo Social Europeo de Desarrollo Regional- FEDER- “Una manera de hacer Europa”. Responsable: Prof. Dra. Ángela Sastre Santos.

- Proyecto de investigación “Agregados Macromoleculares para la preparación de Células Solares Orgánicas e Híbridas Estables y Sostenibles” (referencia: PROMETEO/ CIPROM/2021/059) financiado por la Conselleria de Innovación, Universidades, Ciencia y Sociedad Digital, Generalitat Valenciana. Responsable: Prof. Dra. Ángela Sastre Santos.

Agradecimientos

Al final de un largo camino siempre encontraras un tesoro, en este caso no solo el título de doctor, sino también un sinfín de experiencias, aprendizaje y poder conocer gente maravillosa que me ha ido acompañando durante este viaje. Algunos han estado conmigo de inicio a fin, otros solo en ciertos momentos, igualmente han sido importantes y por ello les quiero agradecer:

No podía ser de otra forma, sino en primer lugar a la persona que ha hecho posible que pudiese realizar esta tesis doctoral, **Ángela Sastre**. Desde aquella primera llamada por la cual nos reunimos y comencé mis andadas en el mundo de la química a través del Máster Universitario en Nanociencia y Nanotecnología Molecular. Ha llovido mucho desde entonces, y estando en Elche esta expresión cobra más valor, sin embargo, lo hemos conseguido, hemos llegado a la meta. Al menos, a una las importantes. Por ello quiero agradecerte sinceramente todo lo que has hecho por mí. La otra persona sin la cual no estaríamos aquí es **Javier Ortiz**, porque desde el inicio fue él quien me enseñó a trabajar en un laboratorio de química y hasta el día de hoy hace lo posible por ayudar y explicar cualquier cosa que pudiese necesitar, gracias.

Al resto de integrantes del grupo DYSMOL, incluidos aquellos que ya no forman parte de el:

Jorge Follana, que decir, cuando llegué estabas acabando el doctorado y desde entonces te he considerado un ejemplo a seguir. Es posible que por ello siempre te preguntase tanto, gracias por intentar ayudar siempre en lo que pudieses. **Desiré Molina** y **Nathalie Zink**, las mamas del grupo, aunque haya coincidido por casualidad, en el laboratorio os echamos en falta. Gracias por toda la ayuda que me habéis dado. **Ana María Gutiérrez**, mi profesora de Química Orgánica de segundo de carrera. Quien me iba a decir por aquel entonces que acabaríamos trabajando juntos, y más aún, que nos llevásemos tan bien. **María Joao**, puedo decir con sinceridad que, en los momentos más duros de este viaje, estuvieses ahí me ha ayudado más de lo que puedas imaginar. Es posible que fuese por las bromas, o por los desvaríos de una princesa, pero sin duda alguna has sido una de las mejores compañeras de doctorado que podía tener, gracias. **Jose Garcés**, compañero doctor, doctor al fin. Se lo mucho que ha costado ya que lo hemos vivido de la mano. Estoy muy orgulloso de ti, que ganas de poder hablar contigo de Dr. a Dr., además de como amigo. **Valeria Navarro** empezamos juntos esta etapa y eso es algo que me llena de alegría, porque aun habiendo separado caminos, todo lo que vivimos juntos no desaparece, sé que me llevo una buena amiga. **David Herrero** y **María Castillo**, aunque no haya sido posible, sabéis lo mucho que me hubiese gustado ser compañeros de tesis. Espero que os vaya bien, siempre fiel al club. **Víctor Sobrino** y **Lydia Ferrer**, los actuales doctorandos. Víctor, has sido un descubrimiento de persona, no pensé que me pudieses caer tan bien en tan poco tiempo… puede que compartir habitación agilice el proceso. Lydia, mi actual compañera de despacho, gracias por aguantar mi humor sin muchas quejas. **Belén Rufete** todos sabemos que eres el corazón del laboratorio, gracias por preocuparte tanto por nosotros. Gracias a todo el grupo DYSMOL.

Gracias al Prof. **Shahzada Ahmad** por permitirme realizar una estancia en su grupo de investigación. A sus estudiantes de doctorado **Naveen Harindu**, ahora ya doctor, y **Muhammed Haris**, por ayudarme y dedicarme todo el tiempo que fue necesario.

Finalmente, ellos no podían ser menos, mis padres. **María José** y **Pepe**, mamá y papá. Aunque no os lo diga lo suficiente os quiero. Os quiero muchísimo. Puede que no lo diga lo suficiente

porque no se expresar todo lo que os quiero, pero os quiero. Sois los mejores padres que alguien podría desear y sois mis padres. No sabéis cuan afortunado me siento por ello. No importan los méritos que consiga en la vida, porque os tengo a vosotros. Y, aun así, todo lo que consiga es vuestro. Es vuestro porque siempre habéis estado ahí, es vuestro porque siempre me habéis apoyado, es vuestro porque siempre me habéis animado a conseguirlo y, en definitiva, es vuestro porque gracias a vosotros soy quien soy. Os quiero

Como no, también el resto de mi familia. Sobre todo, mi abuela, casi segunda madre, **Mercedes**, llalla, se todo lo que me quieres y lo que sufres por nosotros, gracias. Así como todos mis amigos y gente que ha formado parte de mi vida durante estos años. Gracias a todos.

Aún me queda una persona a la que agradecer, una persona que he decidido dejar para el final, esperando que viniesen a mí las palabras perfectas. Porque leyendo esto podrías esperar que haya tenido todo el tiempo del mundo para pensar y escribir este párrafo, pero no. Decidí escribirlo con el corazón y no la cabeza. Eres tú, **Marta**. La persona que ha querido compartir el camino más largo conmigo, la vida. Gracias, gracias por todo. Pues en la vida no hay tesoro más grande que el propio viaje y quien te acompaña. Te quiero. No se sí serán las mejores palabras, pero espero poder perfeccionarlas a lo largo del camino.

Resumen

Las ftalocianinas (Pcs) son macrociclos aromáticos planos constituidos por cuatro unidades de isoindol. Su aromaticidad viene dada por 18 electrones tipo π deslocalizados en el interior del anillo, proporcionándole una gran estabilidad química, térmica y fotoquímica. Por otro lado, poseen una gran versatilidad ya que los dos hidrógenos internos se pueden sustituir por un ion metálico dando lugar a ftalocianinas metálicas (MPcs) y la posibilidad de utilizar diferentes sustituyentes. Dependiendo de los sustituyentes y el ion utilizados se pueden modular sus propiedades físicas, químicas y electrónicas. La presente tesis está dividida en 3 capítulos que se desarrollan en torno a la preparación de estas moléculas y sus aplicaciones.

En el **capítulo uno** se introduce a las protagonistas de esta tesis doctoral, las ftalocianinas. Se explora su descubrimiento, estructura, y, con especial importancia, la química de estas moléculas orgánicas. Desde la síntesis a partir de precursores ya sustituidos o la preparación de derivados a partir de ftalocianinas preformadas, los métodos de síntesis de Pcs asimétricas y sustituidas en posición axial. También se presentan sus propiedades y campos de aplicación.

En el **capítulo dos** se han sintetizado distintos derivados de MPcs para su uso como material transportador de huecos (HTM) en células solares de perovskita (PSC). La contaminación y el calentamiento global debidos al uso de combustibles fósiles está impulsando la búsqueda de fuentes de energía limpias y renovables, siendo la energía solar la alternativa con mayor potencial. Las células solares de perovskita podrían ser una buena alternativa a las células actuales de silicio gracias a su facilidad de preparación y bajo coste, más aún ahora que han alcanzado una eficiencia del 25.8% en células de laboratorio. Sin embargo, para llevarlas a nivel industrial, es necesario aumentar su estabilidad y sustituir a 2,2',7,7'-tetrakis[*N*,*N*-di(4-metoxifenil)amino]-9,9'-espirobifluoreno (spiro-OMeTAD) por un material transportador de huecos económico y estable a largo plazo. Las Pcs son candidatas prometedoras debido a su excelente estabilidad y a sus altas prestaciones fotovoltaicas, por lo cual se han sintetizado ftalocianinas simétricas y asimétricas, con cinc o cobre como iones metálicos y diferentes grupos funcionales. Entre ellos cabe destacar sustituyentes con gran conjugación para aumentar las propiedades de conductividad. En primer lugar, se sintetizó una ftalocianina de cinc tetrasustituida con grupos tienil-trifenilamina (ZnTTPc 1). A continuación, se quiso estudiar distintas ftalocianinas asimétricamente sustituidas de cinc y de cobre, con tres grupos *terc*-butilo y un grupo de tienil-trifenilamina, o un grupo amino terminal con capacidad de interaccionar con la capa de perovskita. Por último, se sintetizaron diferentes ftalocianinas tetrasustituidas simétricas y asimétricas de cinc y cobre con grupos arilamino con y sin flúor. Los dispositivos fabricados con dichas MPcs como HTM sin dopar han obtenido eficiencias cercanas a los HTM de referencia y en todas ellas se ha demostrado una estabilidad mucho mayor.

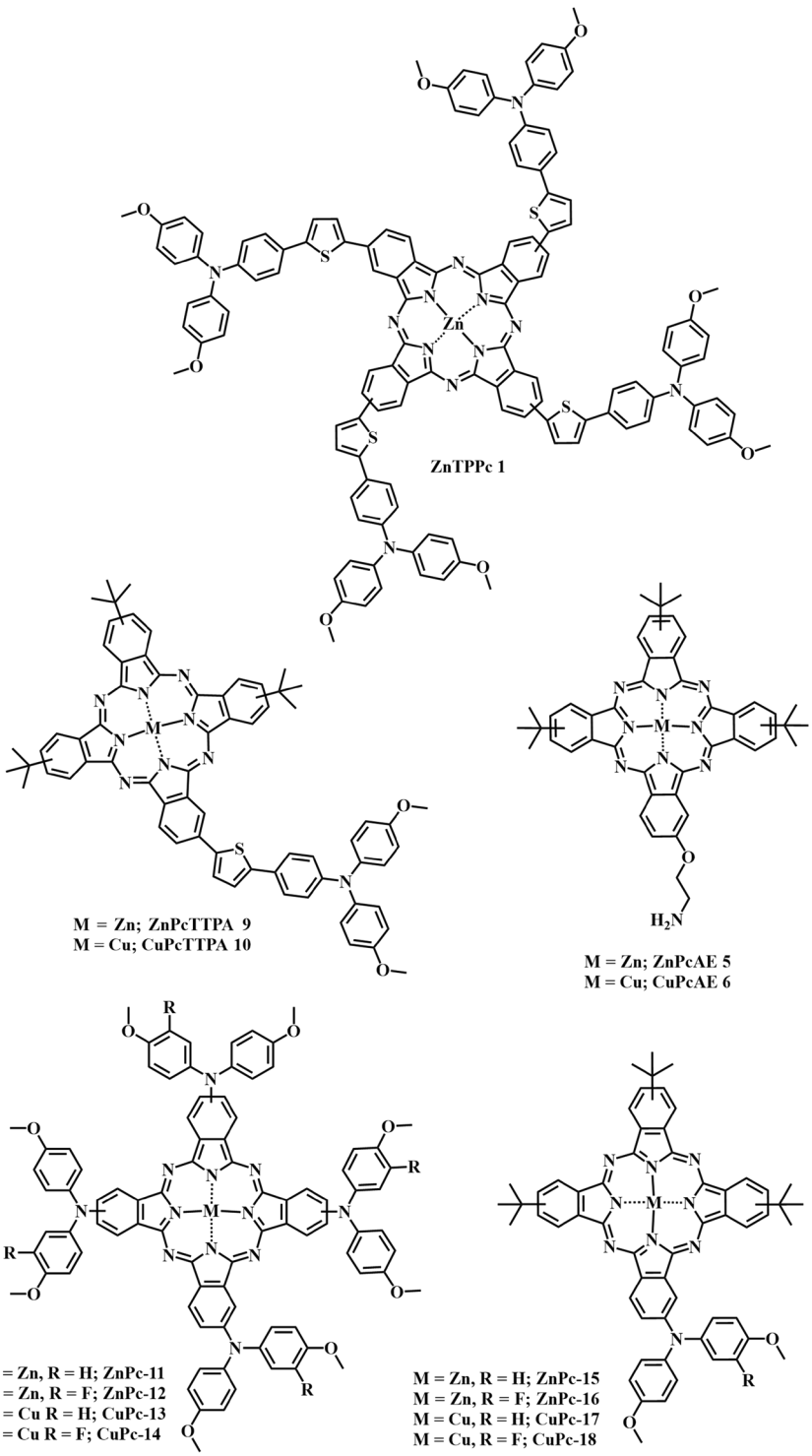

Figura 1. Estructura de las moléculas objetivo del Capítulo 2.

En el **capítulo tres**, se han sintetizado dos ftalocianinas para su aplicación como agente de reconocimiento de cuadruplejos de guanina (G4s). Además de la ya conocida estructura de doble hélice del ADN, existen otras morfologías que se puede adoptar esta molécula. Los G4s se generan mediante el apilamiento de dos o más tétradas planas de guanina. Las secuencias de ADN que permiten estas estructuras se encuentran en telómeros, regiones promotoras de varios oncogenes e intrones que se han identificado como potenciales dianas terapéuticas. La estructura de agentes de reconocimiento de G4s, viene definido por la presencia de anillos aromáticos con electrones π deslocalizados. Por ello, se han sintetizado una ftalocianina de cinc (ZnPc 21) y otra de níquel (NiPc 22) solubles en agua. Para conseguir dicha solubilidad se han funcionalizado con grupos 2-aminoetoxilo y formado su sal con ácido trifluoroacético. Se han utilizado cadenas alquílicas para aprovechar su flexibilidad y aumentar la interacción con el esqueleto de fosfato de los nucleótidos. Ambas MPcs han mostrado alta selectividad hacia los G4s frente al ADN de doble cadena. Además, se ha comprobado la importancia del metal en la capacidad de generar especies reactivas de oxígeno (ROS), siendo ZnPc 21 la única capaz de ello.

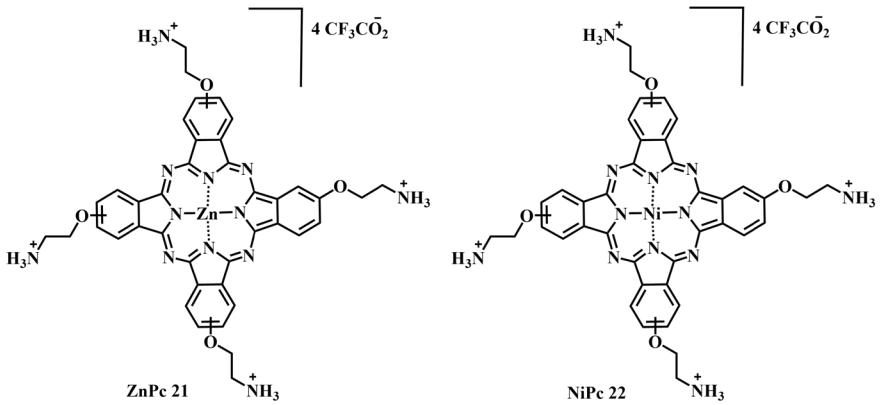

Figura 2. Estructura de las moléculas objetivo del Capítulo 3.

Abstract

Phthalocyanines (Pcs) are flat aromatic macrocycles consisting of four isoindole units. Their aromaticity is provided by 18 π-type electrons located inside the ring, giving them great chemical, thermal and photochemical stability. On the other hand, they are highly versatile, as the two internal hydrogens can be replaced by a metal ion, giving rise to metal phthalocyanines (MPcs) and the possibility of using different substituents. Depending on the substituents and ion used, their physical, chemical and electronic properties can be modulated. The present thesis is divided into 3 chapters that focus on the preparation of these molecules and their applications.

In **chapter one**, the protagonists of this doctoral thesis, the phthalocyanines, are introduced. It explores their discovery, structure, and, with special importance, the chemistry of these organic molecules. From the synthesis of already substituted precursors or the preparation of derivatives from preformed phthalocyanines, the methods of synthesis of asymmetric and axially substituted Pcs. Their properties and fields of application are also presented.

In **chapter two**, different MPcs derivatives have been synthesized for use as a hole transporting material (HTM) in perovskite solar cells (PSCs). Pollution and global warming due to the use of fossil fuels is driving the search for clean and renewable energy sources, with solar energy being the alternative with the greatest potential. Perovskite solar cells could be a good alternative to current silicon cells due to their ease of preparation and low cost, especially now that they have reached an efficiency of 25.8% in laboratory cells. However, to bring them to the industrial level, it is necessary to increase their stability and replace 2,2',7,7'-tetrakis[*N*,*N*-di(4-methoxyphenyl)amino]-9,9'-spirobifluorene (spiro-OMeTAD) with an inexpensive and long-term stable hole transporting material. Pcs are promising candidates due to their excellent stability and high photovoltaic performance, so symmetric and asymmetric phthalocyanines, with zinc or copper as metal ions and different functional groups, have been synthesized. These include highly conjugated substituents to increase the conductivity properties. First, a tetrasubstituted zinc phthalocyanine with thienyl-triphenylamine groups (ZnTTPc 1) was synthesized. Then, different asymmetrically substituted zinc and copper phthalocyanines with three tert-butyl groups and a thienyl-triphenylamine group, or a terminal amino group with the ability to interact with the perovskite layer, were studied. Finally, different symmetric and asymmetric tetrasubstituted zinc and copper phthalocyanines with arylamino groups with and without fluorine were synthesized. Devices fabricated with these MPcs as undoped HTMs have obtained efficiencies close to the reference HTMs and all of them have shown a much higher stability.

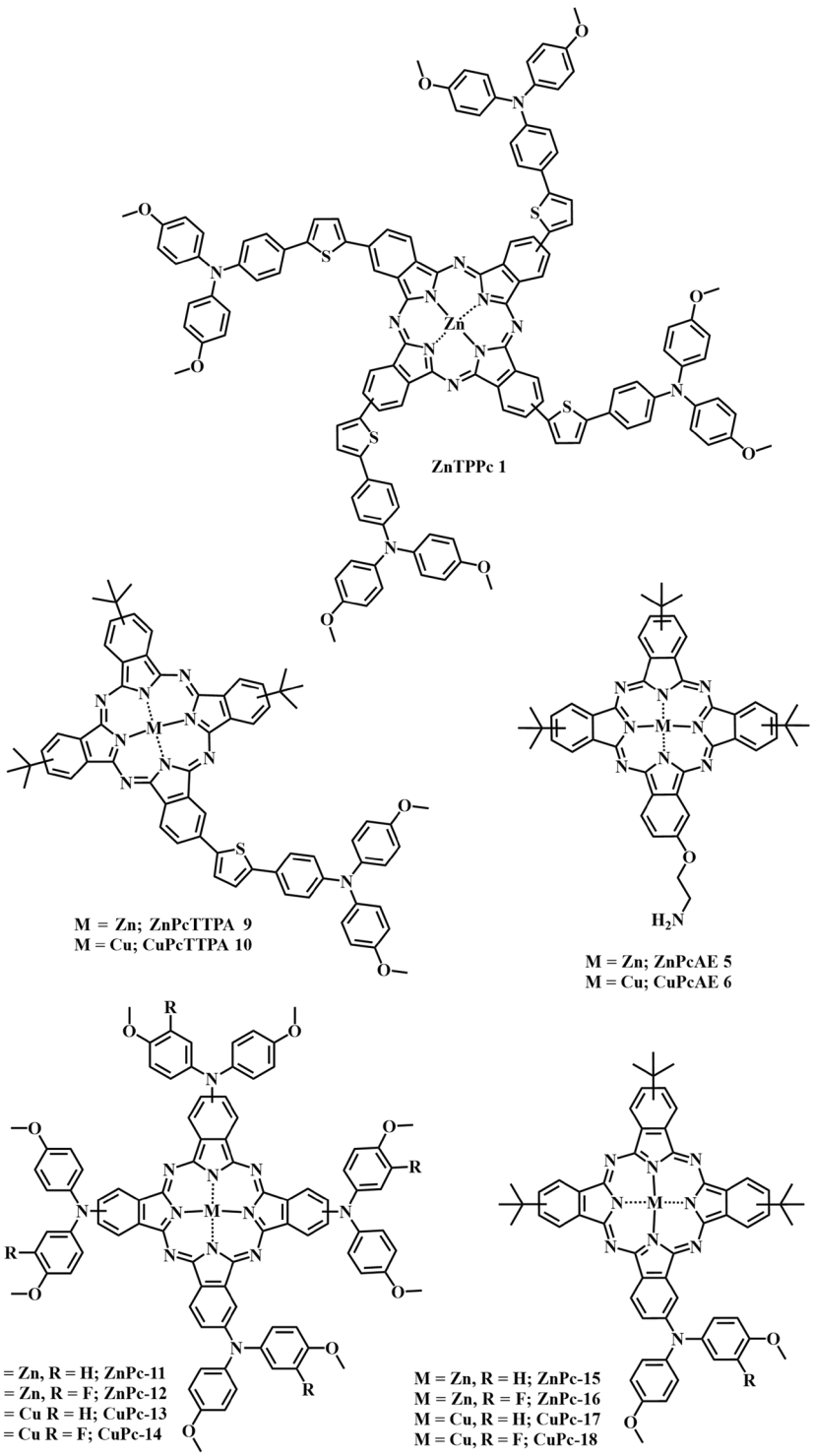

Figure 1. Structure of the target molecules in Chapter 2.

In **chapter three**, two phthalocyanines have been synthesized for their application as a recognition agent for guanine quadruplexes (G4s). In addition to the well-known double helix structure of DNA, there are different morphologies that can be adopted. G4s are generated by stacking two or more flat guanine tetrads. The DNA sequences that enable these structures are found in telomeres, promoter regions of several oncogenes and introns. Consequently, they have been identified as potential targets for therapeutic intervention. The design of G4s recognition agents is defined by the presence of aromatic rings with delocalized π-type electrons. Therefore, water-soluble zinc (ZnPc 21) and nickel (NiPc 22) phthalocyanines have been synthesized. To achieve this solubility, they have been functionalized with amino groups and their salt has been formed with trifluoroacetic acid. Alkyl chains have been used to take advantage of their flexibility and to increase the interaction with the phosphate backbone of the nucleotides. Both MPcs have shown high selectivity towards G4s and not double-stranded DNA. In addition, the importance of the metal in the ability to generate reactive oxygen species (ROS) has been demonstrated, with ZnPc 21 being the only one capable of this.

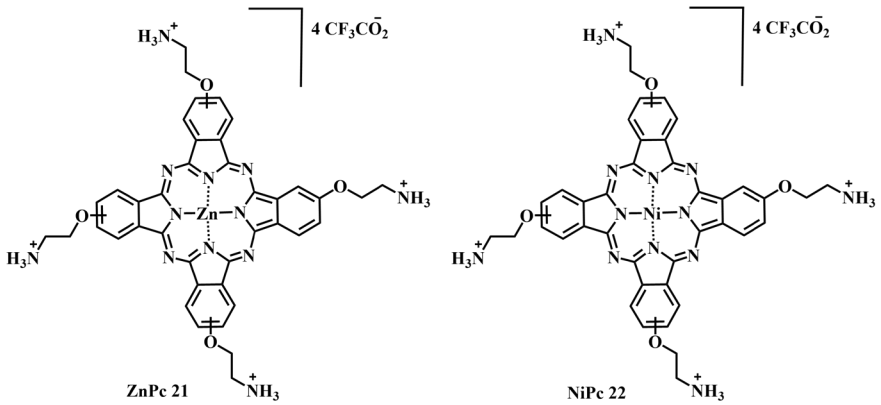

Figure 2. Structure of the target molecules in Chapter 3.

Contenido

Lista de acrónimos y abreviaturas

^{1}H-RMN	Resonancia Magnética Nuclear de hidrógeno
^{13}C-RMN	Resonancia Magnética Nuclear de carbono
ADN	Ácido desoxirribonucleico
ADNct	ADN complementario
ARN	Ácido ribonucleico
BHJ	Heterounión masiva, del inglés *bulk heterojunction*
BRCA	Cáncer de mama, del inglés *breast cancer*
CdTe	Telururo de cadmio
CIGS	Seleniuro de cobre, indio y galio
cm	Centímetros
CoPc	Ftalocianina de cobalto
c-TiO_2	Óxido de titanio compacto
CuPc	Ftalocianina de cobre
DBN	1,5-Diazabiciclo[4.3.0]non-5-eno
DBU	1,8-Diazabiciclo[5.4.0]undec-7-eno
DCM	Diclorometano
DMAE	2-Dimetilaminoetanol
DMF	*N*,*N*-Dimetilformamida
DMSO	Dimetilsulfóxido
DPA	Difenilamina
DPBF	1,3-Difenilisobenzofurano
DPP	Dicetopirrolopirrol
DSSC	Célula solar sensibilizada por colorante, del inglés, *dye sensitized solar cell*
EQE	Eficiencia cuántica externa, del inglés *external quantum efficiency*
ETA	(Capa) Absorbente extremadamente delgada, del inglés *extremely thin absorbing layer*
ETM	Material transportador de electrones, del inglés *electron transporting material*
eV	Electronvoltios
FHJ	Heterounión plana, del inglés *flat heterojunction*
FRET	Transferencia de energía de resonancia de Förster, del inglés *Förster resonance energy transfer*
FT-IR	Infrarrojo por transformada de Fourier, del inglés Fourier transform infrared
G4s	Cuadruplejos de guanina
HeLa	Línea celular de cáncer cervicouterino, Henrietta Lacks
HOMO	Orbital molecular ocupado de mayor energía, del inglés *highest ocuppied molecular orbital*
HPLC	Cromatografía liquida de alta resolución, del inglés *high performance liquid chromatography*

HRMS	Espectrometría de masas de alta resolución, del inglés *high resolution mass spectrometry*
HTM	Material transportador de huecos, del inglés *hole transporting material*
IC50	Concentración necesaria para lograr una inhibición del 50% in vitro
IPCE	Eficiencia de conversión de fotón incidente a corriente, del inglés *incident photon-to-current conversion efficiency*
IR	Espectroscopía infrarroja
ISC	Cruce intersistémico, del inglés *intersystem corssing*
kW	Kilovatio
Li-TFSI	Bis(trifluorometanosulfonil)imida de litio
LUMO	Orbital molecular desocupado de menor energía, del inglés *lowest unocuppied molecular orbital*
M	Molar
$MAPbBr_3$	Bromuro de plomo (II) y metilamonio
$MAPbI_3$	Yoduro de plomo (II) y metilamonio
MALDI-TOF	Desorción/ionización láser asistida por matriz, del inglés *matrix-assisted laser desorption/ionization*; Tiempo de vuelo, del inglés *time-of-flight*
µM	Micromolar
mmol	Milimol
MOFs	Redes metal-orgánicas, del inglés m*etal-organic frameworks*
MPcs	Ftalocianinas metálicas
MPP	Punto de máxima potencia, del inglés *maximum power point.*
mp-TiO2	Óxido de titanio mesoporoso
MTT	Bromuro de 3-(3,4 -dimetiltiazol-2-il)-2,5-difeniltetrazolio
NBS	*N*-bromosuccinimida
NHE	Elemento hipersensible a nucleasas, del inglés *Nuclease hipersensitive element*
NiPc	Ftalocianina de níquel
nm	Nanómetros
$^1O_2$	Oxígeno singlete
ºC	Grados centígrados
OFET	Transistor de efecto de campo orgánico, del inglés *organic field-effect transistor*
p. ej.	Por ejemplo
PCE	Eficiencia de conversión de energía, del inglés *power conversion efficiency*
Pc	Ftalocianina
PDT	Terapia fotodinámica, del inglés *photodynamic therapy*
ppm	Partes por millón
PS	Fotosensibilizador

PSC	Célula solar de perovskita, del inglés *perovskite solar cell*
PTAA	Poli(triarilamina)
RB	Rosa de Bengala
ROS	Especies reactivas de oxígeno, del inglés *reactive oxygen species*
SiPc	Ftalocianina de silicio
Spiro-OMeTAD	2,2',7,7'-tetrakis(*N*,*N*'-di-*p*-metoxifenilamino)-9,9'-espirobifluoreno
tBP	4-*terc*-butilpiridina
TCO	Oxido conductor transparente, del inglés *transparent conductive oxide*
TFA	Ácido trifluoroacético, del inglés *trifluoroacetic acid*
THF	Tetrahidrofurano
TPA	Trifenilamina
UV-vis	Ultravioleta-visible
ZnPc	Ftalocianina de cinc

Capítulo 1

Introducción: Química de las Ftalocianinas

1 Ftalocianinas

1.1 Descubrimiento

Las ftalocianinas fueron observadas por primera vez en 1907 por Braun y Tchemiac durante la síntesis de *o*-cianobenzamida como traza de color azul sin identificar (**Esquema 1.1a**). [1] Posteriormente, en 1927, Diesbach y von der Weid obtuvieron fortuitamente la ftalocianina de cobre en la reacción de cianación de 1,2-dibromobenceno (**Esquema 1.1b**). [2] Finalmente, fueron preparadas de forma accidental en 1928 en la planta de Grangemouth de Scottish Dyes. Durante la preparación de ftalimida a partir de anhídrido ftálico y amoniaco, un reactor de vidrio se agrieto y puso la mezcla en contacto con el revestimiento de acero exterior. Se formó una impureza azul junto a la ftalimida (**Esquema 1.1c**). Gracias al trabajo de Reginald Linstead y colaboradores [3, 4] y a los análisis de difracción de rayos X de Robertson, [5] se consiguió elucidar la estructura del material, la ftalocianina de hierro.

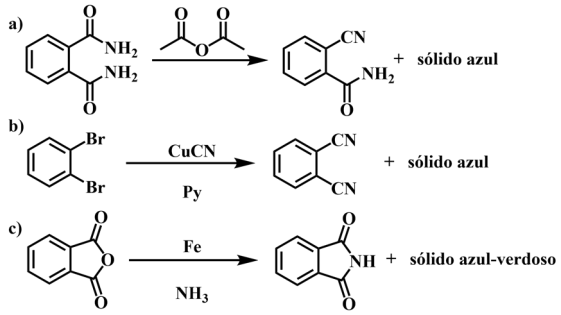

Esquema 1.1. Síntesis de a) 2-cianobenzamina, b) ftalonitrilo y c) ftalimida.

1.2 Estructura

La estructura de las ftalocianinas está directamente relacionada con la de sus análogos naturales, las porfirinas (**Figura 1.1a**), de hecho, su denominación formal es tetrabenzotetraazaporfirinas. Las ftalocianinas son macrociclos aromáticos planos, están constituidas por cuatro unidades de isoindol (**Figura 1.1b**) unidas mediante puentes aza a través de las posiciones 1,3. El esqueleto básico está constituido por un conjunto de 40 átomos, de los cuales 32 son de carbono y 8 de nitrógeno, sobre los que se deslocaliza una nube de 42 electrones π. A pesar de cumplirse la regla de Hückel, la deslocalización electrónica principal no se produce sobre los 40 átomos, sino que ocurre en el anillo interior formado por 18 electrones π y 16 átomos (**Figura 1.1c**).

[1] A. Braun, J. Tcherniac, Berichte der Deutschen Chemischen Gesellschaft, **1907**, 40, 2709-2714.
[2] H. de Diesbach, E. vonder Weid*, Helevtica Chim. Acta*, **1927**, *10*, 886–888.
[3] R.P. Linstead, *J. Chem. Soc*. **1934**, 1016-1017.
[4] a) G.T. Byme, R.P. Linstead, A.R. Lowe, *J. Chem. Soc*., **1934**, 1017-1022. b) R.P. Linstead, A. R. Lowe, *J. Chem. Soc*., **1934**, 1022-1027. c) C.E. Dent, R. E Linstead, A.R. Lowe, *J. Chem. Soc*., **1934**, 1033-1039. d) J.A. Elvidge, R.P. Linstead, *J. Chem. Soc*., **1955**, 3536-3544. e) C.E. Dent, R.E Linstead, *J. Chem. Soc*., **1934**, 1027-1031.
[5] a) J.M. Robertson, *J. Chem. Soc*., **1935**, 615-621. b) J.M. Robertson, *J. Chem. Soc*., **1936**, 1195-1209. c) J.M. Robertson, I. Woodward, *J. Chem. Soc*., **1937**, 219-230.

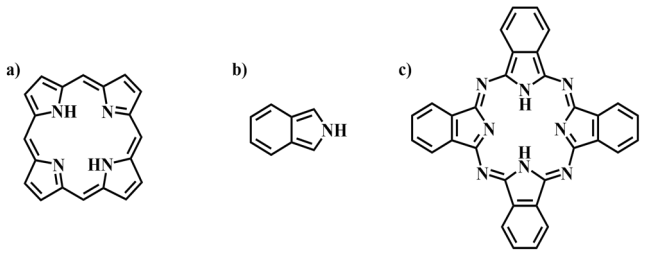

Figura 1.1. Estructuras de a) porfirina, b) isoindol, y c) ftalocianina libre.

Los hidrógenos situados en la cavidad interior pueden reemplazarse por metales, dando lugar a metaloftalocianinas (MPcs). En la cavidad interior se pueden coordinar más de 70 elementos diferentes entre los cuales se encuentran metales de transición, lantánidos, actínidos y semimetales como B, Si, Ge y As. Esto se traduce en una muy amplia química de coordinación, a la que además se le puede sumar la unión de dichos metales a otros ligandos en posición axial. [6] A pesar de ello, es la sustitución en posiciones periféricas, α y β, la que se ha desarrollado mayormente y es la herramienta que más se utiliza para la modulación de las propiedades de las ftalocianinas (**Figura 1.2**).

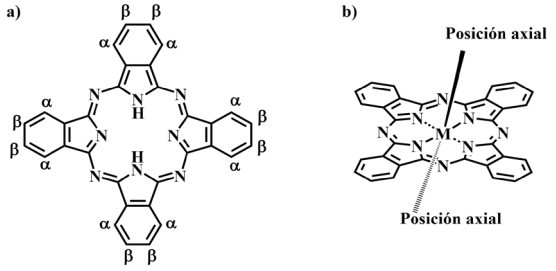

Figura 1.2. Estructuras de ftalocianina libre y metálica con sus posibles posiciones de funcionalización.

Los espectros de absorción de UV-Vis típicos de las ftalocianinas presentan dos bandas distintivas, la banda Soret que aparece como una banda ancha alrededor de 350 nm; y la banda Q que aparece como una banda en MPcs o desdoblada en Pcs libres alrededor de 680 nm. La absorción de la banda Soret se debe a transiciones π-π* HOMO-LUMO, al igual que en el caso de la banda Q, sin embargo, esta última es mucho más intensa con coeficientes de extinción molar en el rango de $10^5 M^{-1}cm^{-1}$ (**Figura 1.3**).

[6] M. Hanack, M. Lang, *Adv. Mater*. **1994**, *6*, 819-833.

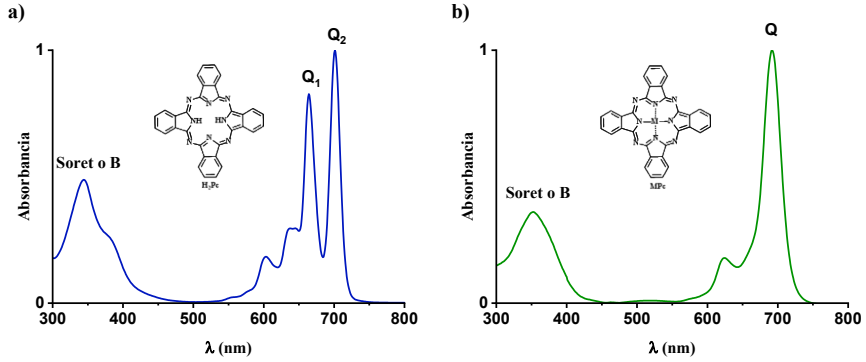

Figura 1.3. Espectro UV-Vis de a) una H_2Pc y b) una MPc.

1.3 Síntesis de ftalocianinas

La ruta sintética más común para la obtención de ftalocianinas es la ciclotetramerización de sus precursores a altas temperaturas y en presencia de un metal o sal metálica. Los precursores más comunes son el ftalonitrilo, la diiminoisoindolina, la ftalimida, la 2-cianobenzamida, el anhídrido ftálico y el ácido ftálico. Excepto en el caso de los dos primeros, el resto de los precursores necesitan una fuente de nitrógeno para que se produzca la ciclotetramerización, normalmente urea. Las MPcs pueden sintetizarse mediante la sustitución del ion metálico al ligando libre (M = $2H^+$) o por transmetalación utilizando complejos lábiles con metales alcalinos (litio, magnesio o sodio) [7] (**Esquema 1.2**).

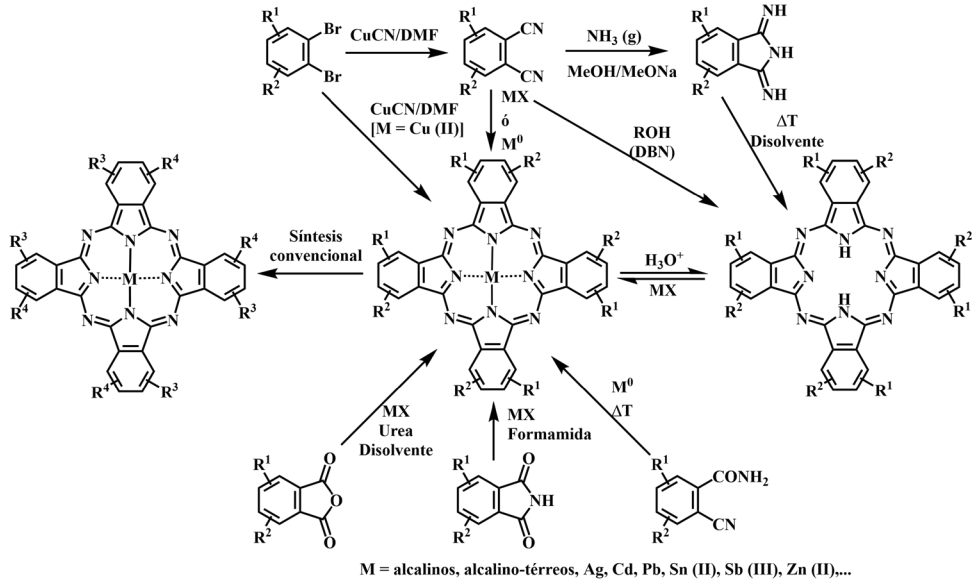

Esquema 1.2. Métodos de síntesis de ftalocianinas simétricas.

[7] P.A. Barrett, D.A. Frye, R.P. Linstead, *J.Chem.Soc*. **1938**, 1157–1165.

Los precursores más utilizados en la síntesis de ftalocianinas tanto libres como metálicas, son el ftalonitrilo y la diiminoisoindolina. Para que se lleve a cabo la ciclotetramerización del ftalonitrilo es necesaria la reducción de dos electrones y la donación de dos protones por parte de un reductor o disolvente. Para la ciclotetramerización en estado sólido (275 ºC), la hidroquinona y 1,2,3,6-tetrahidropiridina son buenos agentes reductores. [8, 9]

El método Linstead consiste en calentar el ftalonitrilo disuelto en un alcohol primario, como pentanol, con litio o sodio, para después deshacerse del ion metálico de la ftalocianina con un ácido acuoso.[7] Una pequeña variación de este método radica en mantener la disolución de ftalonitrilo y alcóxido en alcohol, como el octan-1-ol durante largos periodos a temperatura moderada (60ºC) o incluso temperatura ambiente. [10]

Existe otro método relacionado con el de Linstead que se basa en el uso de una cantidad catalítica de una base no nucleofílica como 1,8-diazabiciclo[5.4.0]undec-7-eno (DBU) o 1,5-diazabiciclo[4.3.0]non-5-eno (DBN) en un disolvente prótico como *n*-pentan-1-ol o 2-(*N*,*N*-dimetilamino)etanol (DMAE). [11] En el caso de la diiminoisoindolina, producto de la adición de amoniaco al ftalonitrilo, se pueden formar ftalocianinas simplemente calentando en un disolvente prótico. [12]

Recientemente se han desarrollado nuevos métodos para preparar ftalocianinas a baja temperatura o alta temperatura, pero con tiempos de reacción muy reducidos. Zheng y col utilizan diisopropil amiduro de litio (LDA) en THF en lugar de alcóxidos metálicos en alcohol para promover la reacción de ciclación. Con una ratio de 1:1 o 1:2 de ftalonitrilo:LDA consiguen rendimientos alrededor del 40% a temperatura ambiente en tres horas con ftalonitrilos sencillos. [13] Para reducir el tiempo de reacción puede ser muy útil sustituir el calentamiento tradicional por radiación de microondas. Por lo general se lleva a cabo mediante la suspensión de los precursores de ftalocianina en un pequeño volumen de un disolvente muy polar, seguido de su exposición a radiación de microondas en un horno especializado. [14]

1.3.1 Ftalocianinas sustituidas

Las ftalocianinas disponen de 16 posiciones para la unión de sustituyentes (cuatro en cada unidad de isoindol). Desde inicios de los años 80 se ha sintetizado un sorprendente número de derivados sustituidos. [15, 16] En la gran mayoría de casos se utilizan el ftalonitrilo o diiminoisoindolina ya sustituidos

[8] A.W Snow, J.R. Griffith, N.P. Marullo, *Macromolecules*, **1984**, *17*, 1614–1624.
[9] J.A. Thompson, K. Murata, D.C. Miller, J.L. Stanton, W.E. Broderick, B.M. Hoffman, J.A. Ibers, *Inorg.Chem*. **1993**, *32*, 3546–3553.
[10] a) C.C. Leznoff, M.G. Hu, K.J.M. Nolan, *Chem.Commun*. **1996**, 1245–1246. b) C.C. Leznoff, A.M. D'Ascanio, S.Z. Yildiz, *J.Porphyr. Phthalocyanines*, **2000**, *4*, 103–111.
[11] A. Tomoda, S. Saito, S. Ogawa, S. Shiraishi, *Chem.Lett*. **1980**, 1277-1280.
[12] P.J. Brach, S.J. Grammatica, O.A. Ossanna, L. Weinberger, *J.Heterocyc l.Chem.,* **1970**, *7*, 1403-1405.
[13] W. Zheng, C.-Z. Wan, J.-X. Zhang, C.-H. Li, X.-Z. You, *Tetrahedron Letters*, **2015**, *56*, 4459-4462.
[14] a) A.C.S. Gonzalez, L. Damas, R.T. Aroso, V.A. Tomé, L.D. Dias, J. Pina, R.M.B. Carrilho, M.M. Pereira, *Journal of Porphyrins and Phthalocyanines*, **2020**, *24*, 947-958. b) E.O. Moiseeva, A.D. Kosov, N.E. Borisova, B.N. Tarasevich, T.V. Dubinina, L.G. Tomilova, *Inorganica Chimica Acta*, **2022**, *535*, 120855-120864.
[15] N.B. McKeown, *Science of Synthesis*; S. Weinreb, Ed.; Georg Thieme Verlag: Stuttgart, Germany, **2003**; Vol. 17, inpress.
[16] M. Hanack, H. Heckmann, R. Polley, In *Houben Weyl: Methods in Organic Chemistry*; M. Hanack, Ed.; Georg Thieme Verlag, Stuttgart, Germany, **1997**; Vol. 9, pp 717–832.

Las ftalocianinas tetrasustituidas, independientemente de si la sustitución se produce en posiciones periféricas o no periféricas, se forman como una mezcla de regioisómeros con simetría C_{4h}, C_{2v}, C_s y D_{2h} (**Figura 1.4**). Esta heterogeneidad isomérica ayuda a proporcionar mayor solubilidad a los derivados, como, por ejemplo, la (*tert*-butil)$_4$Pc que es muy soluble en disolventes orgánicos sin modificar significativamente sus propiedades espectroscópicas y electroquímicas. [17] En contados casos es posible separar dichos isómeros por cromatografía (HPLC) [18] o recristalización. [19]

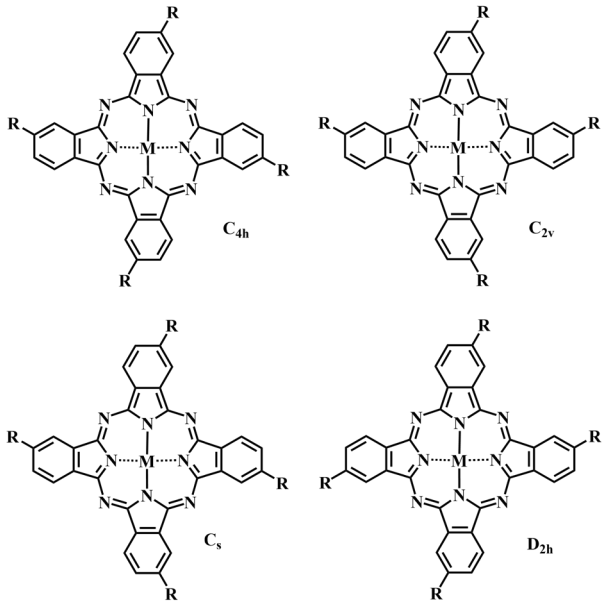

Figura 1.4. Regioisómeros de una ftalocianina tetrasustituida.

En cambio, cuando se utilizan ftalonitrilos disustituidos en posiciones α o β para sintetizar las correspondientes ftalocianinas, se obtienen Pcs solubles que carecen de isómeros al ser octasustituidas.

1.3.2 Preparación de derivados sustituidos a partir de ftalocianinas preformadas

Aunque menos común, también es posible obtener derivados sustituidos a partir de la propia ftalocianina. En la industria, es habitual utilizar reacciones de sustitución electrófila aromática como sulfonilación, [20] halogenación [21] y nitración. [22] El problema de este tipo de reacciones es que al poseer las ftalocianinas 16 posiciones posibles el resultado es una compleja mezcla de productos.[21] Sin embargo, la sustitución o modificación de sustituyentes en una ftalocianina ya formada, mediante reacciones eficientes, es de gran ayuda para la introducción de grupos funcionales que no se podría llevar a cabo con la ciclotetramerización. Por ejemplo, reacciones de desprotección del éter metílico de octametoxiftalocianinas para

[17] S.A. Mikhalenko, S.V. Barknova, O.L. Lebedev, E.A. Luk'yanets, *Zh.Obshch.Khim*. **1971**, 41, 2735–2739.
[18] M. Hanack, D.Y. Meng, A. Beck, M. Sommerauer, L.R. Subramanian, *J.Chem. Soc., Chem.Commun*. **1993**, 58–60.
[19] M. Brewis, G.J. Clarkson, P. Humberstone, S. Makhseed, N.B. McKeown, *Chem.Eur.J*., **1998**, *4*, 1633–1640.
[20] R.P. Linstead, F.T. Weiss, *J.Chem.Soc*., **1950**, 2975-2981.
[21] A.H. Jackson, In *The Porphyrins*; D. Dolphin, Ed.; Academic Press: New York, **1977**; Vol. 1, pp 374–388.
[22] M. Hedayatullah, *Compt.Rend.Acad.Sci. Ser.II C,* **1983**, *296*, 621–623.

obtener octahidroxiftalocianinas, o incluso las posibles alquilaciones posteriores de los grupos hidroxilo resultantes. [23, 24]

1.3.3 Ftalocianinas asimétricas

Las ftalocianinas asimétricas son aquellas en las que al menos una unidad isoindol está sustituida con grupos funcionales diferentes al resto. Pueden diferenciarse tres patrones de sustitución: (I) una de las unidades es diferente a las otras tres (A_3B); (II) las unidades adyacentes poseen los mismos sustituyentes (AABB), y (III) las unidades opuestas tienen los mismos sustituyentes (ABAB) (**Figura 1.5**). A lo largo de la historia se han desarrollado diferentes métodos para la síntesis de ftalocianinas asimétricas, a continuación, se describen los más comunes:

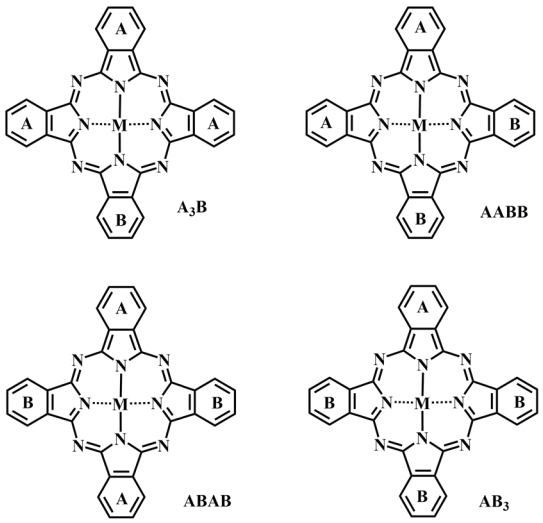

Figura 1.5. Estructura de ftalocianinas asimétricamente sustituidas.

Ciclotetramerización estadística

Es el método más utilizado a pesar de no ser selectivo, consiste en la ciclotetramerización de dos ftalonitrilos o diiminoisoindolina sustituidos con diferentes grupos funcionales, lo que da lugar a la distribución estadística de las 6 posibles ftalocianinas (A_4, A_3B, AABB, ABAB, AB_3, B_4). La reactividad y proporción molar de los precursores definirán la proporción de cada una de ellas. Por ejemplo, para una reacción con precursores de igual reactividad y misma proporción molar se obtendría un 6.25% A_4, un 25% A_3B (AB_3), un 12.5% ABAB, un 25% AABB y un 6.25% B_4. [25] Se puede desplazar la reacción hacia la formación de un producto respecto al resto, por ejemplo, al utilizar una relación molar 3:1 favorece la síntesis de la ftalocianina asimétrica A_3B frente al resto (**Esquema 1.3**). También es importante tener en cuenta la reactividad de los precursores a la hora de ajustar la proporción

[23] J.F. van der Pol, E. Neeleman, J.C. van Miltenburg, J.W. Zwikker, R.J.M. Nolte, W. Drenth, *Macromolecules*, **1990**, *23*, 155–162.
[24] C.C. Leznoff, S. Vigh, P.I. Svirskaya, S. Greenberg, D.M. Drew, E. Ben-Hur, I. Rosenthal, *Photochem. Photobiol*., **1989**, *49*, 279–284.
[25] N.B. McKeown, I. Chambrier, M.J. Cook, *J.Chem. Soc., Perkin Trans. 1,* **1990**, 1169–1177.

a utilizar. El mayor problema de este método es la difícil purificación del producto deseado al ser un método no selectivo y formarse todas las posibles ftalocianinas. [26]

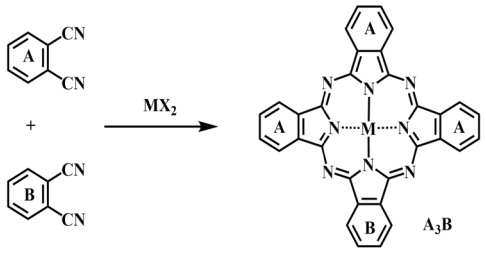

Esquema 1.3. Síntesis de ftalocianinas asimétricas mediante ciclotetramerización estadística.

Expansión del anillo

A finales de los años 80 se desarrolló el que puede considerarse el primer método selectivo para la síntesis de ftalocianinas A_3B. El método necesita la síntesis previa de una subftalocianina. [27] Las subftalocianinas son macrociclos constituidos por tres unidades de isoindol y un átomo de boro en su cavidad central, estructura cónica con geometría C_{3v} y 14 electrones π deslocalizados. Se sintetizan mediante la reacción del ftalonitrilo en presencia de BCl_3 u otros derivados del boro. Una vez obtenida la subftalocianina se hace reaccionar con otro precursor con diferentes grupos funcionales, dando lugar al derivado formado por cuatro unidades isoindólicas abierto, que puede volver a cerrarse para formar la ftalocianina asimétrica A_3B [28] (**Esquema 1.4**).

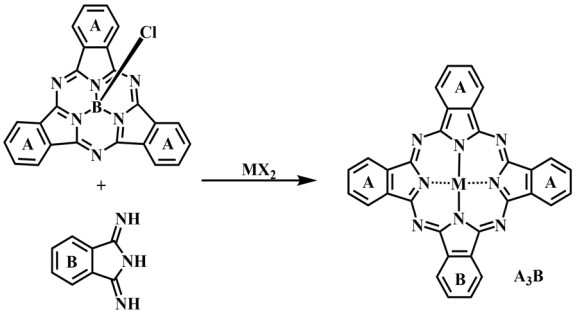

Esquema 1.4. Síntesis de ftalocianina asimétrica mediante expansión del anillo.

A pesar de ser un método selectivo, no es el más utilizado debido a que presenta diferentes inconvenientes como la síntesis y purificación previa de una subftalocianina, o que la subftalocianina puede fragmentarse parcialmente y dar lugar al resto de derivados de ftalocianina posibles. [29]

[26] G. Dilber, A. Nas, M. Pişkin, M. Durmuş, *Transition Metal Chemistry*, **2022**, *47*, 157–168.
[27] J. Labella, T. Torres*, Trends in Chemistry*. **2023**, DOI: 10.1016/j.trechm.2023.02.003
[28] A. Thimiopoulos, E.D. Simandiras, N. Psaroudakis, *Inorganica Chimica Acta*, **2019**, *498*, 119105-119113.
[29] Á. Sastre, B. del Rey, T. Torres, *J. Org. Chem*., **1996**, *61*, 8591-8597.

Soporte polimérico

Leznoff y Hall desarrollaron una forma de obtener ftalocianinas asimétricas gracias a la ayuda de un soporte polimérico. [30] El método consiste en la unión de un polímero a uno de los precursores, seguida de la ciclotetramerización con otro precursor, separación mediante una simple filtración del resto de productos en disolución, para finalmente eliminar el polímero y obtener la ftalocianina asimétrica (**Esquema 1.5**). [31] El mayor punto fuerte de este método es que se evita la formación del resto de derivados de ftalocianina. Sin embargo, son necesarios dos pasos adicionales, la síntesis del precursor unido al polímero y la posterior eliminación de éste.

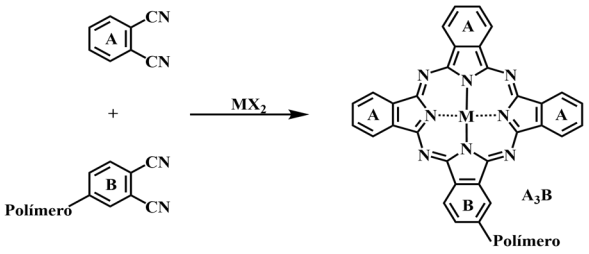

Esquema 1.5. Síntesis de ftalocianina asimétrica mediante soporte polimérico.

Condensación cruzada

La condensación cruzada [32] de los sustratos puede suceder si uno de ellos no puede autocondensarse, como la 1,3,3-tricloroisoindolenina, y si puede reducirse la temperatura de formación de la ftalocianina fomentando así la condensación cruzada frente la autocondensación, favoreciendo la formación de ftalocianinas ABAB y A_3B (**Esquema 1.6a**). Otro método para favorecer la formación de ftalocianinas A_3B y AABB, requiere utilizar unidades triméricas o diméricas de un precursor con otro distinto. El dímero se sintetiza previamente con alcóxido de litio en metanol (**Esquema 1.6b**). [33]

[30] a) C.C. Leznoff, T. W. Hall, *Tetrahedron Lett*., **1982**, *23*, 3023-3026. b) C. C. Leznoff, E I. Svirskaya, B. Khouw, R. L. Cemy, E Seymour, A. B. E Lever, *J. Org. Chem*., **1991**, *56*, 82-90.
[31] a) V.B. Khajone, K.R. Balinge, D.S. Patle, P.R. Bhagat, *Journal of Molecular Liquids*, **2019**, *288*, 111032. b) J. Wang, Q. Duan, *J. Phys.: Conf. Ser*. **2020**, *1637*, 012041-12045.
[32] C.C. Leznoff, S. Greenberg, B. Khouw, A. B. E Lever, *Can. J. Chem*., **1987**, *65*, 1705-1713.
[33] a) E. Güzel, D.P. Medina, M. Medel, M. Kandaz, T. Torres, M.S. Rodríguez-Morgade, *J. Mater. Chem. C*, **2021**, *9*, 10802-10810. b) J.Y.M. Chan, D.K.P. Ng, *J. Org. Chem*., **2022**, *87*, 7213–7218.

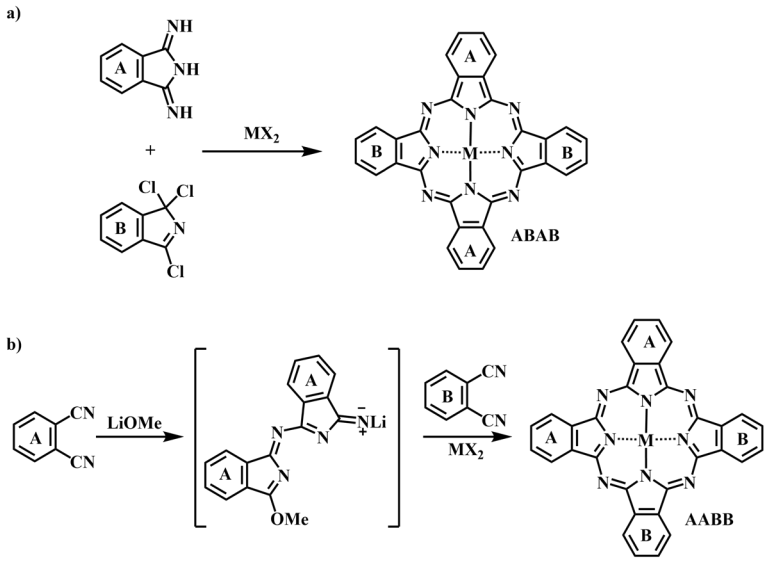

Esquema 1.6. Síntesis de ftalocianinas asimétricas mediante condensación cruzada.

1.3.4 Síntesis de Pcs axiales

Las ftalocianinas pueden sustituirse en posición axial siempre que el metal situado en la cavidad interna lo permita. El silicio es el metal que más se ha utilizado para la sustitución axial de ftalocianinas. [34] La síntesis de este tipo de ftalocianinas requiere la formación previa de un intermediario al cual introducir posteriormente el sustituyente deseado. Las ftalocianinas intermedias más comunes son la dicloroftalocianina de silicio, obtenida a partir de la ciclotetramerización de la diiminoisoindolina y tetracloruro de silicio; y la dihidroxiftalocianina obtenida de la hidrólisis en medio básico de la anterior. Finalmente, se funcionaliza axialmente el intermedio para obtener la SiPc objetivo (**Esquema 1.7**).

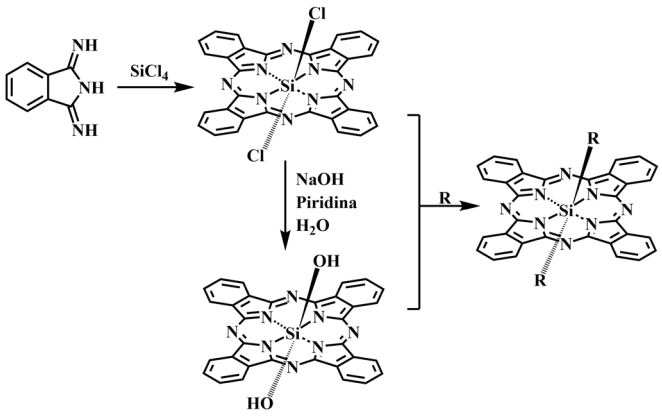

Esquema 1.7. Síntesis de ftalocianinas sustituidas axialmente.

[34] a) K. Mitra, M.C.T Hartman, *Org. Biomol. Chem*., **2021**, *19*, 1168-1190. b) V. Sobrino-Bastán, L. Martín-Gomis, Á. Sastre-Santos, *Journal of Porphyrins and Phthalocyanines*, **2023**, DOI: 10.1142/S1088424622500961.

1.4 Aplicaciones de las ftalocianinas

Su intenso color y alta estabilidad ha hecho que sean explotadas comercialmente como tintes y pigmentos prácticamente desde sus inicios. Además, las ftalocianinas han sido utilizadas en múltiples campos de investigación. [35, 36] Algunas aplicaciones de los cuales se comentan brevemente a continuación.

En catálisis, se han estudiado ftalocianinas para la reducción de CO_2, por ejemplo, las ftalocianinas de níquel sintetizadas por el grupo del profesor Liu, sustituidas con grupos dadores de electrones para aumentar la adsorción del CO_2 y su activación (**Figura 1.6**). [37]

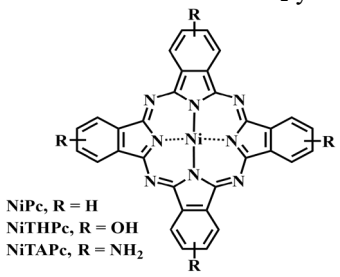

Figura 1.6. Estructura de NiPcs utilizadas para catalizar la reducción de CO_2.

También han sido ampliamente utilizadas como sensores. Por ejemplo, la ftalocianina de cinc en un transistor de efecto de campo orgánico (OFET) en un sensor de NO_2 [38] (**Figura 1.7a**) o la ftalocianina asimétrica de cobalto utilizada como sensor reutilizable de metales pesados (Hg (II), Cu(II), Pb(II) y Cd(II)) (**Figura 1.7b**). [39]

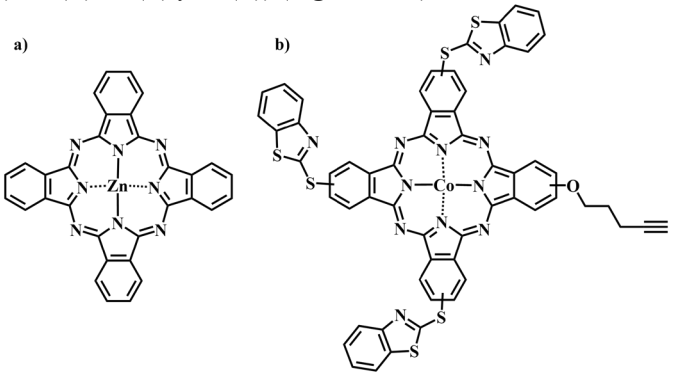

Figura 1.7. Estructura de MPcs utilizadas como sensores de a) NO_2 y b) metales pesados.

[35] a) C.C Leznoff, A.B.P. Lever, *Phthalocyanines: Properties and Applications*, **1989**, VCH, New York, Vols. 1–4. b) N.B. McKeown, *Phthalocyanine Materials: Synthesis, Structure and Function,* **1998**, Cambridge University Press, Cambridge, UK.

[36] a) J. Zhao, H. Lyu, Z. Wang, C. Ma, S. Jia, W. Kong, B. Shen, *Separation and Purification Technology*, **2023**, *312*, 123404-123431. b) J. Rak, M. Kabesova, J. Benes, P. Pouckova, D. Vetvicka, *Life*, **2023**, *13*, 305-324. c) Z. Jiang, Y. Ding, J.F. Lovell, Y. Zhang, *Photoacoustics*, **2022**, *28*, 100426-100440. d) H.-g. Wang, Q. Wu, L. Cheng, L. Chen, M. Li, G. Zhu,
Energy Storage Materials, **2022**, *52*, 495-513.

[37] K. Chen, M. Cao, Y. Lin, J. Fu, H. Liao, Y. Zhou, H. Li, X. Qiu, J. Hu, X. Zheng, M. Shakouri, Q. Xiao, Y. Hu, J. Li, J. Liu, E. Cortés, M. Liu, *Adv. Funct. Mater*. **2022**, *32*, 2111322-2111330.

[38] Y. Zhu, Q. Xie, Y. Sun, L. Wang, Q. Sun, L. Wang, *Adv. Mater. Interfaces,* **2020**, *7*, 1901579-1901586.

[39] G. Fomo, N. Nwaji, T. Nyokong, *Journal of Electroanalytical Chemistry*, **2018**, *813*, 58-66.

En cuanto al almacenamiento de información, el grupo de Lei ha utilizado una poliftalocianina de cobre en forma de lámina delgada por deposición de vapor como capa activa sobre sustratos de silicio en dispositivo de almacenamiento de memoria (**Figura 1.8**). [40]

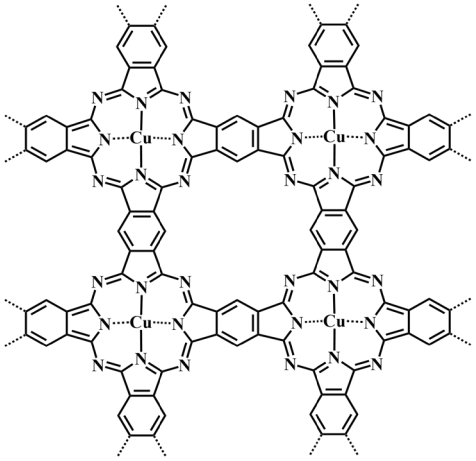

Figura 1.8. Estructura de poliCuPc aplicada en dispositivos de memoria.

Las ftalocianinas han sido empleadas en *redes metal-orgánicas* (MOFs) como se puede observar en el ejemplo de una cavidad óptica formada por un MOF cristalino con ftalocianinas de silicio como andamios (**Figura 1.9a**). [41] La inclusión de MOFs en las cavidades ópticas representa una innovación funcional respecto a otros materiales, ya que permite la carga y liberación reversible de especies huéspedes dentro y fuera de los resonadores ópticos. Esta capacidad abre un nuevo campo de posibilidades para el desarrollo de sensores ópticos avanzados. Otro ejemplo de ello es el MOF-1992, en el que se utiliza una ftalocianina de cobalto con una alta actividad reductora de CO_2 en agua (**Figura 1.9b**). [42]

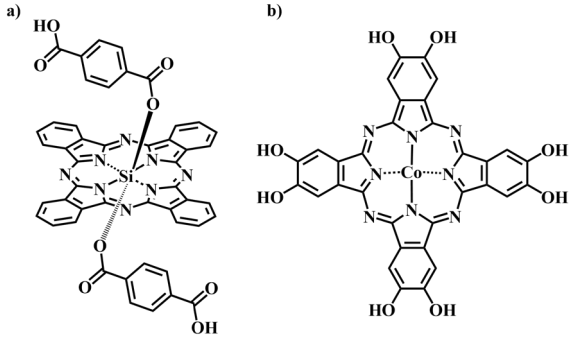

Figura 1.9. Estructura de diferentes MPcs utilizadas en MOFs.

[40] X. Guo, J. Liu, L. Cao, Q. Liang, S. Lei, *ACS Omega,* **2019**, *4*, 10419–10423
[41] R. Haldar, Z. Fu, R. Joseph, D. Herrero, L. Martín-Gomis, B.S. Richards, I.A. Howard, Á. Sastre-Santos, C. Wöll, *Chem. Sci*., **2020**, *11*, 7972-7978.
[42] R. Matheu, E. Gutierrez-Puebla, M.Á. Monge, C.S. Diercks, J. Kang, M.S. Prévot, X. Pei, N. Hanikel, B. Zhang, P. Yang, O.M. Yaghi, *J. Am. Chem. Soc*., **2019**; *141*, 17081-17085.

Las ftalocianinas son cromóforos muy prometedores en el ámbito de la fotosíntesis artificial debido a su capacidad fotoquímica. Específicamente, se han sintetizado y caracterizado dos familias diferentes de ftalocianinas de Zn asimétricas, que absorben en la ventana espectral de 700-800 nm y contienen un sustituyente imidazol-fenilo fusionado o un grupo imidazol-hidroxifenilo fusionado (**Figura 1.10**). Estas ftalocianinas han sido diseñadas como modelos bioinspirados de los cofactores Chlf/TirosinaZ/Histidina190 del PSII. [43]

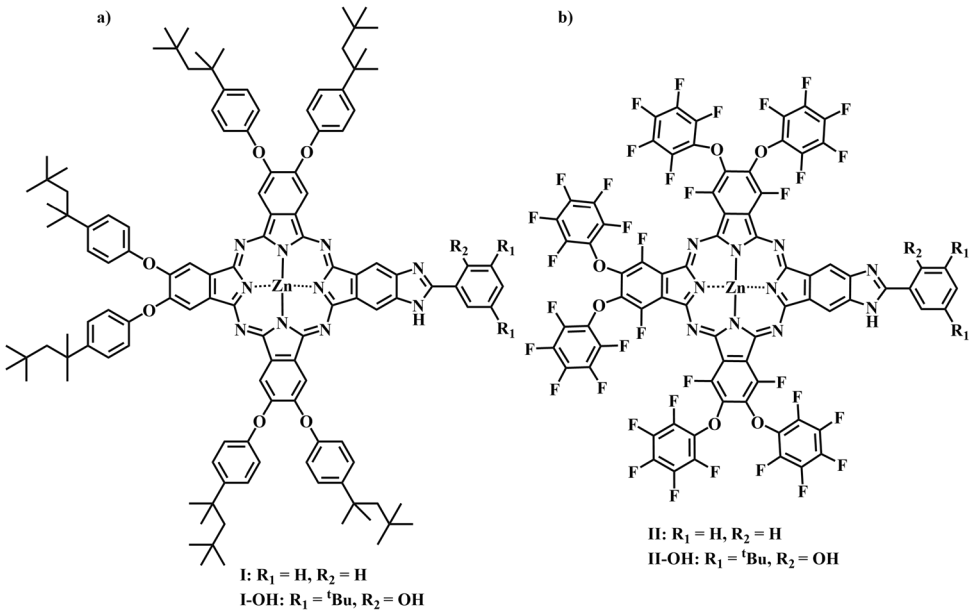

Figura 1.10. Estructura de diferentes ZnPcs utilizadas como análogos fotosintéticos.

Las ftalocianinas se han utilizado en terapia fotodinámica (PDT) gracias a su capacidad de generar especies reactivas de oxígeno (ROS) y $^1O_2$ al ser irradiadas con luz visible. El proceso comienza cuando la luz llega a la Pc, que absorbe la energía y pasa del estado fundamental al primer estado excitado singlete (S^*_1). En este punto, para volver al estado fundamental, la energía puede disiparse en forma de calor o mediante la emisión de radiación (fluorescencia). Otra alternativa es la formación de un estado triplete (T^*_1) a través de un cruce intersistémico (ISC), seguido de desactivación por emisión de radiación (fosforescencia). Además, mientras la Pc se encuentra en T^*_1 pueden producirse dos tipos de procesos: una transferencia electrónica hacia biomoléculas generando ROS (Tipo I) o una transferencia energética al oxígeno molecular ($^3O_2$) que lo transforma en oxígeno singlete ($^1O_2$) (Tipo II). Estas especies oxidan los componentes fundamentales de la célula y desencadenan procesos que conducen a la muerte celular. Ambos mecanismos pueden actuar conjuntamente, según el tipo de fotosensibilizador o la concentración de $^3O_2$. Estas propiedades han permitido a las ftalocianinas actuar como agente bacteriostático y antitumoral. Ejemplo de ello son las ftalocianinas de cinc e indio sintetizadas por el grupo de Nyokong capaces de erradicar *S. aureus* y biopelículas de *E. coli* (**Figura 1.12a**). [44] También las ftalocianinas de cinc tetra y

[43] J. Follana-Berná, R. Farran, W. Leibl, A. Quaranta, Á. Sastre-Santos, A. Aukauloo, *Angew. Chem. Int. Ed.* **2021**, *60*, 12284-12288.
[44] Y. I. Openda, B. Babu and T. Nyokong, *Photodiagnosis and Photodyn. Ther.*, **2022**, *38*, 102863-102876.

octasustituidas utilizadas para terapia fotodinámica en células HeLa por Yurttas y colaboradores (**Figura 1.12b**).[45] Además de su uso en PDT, se pueden combinar funciones como su fluorescencia para el marcaje y su capacidad para reconocer y unirse a regiones específicas del ADN como los G4s que veremos en el capítulo 2.

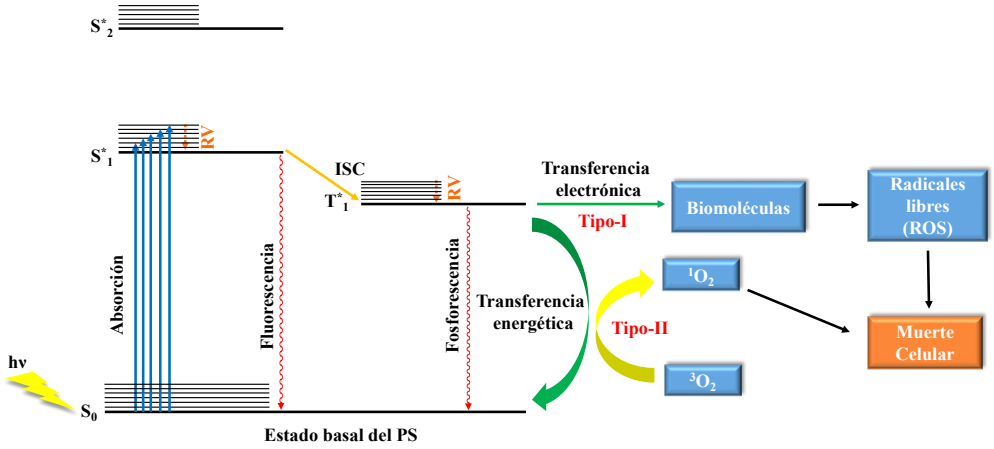

Figura 1.11. Diagrama del mecanismo de acción de la PDT.

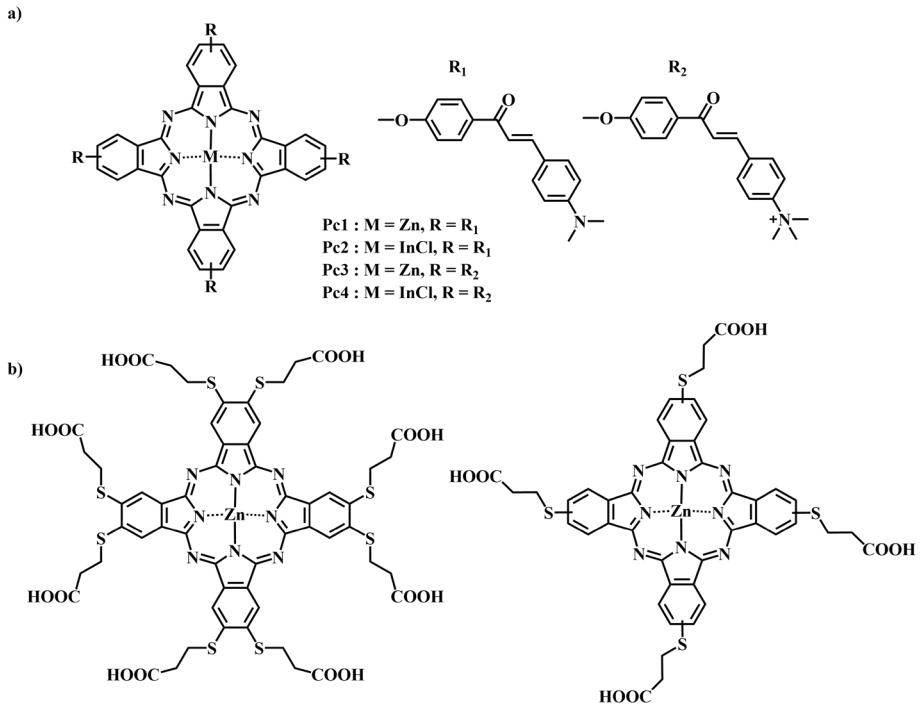

Figura 1.12. Estructura de MPcs utilizadas en terapia fotodinámica.

[45] A. G. Yurttaş, A. M. Sevim, K. Çınar, G. Y. Atmaca, A. Erdoğmuş, A. Gül, *Dyes and Pigments*, **2022**, *198*, 110012-110019.

Además de estas aplicaciones, también se han utilizado en semiconductores orgánicos, [46] cristales líquidos, [47] óptica no lineal [48] o para el almacenamiento de energía, en este caso un nanocompuesto de tetraaminoftalocianina de níquel y oxido de grafeno se ha estudiado como pseudocapacitador (**Figura 1.13**). [49] Finalmente, las ftalocianinas han sido ampliamente utilizadas en los distintos tipos de células solares, tema que se aborda con mayor profundidad en el siguiente capítulo.

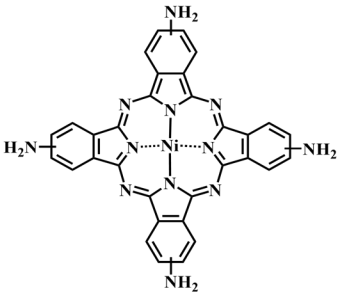

Figura 1.13. Estructura de una NiPc utilizada como pseudocapacitador.

[46] F. Ngassam, E. Urbain, L. Joly, S. Boukari, J. Arabski, F. Bertran, P. Le Fèvre, G. Garreau, P. Wetzel, M. Alouani, M. Bowen, and W. Weber, *J. Phys. Chem. C*, **2019**, *123*, 26475–26480.
[47] B. Canımkurbey, M. C. Taşkan, S. Demir, E. Duygulu, D. Atilla, F. Yuksel, *New J. Chem*., **2020**, *44*, 7424-7435.
[48] S. Mgidlana, D. O. Oluwole, T. Nyokong, *Polyhedron*, **2019**, *159*, 102-115.
[49] K. Makgopa, P. M. Ejikeme, K. I. Ozoemena, *Electrochimica Acta*, **2016**, *212*, 876-882.

Capítulo 2

Derivados de Ftalocianina y su aplicación como Material Transportador de Huecos

2 Ftalocianinas en células solares de perovskita

2.1 Introducción

Actualmente los combustibles fósiles cubren la mayor parte de la necesidad energética mundial, siendo el carbón el principal en la producción de electricidad gracias a su bajo precio. Sin embargo, estos combustibles presentan diversos inconvenientes ya que existe una disponibilidad limitada a largo plazo y, además, contribuyen a la contaminación y al calentamiento global. El Ministerio para la Transición Ecológica y Reto Demográfico publicó en 2021 un comunicado donde se advierte que los niveles de CO_2 atmosférico no solo siguen en aumento, sino que además el aumento es mayor año tras año, según las medidas realizadas por los observatorios de Izaña y Mauna Loa (Figura 2.1). [50] Estos problemas han impulsado la búsqueda de fuentes de energías alternativas para reemplazar los combustibles fósiles que sean respetuosas con el medio ambiente.

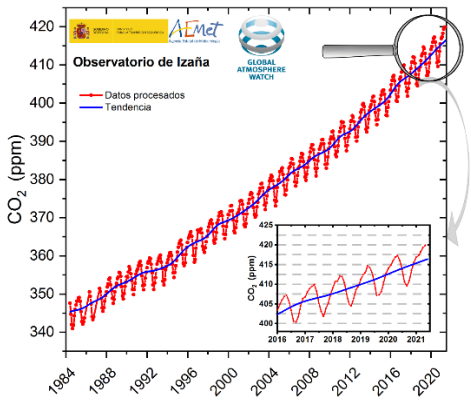

Figura 2.1. Promedios mensuales de concentración de CO_2 (ppm) calculados a partir de las medidas minutales realizadas en el observatorio de Izaña en condiciones de fondo atmosférico (puntos rojos) junto con la tendencia de CO_2 (línea azul).

Así fue como surgieron lo que se conoce como energías renovables, entre las que podemos destacar la energía hidroeléctrica, solar y eólica. La energía solar es la fuente de energía renovable que más se ha desarrollado a lo largo de las últimas décadas. La tierra recibe del sol todos los días $2.9x10^{15}$ kWh de energía en forma de radiación electromagnética, esto es 100 veces más energía de la que se consume durante un año en el planeta.

Las células solares se pueden clasificar en tres categorías conocidas como primera, segunda y tercera generación. La primera generación de células solares se basa en el silicio cristalino. La segunda generación, que se creó con la intención de reducir el consumo de silicio y explorar otros nuevos materiales, está basadas en la tecnología de láminas delgadas. La tercera generación también está basada en láminas delgadas, pretende reducir el coste y utilizar nuevos materiales que sean respetuosos con el medio ambiente y añadan nuevas funcionalidades como flexibilidad o semitransparencia (**Esquema 2.1**).

[50] Ministerio para la Transición Ecológica y el Reto Demográfico, Nota de prensa: *Máximo histórico en Izaña*, 21/06/2021

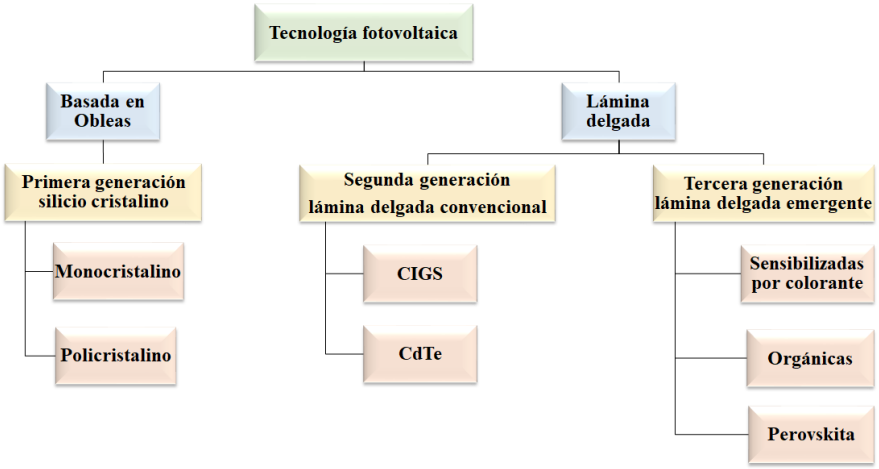

Esquema 2.1. Clasificación de las tecnologías fotovoltaicas.

2.1.1 Primera generación

La primera generación de células solares está basada en el silicio, que es un material muy abundante en la corteza terrestre (silicatos). La eficiencia final de este tipo de dispositivos viene dada por la calidad del silicio. Se pueden distinguir dos subgrupos: las células solares de silicio monocristalino y las de silicio policristalino.

Las células solares de silicio monocristalino están constituidas por obleas de silicio de estructura cristalina homogénea. Esto quiere decir que su parámetro de red, su orientación y sus propiedades electrónicas son constantes en toda la lámina. Por este motivo su desarrollo y fabricación es delicado, lento y requiere condiciones controladas cuidadosamente lo que encarece el coste de producción, sin embargo, poseen una mayor eficiencia de conversión energética, en el rango de 15% a 20% a escala comercial.

La llegada de las células solares de silicio policristalino vino propiciada por el alto coste de fabricación de sus antecesoras y con motivo de aprovechar los residuos de silicio de las industrias electrónicas. En este caso la célula solar se compone de una serie de pequeños cristales de silicio lo que reduce el coste de producción, aunque también la eficiencia del dispositivo. Este tipo de células son las que dominan el mercado actual con eficiencias entre el 13% y 16%.

2.1.2 Segunda generación

Las células solares de segunda generación surgieron de la búsqueda de materiales más baratos y el uso de menor cantidad de estos a partir de rutas de fabricación de películas delgadas. Las principales son de silicio amorfo, seleniuro de cobre, indio y galio (CIGS) y telururo de cadmio (CdTe). A pesar de conseguir reducir los costes de fabricación la eficiencia de conversión energética de estas células es muy inferior, por lo que ha sido necesaria la investigación de otro tipo de materiales capaces de solventar este problema.

2.1.3 Tercera generación

La tercera generación pretendía, además de reducir los costes de fabricación, obtener eficiencias equiparables e incluso superiores a las células solares de silicio monocristalino. Se trata de células solares orgánicas que aportan nuevas propiedades como ligereza, flexibilidad y semitransparencia entre otras. En este grupo se pueden diferenciar las células solares sensibilizadas por colorante (DSSCs), las células solares orgánicas y las células solares de perovskita.

Células solares sensibilizadas por colorante (DSSCs)

Las células solares sensibilizadas por colorante surgieron en 1991 [51] y han sido las más estudiadas en las últimas décadas. Su arquitectura viene definida por un sustrato de vidrio u óxido conductor transparente (TCO), una capa compacta de TiO_2 (c-TiO_2), una capa de TiO_2 mesoporoso (mp-TiO_2) sensibilizada por el colorante, un electrolito líquido y un contraelectrodo de Pt, TCO o vidrio (**Figura 2.2a**).

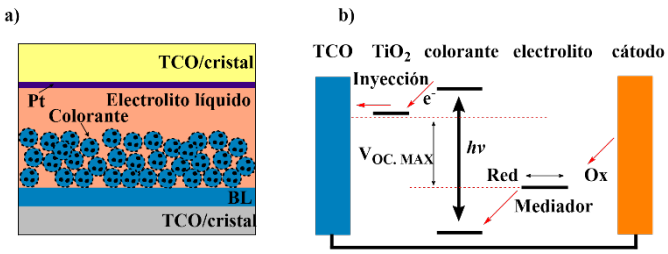

Figura 2.2. a) Diagrama esquemático y b) mecanismo de una célula solar sensibilizada por colorante.

El funcionamiento de una DSSC parte de la fotoexcitación del colorante. Los fotones incidentes son absorbidos por el colorante que recubre la superficie del TiO_2, los electrones pasan del estado fundamental al excitado, tras lo cual son inyectados en la banda de conducción del mp-TiO_2 y finalmente al electrodo frontal (ánodo). En este proceso el colorante queda en estado oxidado, que se reduce al estado fundamental gracias a un electrón procedente del reductor que forma el electrolito líquido (p. ej., I^-). La especie oxidada (p. ej., I_3^-) difunde hacia el electrodo metálico (cátodo) para ser regenerada, cerrando así el circuito de flujo de electrones (**Figura 2.2b**).

Este tipo de células solares presenta diversos problemas, como la falta de colorantes con una cobertura espectral mayor, degradación atmosférica y complicaciones de ingeniería como la encapsulación y sellado del líquido del dispositivo.

Las ftalocianinas han sido ampliamente utilizadas como colorante en DSSCs (células solares sensibilizadas por colorante) desde los años 90, por ejemplo, las ftalocianinas de rutenio de Grätzel y Murrer (**Figura 2.3a**), [52] y siguen siendo protagonistas en la actualidad, publicándose estudios de ellas como la ftalocianina de cinc asimétrica con tres grupos dadores 2,6-di-*terc*-butil-4-metilfenoxilos y un ácido carboxílico como anclaje del grupo de la profesora Güreck, que rindió una buena eficiencia que se podía mejorar añadiendo otros

[51] B. O'Regan, M. Gratzel, *Nature*, **1991**, *353*, 737-740.
[52] a) Md.K. Nazeeruddin, R. Humphry-Baker, M. Grätzel, B.A. Murrer, *Chem. Commun*., **1998**, 719-720. b) L. Martín-Gomis, F. Fernández-Lázaro, Á. Sastre-Santos, *J. Mater. Chem. A*, **2014**, *2*, 15672-15682.

colorantes como cosensibilizadores (**Figura 2.3b**). [53] O las cuatro ftalocianinas octasustituidas de cinc y cobalto estudiadas por el grupo de Gül (**Figura 2.3c**). [54]

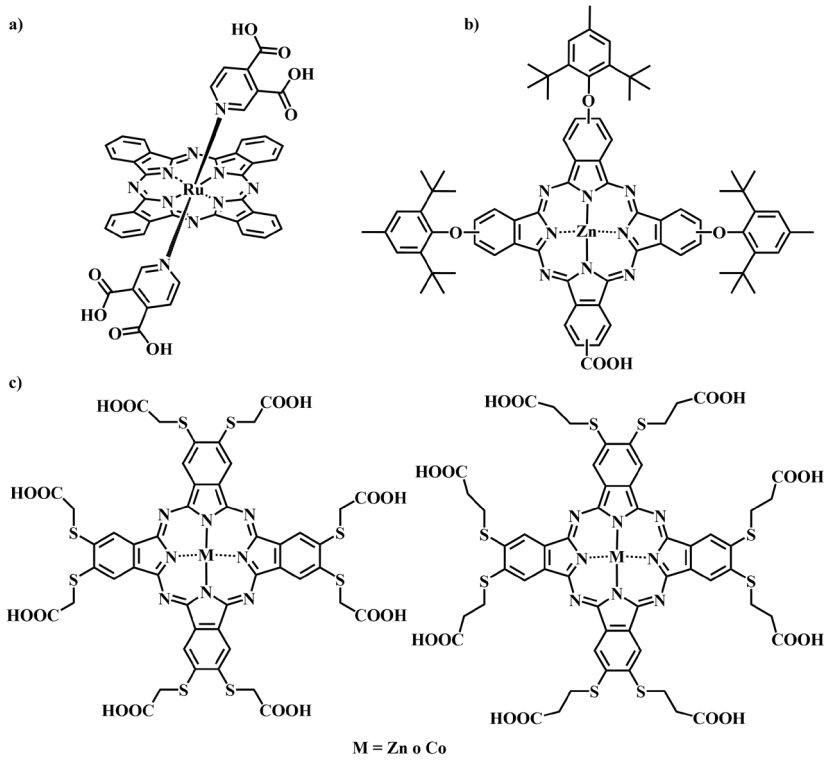

Figura 2.3. Estructuras de MPcs utilizadas como colorante en DSSCs.

En nuestro grupo de investigación también se han sintetizado diferentes ftalocianinas para su aplicación como colorantes en DSSCs. Por ejemplo, las ftalocianinas de silicio SiPc 1 y SiPc 2 sustituidas axialmente con diferentes grupos que portan ácidos carboxílicos (**Figura 2.4a**) o las ftalocianinas asimétricas de cinc como cosensibilizantes de puntos cuánticos en DSSCs, que aumentaban la eficiencia de los dispositivos en comparación con aquellos que no tenían ftalocianina (**Figura 2.4b**). [55]

[53] K. Harmandar, K. Granados-Tavera, M. Gezgin, M. Nebioğlu, İ. Şişman, G. Cárdenas-Jirón, D. Atilla, A. G. Gürek, *New J. Chem*., **2022**, *46*, 714-725.
[54] C. Ilgün, A. M. Sevim, S. Çakar, M. Özacar, A. Gül, *Solar Energy*, **2021**, *218*, 169-179.
[55] a) L. Martín-Gomis, E. M. Barea, F. Fernández-Lázaro, J. Bisquert, Á. Sastre-Santos, *J. Porphyrins Phthalocyanines*, **2011**, *15*, 1005-1010; b) V. M. Blas-Ferrando, J. Ortiz, V. González-Pedro, R. S. Sánchez, I. Mora-Seró, F. Fernández-Lázaro, Á. Sastre-Santos, *Adv. Func. Mater*., **2015**, *25*, 3220-3226; c) V. M. Blas-Ferrando, J. Ortiz, V. González- Pedro, R. S. Sánchez, I. Mora-Seró, F. Fernández-Lázaro, Á. Sastre-Santos, *Chem. Commun*., **2015**, *51*, 1732-1735.

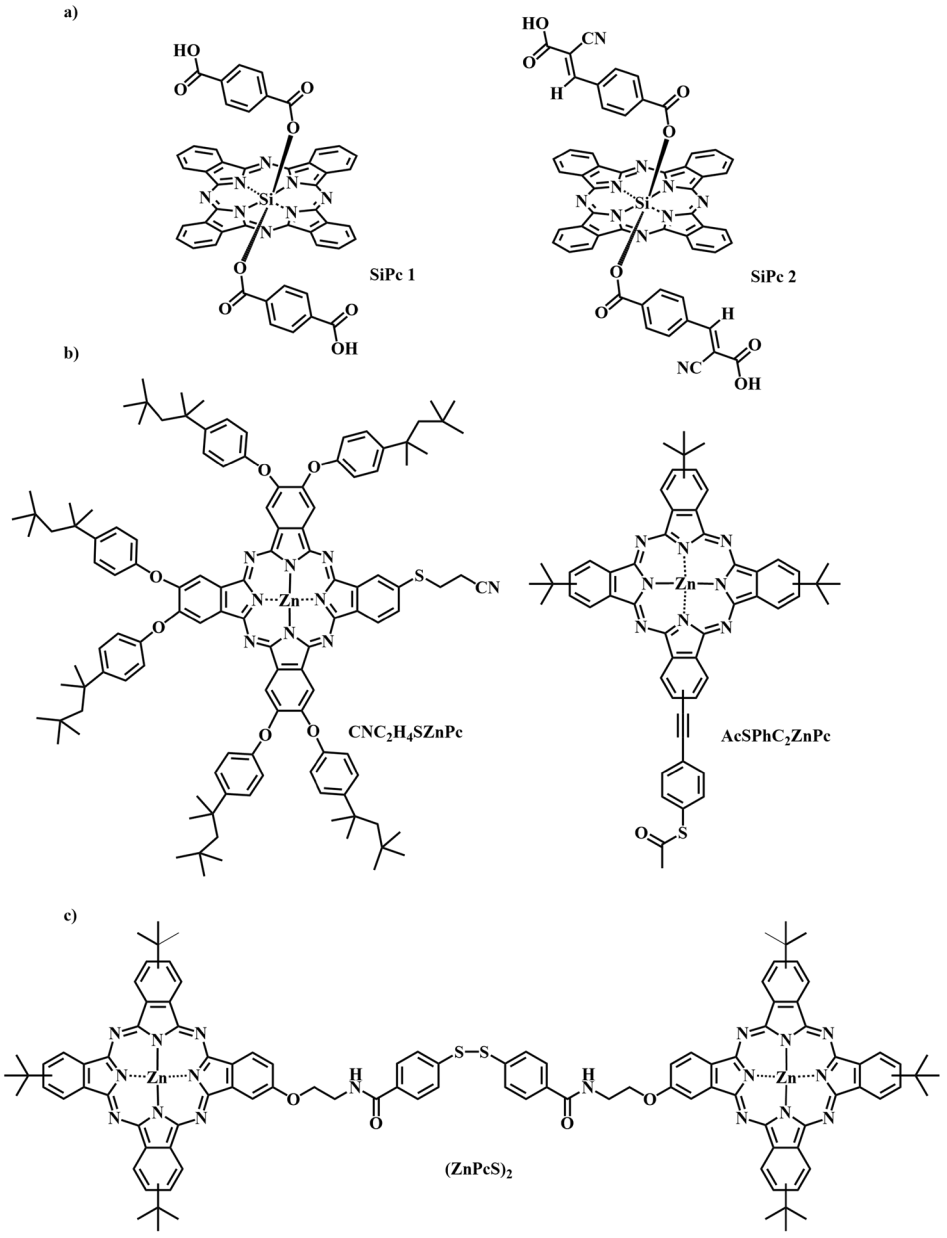

Figura 2.4. Estructura de diferentes ftalocianinas utilizadas en DSSCs.

Células solares orgánicas (FHJ y BHJ)

La estructura típica de estos dispositivos consiste en uno o varios materiales fotoactivos entre dos electrodos. Se puede diferenciar entre células orgánicas de heterounión plana (FHJ) y de heterounión masiva (BHJ).

Los dispositivos de heterounión plana se caracterizan porque el material fotoactivo es una bicapa formada por un material orgánico dador y otro aceptor. El material dador es el

encargado de absorber el fotón, formándose el excitón (par electrón/hueco ligados por atracción electrostática) que debe difundir hasta la interfase dador/aceptor donde se separará en cargas libres. El hueco y el electrón difundirán hasta los electrodos correspondientes a través de la capa dadora y aceptora respectivamente (**Figura 2.5a**).

En el caso de las células solares de heterounión masiva (BHJ), la bicapa de material orgánico dador y aceptor se han sustituido por una única capa en la que ambos materiales se encuentran entremezclados, aumentando así la superficie de contacto entre ambas fases y facilitando la separación de las cargas (**Figura 2.5b**).

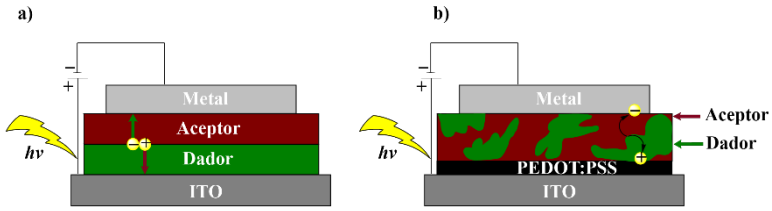

*Figura 2.**5**. Diagrama de una célula solar de a) heterounión plana p-n y b) heterounión masiva.*

En nuestro grupo se ha llevado a cabo la síntesis de ftalocianinas de cobre y zinc con una alta densidad de átomos de flúor, con el propósito de utilizarlas como tercer componente en células solares de heterounión masiva ternarias (**Figura 2.6**). Se han obtenido eficiencias notables en la conversión de energía solar a eléctrica, llegando hasta un valor de 9.92% en el caso de la CuPc. [56]

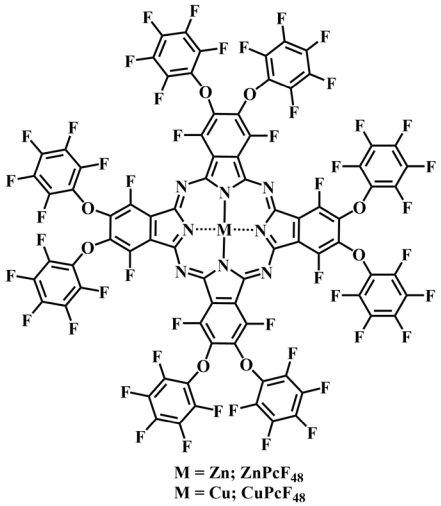

*Figura 2.**6**. Estructura de MPcs utilizadas en células solares de BHJ ternarias.*

[56] A.A.A. Torimtubun, J. Follana-Berná, J.G. Sánchez, J.Pallarès, Á. Sastre-Santos, L.F. Marsal, *ACS Appl. Energy Mater.*, **2021**, *4*, 5201–5211

Células solares de perovskita

Las células solares de perovskita son los dispositivos protagonistas de este capítulo por lo que se presentarán detenidamente en el siguiente apartado.

2.1.4 Células solares de perovskita

Perovskita

La perovskita es un mineral de titanato de calcio con formula $CaTiO_3$ que puede encontrarse en la naturaleza. Fue descubierto en 1839 por Gustav Rose y nombrado así en honor al mineralogista ruso Lev Perovski. [57]

Generalmente se conoce como materiales de perovskita a los materiales que poseen la misma estructura cristalina que $CaTiO_3$. La estructura cristalina típica de estos materiales es cubica o tetragonal con estequiometria AMX_3, siendo A y M cationes metálicos y X un anión. El catión M se coordina octaédricamente con los aniones X para generar el bloque básico de la estructura. En la configuración tridimensional los octaedros MX_6 comparten sus esquinas y el catión A se sitúa en el espacio que forman los octaedros adyacentes neutralizando la carga de la estructura (**Figura 2.7**).

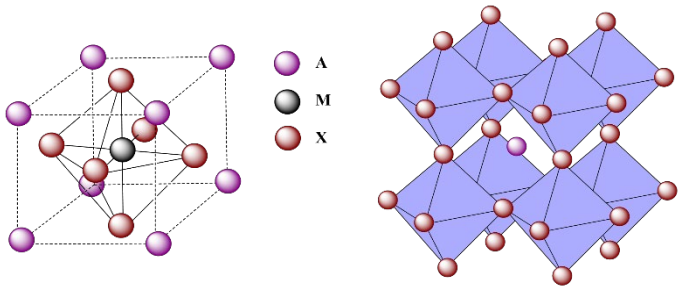

Figura 2.7. Diagramas de la estructura cúbica cristalina de la perovskita.

A lo largo de las últimas décadas, se han estudiado extensivamente los óxidos y haluros de perovskita inorgánicos ($CaTiO_3$, $BaTiO_3$, $LaMnO_3$, $CsSnI_3$, $CsPbI_3$, etc.) dadas sus aplicaciones en óptica, [58] magnetismo, [59] electrónica [60] y como superconductores. [61] En estos últimos años, otro tipo de materiales con esta estructura han captado la atención de las investigaciones. Se trata de perovskitas híbridas orgánicas-inorgánicas. Este nuevo tipo de perovskitas está compuesto por un catión amonio orgánico A como metilamonio o formamidinio ($CH_3NH_3^+$, $H_2N^+{=}CHNH_2$), un catión metálico divalente B (Pb^{2+}, Sn^{2+}, Cd^{2+}, Fe^{2+}, Co^{2+}, Cu^{2+}, etc.) e iones haluro X (Cl^-, Br^- o I^-). Se ha realizado un importante número de

[57] L. J. Schmidt, "Tracking down the truth of perovski," in 38th Rochester Mineralogical Symp. Program Notes, **2011**, pp. 31–32.
[58] U. Schwarz, F. Wagner, K. Syassen, H. Hillebrecht, *Phys. Rev. B: Condens. Matter*, **1996**, *53*, 12545-12548.
[59] R. von Helmolt, J. Wecker, B. Holzapfel, L. Schultz, K. Samwer, *Phys. Rev. Lett*., **1993**, *71*, 2331-2333.
[60] J.H. Haeni, P. Irvin, W. Chang, R. Uecker, P. Reiche, Y.L. Li, S. Choudhury, W. Tian, M. E. Hawley, B. Craigo, A. K. Tagantsev, X. Q. Pan, S. K. Streiffer, L. Q. Chen, S. W. Kirchoefer, J. Levy & D. G. Schlom, *Nature*, **2004**, *430*, 758-761.
[61] J.G. Bednorz, K.A. Müller, *Rev. Mod. Phys*., **1988**, *60*, 585-600.

investigaciones sobre este tipo de materiales para estudiar sus propiedades ópticas, magnéticas y electrónicas. [62, 63, 64]

Historia de las células solares de perovskita

Miyasaka y col. incorporaron por primera vez una perovskita híbrida a una célula solar en 2009. [65] Utilizaron la arquitectura de una DSSC con dos materiales de perovskita distintos sobre el óxido de titanio (TiO_2), uno de yoduro de plomo y metilamonio ($CH_3NH_3PbI_3$, $MAPbI_3$) y otro de bromuro de plomo y metilamonio ($CH_3NH_3PbBr_3$, $MAPbBr_3$). La eficiencia de conversión energética (PCE) para el mejor dispositivo ($MAPbI_3$) fue tan solo del 3.8%, y su estabilidad muy baja debido a la presencia del electrolito líquido. En 2012 se sustituyó el electrolito líquido por un material transportador de huecos (HTM) sólido, 2,2',7,7'-tetrakis(*N*,*N*'-di-*p*-metoxifenilamino)-9,9'-espirobifluoreno (spiro-OMeTAD), aumentando la PCE al 10%. [66, 67]

Estos hallazgos marcaron el inicio de la investigación en las células solares de perovskita. [68] Gracias a la numerosa cantidad de estudios realizados por parte de grupos de todo el mundo, se ha conseguido alcanzar la PCE récord actual de 25.8%. [69] El extraordinario aumento de la PCE ha sido posible gracias a cambios como la sustitución del electrolito líquido por un HTM sólido, modificaciones en la arquitectura de los dispositivos y a las mejoras en los procesos y técnicas de fabricación de los dispositivos.

Evolución de la arquitectura de los dispositivos

Los avances en el diseño de la arquitectura de los dispositivos fueron uno de los factores más importantes que impulsaron la evolución de las PSCs, sobre todo en las primeras etapas del desarrollo.

[62] H. Arend, W. Huber, F.H. Mischgofsky, G.K. Richter-Van Leeuwen, *J. Cryst. Growth*, **1978**, *43*, 213-223.
[63] D.B. Mitzi, *J. Chem. Soc., Dalton Trans*., **2001**, *1*, 1-12.
[64] K. Liang, D.B. Mitzi, M.T. Prikas, *Chem. Mater*., **1998**, *10*, 403-411.
[65] A. Kojima, K. Teshima, Y. Shirai, T. Miyasaka, *J. Am. Chem. Soc*., **2009**, *131*, 6050-6051.
[66] M.M. Lee, J. Teuscher, T. Miyasaka, T.N. Murakami, H.J. Snaith, *Science*, **2012**, *338*, 643-647.
[67] H.-S. Kim, C.-R. Lee, J.-H. Im, K.-B. Lee, T. Moehl, A. Marchioro, S.-J. Moon, R. Humphry-Baker, J.-H. Yum, J. E. Moser, M. Grätzel, N.-G. Park, *Sci. Rep*., **2012**, *2*, 591-597.
[68] [Sin autores], Perovskite fever, *Nat. Mater*., **2014**, *13*, 837-837.
[69] https://www.nrel.gov/pv/cell-efficiency.html

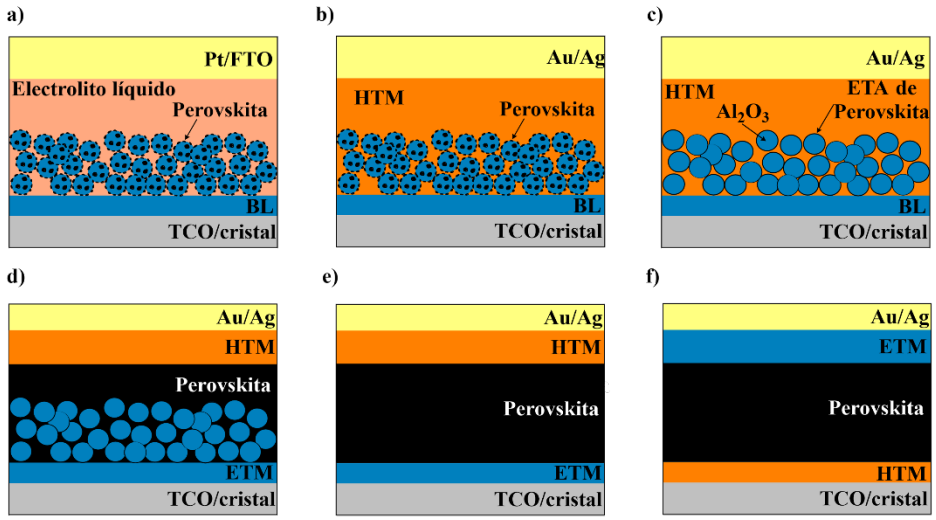

*Figura 2.**8**. Diagramas de las arquitecturas de células solares de perovskita: a) de DSSC con electrolito líquido, b) mesoscópica de estado sólido, c) meso-superestructurada, d) estructura "normal", e) plana n-i-p y f) plana invertida p-i-n.*

Arquitectura de DSSC con electrolito líquido

Como se ha comentado anteriormente, las PSCs se fabricaron inicialmente con la estructura de una DSSC convencional, utilizando perovskita como colorante,[65] sin mucha repercusión debido a su baja eficiencia y a la baja estabilidad derivada del uso de un electrolito líquido (**Figura 2.8a**).

Arquitectura mesoscópica de estado sólido

En el año 2012 se desarrolló la primera PSC de estado sólido utilizando Spiro-OMeTAD como HTM,[67] con la intención de solucionar el problema de estabilidad asociado al electrolito líquido. En esta configuración, el HTM difunde entre los poros de la capa de mp-TiO_2 haciendo contacto directo con la perovskita, y además forma una capa densa sobre el mp-TiO_2 evitando derivaciones entre el material transportador de electrones (ETM) y el electrodo metálico (**Figura 2.8b**).

Arquitectura meso-superestructurada

En el 2012 Snaith *et al*. desarrollaron la estructura meso-superestructurada en la cual se reemplaza la capa de mp-TiO_2 con el aislante Al_2O_3 y se recubre su superficie con una capa absorbente extremadamente delgada (ETA) de perovskita (**Figura 2.8c**).[66]

Esta configuración modifica completamente el mecanismo de transporte de cargas del dispositivo. El carácter aislante y la mayor banda de conducción del Al_2O_3 hacen que la inyección de electrones desde la perovskita sea energéticamente desfavorable, debido a que la capa porosa de Al_2O_3 sirve únicamente como andamio para la perovskita. Así pues, los electrones difunden a través de la capa ETA de perovskita hasta la capa de c-TiO_2, lo cual es posible gracias a que los materiales de perovskita poseen largas distancias de difusión de

electrones y huecos. [70, 71] Estas propiedades eléctricas sugirieron que las PSC podrían fabricarse sin una capa mesoporosa.

Arquitectura "normal"

La configuración "normal" o "típica" de una célula solar de perovskita surgió de la idea de que se podía utilizar una lámina más gruesa y densa de perovskita en lugar de la capa ETA. [72] Esto podía suponer un aumento de la absorción de fotones, así como prevenir las derivas entre los electrodos. El avance en los métodos de deposición de láminas permitió depositar capas de perovskita más gruesas sobre capas de mp-TiO_2 más delgadas, favoreciendo así el éxito de esta estructura que paso a ser conocida como la arquitectura "normal" de una PSC (**Figura 2.8d**). [73, 74, 75]

Heterounión plana n-i-p

La tendencia a utilizar capas de mp-TiO_2 cada vez más delgadas terminó por eliminar completamente esta capa de la estructura "normal" dando lugar a la configuración n-i-p. La arquitectura de este tipo de dispositivos está compuesta por el cátodo de TCO, un ETM tipo-n, la capa de perovskita, un HTM tipo-p, y el ánodo metálico. La baja energía de unión del excitón y la larga distancia de difusión de las cargas en la perovskita, permitía que los electrones y huecos alcanzasen las interfases del ETM y del HTM respectivamente (**Figura 2.8e**). [76, 77]

Heterounión plana invertida p-i-n

Se le denomina comúnmente estructura invertida debido a que las capas del HTM y del ETM se encuentran en sentido opuesto al de la configuración normal. Por lo tanto, la secuencia de la arquitectura p-i-n queda constituida por el ánodo de TCO, un HTM tipo-p, la capa de perovskita, un ETM tipo-n y el cátodo metálico (**Figura 2.8f**). [78, 79]

[70] S.D. Stranks, G.E. Eperon, G. Grancini, C. Menelaou, M.J.P. Alcocer, T. Leijtens, L. M. Herz, A. Petrozza, H. J. Snaith, *Science*, **2013**, *342*, 341-344.
[71] G. Xing, N. Mathews, S. Sun, S.S. Lim, Y.M. Lam, M. Grätzel, S. Mhaisalkar, T. C. Sum., *Science*, **2013**, *342*, 344-347.
[72] J.H. Heo, S.H. Im, J.H. Noh, T.N. Mandal, C.-S. Lim, J.A. Chang, Y. H. Lee, H.-J. Kim A. Sarkar, M. K. Nazeeruddin, M. Grätzel, S. I. Seok, *Nat. Photonics*, **2013**, *7*, 486-491.
[73] J. Burschka, N. Pellet, S.-J. Moon, R. Humphry-Baker, P. Gao, M.K. Nazeeruddin, M. Grätzel, *Nature*, **2013**, *499*, 316-319.
[74] J.-H. Im, I.-H. Jang, N. Pellet, M. Grätzel, N.-G. Park, *Nat. Nano*., **2014**, *9*, 927-932.
[75] F. Giordano, A. Abate, J.P. Correa Baena, M. Saliba, T. Matsui, S.H. Im, S.M. Zakeeruddin, M.K. Nazeeruddin, A. Hagfeldt, M. Grätzel, *Nat. Commun*., **2016**, *7*, 10379-10384.
[76] a) J.M. Ball, M.M. Lee, A. Hey, H.J. Snaith, *Energy Environ. Sci*., **2013**, *6*, 1739-1743. b) G.E. Eperon, V.M. Burlakov, P. Docampo, A. Goriely, H.J. Snaith, *Adv. Funct. Mater*., **2014**, *24*, 151-157. c) M. Liu, M.B. Johnston, H.J. Snaith, *Nature*, **2013**, *501*, 395-398.
[77] a) J.-Y. Seo, T. Matsui, J. Luo, J.-P. Correa-Baena, F. Giordano, M. Saliba, K. Schenk, A. Ummadisingu, K. Domanski, M. Hadadian, A. Hagfeldt, S. M. Zakeeruddin, U. Steiner, M. Grätzel, A. Abate, *Adv. Energy Mater*., **2016**, *6*, 1600767-1600772. b) E.H. Anaraki, A. Kermanpur, L. Steier, K. Domanski, T. Matsui, W. Tress, M. Saliba, A. Abate, M. Grätzel, A. Hagfeldt, J.-P. Correa-Baena, *Energy Environ. Sci*., **2016**, *9*, 3128-3134.
[78] a) J.-Y. Jeng, Y.-F. Chiang, M.-H. Lee, S.-R. Peng, T.-F. Guo, P. Chen, T.-C. Wen, *Adv. Mater*., **2013**, *25*, 3727-3732. b) P. Docampo, J.M. Ball, M. Darwich, G.E. Eperon, H.J. Snaith, *Nat. Commun*., **2013**, *4*, 2761-2766.
[79] a) W. Nie, H. Tsai, R. Asadpour, J.-C. Blancon, A.J. Neukirch, G. Gupta, J. J. Crochet, M. Chhowalla, S. Tretiak, M. A. Alam, H.-L. Wang, A. D. Mohite, *Science*, **2015**, *347*, 522-525. b) C. Bi, Q. Wang, Y. Shao, Y. Yuan, Z. Xiao, J. Huang, *Nat. Commun*., **2015**, *6*, 7747-7753. c) Y. Bai, Q. Dong, Y. Shao, Y. Deng, Q. Wang, L. Shen, D. Wang, W. Wei, J. Huang, *Nat. Commun*., **2016**, *7*, 12806-12814.

2.1.5 Antecedentes

La razón por la cual las PSCs no han sido capaces de llegar al mercado es su menor estabilidad frente a los paneles solares de silicio utilizados actualmente. La pérdida de estabilidad se produce por el efecto del calor y la luz, además de la humedad que afecta mucho debido a la naturaleza iónica de la perovskita. [80, 81] Las funciones de las capas del HTM y ETM son la extracción eficiente de cargas y su transporte hacia los electrodos correspondientes y actuar como aislante de la capa de perovskita. Para ello no es suficiente la correcta deposición del material, sino también su correcta elección para definir el rendimiento de los dispositivos y su estabilidad a largo plazo. Los HTMs que mejor resultado han proporcionado en términos de eficiencia a las PSCs son spiro-OMeTAD y el polímero de poli(triarilamina) (PTAA) como semiconductores orgánicos de tipo p (**Figura 2.9**). Sin embargo, estos materiales presentan diversos inconvenientes, como su alto coste de producción que dificulta su escalado industrial y la necesidad de añadir dopantes para mejorar sus propiedades electrónicas, como la 4-*terc*-butilpiridina (tBP) y la sal bis(trifluorometanosulfonil)imida de litio (Li-TFSI) que generan problemas de estabilidad. [82] Estas razones han dirigido gran parte de la investigación para mejorar las PSCs hacia nuevos materiales que puedan actuar como HTM y ETM. [83, 84, 85]

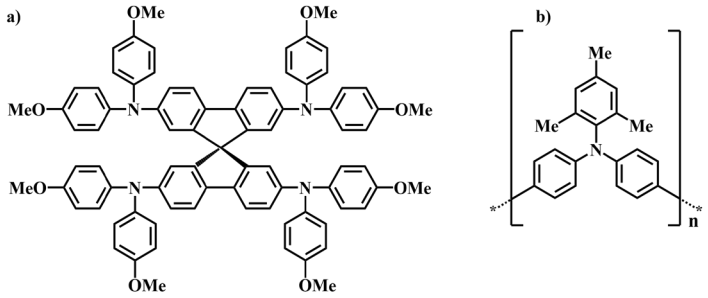

*Figura 2.**9**. Estructura de a) la molécula spiro-OMeTAD y b) el polímero PTAA.*

Las ftalocianinas son un prometedor conjunto de compuestos para su estudio como HTM en PSCs gracias a sus propiedades optoelectrónicas y que son térmica y fotoquímicamente estables. Además, su versatilidad química permite modular dichas propiedades cambiando el metal central, los sustituyentes en diferentes posiciones y variando el grado de simetría. Por todo esto existen en la literatura multitud de publicaciones en la que se utilizan estas moléculas como HTM. [86]

Una de las primeras ftalocianinas utilizada como HTM en células solares de perovskita fue la **CuPc** sin sustituyentes alcanzando una PCE del 5%. [87] Yan *et al*. alcanzaron

[80] Z. Ahmad, A. S. Shikoh, S. Paek, M. K. Nazeeruddin, S. A. Al-Muhtaseb, F. Touati, J. Bhadra and N. J. Al-Thani, J. Mater. *Sci.: Mater. Electron*., **2019**, *30*, 1354-1359.
[81] N. Aristidou, C. Eames, M. S. Islam and S. A. Haque, *J. Mater. Chem. A*, **2017**, *5*, 25469-25475.
[82] F. M. Rombach, S. A. Haque and T. J. Macdonald, *Energy Environ. Sci*., **2021**, *14*, 5161-5190.
[83] Z. Yu, A. Hagfeldt and L. Sun*, Coord. Chem. Rev.*, **2020**, *406*, 213143-213158.
[84] L. Jia, M. Chen and S. Yang, *Mater. Chem. Front.*, **2020**, *4*, 2256-2282.
[85] S. Sajid, H. Huang, J. Ji, H. Jiang, M. Duan, X. Liu, B. Liu and M. Li, *Renew. Sust. Energ. Rev.*, **2021**, *152*, 111689-111732.
[86] D. Molina, J. Follana-Berná, Á. Sastre-Santos, *J. Mater. Chem. C*, **2023**, Advance Article (https://doi.org/10.1039/D2TC04441B).
[87] C. V. Kumar, G. Sfyri, D. Raptis, E Stathatos, P. Lianos, *RSC Adv.*, **2015**, *5*, 3786-3791.

el 15.42% con la misma **CuPc** utilizando una técnica de deposición a vacío. [88] Catchpole *et al*. estudiaron la **(*t*Bu)$_4$CuPc** procesada en disolución como HTM dopado para PSC con un 20% de eficiencia (**Figura 2.10**). [89]

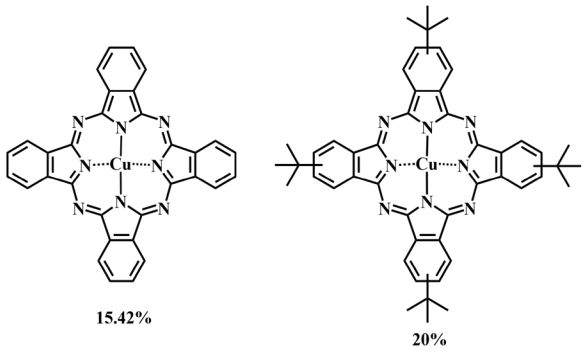

Figura 2.10. Estructura de diferentes CuPcs utilizadas como HTM.

En el caso de las ftalocianinas de zinc, una de las primeras utilizadas fue la **TT80** con grupos muy voluminosos para evitar la agregación, alcanzando un 6.7% de PCE. [90] También se estudió la **(*t*Bu)$_4$ZnPc**, aunque con menor eficiencia 5.2%. [91] Otro ejemplo de esta ftalocianina de cinc por Torres et al. obtuvo una eficiencia del 14.0%. En el mismo estudio, se utilizó un análogo asimétrico de esta Pc, con tres grupos *terc*-butilos y un grupo carboxilo **TT1** con la intención de favorecer la interacción con la capa de perovskita y así mejorar sus propiedades. Sin embargo, la eficiencia obtenida era prácticamente igual a la simétrica, 13.7% (**Figura 2.11**). [92]

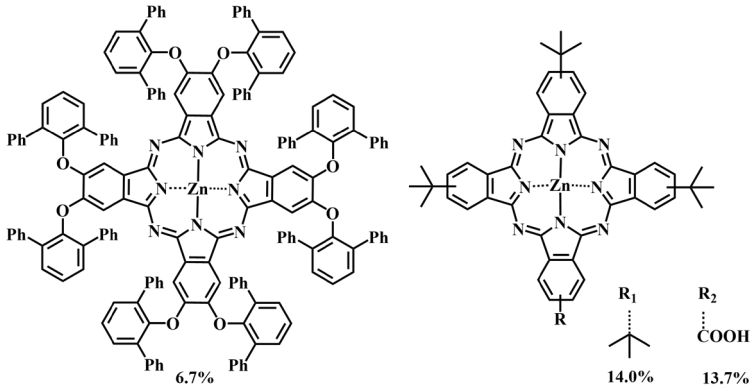

Figura 2.11. Estructura de diferentes ZnPcs utilizadas como HTM.

[88] W. Ke, D. Zhao, C. R. Grice, A. J. Cimaroli, G. Fang and Y. Yan*, J. Mater. Chem. A*, **2015**, *3*, 23888–23894.
[89] T. Duong, J. Peng, D. Walter, J. Xiang, H. Shen, D. Chugh, M. Lockrey, D. Zhong, J. Li, K. Weber, T. P. White and K. R. Catchpole, *ACS Energy Lett*., **2018**, *3*, 2441–2448.
[90] F. J. Ramos, M. Ince, M. Urbani, A. Abate, M. Grätzel, S. Ahmad, T. Torres, M. K. Nazeeruddin, *Dalton Trans*., **2015**, *44*, 10847-10851.
[91] S. Wu, Y. Zheng, Q. Liu, R. Li, T. Peng, *RSC Adv*., **2016**, *6*, 107723-107731.
[92] Y. Zhang, S. Paek, M. Urbani, M. Medel, I. Zimmermann, K. T. Cho, M. Ince, M. K. Nazeeruddin, T. Torres, *ACS Appl. Energy Mater*., **2018**, *1*, 2399–2404.

Además de cobre y cinc, se han utilizado multitud de metales e incluso ftalocianinas libres para su aplicación como HTM en PSCs. Un importante ejemplo es el trabajo de Tang *et al*. en el cual utilizan ftalocianinas tetrasustituidas con grupos 2-metoxietoxi y diferentes átomos en su núcleo (2H, Zn, Cu, Ni y Co). Obtuvieron un valor récord del 21% de PCE para la **NiPc**, además de presentar buenas estabilidades térmicas y frente a la humedad.[93] Otro ejemplo son las ftalocianinas de óxido de titanio con sustituyentes periféricos (***P*-SC$_6$-TiOPc**) y no periféricos (***NP*-SC$_6$-TiOPc**) con PCEs de 6.82 y 16.87% respectivamente (**Figura 2.12**).[94]

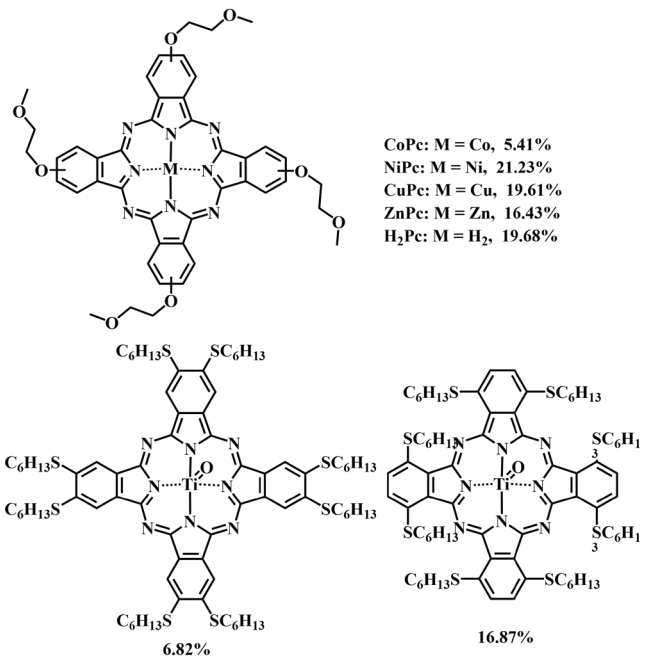

Figura 2.12. Estructura de diferentes MPcs utilizadas como HTM

Igualmente se han estudiado derivados de Pcs con grupos que aumenten la conjugación del anillo como **Sym-HTPcH**, que presentaba un grupo 5-hexil-2-tienilo en cada subunidad y con una eficiencia de 12.8%.[95] Un año más tarde, se sintetizó una ftalocianina análoga a la anterior con un grupo tienilo adicional, **HBT-ZnPc**, que se comparó tanto con la anterior (llamada esta vez **HT-ZnPc**) y con la (*t*Bu)$_4$ZnPc (**TB-ZnPc**) obteniendo unas PCE de 15.5, 17.1 y 13.3% respectivamente (**Figura 2.13**).[96]

[93] Yu, Z.; Wang, L.; Mu, X.; Chen, C.; Wu, Y.; Cao, J.; Tang, Y., *Angew. Chem., Int. Ed*., **2021**, *60*, 6294−6299.
[94] Hu, Q.; Rezaee, E.; Li, M.; Chen, Q.; Cao, Y.; Mayukh, M.; McGrath, D. V.; Xu, Z.-X., *ACS Appl. Mater. Interfaces*, **2019**, *11*, 36535−36543.
[95] P. Gao, K. T. Cho, A. Abate, G. Grancini, P. Y. Reddy, M. Srivasu, M. Adachi, A. Suzuki, K. Tsuchimoto, M. Gr¨atzel and M. K. Nazeeruddin, *Phys. Chem. Chem. Phys*., **2016**, *18*, 27083–27089.
[96] K. T. Cho, O. Trukhina, C. Rold´an-Carmona, M. Ince, P. Gratia, G. Grancini, P. Gao, T. Marszalek, W. Pisula, P. Y. Reddy, T. Torres, M. K. Nazeeruddin, *Adv. Energy Mater*., **2017**, *7*, 1601733-1601739.

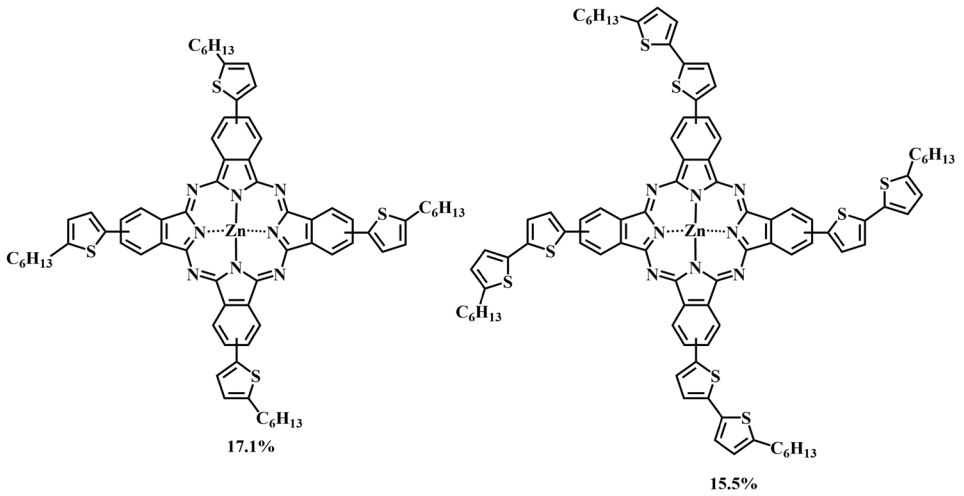

Figura 2.13. Estructuras de ZnPcs con tiofenos.

Siguiendo esta línea, otro grupo funcional muy interesante a introducir en las Pcs son las arilaminas, concretamente la trifenilamina (TPA) o la difenilamina (DPA). En el grupo de Nazeeruddin sinterizaron una ftalocianina de cinc sustituida con grupos DPA (**BL25**) junto con otras dos ZnPcs con grupos carbazol (**BL07**) y 3,6-dimetoxicarbazol (**BL08**) obteniendo con eficiencias de 11.75, 6.65, y 11.44% respectivamente. [97] Sfyri *et al.* utilizaron **TPA-Pc**, una ZnPc con cuatro sustituyentes periféricos TPA, consiguiendo una eficiencia del 5.6%. [98] Del mismo modo, Wang et al. desarrollaron **OTPA-ZnPc**, ftalocianina de zinc con sustituyentes 4-(bis(4-metoxifenil)amino)fenilo que proporcionó una eficiencia del 16,23%. [99] Como pasaba en el caso de **BL07** y **BL08**, la introducción de grupos metoxilo en estas ftalocianinas incrementó considerablemente la eficiencia. Muccini *et al.* se centraron en las ftalocianinas de cobre y compararon el rendimiento fotovoltaico de los dispositivos con **OMe-DPA-CuPc** (16.73%) y **OMe-TPA-CuPc** (19.67%) dopados, CuPcs con cuatro sustituyentes bis(4-metoxifenil)amino y cuatro sustituyentes 4-(bis(4-metoxifenil)amino)fenilo, respectivamente. [100] En un trabajo reciente de Nazeeruddin se comparan Pcs de Zn(II) y Cu(II) sustituidas con grupos bis(4-alcoxifenil)amina, alcanzando una eficiencia del 20.18% para su mejor MPc dopado (**Zn-BL54**). [101] Actualmente, se ha batido el record de eficiencia para una PSC con ftalocianina como HTM con **SMe-TPA-CuPc** y una PCE del 23%. Se trata de una ftalocianina de cobre con grupos 4-(bis(4-metiltiofenil)amino)fenilo (**Figura 2.14**). [102]

[97] K. T. Cho, K. Rakstys, M. Cavazzini, S. Orlandi, G. Pozzi, M. K. Nazeeruddin, *Nano Energy*, **2016**, *30*, 853-857.
[98] G. Sfyri, N. Vamshikrishna, C.V. Kumar, L. Giribabu, P. Lianos, *Sol. Energy*, **2016**, *140*, 60-65.
[99] Z. Cui, Y. Wang, Y. Chen, X. Chen, X. Deng and W. Chen, *Org. Electron*., **2019**, *69*, 248–254.
[100] Y. Feng, Q. Hu, E. Rezaee, M. Li, Z. Xu, A. Lorenzoni, F. Mercuri and M. Muccini, *Adv. Energy Mater*., **2019**, *1901019-1901029*.
[101] N. Klipfel, J. Xia, P. Čulík, S. Orlandi, M. Cavazzini, N. Shibayama, H. Kanda, C. Igci, W. Li, Y.-B. Cheng, V. Jankauskas, K. Genevicius, A. M. Asiri, C. Momblona, K. Rakstys, G. Pozzi, M. K. Nazeeruddin, *Materials Today Energy*, **2022**, *29*, 101110-101120.
[102] G. Qu, L. Dong, Y. Quiao, D. Khan, Q. Chen, P. Xie, X. Yu, X. Liu, Y. Wang, J. Chen, X. Chen, Z.X. Xu, *Adv. Funct. Mater*., **2022**, *32*, 2206585-2206596.

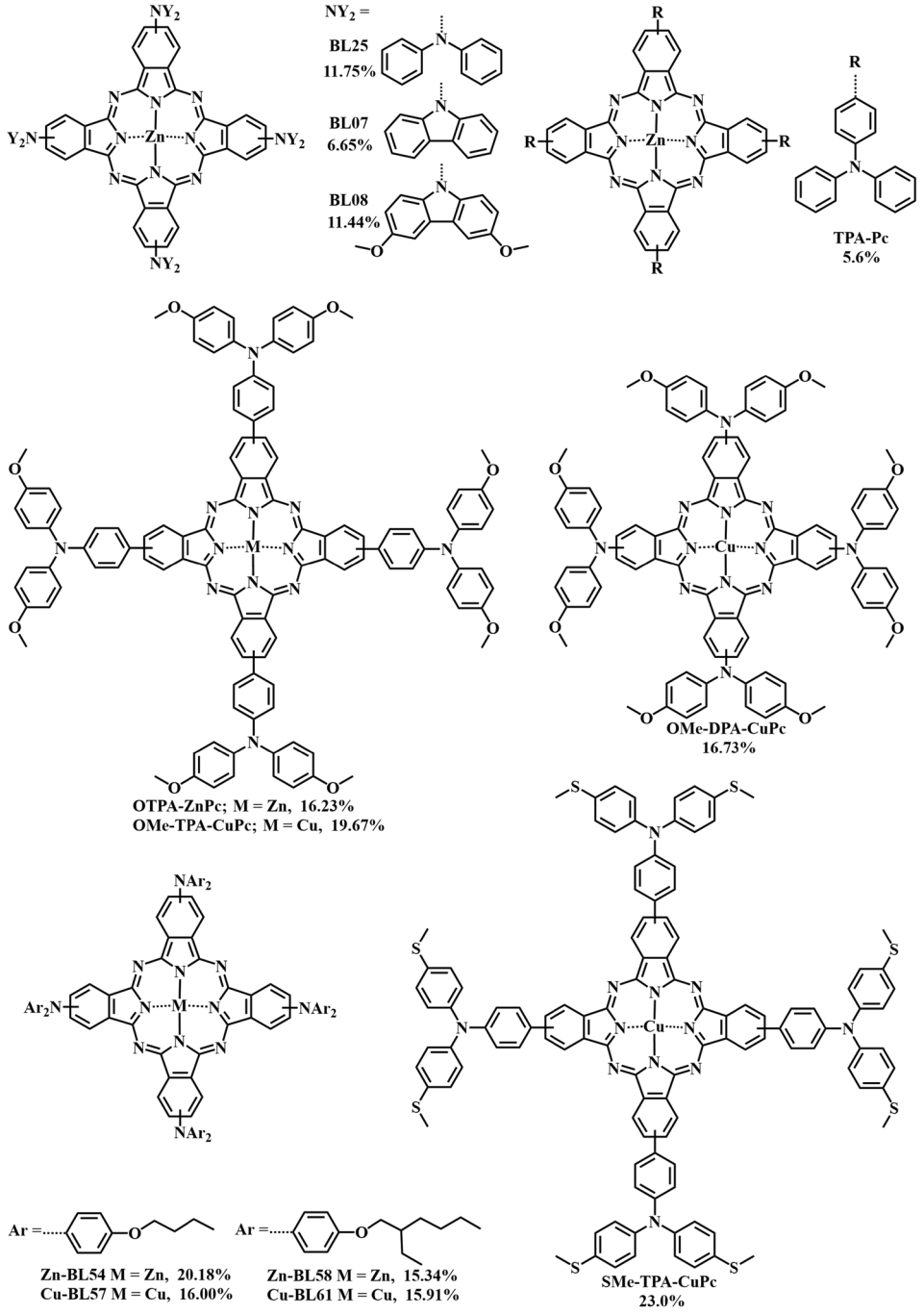

*Figura 2.**14**. Estructuras de ftalocianinas de cinc y cobre con grupos arilamino.*

Además de su función como HTM, las ftalocianinas pueden desempeñar otros roles en las células solares de perovskita (PSCs), como el de aditivos, agentes pasivantes e intercalantes. La adición de la CuPc **8TPAEPC** disuelta en antisolvente sobre la capa de

perovskita mejoró la eficiencia del 20% al 22.10%. Esta mejora se atribuyó no solo a la ampliación de la fotorespuesta en el espectro infrarrojo cercano de 760 a 850 nm, sino también a la supresión de defectos y a una reducción de la densidad de estados trampa a través de la interacción con los aniones yoduro, que pueden quedar expuestos en la superficie de la capa de perovskita. Los dispositivos con **8TPAEPC** mantenían el 80% de la PCE inicial después de 500 horas a 70-80% de humedad relativa, mientras que las PSCs sin tratamiento disminuyeron al 50% de la PCE inicial. Además, se empleó **8TPAEPC** como HTM sin dopantes, lográndose una PCE del 20.42% (Figura 2.15). [103]

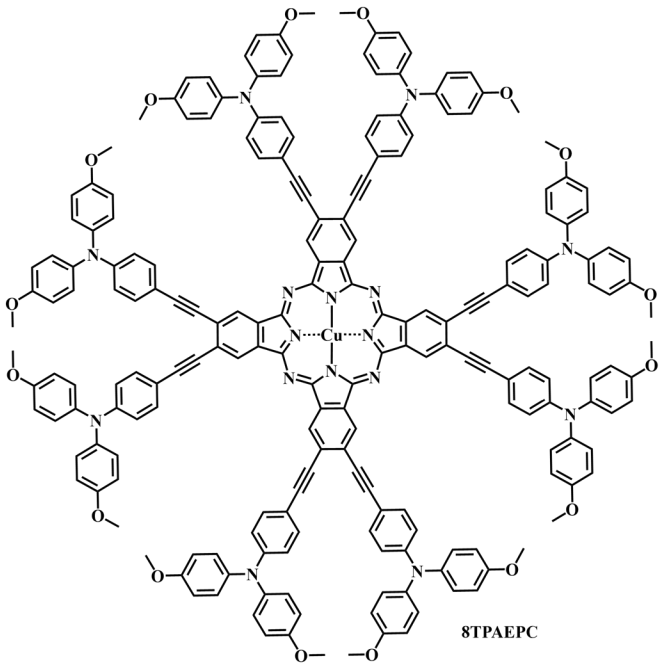

*Figura 2.**15**. Estructura de una CuPc utilizada como agente intercalante en PSCs.*

Antecedentes específicos

La primera publicación de nuestro grupo de investigación utilizando ftalocianinas que actúan como HTM en células solares de perovskita fue en el año 2017. [104] Se trata de Pcs de cinc y cobre sustituidas con grupos *terc*-octilfenoxilos con la intención de dotar de mayor solubilidad estos compuestos y facilitar así su procesabilidad. Las eficiencias obtenidas no superaron a la de Spiro-OMeTAD, 8.33% y 7.25% para **CuPc** y **ZnPc** respectivamente. Sin embargo, su mayor estabilidad gracias a las cadenas hidrofóbicas y su bajo coste son propiedades deseables en un buen HTM (**Figura 2.16**).

[103] Z. Zhang, H. Liu, S. Wang, H. Bao, F. Zhang, X. Li, *Adv. Funct. Mater*., **2022**, *32*, 2208539-2208547.
[104] L. Caliò, J. Follana-Berná, S. Kazim, M. Madsen, H.-G. Rubahn, A. Sastre-Santos, S. Ahmad, *Sustainable Energy Fuels*, **2017**, *1*, 2071-2077.

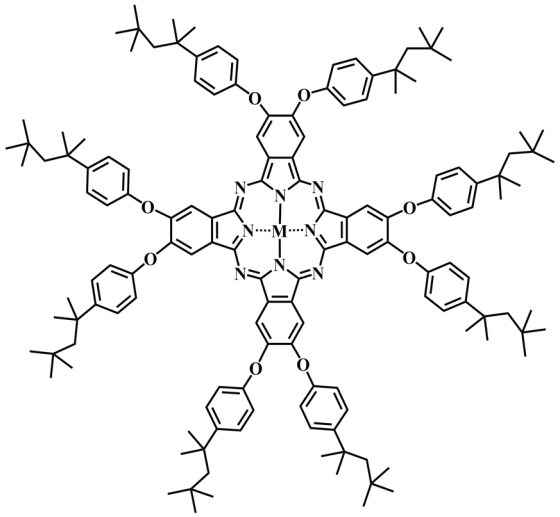

*Figura 2.**16**. Estructuras de ftalocianinas utilizadas como HTM en células solares de perovskita.*

Otro ejemplo son los derivados diméricos de ZnPcs, en el cual dos unidades de (^{t}Bu)$_3$ZnPc se unen por puentes compuestos de diferentes grupos funcionales como fenilo, dicetopirrolopirrol, fluoreno y tiofeno.[105] Estos dispositivos mostraron elevadas PCE y excelente estabilidad, el dímero con puente de DPP obtuvo la mayor eficiencia de los cuatro (16.8%) (**Figura 2.17**). Este hecho promovió la síntesis de tres nuevos derivados en los cuales la unión con el puente se producía mediante triples enlaces.[106] Los dímeros exhibían excelentes capacidades de extracción de cargas lo que se traduce en elevadas PCE, llegando el dímero **ZnPc-t-Spiro-t-ZnPc 3** a superar incluso al dispositivo con Spiro-OMeTAD como HTM con eficiencias de 18.32 y 17.72% respectivamente (**Figura 2.18**).

[105] D. Molina, M. A. Ruiz-Preciado, B. Carlsen, F. T. Eickemeyer, B. Yang, N. Flores-Díaz, M. J. Álvaro-Martins, K. Nonomura, A. Hagfeldt, Á. Sastre- Santos, *ChemPhotoChem*, **2020**, *4*, 307-314.
[106] M. Pegu, D. Molina, M.J. Álvaro-Martins, M. Castillo, L. Ferrer, P. Huang, S. Kazim, Á. Sastre-Santos, S. Ahmad, *J. Mat. Chem. C*, **2022**, *10*, 11975-11982.

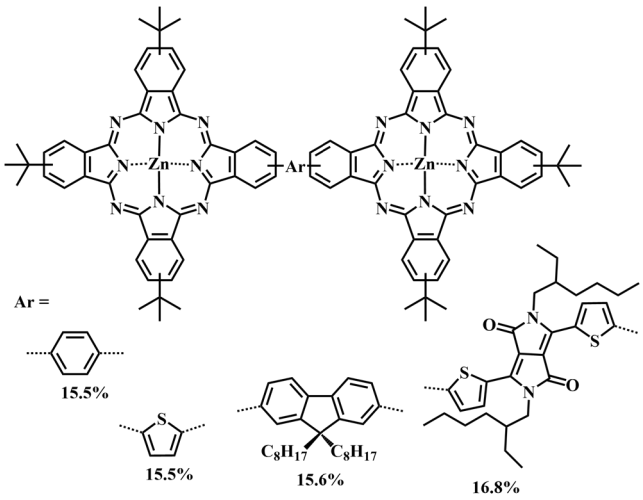

Figura 2.17. Dímeros de ftalocianinas de cinc utilizados como HTM.

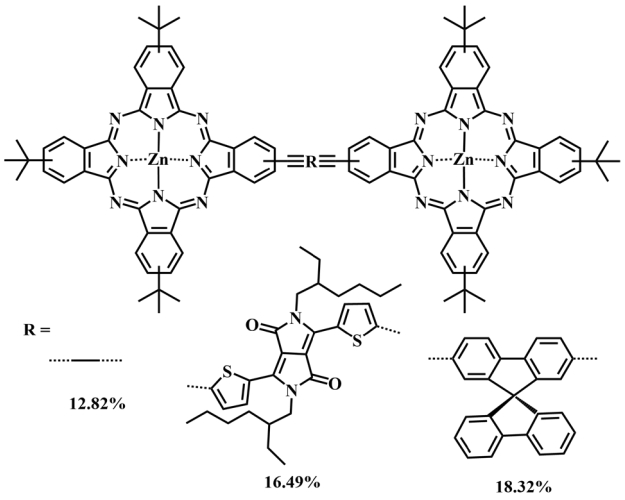

*Figura 2.**18**. Dímeros de ftalocianinas de cinc unidas por puentes con triple enlace para HTM.*

2.2 Objetivos

2.2.1 Síntesis y caracterización de una ftalocianina de cinc tetrasustituida con grupos trifenilaminotienilo

Nuestro objetivo ha sido sintetizar una ZnPc tetrasustituida con grupos trifenilaminotienilo ricos en electrones conjugados. Estos sustituyentes se seleccionaron para mejorar la solubilidad y la movilidad de los huecos en la ftalocianina como HTM (**Figura 2.19**).

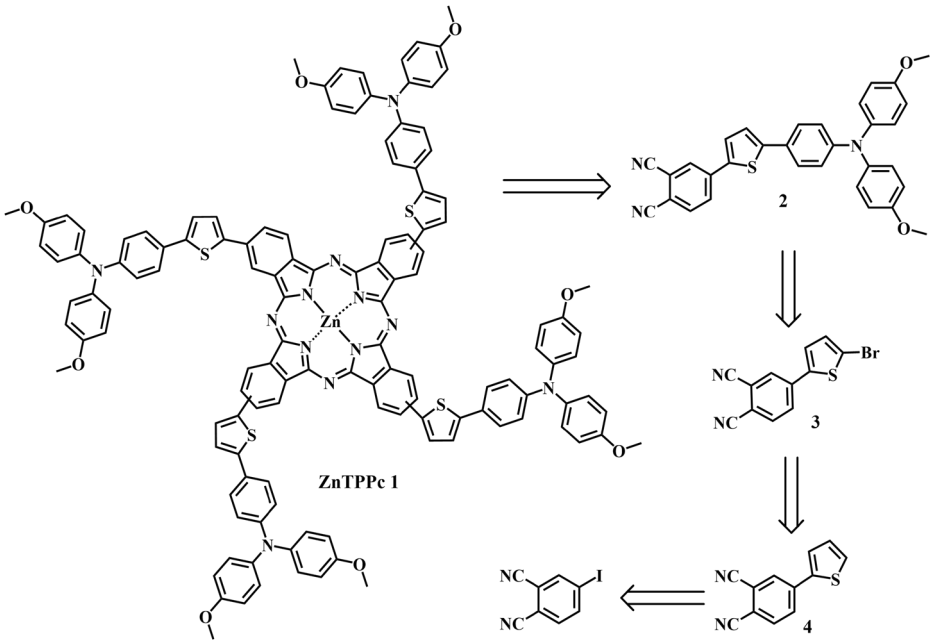

Figura 2.19. Esquema de retrosíntesis de ZnTPPc 1 y sus precursores.

2.2.2 Síntesis y caracterización de ftalocianinas de cinc y cobre sustituidas asimétricamente

El objetivo ha sido utilizar diferentes sustituyentes periféricos como 2-aminoetoxilo (AE) y TTPA para inducir asimetría sobre la conocida MPc simétrica con cuatro grupos *terc*-butilo. Así como estudiar las propiedades que los sustituyentes y el ion metálico central (Zn o Cu) aportan tanto a las propias ftalocianinas como a los dispositivos fotovoltaicos fabricados con ellas como HTM (**Figura 2.20** y **Figura 2.21**).

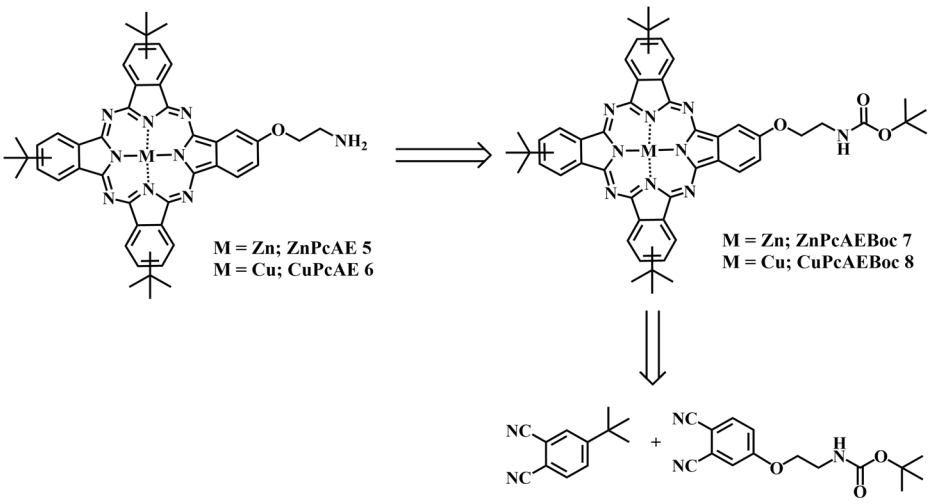

Figura 2.20. Esquema retrosintético de ZnPcAE 5 y CuPcAE 6.

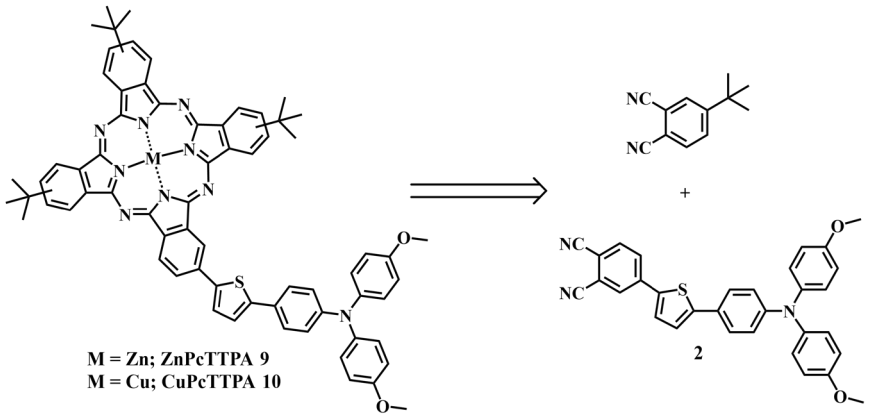

Figura 2.21. Esquema retrosintético de ZnPcTTPA 9 y CuPcTTPA 10.

2.2.3 Síntesis de ftalocianinas de cinc y cobre sustituidas con grupos diarilamino con y sin flúor

El siguiente paso que decidimos tomar fue la reducción de la longitud de la cadena aromática, uniendo directamente el grupo amino al anillo de isoindol de la Pc. En este caso, además de comprobar la influencia de la simetría/asimetría y del ion metálico central, nos dispusimos también a estudiar la posible influencia de átomos de flúor presentes en los anillos aromáticos periféricos (**Figura 2.22**).

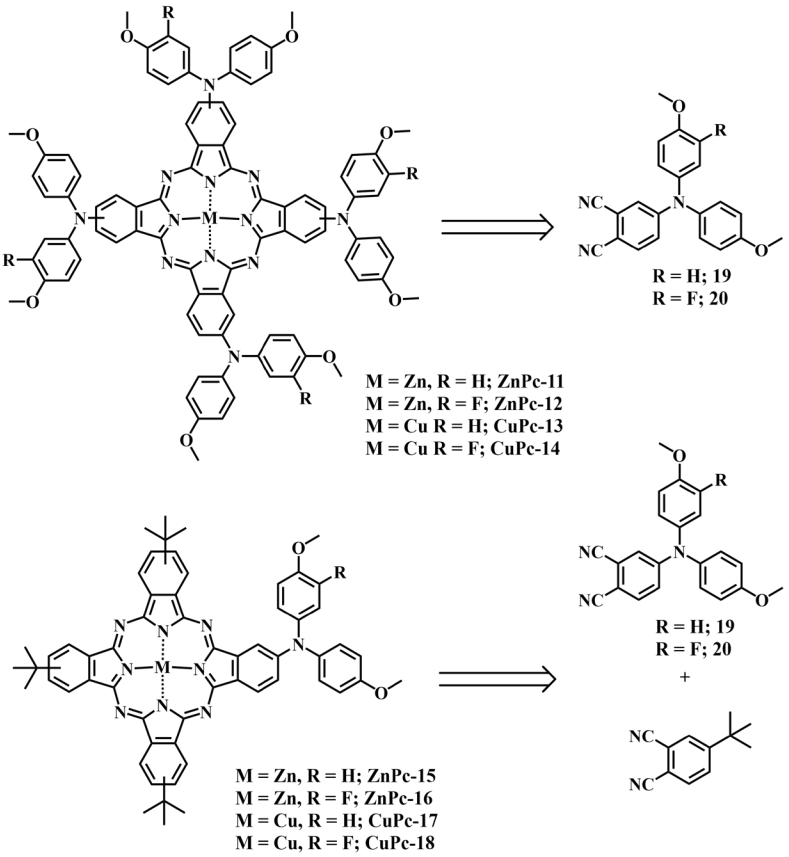

*Figura 2.**22**. Esquema de retrosíntesis de ZnPc 11, ZnPc 12, CuPc 13, CuPc 14, ZnPc 15, ZnPc 16, CuPc 17 y CuPc 18.*

2.2.4 Preparación de células solares de perovskita con ftalocianinas como material transportador de huecos sin dopar

El objetivo final de la síntesis de las MPcs de este capítulo es la fabricación de PSCs en las cuales el HTM está compuesto por las diferentes ftalocianinas sin dopar, estudiar los parámetros fotovoltaicos, así como la estabilidad de los dispositivos. Estudios que se llevarán a cabo por el grupo del Prof. Shahzada Ahmad en el Basque Center for Materials, Aplications, and Nanoestructures (BCMaterials) de la Universidad del País Vasco.

2.3 Resultados:

Los resultados obtenidos en este capítulo se recogen en las siguientes publicaciones:

P. Huang, A. Hernández, S. Kazim, J. Ortiz, Á. Sastre-Santos, S. Ahmad, Molecularly engineered thienyl-triphenylamine substituted zinc phthalocyanine as dopant free hole transporting materials in perovskite solar cells, *Sustain. Energy Fuels*, **2020**, *4*, 6188−6195. DOI: 10.1039/d0se01215g.

P. Huang, A. Hernández, S. Kazim, J. Follana-Berná, J. Ortiz, L. Lezama, Á. Sastre-Santos, S. Ahmad, Asymmetrically Substituted Phthalocyanines as Dopant-Free Hole Selective Layers for Reliability in Perovskite Solar Cells, *ACS Appl. Energy Mater*., **2021**, *4*, 9, 10124–10135. DOI: 10.1021/acsaem.1c02039.

A. Hernández, N. Harindu Hemasiri, S. Kazim, J. Ortiz, S. Ahmad, Á. Sastre-Santos, Fluorinated- and non-fluorinated-diarylamine-Zn(II) and Cu(II) Phthalocyanines as Symmetrical vs Asymmetrical Hole Selective Materials, *J. Mater. Chem. C*, **2023**, DOI: 10.1039/D3TC00254C.

Molecularly Engineered Thienyl-Triphenylamine Substituted Zinc Phthalocyanine as Dopant Free Hole Transporting Materials in Perovskite Solar Cells

Received 15th August 2020,
Accepted 5th October 2020

DOI: 10.1039/d0se01215g

Peng Huang,[a] Adrián Hernández,[b] Samrana Kazim,[a,c] Javier Ortíz,[b] Ángela Sastre-Santos,[*b] and Shahzada Ahmad [*a,c]

To endure the success of perovskite solar cells (PSCs), developing dopant-free hole transporting materials is of paramount importance to induce long-term stability. Phthalocyanine has emerged as a viable alternative for common Spiro-OMeTAD, due to their excellent optoelectrical properties and chemical stability. We report the design and semiconducting properties of a thienyl-triphenylamine tetrasubstituted Zinc (II) phthalocyanine, and its application into PSCs. The PSCs fabricated with Zinc phthalocyanine without the use of any dopant and additives gave a competitive power conversion efficiency in excess of 14.5%, along with long-term stability.

Introduction

The last decade has witnessed an enormous development in the investigation of organic-inorganic hybrid perovskite solar cells (PSCs) due to their power conversion efficiency (PCE) skyrocketing from 3.8% to 25.2%.[1–5] This rapid development is owing to the outstanding properties of organic-inorganic halide perovskites: panchromatic light absorption and long-range ambipolar carrier diffusion as well as the choice of solution-processability at low temperature.[6–8] In the device configuration of PSCs, the light harvester perovskites layers are sandwiched between an electron and hole transporting material (ETM, HTM). This can be categorized into normal (*n-i-p*) and inverted (*p-i-n*) structures according to whether ETM or HTM is in contact with the bottom transparent conductive electrode (TCO).

In a standard normal device structure (TCO/ETM/perovskite/HTM/metal electrode), HTMs atop of perovskite layer play pivotal roles in achieving high efficiency and long-term stability in PSCs. The hole transporting layers extract and transport photo-generated holes from perovskite to the metal electrode rapidly, avoiding undesired charge recombination losses at the interfaces and also inhibits the degradation process induced by oxygen and moisture.[9–11] An effective HTM must fulfill the following requirements: simplified synthesis procedure, solution-processability, uniform film formation (compact morphology) without any pinhole, the relatively high charge transporting abilities, the well aligned highest occupied molecular orbital (HOMO) /valence band with valence band of perovskite, superior stability under ambient and thermal condition.[12–15]

To date, *2,2′,7,7′*-tetrakis-(*N,N*-di-p, methoxyphenylamine)-9,9′-spirobifluorene (Spiro-OMeTAD) is most investigated HTM in *n-i-p* structure type devices because of their simple orthogonal solution-processability (to common perovskites) and high performance of the devices.[16–21] However, Spiro-OMeTAD possesses low conductivity and mobility in its pristine form, and introducing a hygroscopic *p*-type dopant and additive such as lithium bis(trifluoromethanesulfonyl)imide (Li-TFSI)

[a]*BCMaterials, Basque Center for Materials, Applications and Nanostructures, UPV/EHU Science Park, 48940 Leioa, Spain, Tel: +34 946128811*
E-mail: shahzada.ahmad@bcmaterials.net
[b]*Área de Química Orgánica, Instituto de Bioingeniería Universidad Miguel Hernández Avda. de la Universidad, s/n, Elche 03202, Spain E-mail: asastre@umh.es*
[c]*IKERBASQUE, Basque Foundation for Science, Bilbao, 48013, Spain*
[†]Electronic Supplementary Information (ESI) available [1]H-NMR spectroscopy and HR-MALDI-TOF mass spectrometry. See DOI: 10.1039/d0se01215g

and 4-tert-Butylpyridine (t-BP) is prerequisite to enhance the charge transporting ability of Spiro-OMeTAD, but on the contrary, this can also accelerate the degradation of perovskite and lowers the stability of the fabricated devices. The tedious multi-step synthesis and costly purification process of Spiro-OMeTAD along with the use of indispensable hydrophilic dopants and additives limits its further extensive application in PSCs.[22,23]

Recently, among alternatives that meet HTM's criteria, including small molecules, conjugated polymers, and inorganic p-type semiconductors , *etc.*, have been specially designed and synthesized to supersede Spiro-OMeTAD.[12,14,15,24–26] Among them, one such promising category of attractive HTM is metal phthalocyanine (Pcs), analogs which own organic macrocycles with an extended π-conjugated system and planar structure.[27–30] They are cost-effective and attractive due to their facile synthesis and purification, high hydrophobicity, as well as excellent stability under thermal and photo conditions. Moreover, they exhibit a unique combination of chemical, optical and electronic properties that can be tailored by molecular engineering. The peripheral and non-peripheral substitution of Pcs is an effective approach to regulate their chemical and electrical properties. [29,31,32] The efficiency of Pcs- based PSC was significantly improved to nearly 20% since the first paper reported on vacuum-deposited CuPc in PSCs in 2015.[33–35] Catchpole *et al.* applied solution-processed copper (II) 2,9,16,23-tetra-tert-butyl-29*H*,31*H*-phthalocyanine as a doped HTM for PSCs and reported the highest efficiency of the device with Pcs.[35] Recently, Pc derivatives have emerged as an appealing dopant-free HTMs.[27,36–39] Dopant-free Zinc (II) 2,9,16,23-tetra-tert-butyl-29*H*,31*H*-phthalocyanine dimers with 3,6-bisthienylldiketopyrrolopyrrole (ZnPc-DPP-ZnPc) as dopant-free HTM into PSCs yielded 16.8% PCE.[40] Similarly, Wang *et al.* successfully developed tetra-methoxyl triphenylamine substituted zinc phthalocyanine (OTPA-ZnPc) as a dopant-free HTM, and corresponding device gave 16.23% efficiency.[41] Xu *et al.* investigated properties and application of two CuPcs: methoxydiphenylamine / methoxy triphenyl amine-substituted copper Pcs, named as OMe-DPA-CuPc and OMe-TPA-CuPc, respectively. It showed that OMe-TPA-CuPc exhibit better π-π interaction and more parallel orientations of Pcs cores in bulk aggregates compared to OMe-DPA-CuPc, and the corresponding dopant-free HTM based PSCs gave PCE of 19.7%.[37] Substitution with methoxy triphenylamine moieties highlights the strong potential to future design Pc derivatives as dopant-free HTM. Thiophenes or its derivatives as the π-linker are widely investigated as organic semiconducting materials in thin-film devices.[42,43] Particularly, thienyl groups are employed to synthesize dopant-free small molecules HTMs,[43–45] but reports dealing with Pcs analogs with thiophene or its derivatives are in scarce.[29,46,47] In this work, guided by rational design, we synthesize and characterize Zinc (II) 2,9,16,23-tetra-thienyl-methoxytriphenylamine-29*H*,31*H*-phthalocyanine, named as **ZnTPPc** (**Fig. 1**), and its integration as a dopant-free HTM in PSCs is investigated. Notably, the PSC based on dopant-free **ZnTPPc** delivered a PCE of 14.5%, which is very competitive to that of the device employing the well-known undoped HTMs. Particularly, the facile synthesis of **ZnTPPc** based on commercial precursor materials makes it a promising new class of HTMs with high stability.

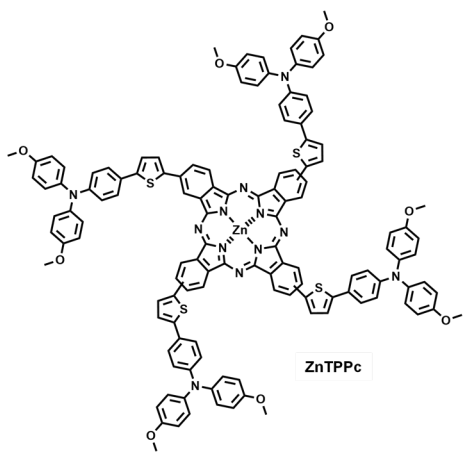

Fig.1 Chemical structure of **ZnTPPc**.

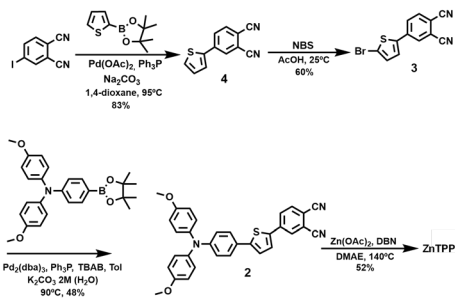

Scheme 1. Synthetic route to **ZnTPPc**.

Results and discussion

Synthesis and characterization of ZnTPPc

Our objective was to synthesize a tetrasubstituted **ZnTPPc** with triphenylamine-thienyl conjugated aromatic electron-rich substituents. These substituents were selected in order to improve the solubility and hole mobility of Pc as a HTM. **ZnTPPc** was synthesized from autocondensation of phthalonitrile **2** in the presence of $Zn(OAc)_2$ and a drop of DBN as catalyst with 52% of yield (**Scheme 1**). The phthalonitrile **2** was obtained by Suzuki coupling of arylboronate and bromo-thienyl-phthalonitrile **3**, which in turn can be easily prepared from 4-(thiophen-2-yl)phthalonitrile **4** by bromination with NBS. Phthalonitrile **4** was synthesized by a Suzuki reaction of 4-iodophthalonitrile and thiophene-2-boronic acid pinacol ester. Palladium acetate was the best catalyst for this reaction, better than the usual $Pd_2(dba)_3$. The phthalonitriles **2-4** were characterized by ^{1}H-NMR and ^{13}C-NMR spectroscopy (Fig. S1-S6, ESI†).

The final product **ZnTPPc** was systematically characterized by ^{1}H-NMR spectroscopy, HR-MALDI-TOF mass spectrometry UV-vis absorption and fluorescence spectra. The ^{1}H-NMR spectra in DMSO-d_6 of **ZnTPPc** showed broad aromatic signals meanwhile the aliphatic ones are well defined. This may be due to aggregation by stacking and to the presence of four different region isomers (Fig. S7, ESI†). The absorption spectra of **ZnTPPc** in DMF (Fig. 2a) presented the Soret bands located in the ultraviolet region around 390 nm and the Q band in the region between 600 nm and 780 nm. Intensive absorptions at 647 nm and 719 nm, respectively, could be ascribed to strong π–π* transitions of Q-band.[37] The ZnTPPc show strong, narrow steady-state fluorescence with peak position at 768 nm (Fig. 2a). The optical bandgap (E_g) of **ZnTPPc** was estimated from the corresponding intersection of absorption and fluorescence spectra, thus, resulting in 1.65 eV.

The electrochemical characterization was performed to evaluate the energy level alignment of the perovskite/**ZnTPPc** interface via using cyclic voltammetry as displayed in Fig. 2b. The ferrocene redox couple was used as the external standard and **ZnTPPc** showed two oxidation peaks at 0.35 V and 0.79 V (vs Fc/Fc^+), respectively. The highest occupied molecular orbital energy level (E_{HOMO}) of **ZnTPPc** was calculated according to Equation: E_{HOMO}=-4.8-E_{ox}, where E_{ox} is the first onset oxidation potential. The E_{HOMO} value was estimated to be -5.15 eV and located in between valence band of perovskite (-5.9 eV) and work function of gold (-5.1 eV), which could facilitate the hole carrier extraction from perovskite to metal electrode.[48] While the lowest unoccupied molecular orbital energy level (E_{LUMO}) of **ZnTPPc** was -3.44 eV, determined by adding the previously obtained E_g to E_{HOMO} value. E_{LUMO} lies higher than the conduction band of perovskite (-4.4 eV), which can efficiently block the photo-generated electron and avoid recombination at the interface of perovskite/HTM.

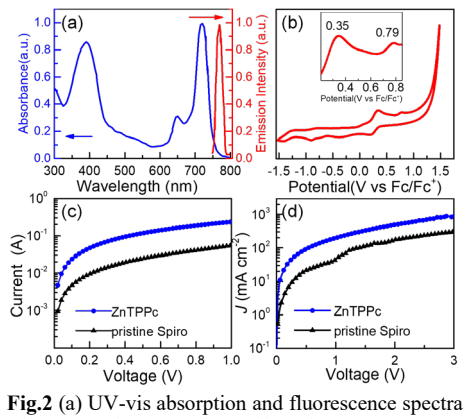

Fig.2 (a) UV-vis absorption and fluorescence spectra of **ZnTPPc** in DMF. (b) cyclic voltammogram (100 mV s^{-1}) of deaerated DMF solution of **ZnTPPc** containing $TBAPF_6$ (0.1 M) at 298K. The inset shows a zoomed view of oxidation peaks . (c) *I-V* curves from conductivity measurements (device structure: FTO/**HTM**/Ag) and (d) *J-V* curves of the **ZnTPPc** based hole-only device with structure: FTO/PEDOT:PSS/**HTM**/Ag. Spiro-OMeTAD is referred to as Spiro.

Particularly, the charge transporting abilities of HTMs are crucial to fabricate high-performance PSCs and the conductivity and hole mobility of **ZnTPPc** were firstly studied. The electrical conductivity was determined by measuring the current-voltage (*I-V*) curve of the device in a structure (FTO/HTM/Ag) following the equation of $\sigma = IA^{-1}V^{-1}d$, where A is the active area of the device, *d* is the thickness of HTM.

The calculated conductivity of **ZnTPPc** was found to be 2.9 x 10^{-6} S cm^{-1}, and for pristine Spiro-OMeTAD was 6.9 × 10^{-7} S cm^{-1}, showing the similar values reported elsewhere (10^{-7}- 10^{-8} S cm^{-1}).[10,49] The conductivity value of ZnTPPc is notably one magnitude higher than the value of pristine Spiro-OMeTAD. Besides, the hole mobility of the **ZnTPPc** and pristine Spiro, was evaluated by space charge limited current (SCLC) method using a hole-only device with the architecture of FTO/PEDOT:PSS/**HTM**/Ag. The current density-voltage (*J-V*) curve was tested under the dark and ambient condition and the hole mobility was calculated using the Mott-Gurney law ($J=9\varepsilon\varepsilon_0\mu V_{app}^2/8d^3$). The obtained hole mobility of **ZnTPPc** was 4.1 × 10^{-5} cm^2 V^{-1} s^{-1}, which is higher than that of pristine Spiro-OMeTAD (1.7 × 10^{-5} cm^2 V^{-1} s^{-1}).[50,51] The relatively higher conductivity and mobility of ZnTPPc will allow improvement of in charge transporting ability and fill factor thus device performance.

The film-forming ability of **ZnTPPc** was investigated with the help of microscopy techniques such as scanning electron microscopy (SEM) and atomic force microscopy (AFM). The **Fig. 3a & 3b** showed the top-view SEM of bare perovskite and perovskite covered with **ZnTPPc** (perovskite/**ZnTPPc**), respectively. Compared to bare perovskite, the surface microstructure of perovskite/**ZnTPPc** film shows full-coverage without any voids or defects. **Fig. 3c & 3d**, suggests similar observation with AFM topographical images and bare perovskite film displayed a root mean square (RMS) roughness value of 29.1 nm. The surface of perovskite/**ZnTPPc** becomes smoother and decreased RMS value of 19.6 nm was noted. The uniform, smooth HTM film can extract photo-generated holes effectively and avoid interfacial recombination loss, and improve the device performance. In all, the **ZnTPPc** armed with such excellent properties such as matched energy level with perovskite and improve electrical properties, film-forming ability demonstrates great potential towards fabricating efficient PSCs.

Photovoltaic performance of PSCs with ZnTPPc as HTM

To validate the potential of **ZnTPPc** as an efficient HTM in PSCs, we fabricated devices with an architect of FTO/*b*&*mp*-TiO_2/perovskite/**ZnTPPc** /Au (*b*&*mp*-TiO_2 presents blocking and mesoporous TiO_2 layer, **Fig 4a**) and for comparative purpose, pristine and doped Spiro-OMeTAD were used as reference HTM. Fig 4b shows a representative cross-sectional SEM image of PSC device with **ZnTPPc** as an HTM, where the mixed perovskite atop of *mp*-TiO_2 was prepared by a two-step deposition method and the thickness was ~ 450 nm.[17,18,25] A thin layer of **ZnTPPc** covered on perovskite film allows around 60 nm thick film. The energy level diagram (Fig. 3c) of **ZnTPPc** based device shows a well-matched HOMO-LUMO energy level with respect the perovskite and thus exhibit the stronger possibility of transporting the holes efficiently.

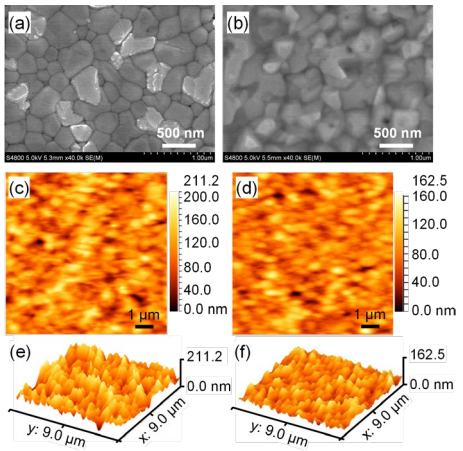

Fig.3 Top-view SEM images of (a) perovskite and (b) perovskite/ZnTPPc film. AFM height images of the (c) perovskite and (d) perovskite/ZnTPPc. Corresponding 3D AFM images of the (e) perovskite and (f) perovskite/ZnTPPc film.

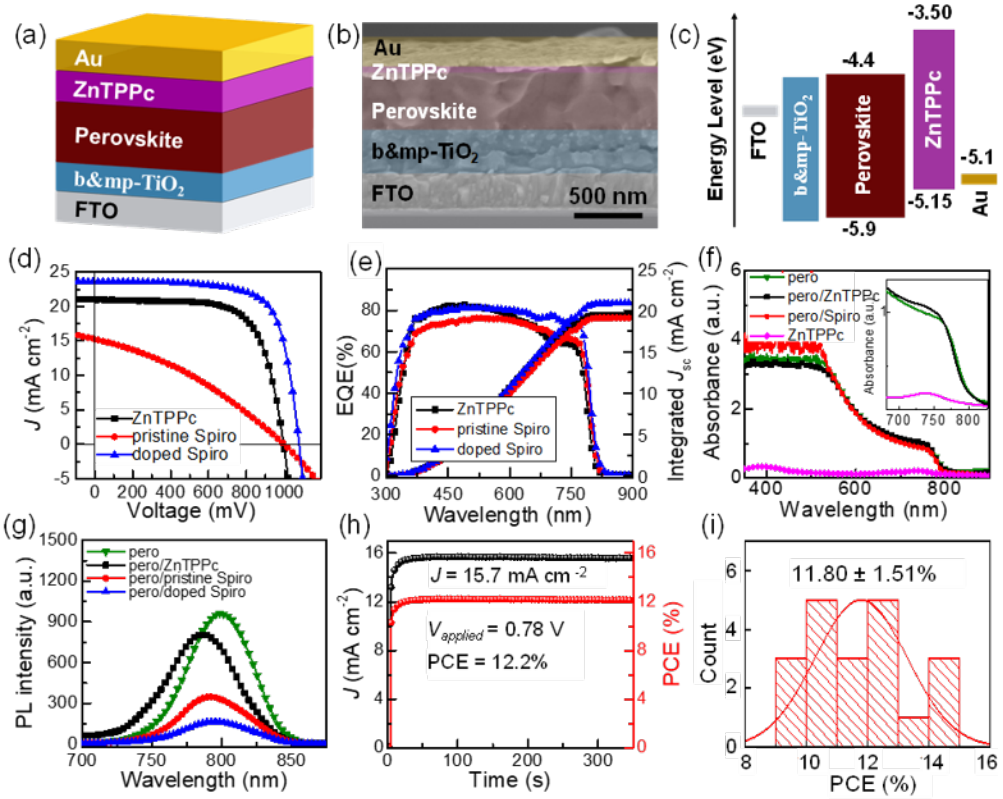

Fig. 4 (a) Device structure , (b) cross-sectional SEM images of the PSCs with ZnTPPc, (c) schematic of the energy level of the PSCs with ZnTPPc, (d) *J-V* curves characterized under simulated AM 1.5G illumination for the devices with different HTMs, (e) EQE and Integrated J_{sc} of the champion device based on different HTMs, (f) absorbance spectra of different thin films, (g) steady state photoluminescence spectra of perovskite with different HTMs, (h) steady-state power output at the maximum power point for the champion device with ZnTPPc as HTM and (i) histograms of PCE performance parameters of PSCs with ZnTPPc as an HTM. The data was analyzed from 20 cells, Spiro-OMeTAD is referred as Spiro.

The *J-V* curves of the champion device with different HTMs were measured under reverse scan and corresponding photovoltaic parameters are shown in Fig. 4d and **Table 1.** The PSC with **ZnTPPc** yielded an overall PCE of 14.5%, with an open-circuit voltage (V_{oc}) of 994.3 mV, a short circuit current current density (J_{sc}) of 21.0 mA cm^{-2}, and a fill factor (*FF*) of 69.42%. A reference device with conventional Spiro-OMeTAD doped with lithium bis(trifluoromethanesulfonyl)imide (LiTFSI) and 4-tert-Butylpyridine (t-BP) was fabricated with the same condition, and exhibited a PCE of 18.47% with a V_{oc} of 1075.9 mV, a J_{sc} of 23.62 mA cm^{-2}, and a FF of 72.69%, which was slightly higher than that of the device with pristine **ZnTPPc**. However, when using pristine Spiro-OMeTAD as a HTM, the device showed inferior PV parameters and registered a PCE of 5.14%, with a V_{oc} of 993.9 mV, J_{sc} of 15.25 mA cm^{-2}, *FF* of 33.92%. Notably, low J_{sc} and FF was found due to the poor electrical properties of Spiro-OMeTAD in its pristine form. The series resistance (R_s) of different HTMs are shown in Table 1. The **ZnTPPc**-based device displayed the R_s of 58 **Ω**, which is comparable with the value of doped Spiro-OMeTAD device (44 **Ω**) and lower than the value of pristine Spiro-OMeTAD device (424 **Ω**). Subsequently, the relative low R_s of **ZnTPPc**-based device allowed us to achieve improved FF and subsequently PCE.[52–54]

Fig. 4e presents the external quantum efficiency (EQE) spectra and the integrated current density (integrated J_{sc}). The integrated J_{sc} values of PSCs with **ZnTPPc**, pristine and doped Spiro-OMeTAD are 19.41, 19.06, and 20.86 mA cm^{-2}, respectively, close to the J_{sc} value attained from *J-V* curves

under the standard solar AM 1.5G. The lower J_{sc} value of the **ZnTPPc**-based device obtained from EQE spectra compared with doped Spiro-OMeTAD is in agreement with the value from the *J-V* curves. The device with **ZnTPPc** and Spiro-OMeTAD own the same EQE value at wavelength ranging from 300 nm to 580 nm, while the device with **ZnTPPc** showed lower EQE value than that of the device with Spiro-OMeTAD at wavelength ranging from 580 nm to 800 nm. Considering the strong absorbance of Pcs at wavelength ranging from 580 nm to 800 nm (Fig. 2a & 4f), one possible reason of decreased EQE and J_{sc} of **ZnTPPc**-based device is that unabsorbed long-wavelength light passing through the perovskite active layer was absorbed by ZnTPPc instead of being reflected by the electrode and reabsorbed by the perovskite layer, leading to the decrease of photocurrent and efficiency.

Photoluminescence (PL) characterization for perovskite with different HTMs on the quartz substrate was used to analyse the charge carrier separation and transport process.[55–58] In order to observe the hole extraction ability of different HTMs, steady state photoluminescence (PL) measurement was made with the

structure of quartz/perovskite/HTM. Fig. 4g. shows the steady state PL spectra for pristine perovskite and with different HTM excited from the quartz side at 600 nm. The strong PL emission peak centred at 798 nm was observed for pristine perovskite while a decrease in PL intensity was noticed with all the HTM samples indicating the efficient hole extraction. Although, HTMs can quench the PL of perovskite, however, doped Spiro-OMeTAD exhibit the maximum PL quenching compared to undoped Spiro and **ZnTPPc**.

Interestingly, in case of **ZnTPPc** , blue shifted PL peak (from 798 to 787 nm at the Pero/ZnTPPC was observed, which can be ascribed to a decrease in the surface trap states[59] on the surface and grain boundaries of perovskite layer, since surface roughness and film morphology was improved after **ZnTPPc** deposition as shown in Figure 3b-d. To evaluate the reliability of the device, the stabilized power output was measured (Fig. 4h). The device with **ZnTPPc** showed 15.7 mA cm^{-2} under the constant bias of near the maximum power point (0.78 V), and yielded stable PCE of 12.2%, in good agreement with the average PCE obtained from forward and reverse scan (12.92%). Besides, to check the reproducibility, 20 independent devices were statistically analysed, and the histograms of PCE (Fig. 4i) as well as V_{oc}, J_{sc} and FF (Fig. S9 ESI†) are summarized in Table 1. The average PCE was 11.80±1.51%. Our results suggest reproducibility of PSCs with **ZnTPPc** as an HTM possibly due to its core structure, which has high tolerance power and nature.

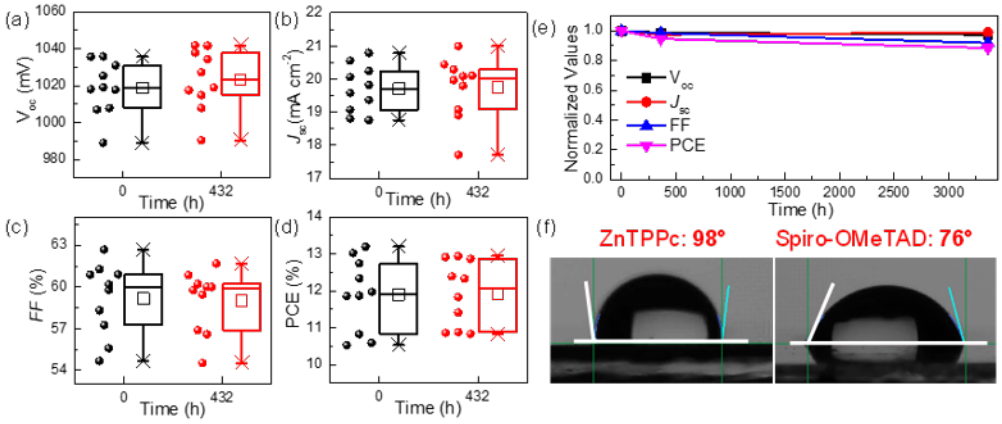

Fig. 5 Statistical box plots of the photovoltaic performance parameters of devices using **ZnTPPc** (a- d) vs storage time; the data was analysed from 20 cells, (e) normalized values of device performance parameters of ZnTPPc-based PSCs during aging and (f) contact angle value of perovskite with different HTMs.

Table 1. Photovoltaic parameters of the PSCs based on different HTMs.

HTM	V_{oc} (mV)	J_{sc}(mA cm^{-2})	FF (%)	PCE (%)	Rs (Ω)	R_{sh} (k Ω)
ZnTPPc (pristine)	994.3	21.00	69.42	14.50	58	19.2
Pristine Spiro	993.9	15.25	33.92	5.14	424	1.7
Doped Spiro	1075.9	23.62	72.69	18.47	44	5.6
ZnTPPc (statistics)	1011.4 ±21	19.92 ±0.81	58.42 ± 5.6	11.80 ±1.51		

Apart from the performance in terms of efficiency, the long-term stability of corresponding devices is another important parameter to further assess the potential of HTMs. These un-encapsulated devices were stored in a dry box under 40 - 50% relative humidity and room temperature condition. The **ZnTPPc**-based PSCs present average PCE of 12.75% after aging for 432 h, while the initial average values of the device were 12.31%, showing slight increases after aging (**Fig. 5** and **Table S2**). Such phenomena typically originated from the optimization of interface contact by solvent drying with storage time. In contrast, the average PCE of the device with doped Spiro-OMeTAD dropped from 18.28% to 16.91% after aging 120 h under similar conditions (Fig. S10 and Table S2, ESI†). Importantly, the average PCE of the **ZnTPPc**-based device remains 88% of initial efficiency after aging for over 3000 h (Fig. 5e and Table S3, ESI†). This point towards **ZnTPPc** based PSCs superior stability. The plausible reasons for improved stability are as follows: the perovskite/ZnTPPc show a higher water contact angle of 98° compared to that of Spiro-OMeTAD (76°) (Fig. 5f), the excellent hydrophobic nature of **ZnTPPc** can effectively block the water penetration into perovskite layers.

To conclude, through molecular engineering, we have designed a tetrasubstituted **ZnTPPc** with electron-rich thienyl-triphenylamine conjugated aromatic substituents. We found that **ZnTPPc** possesses superior electrical properties such as relative high conductivity and mobility compared to pristine Spiro-OMeTAD, suitable energetic level alignment and can supress the trap state on the surface of perovskite. The perovskite solar cells fabricated thereof employing **ZnTPPc** as a hole selective layer gave a highly competitive power conversion efficiency over 14.5%, without the use of any dopant and additives. Furthermore the ultrathin layer will cut down materials consumption and will further lower the cost. **ZnTPPc** maintained the initial efficiency after the aging measurement.

Experimental

Materials

Chemicals were purchased from Sigma Aldrich unless otherwise specified, whereas Na_2CO_3 was acquired from Scharlab, *N*-bromosuccinimide and K_2CO_3 from Alfa Aesar, 4-methoxy-*N*-(4-methoxyphenyl)-*N*-(4-(4,4,5,5-tetramethyl-1,3,2-dioxaborolan-2-yl)phenyl)aniline from Fluorochem, and TBAB from Fluka. All chemicals were employed without any further treatment or purification. 4-iodophthalonitrile was synthesized according to the processes described in the literature.[60]

All reactions were carried out under a nitrogen atmosphere. The solvents for spectroscopic studies were of spectroscopic grade and used as received. Column chromatography was carried out silica gel 60 ACC (40-63 μm). Thin layer chromatography was performed on TLC plates coated with SiO_2 (40-63 μm) 60F254.

Synthesis of ZnTPPc

60 mg (0.12 mmol) of **2**, 10.7 mg (0.058 mmol) of $Zn(OAc)_2$ and a drop of DBN were dissolved in 200 μL of DMAE and heated to reflux under nitrogen atmosphere for 16 h. After cooling at room temperature, DMAE was removed by distillation with toluene. The residue was passed by column chromatography (DCM:MeOH/95:5), the green solid obtained washed with MeOH at reflux, and finally purified by preparative TLC (DCM:MeOH, 96:4) affording **ZnTPPc** (32 mg, 52 %) as a green powder. UV-vis: λ_{max} (DMF)/nm (log Ɛ): 390 (5.01), 647 (4.57), 719 (5.17). HRMS (MALDI-TOF-MS): For $C_{128}H_{92}N_{12}O_8S_4Zn$ $(M)^+$ calc. 2116.533, found 2116.581.

Synthesis of phthalonitrile 2

200 mg (0.69 mmol) of **3**, 300 mg (0.69 mmol) of 4-methoxy-*N*-(4-methoxyphenyl)-*N*-(4-(4,4,5,5-tetramethyl-1,3,2-dioxaborolan-2-yl)phenyl)aniline, 63.4 mg (0.069 mmol) of $Pd_2(dba)_3$, 145.2 mg (0.55 mmol) of PPh_3 and 11.4 mg (0.035 mmol) of TBAB were dissolved in 16 mL of degassed toluene. A degassed 2M solution of K_2CO_3 was added and heated to 90 °C under nitrogen atmosphere for 24 hours. After cooling at room temperature, the crude was filtered and concentrated. Purification by column chromatography using hexane:ethyl acetate (7:3)

afforded **2** (168 mg, 48%) as a red powder. ^{1}H NMR ($CDCl_3$): δ = 3.81 (s, 6H), 6.89 (m, 6H), 7.09 (m, 4H), 7.22 (d, *J*= 3.9, 1H), 7.42 (m, 3H), 7.75 (dd, *J*= 8.3, 0.4, 1H), 7.86 (dd, *J*= 8.3, 1.9, 1H), 7.96 (dd, *J*= 1.9, 0.4, 1H). ^{13}C NMR ($CDCl_3$): δ = 55.5, 112.3, 114.8, 115.3, 115.6, 116.6, 119.7, 123.1, 124.6, 126.5, 127.0, 127.6, 128.5, 129.3, 133.9, 136.5, 139.5, 140.1, 148.6, 149.3, 156.4. UV-vis: λ_{max} ($CHCl_3$)/nm (log Ɛ): 451 (4.39). HRMS (MALDI-TOF-MS): For $C_{32}H_{23}N_3O_2S$ $(M)^+$ calc. 513.151 found 513.122.

Synthesis of phthalonitrile 3

500 mg (2.38 mmol) of **4** were dissolved in 12 mL of DCM and cooled to 0 °C. A solution of 634.8 mg (3.57 mmol) of *N*-bromosuccinimide (NBS) dissolved in 12 ml of acetic acid was added dropwise for 30 minutes, and stayed at room temperature overnight. The reaction was carried in darkness. Then it was cooled to 0 °C, the solid obtained was filtered and washed with hexane (410 mg, 60 %). ^{1}H NMR ($CDCl_3$): δ = 7.15 (d, *J*= 4.0, 1H), 7.25 (d, *J*= 4.0, 1H), 7.80 (s, 1H), 7.80 (s, 1H), 7.90 (t, *J*= 1.2, 1H). ^{13}C NMR ($CDCl_3$): δ = 112.5, 114.3, 114.6, 114.8, 115.7, 126.6, 128.5, 128.9, 131.1, 133.5, 137.6, 140.0.

Synthesis of phthalonitrile 4

1 g (3.94 mmol) of 4-iodophthalonitrile, 910 mg (4.33 mmol) of thiophene-2-boronic acid pinacol ester, 42 mg (0.19 mmol) of palladium(II) acetate and 206.5 mg (0.79 mmol) of triphenylphosphine were dissolved in 10 mL of distilled and degassed 1,4-dioxane. Then, 4 mL of a degassed 2M solution of Na_2CO_3 was added and heated to 95°C under nitrogen atmosphere for 6h. After cooling at room temperature, the crude was treated with NH_4Cl 2M, extracted with DCM, washed with distilled water, dried over $NaSO_4$, filtered and concentrated to afford a white solid. Purification by column chromatography using hexane:toluene (1:4) as solvent, afforded **4** (680 mg, 83 %) as a white powder. ^{1}H NMR ($CDCl_3$): δ = 7.18 (dd, *J*= 5.0, 3.8, 1H), 7.50 (m, 2H), 7.80 (d, *J*= 8.3, 1H), 7.91 (dd, *J*= 8.3, 1.9, 1H), 8.00 (d, *J*= 1.9, 1H). ^{13}C NMR ($CDCl_3$): δ = 111.9, 114.4, 114.6, 115.4, 126.0, 127.9, 128.1, 128.7, 129.0, 133.3, 138.5, 138.6.

Measurements for materials

NMR spectra were measured with a Bruker AC 300. UV-vis were recorded with a Helios Gamma spectrophotometer. Fluorescence spectra were recorded with a Perkin Elmer LS 55 Luminescence spectrophotometer. High-resolution mass spectra were obtained from a Bruker Microflex LRF20 matrix assisted laser desorption/ionization time of flight (MALDI-TOF) using dithranol as matrix.

Cyclic voltammetry was measured in a conventional three-electrode cell using a μ-AUTOLAB type III potentiostat/galvanostat at 298 K over benzonitrile and deaerated sample solutions containing 0.10 M tetrabutylammonium hexafluorophosphate ($TBAPF_6$) as supporting electrolyte. Platinum as working electrode, $Ag/AgNO_3$ as the reference electrode, and platinum as wire counter electrode were employed. Ferrocene/Ferrocenium was used as an internal standard for all measurements.

Device fabrication and characterization

The pre-cleaned FTO (NSG10) substrates were treated with UV-ozone machine for 60 min each time and were heated to 500 °C. A compact blocking layer of TiO_2 were deposited by spray pyrolysis using a 5% titanium (IV) diisopropoxide bis(acetylacetonate) solution diluted by anhydrous ethanol. The substrates were kept at 500 °C for 30 min after the spraying. Mesoporous TiO_2 films were obtained by spin-coating a mesoporous dispersion of TiO_2 nanoparticles (30 NRD from Dyesol) and heated at 500 °C for 30 min to produce the mesoporous structure. The substrates were transferred to an argon-filled glovebox for depositing perovskite films. The two-step deposition method was adopted to prepare perovskite . In short, 1.3M PbI_2 precursor solution dissolving in a mixed solvent (volume ratio of DMF/DMSO=9.5/0.5) was spin coating at 2,000 rpm for 20 s to prepare PbI_2 layer. The mixed organic precursor solution containing formamidinium iodide: methylammonium bromide: methylammonium chloride= 60: 6: 6 in 1 mL isopropanol was dynamically added to the PbI_2 layer and was spin-coated at 2,000 rpm for 20 s. The as-prepared film was annealed at 150 °C for 15 min in the glovebox. The **ZnTPPc** film layer was deposited atop perovskite films at a spin rate of 4,000 rpm for 20 s with 10 mM (~ 21 mg/mL) solution with chlorobenzene as the solvent. The Spio-OMeTAD hole transporting layer was prepared by spin-coated the Spiro-OMeTAD solution prepared by dissolving 72.3 mg material in 1 mL chlorobenzene. Finally, a ~ 70 nm gold electrode was deposited on top of the hole-transporting layer by thermal evaporation. *J–V*

curves were recorded with a Keithley 2400 source-measurement-unit under AM 1.5 G, 100 mW cm^2 illumination from a 450 W 3A solar simulator (ORIEL, 94023 A). This was calibrated using an NREL certified calibrated monocrystalline silicon solar cell. Testing parameters: active area defined by black masks: 0.09 cm^2, scan rate: 100 mV s^{-1}, pre-sweep delay: 10 s). Surface and cross-sectional SEM images were recorded by using a Hitachi S-4800. The EQE spectra was measured using a 150 W Xenon lamp (Newport) attached to IQE200B (Oriel) motorized 1/4m monochromator as the light source. The water contact angle was tested by contact angle goniometer (Ossila). Absorption spectra was collected by Cary 60. Atomic Force Microscopy (AFM) images were acquired with CSI Nano observer AFM.

Acknowledgements

This work received funding from the European Union H2020 Programme under a European Research Council Consolidator grant [MOLEMAT, 726360]. We gratefully acknowledge the financial support provided by European Regional Development Fund ‘‘A way to make Europe and the Spanish Ministerio de Ciencia e Innovacion, Agencia Estatal de Investigación: project CTQ2017-87102-R AEI/FEDER, UE. P.H. acknowledges funding from the European Commission via a Marie-Skłodowska-Curie individual fellowship (Grant Number 896211_SMILIES). We thank David Payno for LabVIEW software.

References

1. *https://www.nrel.gov/pv/cell-efficiency.html*, (accessed: July 2019).
2. A. Kojima, K. Teshima, Y. Shirai and T. Miyasaka, *J. Am. Chem. Soc.*, 2009, **131**, 6050–6051.
3. J. Burschka, N. Pellet, S. J. Moon, R. Humphry-Baker, P. Gao, M. K. Nazeeruddin and M. Grätzel, *Nature*, 2013, **499**, 316–319.
4. M. Liu, M. B. Johnston and H. J. Snaith, *Nature*, 2013, **501**, 395–398.
5. H.-S. Kim, C.-R. Lee, J.-H. Im, K.-B. Lee, T. Moehl, A. Marchioro, S.-J. Moon, R. Humphry-Baker, J.-H. Yum, J. E. Moser, M. Grätzel and N.-G. Park, *Sci. Rep.*, 2012, **2**, 591.
6. S. D. Stranks, G. E. Eperon, G. Grancini, C. Menelaou, M. J. P. Alcocer, T. Leijtens, L. M. Herz, A. Petrozza and H. J. Snaith, *Science* , 2013, **342**, 341–344.
7. C. S. Ponseca Jr., T. J. Savenije, M. a. Abdellah, K. B. Zheng, A. P. Yartsev, T. T. Pascher, T. Harlang, P. Chabera, T. Pullerits, A. Stepanov, J.-P. P. Wolf and V. Sundstrom, *J. Am. Chem. Soc.*, 2014, **136**, 5189–5192.
8. M. Salado, M. Andresini, P. Huang, M. T. Khan, F. Ciriaco, S. Kazim and S. Ahmad, *Adv. Funct. Mater.*, 2020, **30**, 1910561.
9. E. H. Jung, N. J. Jeon, E. Y. Park, C. S. Moon, T. J. Shin, T.-Y. Yang, J. H. Noh and J. Seo, *Nature*, 2019, **567**, 511–515.
10. L. Caliò, M. Salado, S. Kazim and S. Ahmad, *Joule*, 2018, **2**, 1800–1815.
11. S. Kazim, F. J. Ramos, P. Gao, M. K. Nazeeruddin, M. Grätzel and S. Ahmad, *Energy Environ. Sci.*, 2015, **8**, 1816–1823.
12. L. Calió, S. Kazim, M. Grätzel and S. Ahmad, *Angew. Chemie - Int. Ed.*, 2016, **55**, 14522–14545.
13. D. Li, J. Y. Shao, Y. Li, Y. Li, L. Y. Deng, Y. W. Zhong and Q. Meng, *Chem. Commun.*, 2018, **54**, 1651–1654.
14. K. Rakstys, C. Igci and M. K. Nazeeruddin, *Chem. Sci.*, 2019, **10**, 6748–6769.
15. J. Urieta-Mora, I. García-Benito, A. Molina-Ontoria and N. Martín, *Chem. Soc. Rev.*, 2018, **47**, 8541–8571.
16. Z. Hawash, L. K. Ono and Y. Qi, *Adv. Mater. Interfaces*, 2018, **5**, 1700623.
17. P. Huang, L. Yuan, K. Zhang, Q. Chen, Y. Zhou, B. Song and Y. Li, *ACS Appl. Mater. Interfaces*, 2018, **10**, 14796–14802.
18. P. Huang, Q. Chen, K. Zhang, L. Yuan, Y. Zhou, B. Song and Y. Li, *J. Mater. Chem. A*, 2019, **7**, 6213–6219.
19. F. Zhang, C. Xiao, X. Chen, B. W. Larson, S. P. Harvey, J. J. Berry and K. Zhu, *Joule*, 2019, **3**, 1452–1463.
20. F. Zhang, D. Bi, N. Pellet, C. Xiao, Z. Li, J. J. Berry, S. M. Zakeeruddin, K. Zhu and M. Grätzel, *Energy Environ. Sci.*, 2018, **11**, 3480–3490.
21. F. Zhang, W. Shi, J. Luo, N. Pellet, C. Yi, X. Li, X. Zhao, T. J. S. Dennis, X. Li, S. Wang, Y. Xiao, S. M. Zakeeruddin, D. Bi and M. Grätzel, *Adv. Mater.*, 2017, **29**, 1606806.

22. A. K. Jena, Y. Numata, M. Ikegami and T. Miyasaka, *J. Mater. Chem. A*, 2018, **6**, 2219–2230.
23. D. Bryant, N. Aristidou, S. Pont, I. Sanchez-Molina, T. Chotchunangatchaval, S. Wheeler, J. R. Durrant and S. A. Haque, *Energy Environ. Sci.*, 2016, **9**, 1655–1660.
24. N. Arora, M. I. Dar, A. Hinderhofer, N. Pellet, F. Schreiber, S. M. Zakeeruddin and M. Grätzel, *Science* , 2017, **358**, 768–771.
25. P. Huang, Manju, S. Kazim, G. Sivakumar, M. Salado, R. Misra and S. Ahmad, *ACS Appl. Mater. Interfaces*, 2020, **12**, 22881–22890.
26. L. Xu, P. Huang, J. Zhang, X. Jia, Z. Ma, Y. Sun, Y. Zhou, N. Yuan and J. Ding, *J. Phys. Chem. C*, 2017, **121**, 21821–21826.
27. X. Jiang, D. Wang, Z. Yu, W. Ma, H.-B. Li, X. Yang, F. Liu, A. Hagfeldt and L. Sun, *Adv. Energy Mater.*, 2019, **9**, 1803287.
28. M. Cheng, Y. Li, M. Safdari, C. Chen, P. Liu, L. Kloo and L. Sun, *Adv. Energy Mater.*, 2017, **7**, 1602556.
29. M. Urbani, G. de la Torre, M. K. Nazeeruddin and T. Torres, *Chem. Soc. Rev.*, 2019, **48**, 2738–2766.
30. L. Caliò, J. Follana-Berná, S. Kazim, M. Madsen, H.-G. Rubahn, Á. Sastre-Santos and S. Ahmad, *Sustain. Energy Fuels*, 2017, **1**, 2071–2077.
31. M. G. Walter, A. B. Rudine and C. C. Wamser, *J. Porphyr. Phthalocyanines*, 2010, **14**, 759–792.
32. M. E. Ragoussi, J. J. Cid, J. H. Yum, G. De La Torre, D. Di Censo, M. Grätzel, M. K. Nazeeruddin and T. Torres, *Angew. Chemie - Int. Ed.*, 2012, **51**, 4375–4378.
33. W. Ke, D. Zhao, C. R. Grice, A. J. Cimaroli, G. Fang and Y. Yan, *J. Mater. Chem. A*, 2015, **3**, 23888–23894.
34. J. Cao, X. Lv, P. Zhang, T. T. Chuong, B. Wu, X. Feng, C. Shan, J. Liu and Y. Tang, *Adv. Mater.*, 2018, **30**, 1800568.
35. T. Duong, J. Peng, D. Walter, J. Xiang, H. Shen, D. Chugh, M. Lockrey, D. Zhong, J. Li, K. Weber, T. P. White and K. R. Catchpole, *ACS Energy Lett.*, 2018, **3**, 2441–2448.
36. Q. Hu, E. Rezaee, M. Li, Q. Chen, Y. Cao, M. Mayukh, D. V. McGrath and Z. X. Xu, *ACS Appl. Mater. Interfaces*, 2019, **11**, 36535–36543.
37. Y. Feng, Q. Hu, E. Rezaee, M. Li, Z. Xu, A. Lorenzoni, F. Mercuri and M. Muccini, *Adv. Energy Mater.*, 2019, 1901019.
38. Y. Wang, X. Liu, H. Shan, Q. Chen, T. Liu, X. Sun, D. Ma, Z. Zhang, J. Xu and Z. X. Xu, *Dye. Pigment.*, 2017, **139**, 619–626.
39. X. Jiang, Z. Yu, H.-B. Li, Y. Zhao, J. Qu, J. Lai, W. Ma, D. Wang, X. Yang and L. Sun, *J. Mater. Chem. A*, 2017, **5**, 17862–17866.
40. D. Molina, M. A. Ruiz-Preciado, B. Carlsen, F. T. Eickemeyer, B. Yang, N. Flores-Díaz, M. J. Álvaro-Martins, K. Nonomura, A. Hagfeldt and Á. Sastre-Santos, *ChemPhotoChem*, 2020, **4**, 307–314.
41. Z. Cui, Y. Wang, Y. Chen, X. Chen, X. Deng and W. Chen, *Org. Electron.*, 2019, **69**, 248–254.
42. F. Zhang, D. Wu, Y. Xu and X. Feng, *J. Mater. Chem.*, 2011, **21**, 17590.
43. H. Li, K. Fu, P. P. Boix, L. H. Wong, A. Hagfeldt, M. Grätzel, S. G. Mhaisalkar and A. C. Grimsdale, *ChemSusChem*, 2014, n/a-n/a.
44. G. Kim, H. Choi, M. Kim, J. Lee, S. Y. Son and T. Park, *Adv. Energy Mater.*, 2020, **10**, 1903403.
45. I. Zimmermann, J. Urieta-Mora, P. Gratia, J. Aragó, G. Grancini, A. Molina-Ontoria, E. Ortí, N. Martín and M. K. Nazeeruddin, *Adv. Energy Mater.*, 2017, **7**, 1601674.
46. P. Gao, K. T. Cho, A. Abate, G. Grancini, P. Y. Reddy, M. Srivasu, M. Adachi, A. Suzuki, K. Tsuchimoto, M. Grätzel and M. K. Nazeeruddin, *Phys. Chem. Chem. Phys.*, 2016, **18**, 27083–27089.
47. K. T. Cho, O. Trukhina, C. Roldán-Carmona, M. Ince, P. Gratia, G. Grancini, P. Gao, T. Marszalek, W. Pisula, P. Y. Reddy, T. Torres and M. K. Nazeeruddin, *Adv. Energy Mater.*, 2017, **7**, 1601733.
48. Q. Jiang, L. Zhang, H. Wang, X. Yang, J. Meng, H. Liu, Z. Yin, J. Wu, X. Zhang and J. You, *Nat. Energy*, 2017, **2**, 16177.
49. W. H. Nguyen, C. D. Bailie, E. L. Unger and M. D. Mcgehee, .
50. P. Qin, S. Tanaka, S. Ito, N. Tetreault, K. Manabe, H. Nishino, M. K. Nazeeruddin and M. Grätzel, *Nat. Commun.*, 2014, **5**, 1–6.

51. D. Bi, B. Xu, P. Gao, L. Sun, M. Grätzel and A. Hagfeldt, *Nano Energy*, 2016, **23**, 138–144.
52. C. Shen, Y. Wu, H. Zhang, E. Li, W. Zhang, X. Xu, W. Wu, H. Tian and W.-H. Zhu, *Angew. Chemie Int. Ed.*, 2019, **58**, 3784–3789.
53. N. J. Jeon, H. G. Lee, Y. C. Kim, J. Seo, J. H. Noh, J. Lee and S. Il Seok, *J. Am. Chem. Soc.*, 2014, **136**, 7837–7840.
54. P. Huang, Z. Wang, Y. Liu, K. Zhang, L. Yuan, Y. Zhou, B. Song and Y. Li, *ACS Appl. Mater. Interfaces*, 2017, **9**, 25323–25331.
55. P. Liu, B. Xu, Y. Hua, M. Cheng, K. Aitola, K. Sveinbjörnsson, J. Zhang, G. Boschloo, L. Sun and L. Kloo, *J. Power Sources*, 2017, **344**, 11–14.
56. X. Liu, F. Zhang, Z. Liu, Y. Xiao, S. Wang and X. Li, *J. Mater. Chem. C*, 2017, **5**, 11429–11435.
57. F. Zhang, Z. Wang, H. Zhu, N. Pellet, J. Luo, C. Yi, X. Liu, H. Liu, S. Wang, X. Li, Y. Xiao, S. M. Zakeeruddin, D. Bi and M. Grätzel, *Nano Energy*, 2017, **41**, 469–475.
58. F. Zhang, S. Wang, H. Zhu, X. Liu, H. Liu, X. Li, Y. Xiao, S. M. Zakeeruddin and M. Grätzel, *ACS Energy Lett.*, 2018, **3**, 1145–1152.
59. D. W. DeQuilettes, S. M. Vorpahl, S. D. Stranks, H. Nagaoka, G. E. Eperon, M. E. Ziffer, H. J. Snaith and D. S. Ginger, *Science* , 2015, **348**, 683–686.
60. S. M. Marcuccio, P. I. Svirskaya, S. Greenberg, A. B. P. Lever, C. C. Leznoff and K. B. Tomer, *Can. J. Chem.*, 1985, **63**, 3057–3069.

Supporting Info

Molecularly Engineered Thienyl-Triphenylamine Substituted Zinc Phthalocyanine as Dopant Free Hole Transporting Materials in Perovskite Solar Cells

Peng Huang,[a] Adrian Hernández,[b] Samrana Kazim,[a,c] Javier Ortíz,[b] Ángela Sastre-Santos,[*b] and Shahzada Ahmad [*a, c]

[a]BCMaterials, Basque Center for Materials, Applications and Nanostructures, UPV/EHU Science Park, 48940 Leioa, Spain Tel: +34 946128811 E-mail: shahzada.ahmad@bcmaterials.net

[b]Área de Química Orgánica, Instituto de Bioingeniería Universidad Miguel Hernández Avda. de la Universidad, s/n, Elche 03202, Spain E-mail: asastre@umh.es

[b]IKERBASQUE, Basque Foundation for Science, Bilbao, 48013, Spain

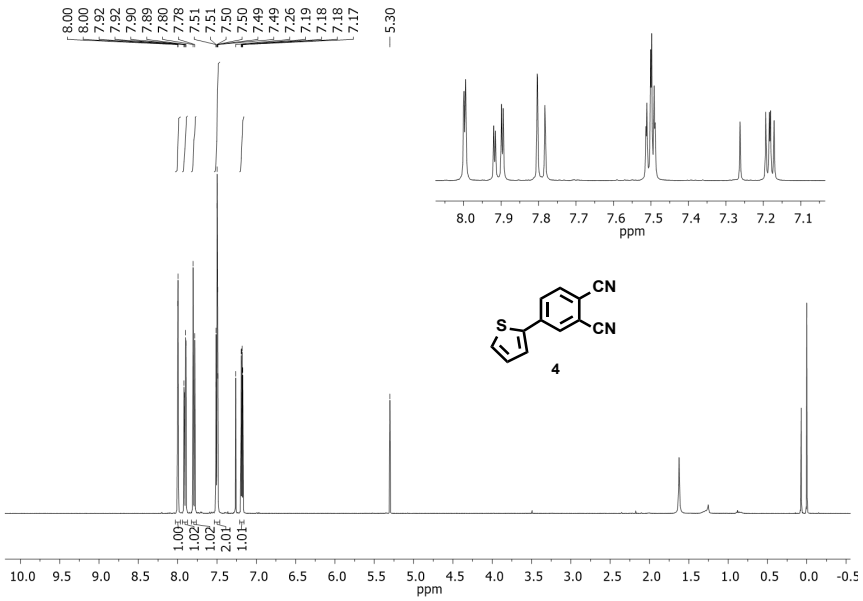

Fig. S1. ^{1}H NMR spectrum of phthalonitrile **4** in $CDCl_3$.

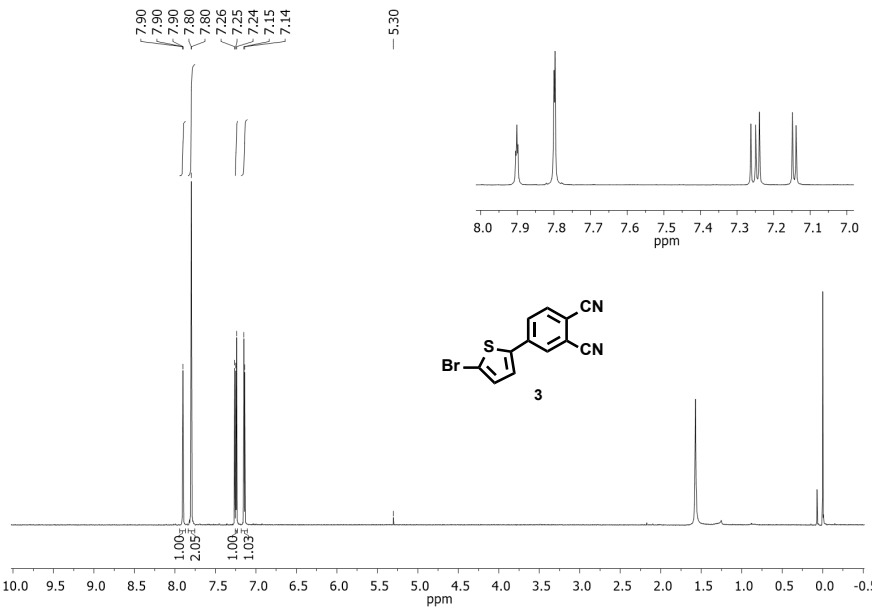

Fig. S2. ^{1}H NMR spectrum of phthalonitrile **3** in $CDCl_3$.

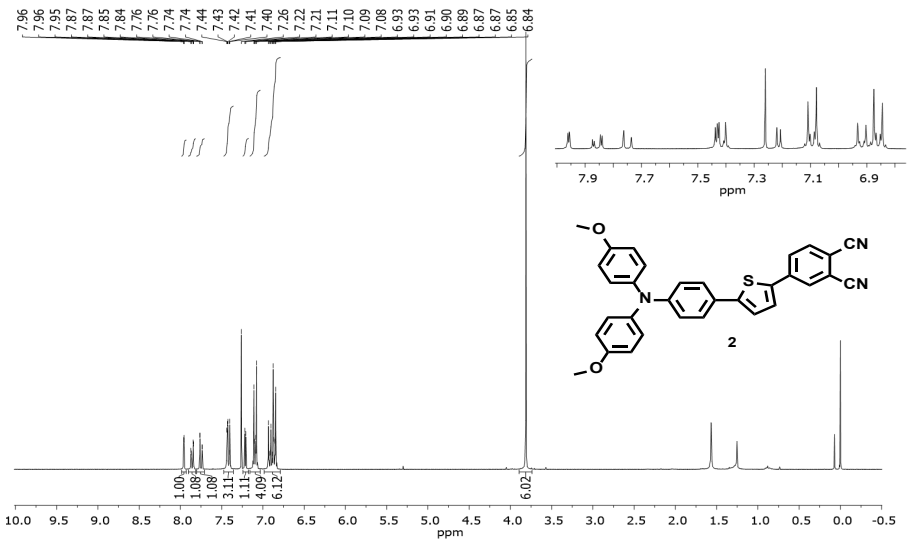

Fig. S3. ^{1}H NMR spectrum of phthalonitrile **2** in $CDCl_3$.

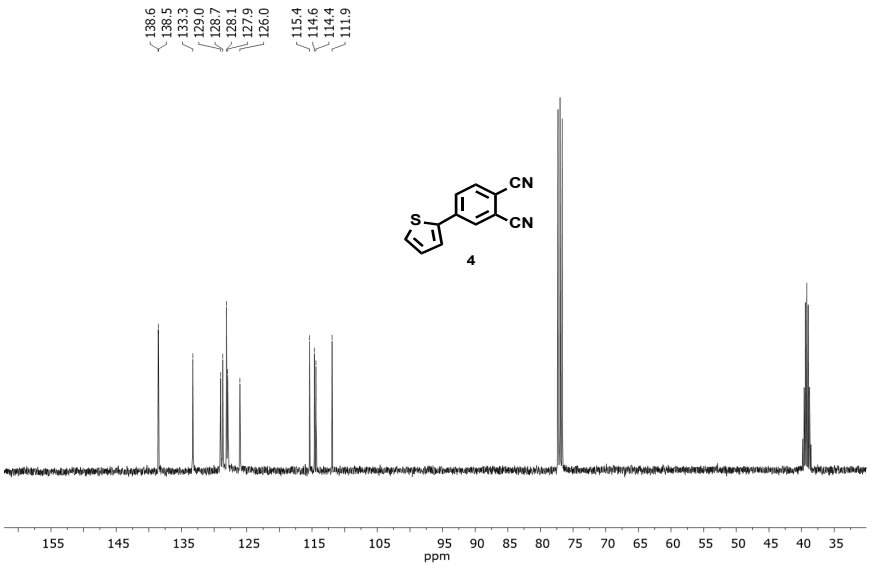

Fig. S4. ^{13}C NMR spectrum of phthalonitrile **4** in $CDCl_3$ + DMSO-*d*$_6$.

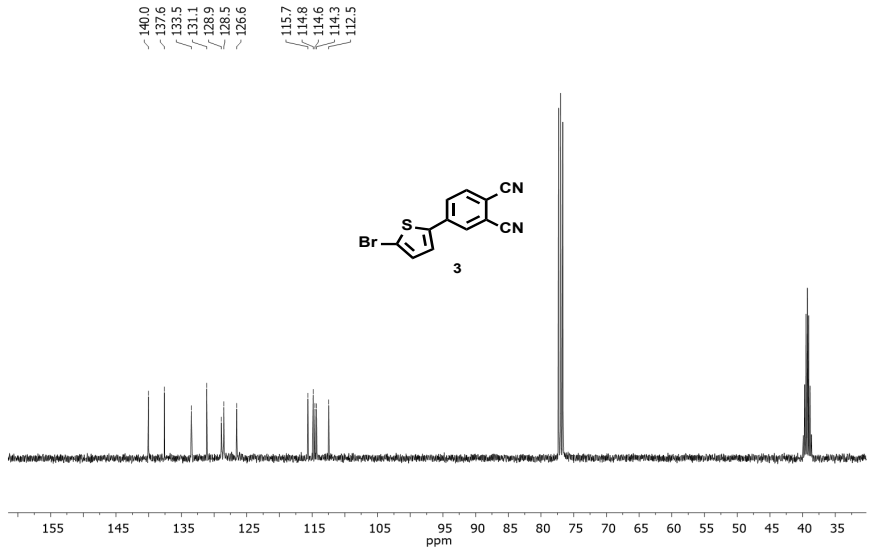

Fig. S5. ^{13}C NMR spectrum of phthalonitrile **3** in $CDCl_3$ + DMSO-d_6.

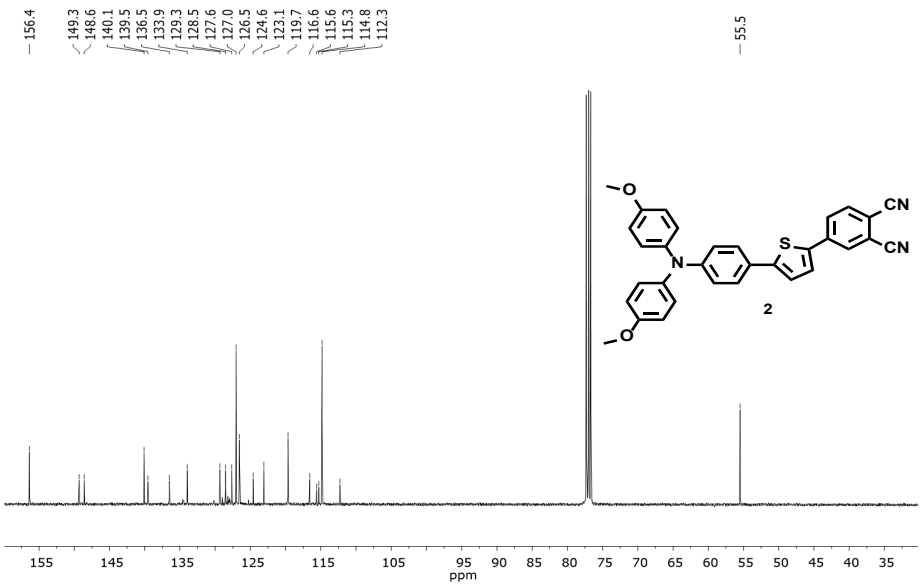

Fig. S6. ^{13}C NMR spectrum of phthalonitrile **2** in $CDCl_3$.

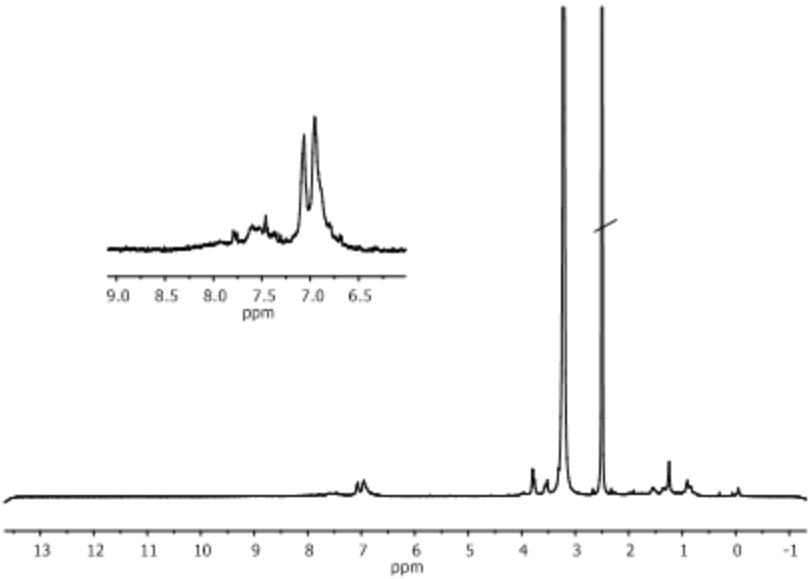

Fig. S7. ^{1}H NMR spectrum of **ZnTPPc** in DMSO-d_6

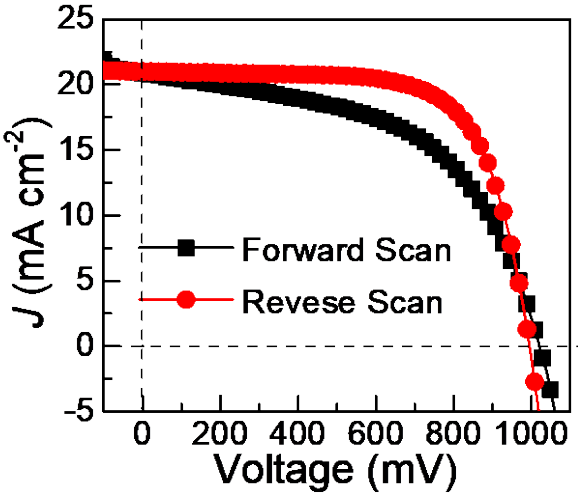

Fig. S8 *J-V* curves of forward and reverse scans under simulated AM 1.5G illumination for the ZnTPPc-based PSC.

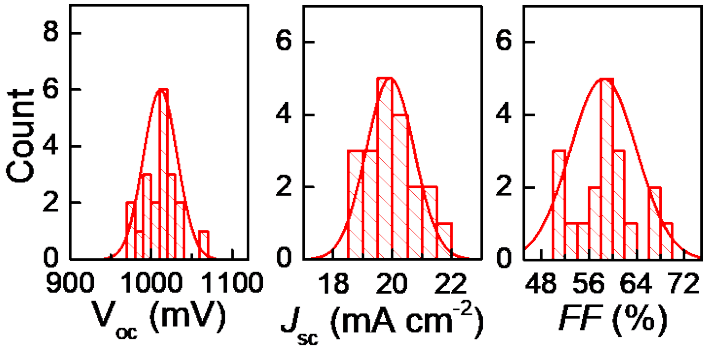

Fig. S9 Histograms of V_{oc}, J_{sc} and FF of PSCs with ZnTPPc as an HTM. The data was analysed from 20 cells.

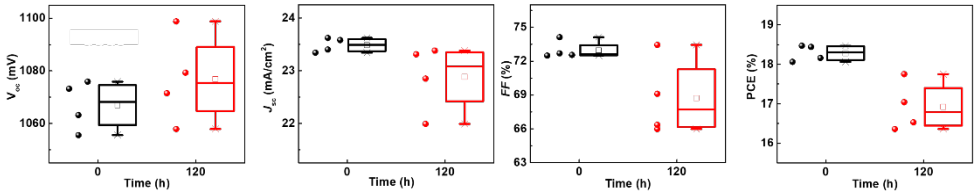

Fig. S10 Statistical box plots of the photovoltaic performance parameters of devices using doped Spiro-OMeTAD vs different storage time.

Table S1 Device performance parameters for the ZnTPPc-based PSC under forward and reverse scans.

Scan direction	V_{oc} (mV)	J_{sc} (mA cm^{-2})	FF (%)	PCE (%)
Forward	994.3	21.0	69.42	14.50
Reverse	1.020	20.91	53.18	11.34
Average	1006.9	20.96	61.3	12.92

Table S2 Average values of device performance parameters of PSCs with different HTMs measured at the different aging time. ZnPPC in its pristine form, while Spiro-OMeTAD is in doped state.

HTM	Time (h)	V_{oc} (mV)	J_{sc} (mA cm^{-2})	FF (%)	PCE (%)
ZnTPPc	0	1018.6±14.6	19.71±0.71	59.15±2.62	11.89±0.98
ZnTPPc	432	1032.2±16.6	19.74±0.94	58.99±2.24	11.92±0.88
Spiro-OMeTAD	0	1068.0±9.3	23.49±0. 14	72.96±0.78	18.28±0.21
Spiro-OMeTAD	120	1076.9±17.1	22.88±0.64	68.72±3.45	16.92±0.62

Table S3 Device performance parameters of PSCs with **ZnTTPc** measured at the different aging time.

Time (h)	No	V_{oc} (mV)	J_{sc} (mA cm^{-2})	FF (%)	PCE (%)
0	1	1027.2	20.99	60.00	12.94
0	2	1034.2	19.80	60.21	12.33
0	3	1041.9	20.29	60.85	12.86
360	1	1019.1	20.25	59.79	12.33
360	2	1018.1	19.37	60.17	11.87
360	3	1025.3	19.83	58.30	11.85
3360	1	1025.8	20.82	54.76	11.70
3360	2	986.8	19.07	57.14	10.75
3360	3	1008.6	20.52	54.38	11.26

Asymmetrically Substituted Phthalocyanines as Dopant-Free Hole Selective Layers for Reliability in Perovskite Solar Cells

Peng Huang,[†] Adrián Hernández,[†] Samrana Kazim, Jorge Follana-Berná, Javier Ortiz, Luis Lezama, Ángela Sastre-Santos,[*] and Shahzada Ahmad[*]

Cite This: *ACS Appl. Energy Mater*. **2021**, *4*, 10124−10135
Received: July 12, 2021
Published: September 10, 2021

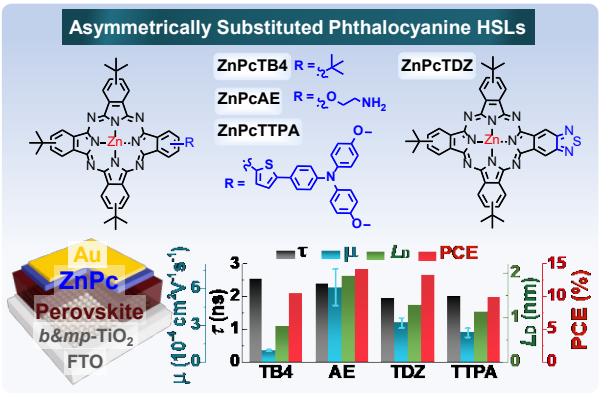

ABSTRACT: Dopant-free metal phthalocyanines are viable alternatives to the classical Spiro-OMeTAD in perovskite solar cells (PSCs), due to their appealing optoelectrical properties and chemical stability. However, low carrier concentration, transportability, and narrow bandgap limit their application. Here, we designed and investigated six innovative asymmetrically substituted metal phthalocyanines (MPcs, M = Zn or Cu), and established the correlation between electronic structure, charge carrier transfer parameter, and core metal/substitutions in MPcs by transient absorbance spectroscopy and electronic paramagnetic resonance. We probed the charge transport properties of ZnPcs including carrier lifetime, diffusion coefficient, and diffusion length by transient absorbance spectroscopy. We noted, ZnPcAE presents a longer diffusion length (1.94 nm) than of control ZnPcTB4 (0.80 nm), which is advantageous for reducing charge recombination and gave higher power conversion efficiency in the fabricated PSCs. Importantly, the devices with MPcs yielded improved stability under multi-stress conditions. Our work provides a molecular guideline for designing MPcs and their application as dopant-free hole-transporting materials for perovskite solar cells fabrication.

KEYWORDS: perovskite solar cells, metal phthalocyanine, hole transporting materials, improved stability, electron paramagnetic resonance, transient absorbance.

1. Introduction

Hybrid organic-inorganic perovskite solar cells (PSCs) have attracted significant interest, as their certificated power conversion efficiency (PCE) swiftly soared from 10% to 25.5% in less than a decade.[1−3] This rapid advancement in the figure of merit was due to the unparalleled characteristics of hybrid organic-inorganic perovskites: tuneable panchromatic light absorption, long carrier diffusion lengths for electrons/holes, and low-temperature solution-processability.[4−6] To accelerate the commercial viability of perovskite-based devices, the investigation on the stability of perovskite and the device is receiving substantial attention. Designing innovative electron/hole-transporting materials (ETM/HTM),[7,8] placement of a buffer layer at the different interfaces[9] allowed to optimize the photovoltaic (PV) performance and device stability.[10,11]

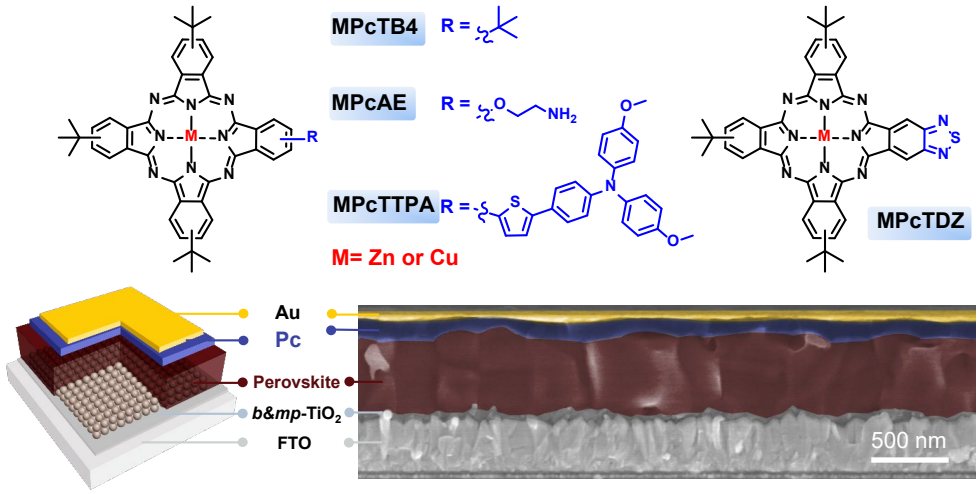

Figure 1. the molecular structures of unsymmetrical MPcs and device architect employing MPc as an HTM, and the representative cross-sectional image of PSC with standard architecture FTO/*b&mp*-TiO_2/perovskite/ZnPcAE/Au.

In typical (*n-i-p*) PSCs, the HTMs coated perovskite layers play crucial roles in separating and extracting photo-generated holes, suppressing interface charge recombination, to achieve high PCE. The choice of HTMs can extend the durability of the devices by isolating the perovskite active layer from oxygen, moisture, and passivating the surface defect. Although *2,2′,7,7′*-tetrakis-(*N,N*-di-p-methoxyphenylamine)-9,9′-spirobifluorene (Spiro-OMeTAD), is the most employed HTM in *n-i-p* type PSCs, the pristine Spiro-OMeTAD possesses poor electrical properties, UV instability, and is cost-ineffective.[12,13] Further the use of hygroscopic *p*-type dopants and additives such as lithium bis(trifluoromethanesulfonyl)imide (Li-TFSI) and 4-*tert*-butylpyridine (*t*-BP), or metal complex is a prerequisite to improve electrical properties, which diffuses into perovskite layers and accelerate degradation under real operating conditions.[12,13] Alternatively, developing dopant-free HTMs that can yield high PV performance and stability is paramount research.

Recently, the dopant-free HTMs based on small molecules, macrocycle molecules, and conjugated polymers, have been designed and their performance was reported.[14] Phthalocyanines (Pcs) are attractive as HTMs due to their ease of synthesis, purification steps and are thermally and photochemical stable. In most of the cases, they yield competitive performance in PSC,[15] except the report of symmetrical NiPc with four methoxy-ethoxy measured over 21% efficiency.[16]

The PV performance of the PSCs employing Pcs is limited by two major factors: (i) poor conductivities of pristine Pcs. In the early stages of Pcs based HTMs development, dopants (lithium salts and *t*-BP) were inevitable to introduce for improvement of transporting ability, which sacrifices the device stability.[17] Aiming for developing dopant-free Pc HTMs, various peripheral / non-peripheral substituents, and different core atoms were applied into phthalocyanine.[18] Non-peripheral *P*-SC_6-TiOPc / peripheral-substituted *NP*-SC_6-TiOPc dopant-free HTMs were synthesized.[19] We have designed peripheral-substituted ZnTTPc with tetra-thienyl-methoxytriphenylamine (TTPA),[20] while report of different tetra-methoxy-ethoxy-based Pcs with diverse core atoms (H_2, Zn, Cu, Ni, and Co) also appears.[16]

(ii) Interface recombination triggered their narrow bandgap ranging from 1.4 eV − 2.1 eV. The phenomena induced poor electron blocking and charge recombination at the perovskite/HTM interface. Although the introduction of substituents or the interplay of central atoms can tune the bandgap of Pcs and alleviate the interface recombination, the limited opportunity of bandgap tuning is not effective. Improving the carrier diffusion length (L_D) of the Pcs, which was determined by the exciton or carrier lifetime (τ_E) and diffusion coefficient (D_E), as well as the carrier mobility (μ) is an effective protocol to impede the interfacial charge recombination. In this context, heavy palladium as core atom to replace copper

atom in Pcs with octamethyl substituents was investigated and it was noted that PdPc presented longer L_D, and thus delivered a higher performance.

Until now, the correlation between electronic structure, charge carrier transfer parameters (lifetime, diffusion coefficient, diffusion length), and the core metal and substitutions in MPcs are not well deciphered. Herein, we elaborately designed a series of peripheral substituents including 2-methoxyethan-1-amine (AE), thiadiazole (TDZ), and TTPA to induce asymmetry in terms of the symmetrical MPc with four tert-butyl groups (M= Zn or Cu, **Figure 1**). Notably, asymmetrical substituted-phthalocyanines owned unique photophysical and electrochemical properties as compared to symmetrical Pcs, stems from the perturbing the distribution of the 18-π-delocalized electrons over the macrocycle. We unravel the Pcs properties are controlled by core metal and substitutions, through transient absorbance, electron paramagnetic resonance, respectively. Further, to probe the practical utility, we fabricated PSCs by employing MPcs as dopant-free HTM (Figure 1). Arguably, the fabricated devices gave excellent stability under multi-stress conditions (moisture, heating, and light).

2. Results and discussion

2.1 Synthesis

Synthesis of ZnPcTB4, ZnPcTDZ and ZnPcAE were carried out following the procedures for ZnPcTB4,[21] ZnPcTDZ,[22] and ZnPcAE.[23] Firstly, we describe the synthesis of CuPcTB4 and CuPcTDZ (Figure S1a). Due to the difficulty in the purification of CuPcTB4 and CuPcTDZ obtained from statistical cyclotetramerization of respectively phthalonitriles in the presence of $Cu(OAc)_2$, it was essential to synthesize the free-base phthalocyanines from the corresponding diiminoisoindolines. H_2PcTB4 and H_2PcTDZ, were obtained by reaction of diiminoisoindoline 1[24] and diiminoisoindoline 2 and subsequent isolation by chromatographic column with 13% and 9% yield, respectively. Then, metallation using $Cu(OAc)_2$ allowed to obtain CuPcTB4 and CuPcTDZ with 76% and 79% yield, respectively. Second, we prepared CuPcAEBoc (Figure S1b) by statistical cyclotetramerization of phthalonitrile 3 and phthalonitrile 4 with $CuCl_2$. After a careful purification by chromatography column (Et_3N-deactivated SiO_2) the product was obtained with a 5% yield. We removed the 2-*tert*-butoxycarbonyl group in acid conditions yielding CuPcAE in 88% yield.

Third, synthesis of ZnPcTTPA (Figure S1c) was performed by statistical cyclotetramerization of *tert*-butyl-phthalonitrile 3 and thienyl-methoxytriphenylamine- phthalonitrile 5,[20] in the presence of $Zn(OAc)_2$. After purification by column chromatography ZnPcTTPA was obtained (18% yield). The ^{1}H-NMR spectra of ZnPcTTPA in THF-d_8 showed well-defined aromatic and aliphatic signals (Figure S16). The three isoindole units with the *tert*-butyl groups show different signals in the aromatic zone at 9.55, 9.39, and 8.32 ppm. Instead, the isoindole with the aromatic chain shows three signals at 9.39, 8.45, and 7.95 ppm. Regarding the aromatic chain, two doublets from the thiophene (9.67 and 7.50 ppm), four doublets from the phenyl group (7.91, 7.65, 7.12, and 7.00 ppm), and a singlet from the methoxy groups (3.80 ppm) are shown. Finally, for the synthesis of CuPcTTPA (Figure S1c) a similar procedure was followed, using $CuCl_2$ instead of $Zn(OAc)_2$. Subsequently, purification was made by column chromatography (Et_3N-deactivated SiO_2), CuPcTTPA was obtained (12% yield). Due to the paramagnetic character of copper (II), characterization by NMR experiments was not possible for any CuPcs. Nevertheless, they were characterized by FT-IR, HR-MALDI-TOF, and UV-Vis experiments, respectively. (Figure S2−S22).

2.2 Electro-optical and physical properties

The normalized absorption spectra of MPcs in solvents and solid films (Figure 2a & 2b), are displayed and the stronger peak at the Q band was used as the standard for normalization. The Soret bands (B bands) are located in the ultraviolet region (300−430 nm), which is linked to the transitions from S_0 to S_2 (ground state to second excited state). We attribute the appearance of a trivial shoulder at ~615 nm to the vibronic band. Strong absorption (600 − 800 nm) suggests the Q band signal and is related to the transition from S_0 to S_1 (ground state to first excited state), and interpreted as π-π* excitation between bonding and antibonding molecular orbitals.

For the absorption spectra of the MPc in solvents, the Q band of MPcAE in the solvent is similar to MPcTB4 (Figure 2a), while the Q band

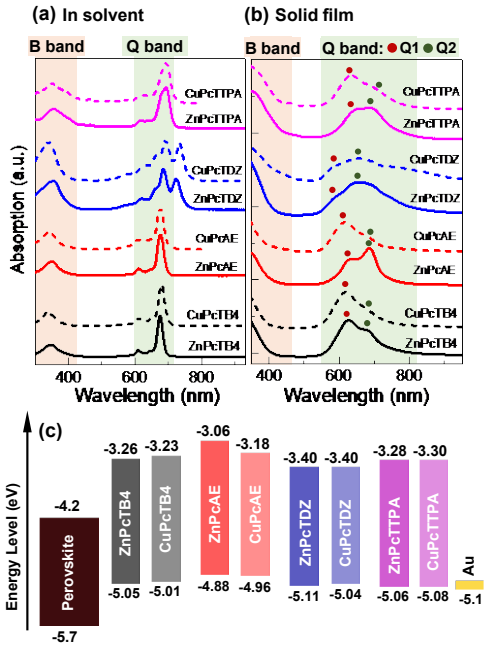

Figure 2. UV-vis absorption spectra of MPcs in (a) solution and (b) solid films, and (c) energy level diagram for the hole transporting side for all the MPcs.

of MPcTDZ and MPcTTPA split into doublet Q bands, which is attributed to the presence of different regioisomers and also by the breaking of the D_{4h} symmetry.[25] Besides, the Q band of MPcTDZ displays the widest absorbance from 500 − 785 nm and showing another band situated at 723 nm for ZnPcTDZ and 736 nm for CuPcTDZ, respectively because of the thiadiazole ring. The absorption spectra of MPcTTPA is bathochromically shifted compared to that of MPcTB4 and exhibited broadened absorption in contrast to that of MPcTB4.

The absorption spectra of the films on quartz (Figure 2b) display a spread of the signals from red and blue by comparing with the solution spectra (Figure 2a), the absorption of MPc films displays wide Q bands from 550 − 800 nm. When compared with the MPcTB4, a slight bathochromic shift is observed in MPc with other substitutions. This phenomenon can be related to the formation of aggregates, which can affect the charge carrier transport in the solid film.[26,27]

The peak absorption band at short wavelength named Q1 is contributed to aggregated species, and face-to-face stacking of the molecules, while the other peak absorption at long wavelength called Q2 is attributed to the monomeric species.[28] The primary species of MPcs were evaluated from the relative intensities of Q1 and Q2 bands. For ZnPcs, the ZnPcTB4 holds the main aggregated species, but other ZnPcs owned the main monomeric species. It illustrates that different substitutions can control the aggregation in the film and charge carrier transport. However, apart from CuPcTDZ with monomeric species, the other CuPcs show rich aggregated species.[28,29]

The asymmetrical MPcs with TDZ and TTPA substituents displayed distinct absorption in the solution while MPcs with AE group display similar absorption curves as of reference (MPcTB4). Arguably, the optical properties of the new MPcs could be controlled by the asymmetrical substitution groups. Importantly, the primary species of MPcs in the solid films for asymmetrical ZnPcs is monomeric species, while in ZnPcTB4 is aggregated ones. In contrast, the trend of primary species in CuPcs is not in a similar fashion as ZnPcs, suggesting the primary species can be tuned by the asymmetrical group and core metal synergistically.

To evaluate the energy level alignment of the perovskite/MPcs interface, we performed electrochemical characterization using differential pulse voltammetry (Figure S23-S27 in the supporting information) and ferrocene redox couple as the external standard (Table S1 in the supporting information). The highest occupied molecular orbital energy levels (E_{HOMO}) deduce from the Equation: E_{HOMO}=-4.8-E_{ox}, where E_{ox} is the first onset oxidation potential. The lowest unoccupied molecular orbital energy levels (E_{LUMO}) of MPcs were determined by adding the optical bandgap to E_{HOMO} value. The schematic diagram displays the energy level of PSCs (Figure 2c) and the energy levels of reported MPcs (ZnPcTB4, ZnPcAE, and ZnPcTDZ) noted from the literature. We noted that asymmetrical MPc with a similar substitution but with different core metals presents similar E_{HOMO} and E_{LUMO}, while different substitutions influence the semiconducting properties. The energy levels of the asymmetrically MPc with TDZ, TTPA show a trivial difference, but asymmetrical MPcAE have slightly higher than reference, may be ascribed to the ammonia as end arms. Assuming the valence band/conduction band of mixed-ion perovskite are at -5.7 eV/-4.2 eV, all the E_{HOMO} of MPcs are energetically favorable, signaling an efficient charge extraction at the interfaces. The E_{HOMO} of

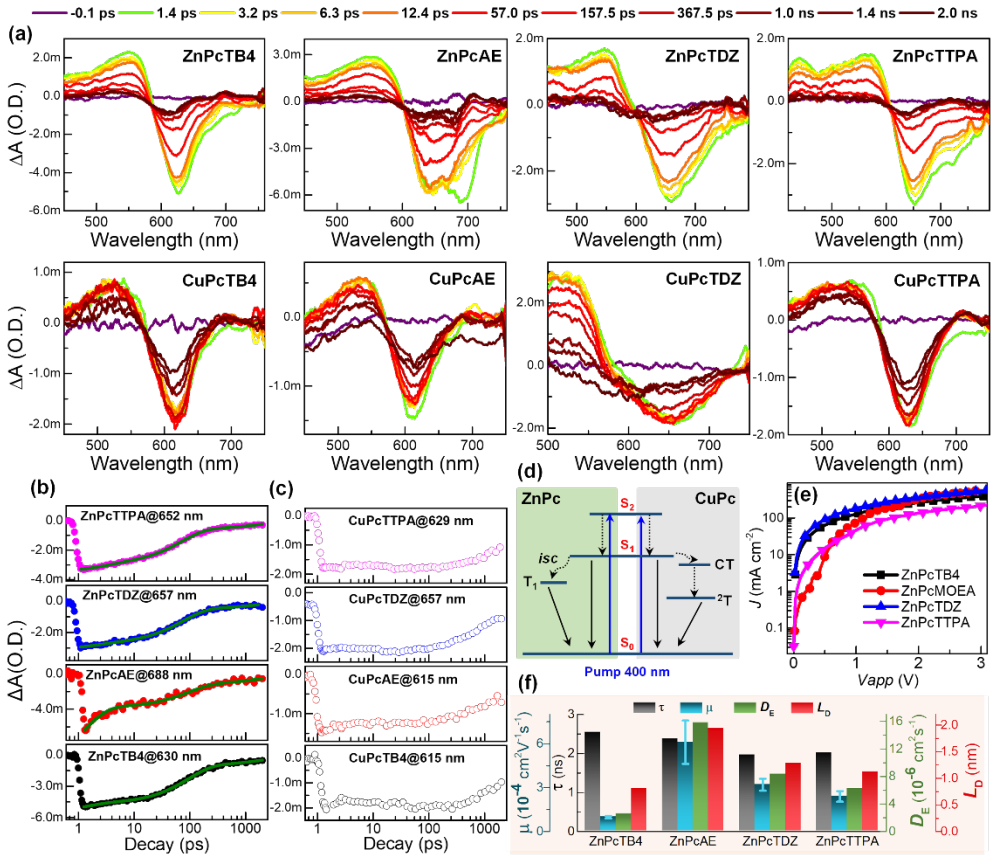

Figure 3. (a) TA spectra evolution of ZnPcs and CuPcs at indicated times (details in the legend). All the samples were spin-coated on a quartz substrate. Kinetic traces of (b) ZnPcs and (c) CuPcs at maxima GSB signal point, (d) schematic diagram of the energy relaxation dynamics of the ZnPc and CuPc, (e) *J-V* curves of the ZnPcs based hole-only device with the structure: FTO/PEDOT:PSS/HTM/Ag and (f) summary of the charge transfer parameters of ZnPcs.

MPcTDZ is lying lowest than that of other MPcs, thus a higher open-circuit voltage (V_{oc}) of the corresponding device can be expected. Owing to the narrow bandgap of MPcs, the highest value is 1.82 eV for ZnPcAE, and the lowest value is 1.64 eV for CuPcTDZ. Arguably, the photo-generated electron will be also transported by MPcs and increase the interface recombination, while ZnPcAE with higher E_{LUMO} is potentially attractive to block the electron effectively as compared to others.[30]

2.3 Ultrafast Transient Absorbance Studies

To unravel the carrier transport properties in these asymmetrical MPcs and probe its correlation with core metal and substitution, we investigated the charge carrier dynamics of thin films via transient absorption spectroscopy (TAS). The TAS spectra (Figure 3a) in the visible range at the indicated delay times, presented a broad positive signal (peak) at the wavelength region between the B band and Q band, which is typically associated with the singlet and triplet excited-state absorption of photo-generated carrier or excitons in the film.[31,32] The broad negative signals (trough) at the wavelength region of the Q band was characterized to the overlapping between the ground-state bleaching (GSB) and the stimulated emission (SE) for Soret fluorescence, where the GSB is stemmed from the depletion of the population in the ground electronic state following photoexcitation. We noted the profile of TAS mismatch with the static absorption (Figure S28). All the ZnPc samples display a faster decaying on a picosecond timescale (10 ps) and near-complete decay reaching nanoseconds. However, the CuPcs presents dissimilar decay phenomena except for CuPcAE, compared to Zn-based counterparts,

CuPcTB4 showed a signal increase within hundreds of picoseconds, but CuPcTDZ and CuPcTTPA presented no decay within this time frame (hundred of picoseconds). The signal of all CuPcs showed only half decay value reaching nanoseconds.

We investigated the dynamic traces of ZnPcs and CuPcs at the trough point (Figure 3b&3c) to clarify the charge kinetic decay process. The three timescales can be distinguishably observed for ZnPcs: the first fast decay within the first few picoseconds can be ascribed to the intersystem crossing (*isc*) from ($S_1 \rightarrow T_1$) because the internal conversion ($S_2 \rightarrow S_1$) occurs within femtoseconds timescale. The other two components correspond with the repopulation of the ground state (S_0) including two branches: a substantial decay from exciton state via exciton-phonon coupling ($S_1 \rightarrow S_0$) with hundred picoseconds and slow decay with nanoseconds via non-radiative relaxation of the triplet state ($T_1 \rightarrow S_0$). We draw a schematic diagram for MPcs illustrating the entire transient process (Figure 3d).

The traces of ZnPcs were well fitted with a tri-exponential function with the decay equation: $I(t) = \Sigma \alpha_i \exp(-t/\tau_i)$, where $I(t)$ is the total transient absorption decay curve, and α_i and τ_i are relative amplitude and lifetime of the ith component (the normalization condition being $\Sigma_i \alpha'_i = 1$), respectively (Table S2). The range of carrier lifetime is in agreement with the reported values.[33,34] The carrier lifetime for asymmetrical ZnPcs with different substitutes is similar with reference (ZnPcTB4). However, ZnPcAE have the larger amplitude value (0.65) than ZnPcTB4 (0.21), ZnPcTDZ (0.12), and ZnPcTTPA (0.16). We attribute this discrepancy in lifetime and amplitude to the stronger spin-orbit coupling effect introduced by substitution groups in asymmetrical ZnPcs.

All the CuPcs showed longer relaxation kinetics than the Zn-based counterparts. The CuPcTB4 and CuPcMOEA samples showed faster relaxation within the first 2 picoseconds. The Cu element (atomic number 29) has an unfilled d-orbital with an electronic configuration of $3d^9 4s^2$ in contrary to Zn element (atomic number 30) owned a fill d-orbital with an electronic configuration of $3d^{10} 4s^2$, indicating that Cu-based Pcs achieve a higher probability of donor-acceptor interaction between core Cu metal and peripheral groups.

The CuPc derivatives can be populated by relaxing its excited singdoublet state (^2S) through the ligand-to-metal charge transfer (CT) to a triplet (tripdoublet) state of ^2T with a sequential decay passage of $^2S_1 \rightarrow {}^2CT \rightarrow {}^2T$.[25,31,35] Because the decay process in CuPcs does not accept a direct flip of the electronic spin state,[31,36,37] which was evidenced to be more swift and efficacious than the decay process in ZnPcs, in which i_{sc} transition is accountable for the $S_1 \rightarrow T_1$ decay. Similar phenomena were reported in copper-based porphyrins and phthalocyanines.[31,37,38] Faster decay curves for CuPcTDZ and CuPcTTPA were not observed by us within the first 2 ps can be explained mainly by the fast decay via CT and stimulated emission.

Unlike the signal of corresponding ZnPcs at maxima point showing a continuous decay, the CuPc(TB4, TDZ, TTPA) shows no significant change in decay within the hundred picoseconds, and CuPcAE have slower decay than ZnPcAE. As referred above, the trough signal was controlled by GSB and SE, the absent decay or slower decay of CuPcs resulted from the stimulated emission. It indicates that stimulated emission in CuPcs can increase the decay lifetime because of the unique electronic structure of Cu elements.[39,40] The decay curves divergence of all CuPcs ascribed to that different substitution, which can affect the triplet process, and probably originated from the improved molecular interaction and increase of the Forster energy transfer process, which lead to excitation coupling with $\pi \rightarrow \pi^*$ transitions between closed molecules.

For phthalocyanine, the energy relaxation process should make the signal eventually decay to zero at a more extended time decay. The strong GSB of CuPcs finally evolves into a long-lived process and does not finish their decay in our detection window (2.0 ns). We ascribed the longer lifetime in CuPcs to the strong spin-orbit coupling effect introduced by the Cu atom. The stimulated emission phenomena in CuPc are stronger than the corresponding ZnPcs, which can increase the lifetime of CuPcs.

In all, the core metals and different substitutions of the asymmetrical MPcs, the charge decay process is synergistically controlled in the solid film. The asymmetrical MPcs have no measurable influence on the lifetime of the decay process, their impact on the amplitude for intersystem crossing by inhibiting molecular

aggregation, playing role in donor/acceptor. Compared to Zn as core metal, the Cu element with unfilled d-orbitals own unique decay process ($^2S_1 \rightarrow {}^2CT \rightarrow {}^2T$) and increase decay via stimulated emission, and has a longer lifetime. The asymmetrical MPcs and core metals can affect the triplet state properties that in turn influence the transportation of electrons and holes.

At first instance, the longer τ_e of MPcs of triplet state excitons emerge to show viability for increasing diffusion length (L_D) via the triplet sensitization pathway. On the contrary, the longer τ_e are offset for the significantly reduced diffusion coefficient (D_E), Because the Forster resonance energy transfer for (pure) triplet state diffusion is spin-forbidden, while a Dexter energy transfer with a much shorter operating range will essentially take charge of the energy migration process.[41]

The hole mobility (μ) of ZnPcs were determined by space-charge-limited current measurement (Figure 3e), and the corresponding D_E was derived according to the Einstein relation with a classical equation: $D_E/\mu = kT/q$, where k is the Boltzmann coefficient, q is the charge of electron or hole, and T is the measuring temperature. The average value of hole mobilities for ZnPcs follows the order: ZnPcAE (~ 6.10×10^{-4} cm^2 V^{-1} s^{-1}) > ZnPcTDZ (~ 3.21×10^{-4} cm^2 V^{-1} s^{-1}) > ZnPcTTPA (~ 2.4×10^{-4} cm^2 V^{-1} s^{-1}) > ZnPcTB4 (~ 0.97×10^{-4} cm^2 V^{-1} s^{-1}). The corresponding D_E of ZnPcs was calculated (Figure 3f and Table 1) and follows the order ZnPcAE (15.81×10^{-6} cm^2 s^{-1}) > ZnPcTDZ (~ 8.32×10^{-6} cm^2 s^{-1}) > ZnPcTTPA (6.22×10^{-6} cm^2 s^{-1}) > ZnPcTB4 (2.52×10^{-6} cm^2 s^{-1}). Although the Forster resonance energy transfer for pure triplet state diffusion is spin-forbidden, the highest amplitude of ZnPcAE for i_{sc} process showing a substantial singlet character in its T_1 state, and enhanced spin-orbit coupling. It is sufficient to enable Forster resonance energy transfer to appear. This singlet-triplet mixing could increase the μ and D_E, and then L_D. The L_D of ZnPcs was thus calculated according to the equation $L_D = (D_E\tau_E)^{1/2}$, and the relevant parameters are summarized (Table 1). The L_D of ZnPcs showed the following order: ZnPcAE (1.94 nm) > ZnPcTDZ (1.28 nm) > ZnPcTTPA (1.12 nm) > ZnPcTB4 (0.80 nm). Longer L_D can improve charge transportability via inhibiting the carrier recombination induced by their narrow bandgap in the transporting layer and thus boost the higher efficiency.

Table 1 Summary of the charge transfer parameters of MPcs.

HTM	τ_{ave} (ps)	μ (10^{-4} cm^2 V^{-1} s^{-1})	D_E (10^{-6} cm^2 s^{-1})	L_D (nm)
ZnPcTB4	253 5.7	0.97	2.52	0.80
ZnPcAE	238 0.0	6.10	15.81	1.94
ZnPcTDZ	196 3.2	3.21	8.32	1.28
ZnPcTTPA	200 5.1	2.40	6.22	1.12

To establish the variation in electrical properties of ZnPcs with different substitutions, molecular orientation, and microstructure of MPcs was investigated. The grazing incidence X-ray diffraction (GIXRD) pattern was measured on FTO and perovskite coated Pc substrates (Figure S29 in the supporting information). The ZnPcs with substitutions showed no peak in the GIXRD patterns, indicating the amorphous nature. We investigated the film-forming ability of ZnPcs with the aid of scanning electron microscopy (SEM) and atomic force microscopy (AFM) (Figure S30) techniques. The uniform and fine coverage of perovskite layers with symmetrical ZnPc suggest its film-forming ability.

2.4 Electron paramagnetic resonance

To probe the possible interaction and relationship between the electronic structure of the phthalocyanine metal center and its photovoltaic performance, we recorded the electron paramagnetic resonance (EPR) spectra of the isostructural copper compounds.

The X-band room temperature EPR spectra of CuPcTB4, CuPcAE, CuPcTDZ, and CuPcTTPA solid samples show quasi-isotropic signals, centered about g=2.07. We noted that neither the shape nor the position of the signal showed any noticeable changes, a clear variation of the peak-to-peak line width was observed in the order: CuPcTB4 < CuPcTDZ < CuPcAE < CuPcTTPA. The Q-band spectra are better resolved showing the axial g anisotropy characteristic of copper (II) phthalocyanine complexes (Figure 4a & 4b).[42–46] The g values are obtained by simulation of the experimental spectra (Table S3). In all the cases, the lowest g deviates significantly from the free-electron value (g_e=2.0023) and $g_{\|}$ is higher than $g_{\perp}$,

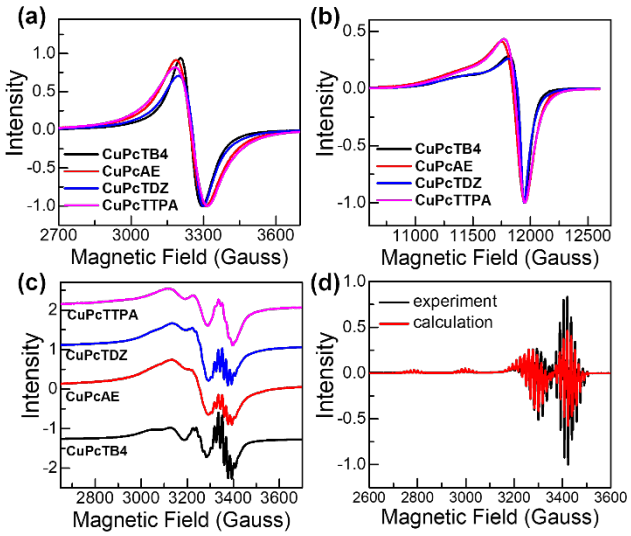

Figure 4. (a) X-band and (b) Q-band EPR spectra of CuPc solid samples at room temperature, (c) X-band room temperature EPR spectra of CuPc complexes dissolved in toluene, and (d) experimental and simulated EPR spectra of CuPcTB4 in toluene at 100 K.

thus the unpaired electron is occupying the d_{x2-y2} orbital in the equatorial plane of a Cu (II) chromophore with elongated tetragonal symmetry. The calculated g values are in agreement with those observed in other CuPc complexes.[44,45] The absence of resolved copper and nitrogen hyperfine structure is due to dipolar and/or exchange interactions between Cu (II) ions from different molecules.

To elucidate if the g values obtained from the solid-state experiments are molecular, we also investigated using the G parameter proposed by Hathaway [$G=(g_{\|}-2)/(g_{\perp}-2)$] which lies in the 4.4−4.9 range when the g values are equal to molecular values.[47] In this case, G is close to 3 for all the compounds, which implies that the g values are averaged due to spin-spin interactions. In this context, the smaller peak-to-peak linewidth observed in the EPR spectra of CuPcTB4 implies that the exchange interactions in this solid are more efficient than in the other complexes.

To reduce the spin-spin interactions, to improve the resolution of the EPR signal, and to derive further information over the effects of the substitution of peripheral ligands on the electronic structure and bonding, the copper complexes were dissolved in toluene. In all the cases, the X-band solution of EPR spectra recorded at room temperature (Figure 4c) show four hyperfine lines due to the interaction of Cu(II) unpaired electron with the copper nuclei (I= 3/2, isotopes ^{63}Cu and ^{65}Cu). Besides, a super hyperfine splitting due to the presence of four geometrically equivalent ^{14}N nuclei (I=1) can be observed. Moreover, the line widths show the typical dependence with the nuclear quantum number M_I ($\Gamma = \alpha + \beta M_I + \gamma M_I^2$)[48] due to molecular tumbling effects, with better resolution on the M_I = +1/2 and +3/2 lines, especially for the CuPcTB4 compound. Considering that the concentration of spins was similar in all solutions, the main causes of the different resolutions observed for each compound must be the molecular tumbling. The tumbling coefficients depend on the anisotropies of g and of the hyperfine couplings and on the rotational rate[44]. By simulation of the room temperature solution spectra (Figure S31) the isotopic values of g, A_{Cu}, and A_N (Table S4) have been determined, showing that within the experimental uncertainty the electronic distribution around Cu(II) ions is similar for all the studied compounds. When the molecular rotation is stopped upon freezing all the spectra become analogous. Arguably, the replacement of ligands carried out is mainly affecting the motional behavior of the complexes.

Finally, the X-band EPR spectrum of a frozen toluene solution of CuPcTB4 (Figure 4d) was simulated to determine the principal values of the g, A_{Cu}, and A_N tensors. We fitted the spectrum by taking into consideration the presence of two resonant species, one containing ^{63}Cu and the other ^{65}Cu, both in their natural abundance (69.15 and

30.85 %, respectively). The derived parameters (Table S4), confirm the D_{4h} symmetry around the copper (II) ions in this compound as well as a considerable delocalization of the d electrons over the isoindole nitrogens.

As compared to the reference (CuPcTB4), the asymmetrical CuPcs has dissimilar electronic structure. However, it signals unique solid-state magnetic exchange, *i.e.* the packing of the molecules and thus the π-π interactions and the energy of the frontier orbitals. These results are following the results of transient absorption, which suggests dissimilar substitutions show different lifetimes of excited state relaxation.

2.5 Photovoltaic performance of PSCs with ZnPcs as HTMs

To elucidate the significance of different substitutions and core metals on the performance of PSCs, we fabricated PSCs with the architect of FTO/*b&mp*-TiO_2/perovskite/Pcs/Au (*b&mp*-TiO_2: compact and mesoporous TiO_2 layers). The schematic of the PSCs and the cross-sectional SEM image of the device with ZnPcAE as an HTM (Figure 1) display, well-defined layer-by-layer structure with sharp interfaces. The perovskite ($FA_{1-y}MA_yPbI_{3-x}Br_x$) layer was prepared by a two-step deposition method (t = ~ 500 nm), while ZnPcAE was spin-casted on the perovskite layer to serve as an HTM (t = ~ 112 nm).

Firstly, chloroform and chlorobenzene were probed to investigate the effect of solvents on the charge transport performance of ZnPcAE. The film deposited by chloroform solvent shows better PV performance than chlorobenzene (Figure S32), and to decipher this, we analyzed the microstructure systemically. The UV-vis absorption of ZnPcAE deposited in different solvents gave similar peak and absorption intensity. We examined the surface microstructure of perovskite coated with ZnPcAE derived from different solvents (Figure S33). The film deposited by chlorobenzene displays undissolved solids on the surface, which will promote recombination centers and reduce the charge extraction abilities. The root-mean-square roughness (RMS) of perovskite/ZnPcAE prepared by chlorobenzene with ~17.2 nm is higher than that prepared by chloroform, signals uniformity and smoothness which in turn will allow building the sharper interface for efficient hole transportation.

The *J-V* curves of the device using different HTMs are shown (Figure 5a&5b) and the corresponding photovoltaic parameters are listed (Table 2). For the device with ZnPc as HTMs, the device employing ZnPcTB4 exhibits a PCE of only 10.52% with a V_{oc} of 1042.6 mV, J_{sc} of 18.46 mA cm^{-2}, and FF of 54.7%. Interestingly, after substitutions with other groups, all compounds show better device performance. Especially, the ZnPcAE HTM exhibit the highest PCE with 14.25% with a V_{oc} of 1063.5 mV, J_{sc} of 21.19 mA cm^{-2}, and FF of 63.2%, which mainly resulted from the enhanced J_{sc} and *FF*. The average of PCE from the device with different HTMs show the similar trend (Figure 5c and Table S5). The J_{sc} values match with integrated current densities (20.8 mA cm^{-2}) obtained from the incident photon-to-current conversion efficiency (IPCE) (Figure 5d), were indicating that ZnPcAE exhibits higher photon to electron conversion efficiency than ZnPcTB4 for the whole visible wavelength region. The V_{oc} of ZnPcTDZ presents the highest values than other ZnPcs, originated from the well-matched energy level. For the Zn-based Pcs, ZnPcAE (1.94 nm) and ZnPcTDZ (1.28 nm) owned the higher L_D than ZnPcTB4 (0.80 nm), and ZnPcTTPA (1.12 nm), and thus yield higher efficiency than ZnPcTB4/ZnPcTTPA.

Table 2 The champion photovoltaic parameters of the PSCs based on different MPcs.

HTM	V_{oc} (mV)	J_{sc} (mA cm^{-2})	FF (%)	PCE (%)
ZnPcTB4	1042.6	18.46	54.7	10.52
ZnPcAE	1063.5	21.19	63.2	14.25
ZnPcTDZ	1076.3	21.02	58.8	13.30
ZnPcTTPA	1016.6	19.83	49.5	9.97
ZnPcAE[a]	974.3	24.35	65.8	15.61
CuPcTB4	1044.9	21.29	66.9	14.87
CuPcAE	915.7	22.66	59.2	12.29
CuPcTDZ	925.2	22.32	50.1	10.34
CuPcTTPA	1028.8	21.14	66.0	14.35

[a] PSC based on SnO_2 as ETM, the rest are with *b&mp*-TiO_2 as ETM.

We optimize the device performance of ZnPc based PSCs by replacing *mp*-TiO_2 with planar SnO_2 quantum dot as an ETM, reaching a PCE of 15.61% with V_{oc} of 974.2 mV, J_{sc} of 24.35 mA cm^{-2}, and FF of 65.79% (Figure S34).

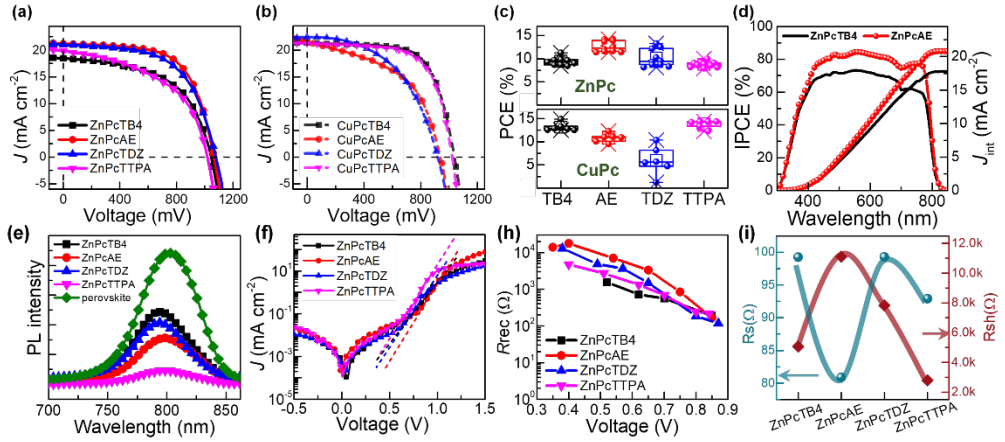

Figure 5. *J-V* curves of the champion device with different (a) ZnPcs and (b) CuPcs as HTM and *bc*&*mp*-TiO_2 as an ETM, (c) statistical efficiency performance of PSCs with ZnPc and CuPc HTMs. The average values were analyzed from ten devices for ZnPcs-based PSCs and six devices for CuPcs-based PSCs, respectively, (d) IPCE and integrated J_{int} of the device with ZnPcTB4, ZnPcAE as HTMs, (e) steady-state photoluminescence spectra of bare perovskite and perovskite with different ZnPc HTMs, (f) *J-V* curves in the dark (the dash-dot lines present the fitting lines for J_0 and n). (h) the recombination resistance extracted from the impedance spectra plots for the device with different ZnPcs under different photovoltage. (i) R_s and R_{sh} values extracted from champion *J-V* curves of the device with different ZnPcs under reverse scan.

We attribute this to SnO_2 unique properties such as higher conductivity and optical transparency compared to *mp*-TiO_2. We investigated the hysteresis index (*HI*) in champion devices by measuring *J-V* curves under the forward and reverse scan directions. The device with ZnPcAE and ZnPcTDZ have quite small *HI* with 0.09 and 0.07, respectively (Figure S35 and Table S6).

On the other hand, considering the results of the PV device with ZnPcs, the device with CuPc analogs as HTMs should have a similar trend as of ZnPcs, however, they are dissimilar to the ZnPcs. The device with CuPcTB4 and CuPcTTPA yields higher efficiency than that of CuPcAE, CuPcTTPA. The device with CuPcTB4, CuPcTTPA exhibits the highest PCE of 14.87%, 14.35%, higher than CuPcAE and CuPcTDZ with 12.29% and 10.34%, respectively. We noted difficulties to deposit uniform films for CuPcAE and CuPcTDZ. Although solvent engineering including chloroform/methanol mixed solvents for CuPcAE, chlorobenzene/tetrahydrofuran mixed solvent for CuPcTDZ, the corresponding efficiency is lower. The device with CuPcs (CuPcTB4, CuPcTTPA) shows higher efficiency than that of the device with Zn-based counterparts. The CuPcs owned a higher efficiency than the Zn-based counterparts, which can result in the higher charge transporting ability originated from their long lifetime. Considering the solubility issues with CuPcs, the discrepancy in device performance is difficult to correlate with their transportability. We investigated the carrier transportation difference employing ZnPc HTMs.

Steady-state photoluminescence (PL) measurement for perovskite using different ZnPcs with the film structure of quartz/perovskite/ZnPc was used to analyze the charge carrier transport process (Figure 5e). An emission peak centered at 803 nm for the pristine perovskite was observed. A reduced PL intensity was recognized for all the ZnPcs, indicating efficient hole carrier extraction from perovskite. Remarkably, a blue-shifted PL peak was observed for all the perovskite/ZnPcs, which can be ascribed to a decrease in the bulk and/or surface trap states in the perovskite layer after the deposition of thin layer of HTM. [49] ZnPcAE and ZnPcTDZ showed a large blue shift compared to other one, consequently, they showed lesser charge recombination at the interface between the perovskite and HTM layers measured by EIS and dark *J-V* measurements indicating low value of reverse saturation current as discussed in below section. Subsequently, we noted improved PCE, due to enhancement in open circuit voltage (V_{oc}) and short-circuit current.

To evaluate the function of different ZnPc HTMs on the performance of the PSCs dark current was measured (Figure 5f), the linear parts of the dark *J-V* curves were fitted with the Shockley diode equation: $J_D = J_0[\exp(qV/nK_BT)-1]$, where J_0 is the reverse saturation current

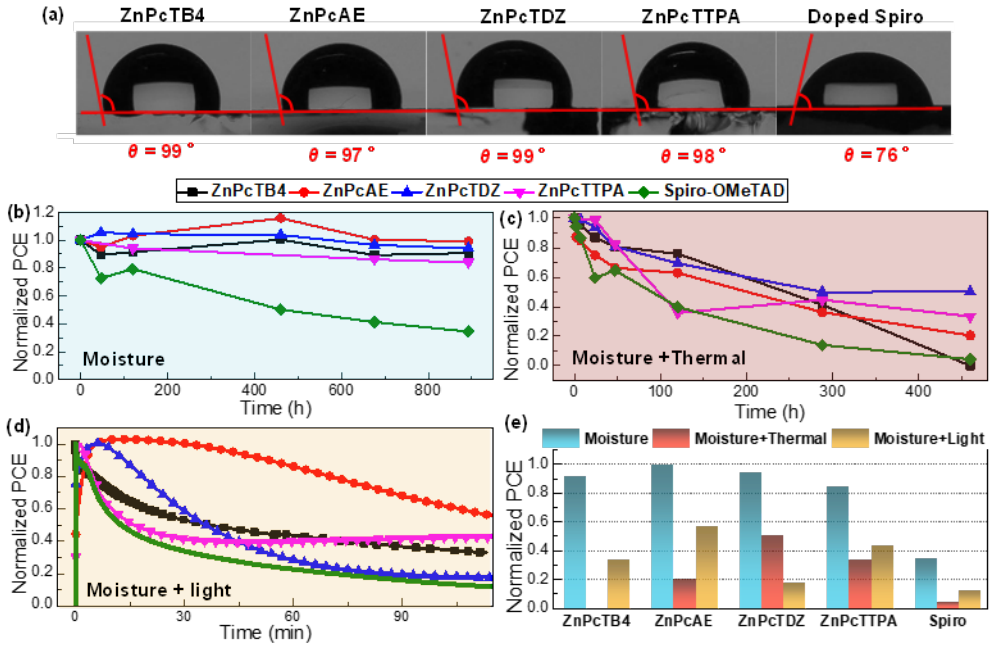

Figure 6. (a) Contact angles of perovskite with different ZnPcs and Spiro-OMeTAD, (b) PCE plots of PSCs with different ZnPcs and Spiro-OMeTAD aged under ambient condition (30-70% RH) for around 900 h, (c) plots of efficiency of PSCs based on different ZnPc and Spiro-OMeTAD HTMs under moisture and heat conditions, (d) maximum power point tracking under humidity and 1-sun illumination of the unencapsulated device with different HTMs and (e) normalized PCE obtained after aging condition. (Spiro: Spiro-OMeTAD).

density, J_D is the dark current density, V is the applied bias, q is the electron charge, K_B is the Boltzmann constant, T is the temperature, n is the ideal factor of the real diode.[50,51] For devices with different ZnPc as HTMs, n, and J_0 are listed in Table S7. The values of [n, J_0] was [2.94, 5.5×10^{-6} mA cm^{-2}], [2.3, 1.4×10^{-7} mA cm^{-2}], [2.6, 2.2×10^{-6} mA cm^{-2}], and [2.4, 2.4×10^{-6} mA cm^{-2}] for the PSCs based on ZnPcTB4, ZnPcAE, ZnPcTDZ, ZnPcTTPA, respectively. The smaller value of n and J_0 indicates a decrease in charge recombination at the interface between the perovskite and HTM layers. Thus, it is revealed that ZnPcAE reduces interface recombination and improves the transfer efficiency of the charge in the device, and leads to the high FF of the corresponding device.

To elucidate the charge transport kinetics (surface recombination, charge carrier diffusion, *etc*.) in devices based on developed ZnPcs, electrical impedance spectroscopy (EIS) was measured under different light intensities (0 − 0.2 Sun) of white LED illumination to produce different photovoltages.[52] An equivalent circuit was proposed (R-R_{rec}/C, Figure S37) to interpret the interface recombination. R is seen as the series resistance of the external circuit including connecting wires and two electrodes, and R_{rec} reflects the impact of recombination resistance of the device. In the typical Nyquist diagram of different devices with varying photovoltages (Figure S38), only R_{rec} values under a series of photovoltages from different ZnPc-based devices were extracted and plotted (Figure 5h) for discussion. With the increase in photovoltages, the value of R_{rec} decreases, due to the improvement in carrier concentration. At a similar potential bias, the R_{rec} values of the ZnPcAE-based device are beyond the values from other devices, which implies that ZnPcAE steeply reduced charge recombination at the perovskite/HTM interface.

The series resistance (R_s) and shunt resistance (R_{sh}) of devices was derived by fitting the J-V curves measured in the reverse scan (Figure 5i). The ZnPcAE-based PSCs showed the lowest R_s of 81 Ω, whereas ZnPcTB4, ZnPcTDZ, ZnPcTTPA based- PSCs displayed the R_s of 99 Ω, 99 Ω, and 92 Ω, respectively. Moreover, the ZnPcAE-based device owned the highest R_{sh} of 11.1 kΩ, whereas ZnPcTB4, ZnPcTDZ, ZnPcTTPA based-device

showed the R_{sh} of 5.1 kΩ, 7.8 kΩ, and 2.8 kΩ, respectively. The abilities to transport charge effectively are decisive for their performance of PSCs and the electrical conductivity for HTMs (Figure S36) was measured. The trend of R_{sh} is in agreement with the R_{rec}. The conductivity value in our condition follows the order: ZnPcAE (0.22 μS cm^{-1}) > ZnPcTDZ (0.19 μS cm^{-1}) > ZnPcTTPA (0.15 μS cm^{-1}) > ZnPcTB4 (0.08 μS cm^{-1}). Overall, the lowest R_s and highest R_{sh} of the ZnPcAE-based device yielded improved PCE with higher FF, which is ascribed to the relatively higher conductivity.

2.6 Device Stability performance

In addition to PSC performance, reliability is the crucial aspect to evaluate the performance of HTMs. To evaluate the surface nature, goniometer experiments were made to evaluate the hydrophobicity of perovskite films coated by different ZnPcs. The contact angles showed 99°, 97°, 99°, and 98°, respectively after spin-coating ZnPcTB4, ZnPcAE, ZnPcTDZ, and ZnPcTTPA atop of perovskite (Figure 6a), while that of perovskite with doped Spiro-OMeTAD is 75°. The perovskite coated ZnPcs samples yielded a contact angle over 90° and perovskite/ZnPcAE gave the highest value among them. The hydrophobic properties induced by ZnPcs can effectively prevent water from diffusing into the perovskite layer, thus leading to enhanced moisture stability. The substituted groups in asymmetrical ZnPcs also influence the surface properties marginally.

For reliability purposes, the PSCs should operate under combined stress conditions instead of only one factor. To evaluate the potential of ZnPcs based PSCs, we investigated the stability of PSCs with ZnPcs under various stress conditions. Firstly, we measured the unencapsulated PSCs under the ambient condition with 30-70% relative humidity (RH), around 900 h (Figure 6b). The PCE based on ZnPcTB4, ZnPcAE, ZnPcTDZ, and ZnPcTTPA can retain 91%, 99%, 94%, and 84% of their initial PCE after aging, respectively, while the control device employing doped Spiro-OMeTAD as a HTM yielded around 17% (Figure S39) lost 70% of its initial PCE. The detailed PV parameters contain V_{oc}, $J_{sc,}$ and FF are shown (Figure S40). The J_{sc} values of ZnPc based PSCs remain unchanged, suggesting the perovskite can maintain the role as an active layer, but the J_{sc} value of the control device decrease to 50% of its initial value. UV-vis absorption spectra to study the degradation process of perovskite with different HTMs, was recorded at 550 nm wavelength vs time (Figure S41a). The perovskite with ZnPcs retains 80% absorbance of its initial values, while perovskite/Spiro-OMeTAD holds only 60% of the initial value. The visual image of perovskite layers with different HTMs after aging around 900 h was documented (Figure S41b). The perovskite/Spiro-OMeTAD displayed brown color instead of intense dark color, suggesting degradation of phase change. However, perovskite with ZnPcs showed dark color, indicating the entirety of perovskite with ZnPcs, which is consistent with the PV performance. *FF* value is related to the series resistance and ZnPcs-based PSCs retain >95% of their initial values after aging, suggesting ZnPcs create the rational interface between ZnPcs and perovskite. While the R_s value threefolds in the case of the control device (Figure S41c) suggesting, both the intrinsic poor stability of doped Spiro-OMeTAD and the decomposition of perovskite-induced dopant (lithium salt and *t*-BP) in Spiro-OMeTAD deteriorate the perovskite/HTM interface and the active layer.

Secondly, the devices were exposed to both environmental stress conditions (heat and humidity). The PV performance of PSCs was recorded under continuous thermal stress (85 ºC) and ambient condition with 30-70% RH for around 500 h (Figure 6c), The PCE held 20%, 50%, and 33% of the initial value in the case of a device with ZnPcAE, ZnPcTDZ, ZnPcTTPA, respectively, but nearly 0% of the initial value was noted for ZnPcTB4, Spiro-OMeTAD-based PSCs. We noted that ZnPcAE, ZnPcTDZ, ZnPcTTPA showed competitive performance when exposed to heat and high humidity conditions. The rate of the change of J_{sc} and *FF* for ZnPcAE, ZnPcTDZ, ZnPcTTPA-based PSCs was lower than that of ZnPcTB4 and control device (Figure S42). The change in R_s calculated by fitting the *J-V* curves as a function of time (Figure S41d), for ZnPcAE, ZnPcTDZ, ZnPcTTPA-based PSCs displayed increases to 3.0, 1.5, and 2.6 times of its initial values, respectively, while the control device expands to 24 times of initial value, which has a negative influence on device performance, especially J_{sc} and FF values. The Spiro-OMeTAD doped with lithium salt and *t*-BP undergoes morphological deformation at relatively high-temperature and produced large voids.[53] Besides,

the photo-oxidation induced in an oxygen-rich environment and the crystallization and the aggregate formation of Spiro-OMeTAD deteriorate its transporting properties.[54] The poor performance of ZnPcTB4 under heat stress originates from an anchoring group that does not interact with the perovskite layer judiciously, as the presence of tert-*t*-butyl with other phthalocyanines can passivate the perovskite.

Further, we conducted maximum power point tracking of the unencapsulated devices under moisture (30-70% RH) with constant 1 sun illumination offered by white LED at room temperature (Figure 6d). The control device drastically drops to 11% of its initial value after 118 min. However, the device with ZnPcTB4, ZnPcAE, ZnPcTDZ, ZnPcTTPA maintained 33.4%, 56.8%, 17.7%, and 43.1% of their initial PCE, respectively. ZnPcs, especially ZnPcAE own excellent stability under humidity and light. The performance of the PSCs with different HTM under stress conditions (Figure 6e), suggests dopant-free ZnPcAE yielded improved stability as compared to ZnPc and traditional Spiro-OMeTAD.

3. Conclusion

We designed and quantify the physicochemical properties of a series of asymmetrically MPcs based on MPcTB4 (M = Zn or Cu) with AE, TDZ, and TTPA substituents and their influence on electro-optical and photovoltaic properties. The charge carrier dynamics of MPcs suggest a comparable average lifetime in ZnPc for varied substitutions, while CuPcs own a longer lifetime than Zn-based analog. However, the ZnPcs signals a substantial difference in the amplitude, which can lead to an ample singlet character in the T_1 state. This, in turn, impact the charge transport parameters such as mobility, the diffusion length of ZnPcAE, which are higher than similar ZnPcs. which is favorable for charge carrier extraction and transport in perovskite-based devices. The fabricated perovskite solar cells with ZnPcAE as hole selective layer gave a competitive photovoltaic performance in its pristine form. Notably, the devices showed significant stability under multi-stress conditions.

ASSOCIATED CONTENT

Supporting Information:

The Supporting Information is available at https://pubs.acs.org/doi/10.1021/acsaem.1c02039.

The materials, and detailed synthesis and corresponding characterization such as FT-IR, NMR, HR-MALDI-TOF, Cyclic voltammetry for all novel developed materials; Additional experimental details for device fabrication and characterizations; Experimental details for transient absorbance absorption and electron paramagnetic resonance; GIXRD patterns of ZnPc on different substrates, morphology analysis for perovskite/ZnPc films; experimental and simulated X-band EPR; Solvent optimization for ZnPcAE HTM; device performance for ZnPcAE and ZnPcTDZ, and Spiro-OMeTAD HTM; Nyquist curves for device with different ZnPc HTMs. Additional stability performance under different conditions; Additional table for CV, and fitting paraments for ZnPc's curves, Spin Hamiltonian parameters and average PV parameters.

AUTHOR INFORMATION:

Corresponding Author

Ángela Sastre-Santos − Miguel Hernandez University of Elche, 03202 Elche, Spain; orcid.org/0000-0002-8835-2486; Email: asastre@umh.es

Shahzada Ahmad − BCMaterials, Basque Center for Materials, Applications and Nanostructures, 48940 Leioa, Spain; IKERBASQUE, Basque Foundation for Science, 48013 Bilbao, Spain; orcid.org/0000-0002-1218-2556; Phone: +34 946128811; Email: shahzada.ahmad@bcmaterials.net

Authors

Peng Huang − BCMaterials, Basque Center for Materials, Applications and Nanostructures, 48940 Leioa, Spain

Adrián Hernández − Miguel Hernandez University of Elche, 03202 Elche, Spain

Samrana Kazim − BCMaterials, Basque Center for Materials, Applications and Nanostructures, 48940 Leioa, Spain; IKERBASQUE, Basque Foundation for Science, 48013 Bilbao, Spain

Jorge Follana-Berná − Miguel Hernandez University of Elche, 03202 Elche, Spain

Javier Ortiz − Miguel Hernandez University of Elche, 03202 Elche, Spain

Luis Lezama − Departamento de Química Orgánica e Inorgánica, Facultad de Ciencia y Tecnología, Universidad del País Vasco, 48940 Leioa, Spain; orcid.org/0000- 0001-6183-2052

Author Contributions

† P.H. and A.H. contributed equally to this work.

Notes:

The authors declare no competing financial interest.

ACKNOWLEDGMENTS

This work received funding from the European Union H2020 Programme under a European Research Council Consolidator grant [MOLEMAT, 726360]. We gratefully acknowledge the financial support provided by European Regional Development Fund ‘‘A way to make Europe and the Spanish Ministerio de Ciencia e Innovacion, Agencia Estatal de Investigación: project CTQ2017-87102-R AEI/FEDER, UE. P. H. acknowledges funding from the European Commission via a Marie-Skłodowska-Curie individual fellowship (SMILIES, No. 896211).

REFERENCES

(1) NREL Best Research-Cell Efficiencies. *https://www.nrel.gov/ pv/cell-efficiency.html* (accessed in March, 2021).

(2) Liu, Z.; Li, J.; Yan, F. Package-Free Flexible Organic Solar Cells with Graphene Top Electrodes. *Adv. Mater.* **2013**, *25* (31), 4296–4301. https://doi.org/10.1002/adma.201205337.

(3) Kojima, A.; Teshima, K.; Shirai, Y.; Miyasaka, T. Organometal Halide Perovskites as Visible-Light Sensitizers for Photovoltaic Cells. *J. Am. Chem. Soc.* **2009**, *131* (17), 6050–6051. https://doi.org/10.1021/ja809598r.

(4) Ponseca, C. S.; Savenije, T. J.; Abdellah, M.; Zheng, K.; Yartsev, A.; Pascher, T.; Harlang, T.; Chabera, P.; Pullerits, T.; Stepanov, A.; Wolf, J.-P.; Sundström, V. Organometal Halide Perovskite Solar Cell Materials Rationalized: Ultrafast Charge Generation, High and Microsecond-Long Balanced Mobilities, and Slow Recombination. *J. Am. Chem. Soc.* **2014**, *136* (14), 5189–5192. https://doi.org/10.1021/ja412583t.

(5) Stranks, S. D.; Eperon, G. E.; Grancini, G.; Menelaou, C.; Alcocer, M. J. P.; Leijtens, T.; Herz, L. M.; Petrozza, A.; Snaith, H. J. Electron-Hole Diffusion Lengths Exceeding 1 Micrometer in an Organometal Trihalide Perovskite Absorber. *Science (80-.).* **2013**, *342* (6156), 341–344. https://doi.org/10.1126/science.1243982.

(6) Salado, M.; Andresini, M.; Huang, P.; Khan, M. T.; Ciriaco, F.; Kazim, S.; Ahmad, S. Interface Engineering by Thiazolium Iodide Passivation Towards Reduced Thermal Diffusion and Performance Improvement in Perovskite Solar Cells. *Adv. Funct. Mater.* **2020**, *30* (14), 1910561. https://doi.org/10.1002/adfm.201910561.

(7) Huang, P.; Yuan, L.; Zhang, K.; Chen, Q.; Zhou, Y.; Song, B.; Li, Y. Room-Temperature and Aqueous Solution-Processed Two-Dimensional TiS 2 as an Electron Transport Layer for Highly Efficient and Stable Planar n–i–p Perovskite Solar Cells. *ACS Appl. Mater. Interfaces* **2018**, *10* (17), 14796–14802. https://doi.org/10.1021/acsami.8b03225.

(8) Huang, P.; Wang, Z.; Liu, Y.; Zhang, K.; Yuan, L.; Zhou, Y.; Song, B.; Li, Y. Water-Soluble 2D Transition Metal Dichalcogenides as the Hole-Transport Layer for Highly Efficient and Stable p-i-n Perovskite Solar Cells. *ACS Appl. Mater. Interfaces* **2017**, *9* (30), 25323–25331. https://doi.org/10.1021/acsami.7b06403.

(9) Huang, P.; Chen, Q.; Zhang, K.; Yuan, L.; Zhou, Y.; Song, B.; Li, Y. 21.7% Efficiency Achieved in Planar n-i-p Perovskite Solar Cells via Interface Engineering with Water-Soluble 2D TiS2. *J. Mater. Chem. A* **2019**, *7* (11), 6213–6219. https://doi.org/10.1039/c8ta11841h.

(10) Urbani, M.; de la Torre, G.; Nazeeruddin, M. K.; Torres, T. Phthalocyanines and Porphyrinoid Analogues as Hole- and Electron-Transporting Materials for Perovskite Solar Cells. *Chem. Soc. Rev.* **2019**, *48* (10), 2738–2766. https://doi.org/10.1039/C9CS00059C.

(11) Calió, L.; Kazim, S.; Grätzel, M.; Ahmad, S. Hole-Transport Materials for Perovskite Solar Cells. *Angew. Chemie Int. Ed.* **2016**, *55* (47), 14522–14545. https://doi.org/10.1002/anie.201601757.

(12) Caliò, L.; Salado, M.; Kazim, S.; Ahmad, S. A Generic Route of Hydrophobic Doping in Hole Transporting Material to Increase Longevity of Perovskite Solar Cells. *Joule* **2018**, *2* (9), 1800–1815. https://doi.org/10.1016/j.joule.2018.06.012.

(13) Ren, G.; Han, W.; Deng, Y.; Wu, W.; Li, Z.; Guo, J.; Bao, H.; Liu, C.; Guo, W. Strategies of

Modifying Spiro-OMeTAD Materials for Perovskite Solar Cells: A Review. *J. Mater. Chem. A* **2021**, *9* (8), 4589–4625. https://doi.org/10.1039/D0TA11564A.

(14) Yin, X.; Song, Z.; Li, Z.; Tang, W. Toward Ideal Hole Transport Materials: A Review on Recent Progress in Dopant-Free Hole Transport Materials for Fabricating Efficient and Stable Perovskite Solar Cells. *Energy Environ. Sci.* **2020**, *13* (11), 4057–4086. https://doi.org/10.1039/D0EE02337J.

(15) Kim, S. W.; Kim, G.; Moon, C. su; Yang, T. Y.; Seo, J. Metal-Free Phthalocyanine as a Hole Transporting Material and a Surface Passivator for Efficient and Stable Perovskite Solar Cells. *Small Methods* **2021**, *5* (5). https://doi.org/10.1002/smtd.202001248.

(16) Yu, Z.; Wang, L.; Mu, X.; Chen, C.; Wu, Y.; Cao, J.; Tang, Y. Intramolecular Electric Field Construction in Metal Phthalocyanine as Dopant-Free Hole Transporting Material for Stable Perovskite Solar Cells with >21 % Efficiency. *Angew. Chemie Int. Ed.* **2021**, *60* (12), 6294–6299. https://doi.org/10.1002/anie.202016087.

(17) Cheng, M.; Li, Y.; Safdari, M.; Chen, C.; Liu, P.; Kloo, L.; Sun, L. Efficient Perovskite Solar Cells Based on a Solution Processable Nickel(II) Phthalocyanine and Vanadium Oxide Integrated Hole Transport Layer. *Adv. Energy Mater.* **2017**, *7* (14), 1602556. https://doi.org/10.1002/aenm.201602556.

(18) Molina, D.; Ruiz-Preciado, M. A.; Carlsen, B.; Eickemeyer, F. T.; Yang, B.; Flores-Díaz, N.; Álvaro-Martins, M. J.; Nonomura, K.; Hagfeldt, A.; Sastre-Santos, Á. Zinc Phthalocyanine Conjugated Dimers as Efficient Dopant-Free Hole Transporting Materials in Perovskite Solar Cells. *ChemPhotoChem* **2020**, *4* (4), 307–314. https://doi.org/10.1002/cptc.201900245.

(19) Hu, Q.; Rezaee, E.; Li, M.; Chen, Q.; Cao, Y.; Mayukh, M.; McGrath, D. V.; Xu, Z.-X. Molecular Design Strategy in Developing Titanyl Phthalocyanines as Dopant-Free Hole-Transporting Materials for Perovskite Solar Cells: Peripheral or Nonperipheral Substituents? *ACS Appl. Mater. Interfaces* **2019**, *11* (40), 36535–36543. https://doi.org/10.1021/acsami.9b09490.

(20) Huang, P.; Hernández, A.; Kazim, S.; Ortiz, J.; Sastre-Santos, Á.; Ahmad, S. Molecularly Engineered Thienyl-Triphenylamine Substituted Zinc Phthalocyanine as Dopant Free Hole Transporting Materials in Perovskite Solar Cells. *Sustain. Energy Fuels* **2020**, *4* (12), 6188–6195. https://doi.org/10.1039/D0SE01215G.

(21) Fukuzumi, S.; Ohkubo, K.; Ortiz, J.; Gutiérrez, A. M.; Fernández-Lázaro, F.; Sastre-Santos, Á. Formation of a Long-Lived Charge-Separated State of a Zinc Phthalocyanine-Perylenediimide Dyad by Complexation with Magnesium Ion. *Chem. Commun.* **2005**, No. 30, 3814. https://doi.org/10.1039/b506412k.

(22) Blas-Ferrando, V. M.; Ortiz, J.; Follana-Berná, J.; Fernández-Lázaro, F.; Campos, A.; Mas-Torrent, M.; Sastre-Santos, Á. Large-Size Star-Shaped Conjugated (Fused) Triphthalocyaninehexaazatriphenylene. *Org. Lett.* **2016**, *18* (6), 1466–1469. https://doi.org/10.1021/acs.orglett.6b00412.

(23) Fukuzumi, S.; Ohkubo, K.; Ortiz, J.; Gutiérrez, A. M.; Fernández-Lázaro, F.; Sastre-Santos, Á. Control of Photoinduced Electron Transfer in Zinc Phthalocyanine- Perylenediimide Dyad and Triad by the Magnesium Ion. *J. Phys. Chem. A* **2008**, *112* (43), 10744–10752. https://doi.org/10.1021/jp805464e.

(24) Leznoff, C. C.; Svirskaya, P. I.; Khouw, B.; Cerny, R. L.; Seymour, P.; Lever, A. B. P. Syntheses of Monometalated and Unsymmetrically Substituted Binuclear Phthalocyanines and a Pentanuclear Phthalocyanine by Solution and Polymer Support Methods. *J. Org. Chem.* **1991**, *56* (1), 82–90. https://doi.org/10.1021/jo00001a019.

(25) Liao, M.-S.; Scheiner, S. Electronic Structure and Bonding in Metal Phthalocyanines, Metal=Fe, Co, Ni, Cu, Zn, Mg. *J. Chem. Phys.* **2001**, *114* (22), 9780–9791. https://doi.org/10.1063/1.1367374.

(26) Bhattacharya, S.; Reddy, G.; Paul, S.; Hossain, S. S.; Kumar Raavi, S. S.; Giribabu, L.; Samanta, A.; Soma, V. R. Comparative Photophysical and Femtosecond Third-Order Nonlinear Optical Properties of Novel Imidazole Substituted Metal Phthalocyanines. *Dye. Pigment.* **2021**, *184* (July 2020), 108791. https://doi.org/10.1016/j.dyepig.2020.108791.

(27) Doria, S.; Lapini, A.; Di Donato, M.; Righini, R.; Azzaroli, N.; Iagatti, A.; Caram, J. R.; Sinclair, T. S.; Cupellini, L.; Jurinovich, S.; Mennucci, B.; Zanotti, G.; Paoletti, A. M.; Pennesi, G.; Foggi, P. Understanding the Influence of Disorder on the Exciton Dynamics and Energy Transfer in Zn-Phthalocyanine H-Aggregates.

Phys. Chem. Chem. Phys. **2018**, *20* (34), 22331–22341. https://doi.org/10.1039/c8cp02172d.

(28) Feng, Y.; Hu, Q.; Rezaee, E.; Li, M.; Xu, Z. X.; Lorenzoni, A.; Mercuri, F.; Muccini, M. High-Performance and Stable Perovskite Solar Cells Based on Dopant-Free Arylamine-Substituted Copper(II) Phthalocyanine Hole-Transporting Materials. *Adv. Energy Mater.* **2019**, *9* (26), 1901019. https://doi.org/10.1002/aenm.201901019.

(29) Ling, X.; Wu, J.; Xu, W.; Zhang, J. Probing the Effect of Molecular Orientation on the Intensity of Chemical Enhancement Using Graphene-Enhanced Raman Spectroscopy. *Small* **2012**, *8* (9), 1365–1372. https://doi.org/10.1002/smll.201102223.

(30) Hu, L.; Wang, W.; Liu, H.; Peng, J.; Cao, H.; Shao, G.; Xia, Z.; Ma, W.; Tang, J. PbS Colloidal Quantum Dots as an Effective Hole Transporter for Planar Heterojunction Perovskite Solar Cells. *J. Mater. Chem. A* **2015**, *3* (2), 515–518. https://doi.org/10.1039/C4TA04272G.

(31) Zheng, X.; Wang, Y.; Hu, J.; Yang, G.; Guo, Z.; Xia, J.; Xu, Z.; Fang, G. Octamethyl-Substituted Pd(<scp>ii</Scp>) Phthalocyanine with Long Carrier Lifetime as a Dopant-Free Hole Selective Material for Performance Enhancement of Perovskite Solar Cells. *J. Mater. Chem. A* **2017**, *5* (46), 24416–24424. https://doi.org/10.1039/C7TA07216C.

(32) Iagatti, A.; Doria, S.; Marcelli, A.; Angelini, N.; Notarantonio, S.; Paoletti, A. M.; Pennesi, G.; Rossi, G.; Zanotti, G.; Calogero, G.; Foggi, P. Photophysical Processes Occurring in a Zn-Phthalocyanine in Ethanol Solution and on TiO 2 Nanostructures. *J. Phys. Chem. C* **2015**, *119* (35), 20256–20264.
https://doi.org/10.1021/acs.jpcc.5b04978.

(33) Kakade, S.; Ghosh, R.; Palit, D. K. Excited State Dynamics of Zinc–Phthalocyanine Nanoaggregates in Strong Hydrogen Bonding Solvents. *J. Phys. Chem. C* **2012**, *116* (28), 15155–15166. https://doi.org/10.1021/jp304369r.

(34) Peumans, P.; Yakimov, A.; Forrest, S. R. Small Molecular Weight Organic Thin-Film Photodetectors and Solar Cells. *J. Appl. Phys.* **2003**, *93* (7), 3693–3723. https://doi.org/10.1063/1.1534621.

(35) Abramczyk, H.; Brozek-Płuska, B.; Kurczewski, K.; Kurczewska, M.; Szymczyk, I.; Krzyczmonik, P.; Błaszczyk, T.; Scholl, H.; Czajkowski, W. Femtosecond Transient Absorption, Raman, and Electrochemistry Studies of Tetrasulfonated Copper Phthalocyanine in Water Solutions. *J. Phys. Chem. A* **2006**, *110* (28), 8627–8636. https://doi.org/10.1021/jp060322a.

(36) Caplins, B. W.; Mullenbach, T. K.; Holmes, R. J.; Blank, D. A. Femtosecond to Nanosecond Excited State Dynamics of Vapor Deposited Copper Phthalocyanine Thin Films. *Phys. Chem. Chem. Phys.* **2016**, *18* (16), 11454–11459. https://doi.org/10.1039/c6cp00958a.

(37) Nikolaitchik, A. V. Crown Ether Substituted Monomeric and Cofacial Dimeric Metallophthalocyanines. 1. Photophysical Studies of the Free Base, Zinc(II), and Copper(II) Variants. *J. Phys. Chem. A* **1999**, *103* (38), 7587–7596. https://doi.org/10.1021/jp9911651.

(38) Ha-Thi, M.-H.; Shafizadeh, N.; Poisson, L.; Soep, B. An Efficient Indirect Mechanism for the Ultrafast Intersystem Crossing in Copper Porphyrins. *J. Phys. Chem. A* **2013**, *117* (34), 8111–8118. https://doi.org/10.1021/jp4008015.

(39) Kumar, P. H.; Venkatesh, Y.; Siva, D.; Ramakrishna, B.; Bangal, P. R. Ultrafast Relaxation Dynamics of 5,10,15,20- Meso-Tetrakis Pentafluorophenyl Porphyrin Studied by Fluorescence up-Conversion and Transient Absorption Spectroscopy. *J. Phys. Chem. A* **2015**, *119* (8), 1267–1278. https://doi.org/10.1021/jp512137a.

(40) Bhattacharya, S.; Biswas, C.; Raavi, S. S. K.; Venkata Suman Krishna, J.; Koteshwar, D.; Giribabu, L.; Venugopal Rao, S. Optoelectronic, Femtosecond Nonlinear Optical Properties and Excited State Dynamics of a Triphenyl Imidazole Induced Phthalocyanine Derivative. *RSC Adv.* **2019**, *9* (63), 36726–36741. https://doi.org/10.1039/C9RA07758H.

(41) Kroeze, J. E.; Savenije, T. J.; Candeias, L. P.; Warman, J. M.; Siebbeles, L. D. A. Triplet Exciton Diffusion and Delayed Interfacial Charge Separation in a Tio2/PdTPPC Bilayer: Monte Carlo Simulations. *Sol. Energy Mater. Sol. Cells* **2005**, *85* (2), 189–203. https://doi.org/10.1016/j.solmat.2004.04.015.

(42) Abkowitz, M.; Chen, I.; Sharp, J. H. Electron Spin Resonance of the Organic Semiconductor, α -Copper Phthalocyanine. *J. Chem. Phys.* **1968**, *48* (10), 4561–4567. https://doi.org/10.1063/1.1668028.

(43) Guzy, C. M.; Raynor, J. B.; Symons, M. C. R. Electron Spin Resonance Spectrum of Copper-63 Phthalocyanin. A Reassessment of the

Bonding Parameters. *J. Chem. Soc. A Inorganic, Phys. Theor.* **1969**, 2299. https://doi.org/10.1039/j19690002299.

(44) Finazzo, C.; Calle, C.; Stoll, S.; Van Doorslaer, S.; Schweiger, A. Matrix Effects on Copper(Ii)Phthalocyanine Complexes. A Combined Continuous Wave and Pulse EPR and DFT Study. *Phys. Chem. Chem. Phys.* **2006**, *8* (16), 1942. https://doi.org/10.1039/b516184c.

(45) Moons, H.; Łapok, Ł.; Loas, A.; Van Doorslaer, S.; Gorun, S. M. Synthesis, X-Ray Structure, Magnetic Resonance, and DFT Analysis of a Soluble Copper(II) Phthalocyanine Lacking C−H Bonds †. *Inorg. Chem.* **2010**, *49* (19), 8779–8789. https://doi.org/10.1021/ic100814j.

(46) Greiner, S. P.; Rowlands, D. L.; Kreilick, R. W. EPR and ENDOR Study of Selected Porphyrin- and Phthalocyanine-Copper Complexes. *J. Phys. Chem.* **1992**, *96* (23), 9132–9139. https://doi.org/10.1021/j100202a012.

(47) Hathaway, B. J.; Billing, D. E. The Electronic Properties and Stereochemistry of Mono-Nuclear Complexes of the Copper(II) Ion. *Coord. Chem. Rev.* **1970**, *5* (2), 143–207. https://doi.org/10.1016/S0010-8545(00)80135-6.

(48) Hudson, A.; Luckhurst, G. R. Electron Resonance Line Shapes of Radicals in Solution. *Chem. Rev.* **1969**, *69* (2), 191–225. https://doi.org/10.1021/cr60258a003.

(49) de Quilettes, D. W.; Vorpahl, S. M.; Stranks, S. D.; Nagaoka, H.; Eperon, G. E.; Ziffer, M. E.; Snaith, H. J.; Ginger, D. S. Impact of Microstructure on Local Carrier Lifetime in Perovskite Solar Cells. *Science (80-.).* **2015**, *348* (6235), 683–686. https://doi.org/10.1126/science.aaa5333.

(50) Kyaw, A. K. K.; Wang, D. H.; Gupta, V.; Leong, W. L.; Ke, L.; Bazan, G. C.; Heeger, A. J. Intensity Dependence of Current–Voltage Characteristics and Recombination in High-Efficiency Solution-Processed Small-Molecule Solar Cells. *ACS Nano* **2013**, *7* (5), 4569–4577. https://doi.org/10.1021/nn401267s.

(51) Shi, J.; Dong, J.; Lv, S.; Xu, Y.; Zhu, L.; Xiao, J.; Xu, X.; Wu, H.; Li, D.; Luo, Y.; Meng, Q. Hole-Conductor-Free Perovskite Organic Lead Iodide Heterojunction Thin-Film Solar Cells: High Efficiency and Junction Property. *Appl. Phys. Lett.* **2014**, *104* (6), 063901. https://doi.org/10.1063/1.4864638.

(52) Huang, P.; Manju; Kazim, S.; Sivakumar, G.; Salado, M.; Misra, R.; Ahmad, S. Pyridine Bridging Diphenylamine-Carbazole with Linking Topology as Rational Hole Transporter for Perovskite Solar Cells Fabrication. *ACS Appl. Mater. Interfaces* **2020**, *12* (20), 22881–22890. https://doi.org/10.1021/acsami.0c03584.

(53) Jena, A. K.; Ikegami, M.; Miyasaka, T. Severe Morphological Deformation of Spiro-OMeTAD in (CH3NH3)PbI3 Solar Cells at High Temperature. *ACS Energy Lett.* **2017**, *2* (8), 1760–1761. https://doi.org/10.1021/acsenergylett.7b00582.

(54) Sanchez, R. S.; Mas-Marza, E. Light-Induced Effects on Spiro-OMeTAD Films and Hybrid Lead Halide Perovskite Solar Cells. *Sol. Energy Mater. Sol. Cells* **2016**, *158*, 189–194. https://doi.org/10.1016/j.solmat.2016.03.024.

Supporting information for

Asymmetrically Substituted Phthalocyanines as Dopant-Free Hole Selective Layers for Reliability in Perovskite Solar Cells

Peng Huang,[a†] Adrián Hernández,[b†] Samrana Kazim,[a,d] Jorge Follana-Berná,[b] Javier Ortiz,[b] Luis Lezama,[c] Ángela Sastre-Santos,[b] and Shahzada Ahmad [a,d*]*

[a]BCMaterials, Basque Center for Materials, Applications and Nanostructures, UPV/EHU Science Park, 48940 Leioa, Spain,
Tel: +34 946128811 E-mail: shahzada.ahmad@bcmaterials.net
[b]Avda. de la Universidad, s/n, Elche 03202, Spain, E-mail: asastre@umh.es
[c]Departamento de Química Orgánica e Inorgánica, Facultad de Ciencia y Tecnología, Universidad del País Vasco, UPV/EHU, Sarriena s/n, 48940 Leioa, Spain
[d]IKERBASQUE, Basque Foundation for Science, Bilbao, 48013, Spain

Experimental Section

The synthesis Scheme and necessary characterization of different MPcs are shown in the below part.

Characterization for materials. NMR spectra were measured with a Bruker AC 300. UV-vis were recorded with a Helios Gamma spectrophotometer. Fluorescence spectra were recorded with a Perkin Elmer LS 55 Luminescence spectrophotometer. High-resolution mass spectra were obtained from a Bruker Microflex LRF20 matrix-assisted laser desorption/ionization time of flight (MALDI-TOF) using dithranol as a matrix. Cyclic voltammetry was measured in a conventional three-electrode cell using a μ-AUTOLAB type III potentiostat/galvanostat at 298 K over benzonitrile or DMF and deaerated sample solutions containing 0.10 M tetrabutylammonium hexafluorophosphate ($TBAPF_6$) as supporting electrolyte. Platinum as working electrode, $Ag/AgNO_3$ as the reference electrode, and platinum as wire counter electrode were employed. Ferrocene/Ferrocenium was used as an internal standard for all measurements. IR spectra were measured with PerkinElmer Spectrum 3 FT-IR/NIR/FIR spectrophotometer.

Device fabrication. PbI_2 (99.999%) was ordered from Alfa Aesar. formamidinium iodide (FAI) was purchased from Tokyo Chemical Industry Co., Ltd. Mesoporous dispersion of TiO_2 nanoparticles (30 NRD) and methylammonium bromide (MABr) was purchased from GreatCell Solar Ltd. MACl were synthesized using the methods reported previously. anhydrous solvents such as DMF, DMSO, isopropanol, ethanol were ordered from Sigma-Aldrich. SnO_2 QDs were synthesized according to the receipt reported by Fang *et al*.[8]

The pre-cleaned FTO (NSG10) substrates were heated to 500 °C after UV-ozone treatment. A compact blocking layer of TiO_2 was deposited by spray pyrolysis using a 5% titanium (IV) diisopropoxide bis(acetylacetonate) solution diluted by anhydrous ethanol with a volume ratio of 1/19. The substrates were kept at 500 °C for 30 min after the spraying. The mesoporous TiO_2 films were spin-coated on top of a compact TiO_2 layer from a mesoporous dispersion of TiO_2 nanoparticles (30 NRD from Dyesol) and heated at 500 °C for 30 min. After cooling down to room temperature, the substrates were transferred to an argon-filled glovebox for ongoing use. Perovskite films were deposited by the two-step deposition method. In short, 1.3M PbI_2 precursor solution dissolving in a mixed solvent (volume ratio of DMF/DMSO=9.5/0.5) was spin coating at 2,200 rpm for 20 s on top of ETM to prepare PbI_2 film. The mixed organic precursor solution containing FAI: MABr: MACl= 60: 6: 6 in 1 mL isopropanol was dynamically dropped on the PbI_2 layer and was spin-coated at 2,000 rpm for 20 s. The as-prepared perovskite film was annealed at 150 °C for 15 min in the glovebox. The Pc HTM films was spin-coated at 1,500 rpm for 20 s from ~ 5 mg/mL chloroform solution. Finally, a ~ 70 nm gold electrode was evaporated by thermal evaporation.

Device characterization J–V curves were measured with a Keithley 2400 source-measurement-unit under AM 1.5 G, 100 mW cm^2 illumination from a 450 W 3A solar simulator (ORIEL, 94023 A). This was calibrated using an NREL-certified calibrated monocrystalline silicon solar cell. Testing parameters: active area defined by black cycle mask: 0.09 cm^2, scan rate: 100 mV s^{-1}, pre-sweep delay: 10 s. Surface and cross-sectional SEM images were recorded by using a Hitachi S-4800. The EQE spectra were measured using a 150 W Xenon lamp (Newport) attached to IQE200B (Oriel) motorized 1/4m monochromator as the light source. The water contact angle was tested by a contact angle goniometer (Ossila). Absorption spectra were collected by Cary 60. Atomic Force Microscopy (AFM) images were acquired with CSI Nano observer AFM.

Transient absorbance absorption *(TAS).* The femtosecond transient absorption measurements are described elsewhere.[9] Ultrashort laser pulses were generated in an oscillator- regenerative amplifier laser system (Coherent, Mantis-Legend) that provides a 1 KHz train of 35 fs pulses at 800 nm. Pump pulse wavelength in the range 470-540 nm is obtained utilizing the sum frequency of the fundamental 800 nm and the signal beam of an optical parametric amplifier (Coherent, TOPAS), while the 400 nm is generated as the second harmonic of the fundamental beam. The white light continuum probe is produced by focusing (f = 100 mm) a small fraction of the amplifier output on a 2 mm thick CaF2 window. Pump-probe delay is achieved with a translation stage (Thorlabs, DDS220) that allows a maximum range of 2 ns. Transient absorbance (TA) was measured with a fiber-coupled spectrometer (Avantes, Avaspec) as a function of the pump-probe delay. Samples were continuously scanned across the focal plane to avoid

thermal effects on the sample. The spot radii of the pump and probe pulses (0.55 and 0.2 mm) at the sample surface were measured using a CMOS camera. Pump pulse energies were varied in the range 15–85 nJ.

Electron paramagnetic resonance. It was performed using a Bruker ELEXSYS E500 spectrometer operating at the X-band. The spectrometer was equipped with a super-high-Q resonator ER-4123-SHQ. Solid samples and toluene solutions were placed in quartz tubes and spectra were recorded at different temperatures between 5 and 300 K with standard Oxford Instruments low-temperature devices using typical modulation amplitudes of 1.0 G at a frequency of 100 kHz. The magnetic field was calibrated by an NMR probe and the frequency inside the cavity (~9.4 GHz) was determined with an integrated MW-frequency counter. Room temperature Q-band spectra were also recorded on solid samples using a Bruker EMX system equipped with an ER-510-QT resonator. Data were collected and processed using the Bruker Xepr suite.

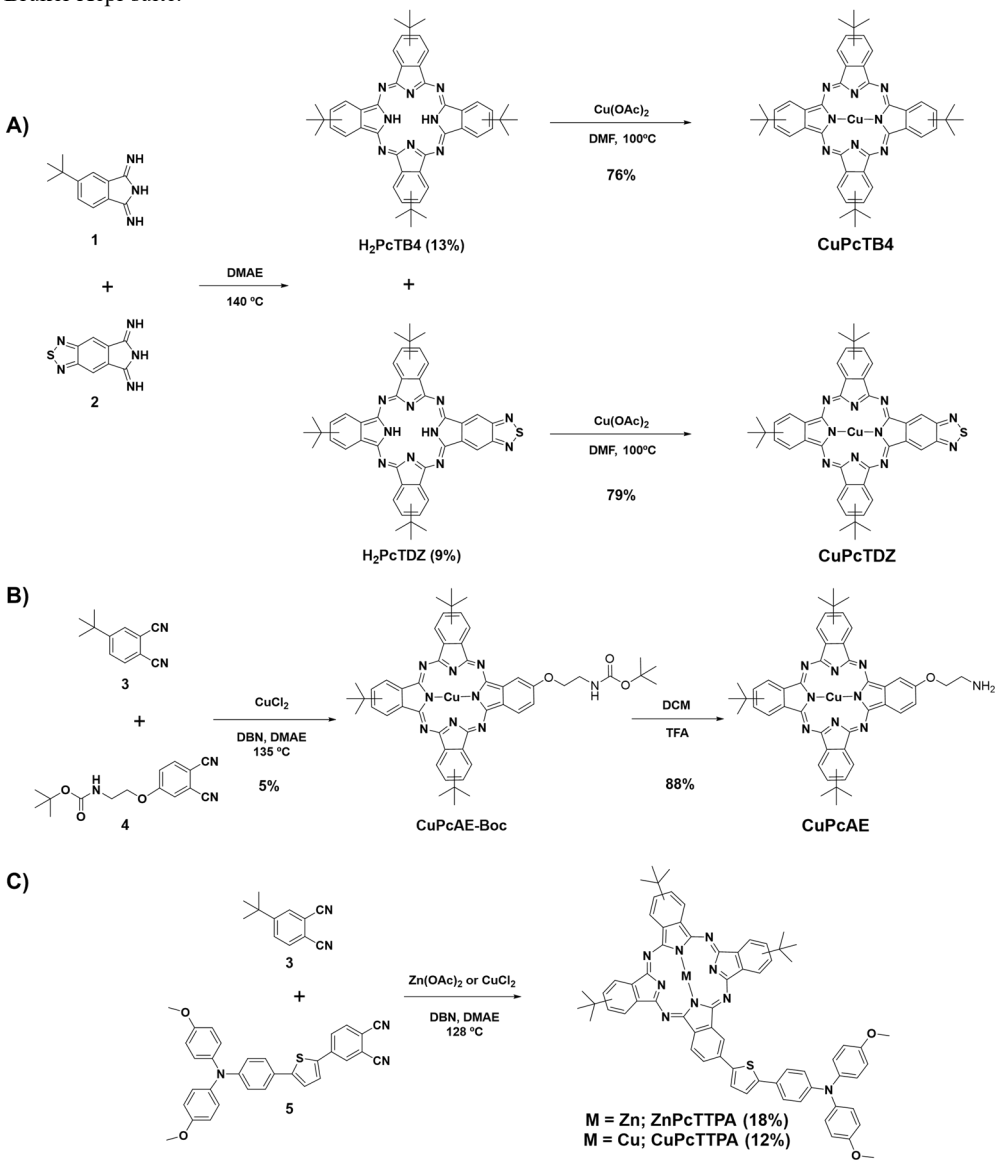

***Figure S1**. Synthetic route of CuPcTB4, CuPcTDZ, CuPcAE, ZnPcTTPA and CuPcTTPA.*

1.1 Synthesis of CuPcTB4 and CuPcTDZ

1.1.1 H_2PcTB4 and H_2PcTDZ

500 mg (2.5 mmol) of 5-*tert*-butyl-1,3-diiminoisoindoline **1** and 170 mg (0.8 mmol) of 2,1,3-benzothiadiazole-5,6-dicarboximide diamine 2[10] in 2 mL of DMAE under inert atmosphere were stirred at 140ºC for 20 hours. The green mixture of different phthalocyanines was cooled at room temperature, concentrated under vacuum and purified by column chromatography (Toluene/AcOEt 99:1) yielding 59 mg of H_2PcTB4 (13%) and 77 mg of H_2PcTDZ (13%) as blue solids. H_2PcTB4: ^{1}H-NMR (300 MHz, $CDCl_3$): (mixture of regioisomers), -1.96 – -2.36 (br, 2H, NH), 1.90-1.87 (m, 36H), 8.22-8.14 (m, 4H), 9.28-8.90 (m, 8H). HR-MALDI-TOF (dithranol): *m/z* for $C_{48}H_{50}N_8$: calcd. 738.4153 [M^+]; found, 738.4129. UV-vis ($CHCl_3$) λ_{max}/nm (log ε): 342 (4.86), 603 (4.42), 645 (4.68), 664 (5.09), 701 (5.15). FT-IR: ν_{max}/cm^{-1} 3289, 2952, 2902, 2861, 1615, 1482, 1392, 1361, 1258, 1089, 1006, 891, 824, 744, 666, 599, 520. H_2PcTDZ: ^{1}H-NMR (300 MHz, $CDCl_3$): 8.76-7.63 (m, 11H), 1.90-1.73 (m, 27H), -4 (br, 2H, NH) (mixture of regioisomers). HR-MALDI-TOF (dithranol): *m/z* for $C_{44}H_{40}N_{10}S$: calcd. 740.3153 [M^+]; found, 740.3123. UV-vis ($CHCl_3$) λ_{max}/nm (log ε): 337 (4.80), 660 (4.83), 684 (4.74), 736 (5.10). FT-IR: ν_{max}/cm^{-1} 3298, 2954, 2902, 2864, 1616, 1483, 1414, 1325, 1258, 1072, 1004, 875, 818, 742, 666, 508.

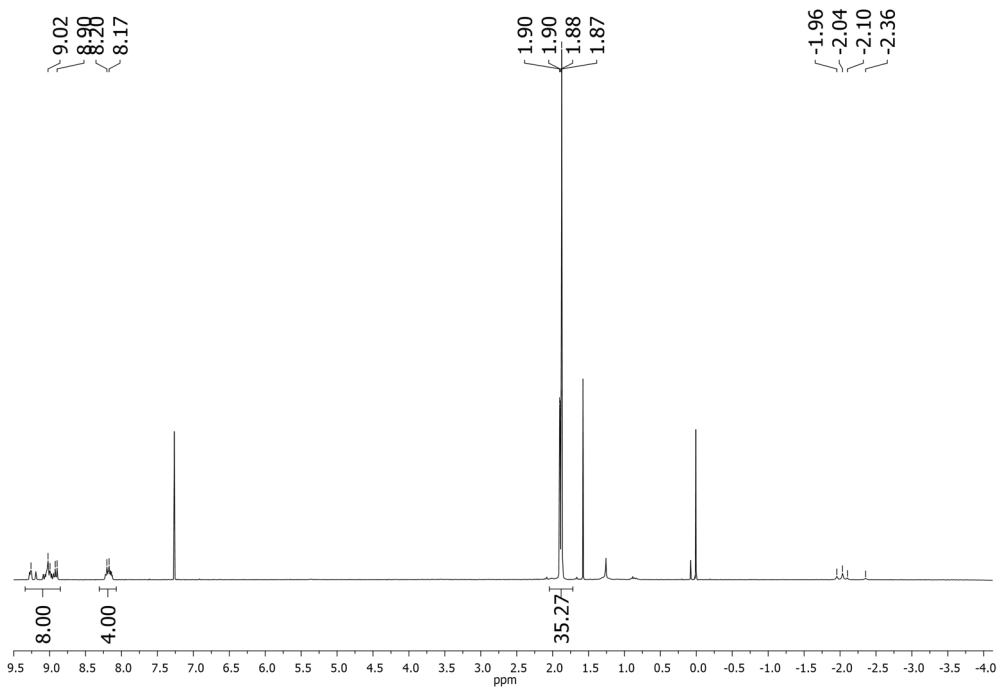

Figure S2. *^{1}H-NMR spectrum of H_2PcTB4 in $CDCl_3$.*

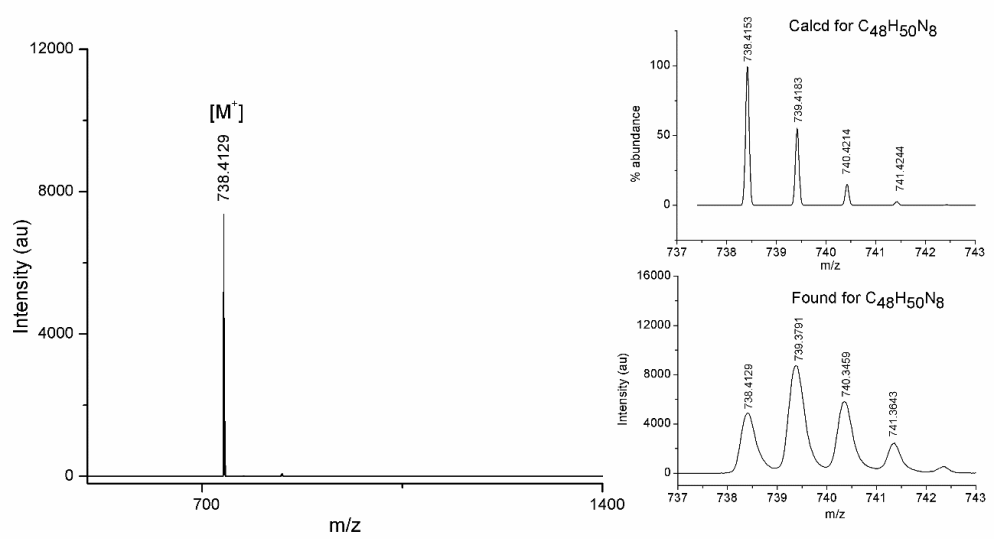

Figure S3. *HR-MALDI-TOF spectrum of H_2PcTB4.*

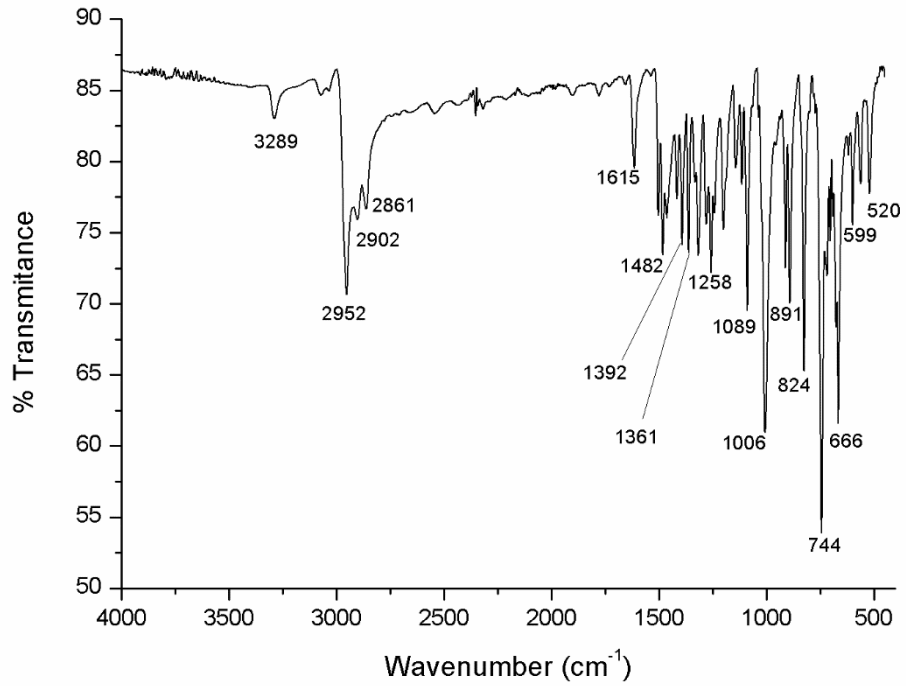

Figure S4. *FT-IR spectrum of H_2PcTB4.*

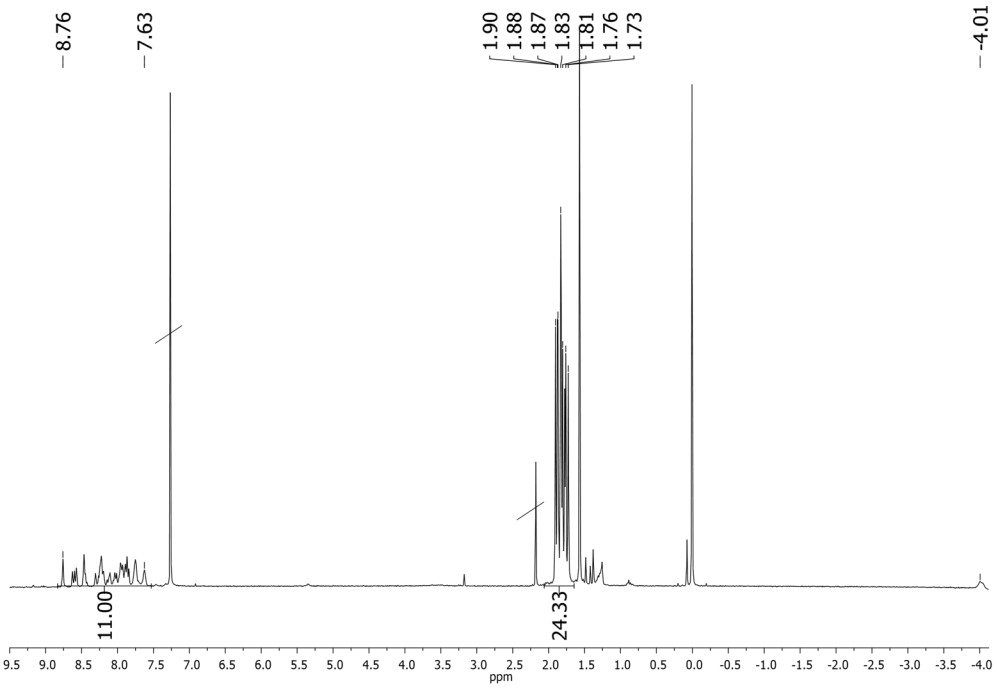

Figure S5. *^{1}H-NMR spectrum of H_2PcTDZ in $CDCl_3$.*

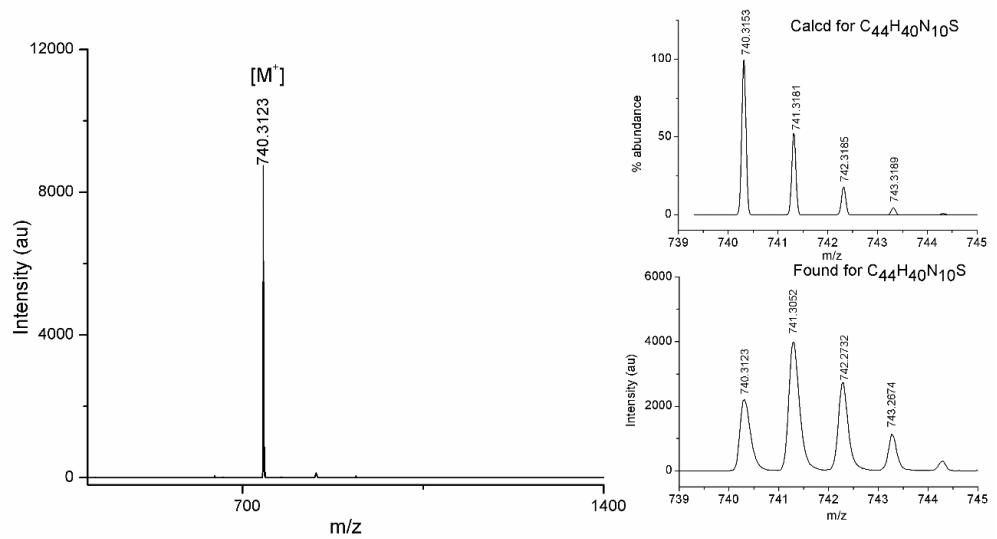

Figure S6. *HR-MALDI-TOF spectrum of H_2PcTDZ.*

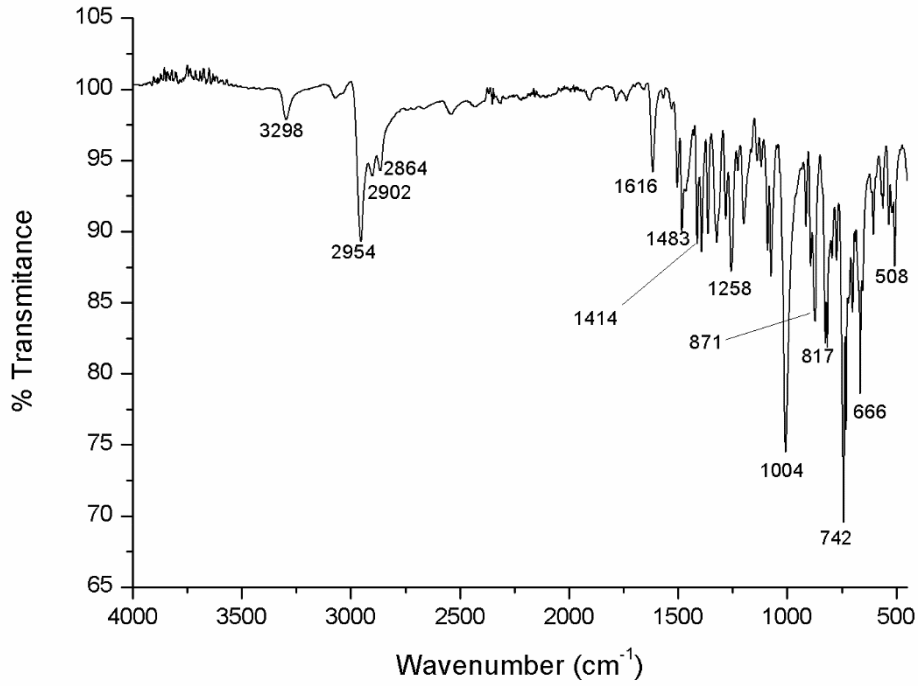

***Figure S7**. FT-IR spectrum of H_2PcTDZ.*

1.1.2 CuPcTB4

50 mg (0.1 mmol) of H_2PcTB4 and 25 mg (0.1 mmol) of $Cu(OAc)_2$ were dissolved in dry DMF under inert atmosphere and stirring at 100ºC for 18 hours. The solution was cooled to room temperature, washed with MeOH and purified by column chromatography (DCM/Hexane 1:1), yielding 41 mg (76%) of CuPcTB4. HR-MALDI-TOF (dithranol): *m/z* for $C_{48}H_{48}CuN_8$: calcd. 799.3292 [M^+]; found, 799.3261. UV-vis ($CHCl_3$) λ_{max}/nm (log ε): 340 (4.90), 612 (4.62), 680 (5.35).FT-IR: ν_{max}/cm^{-1}: 3217, 3070, 2952, 2898, 2858, 1712, 1615, 1508, 1482, 1392, 1361, 1325, 1256, 1200, 1146, 1086, 1050, 930, 891, 825, 746, 694, 669, 600, 564, 529.

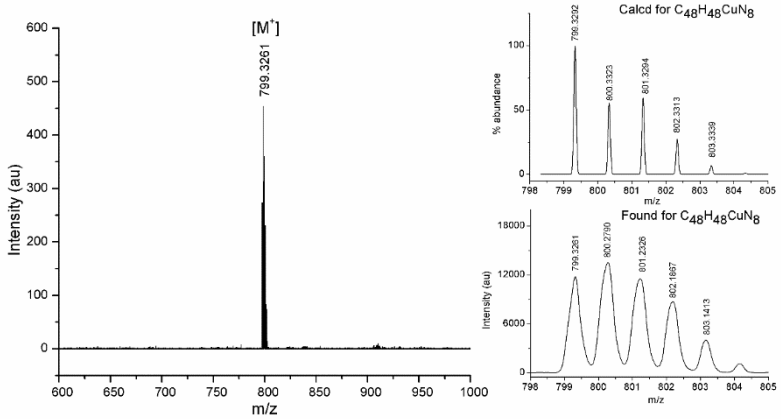

***Figure S8**. HR-MALDI-TOF spectrum of CuPcTB4.*

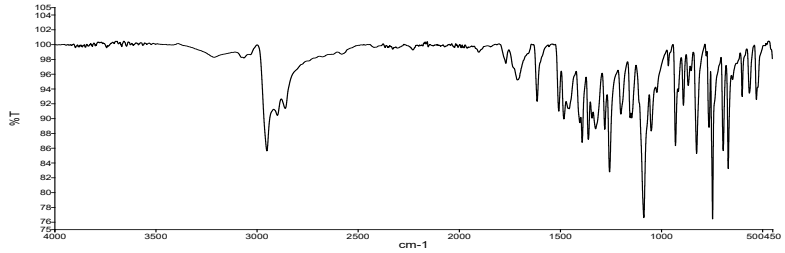

***Figure S9**. FT-IR spectrum of CuPcTB4.*

1.1.3 CuPcTDZ:

57 mg (0.1 mmol) of H_2PcTDZ and 28 mg (0.2 mmol) of $Cu(OAc)_2$ were dissolved in dry DMF under inert atmosphere and stirring at 100ºC for 18 hours. The solution was cooled to room temperature, washed with MeOH and purified by column chromatography (DCM/Hexane 1:1), yielding 49 mg (79%) of CuPcTDZ. HR-MALDI-TOF (dithranol): *m/z* for $C_{44}H_{38}CuN_{10}S$: calcd. 801.2292 [M^+]; found, 801.2224. UV-vis ($CHCl_3$) λ_{max}/nm (log ε): 342 (4.89), 667 (4.73), 691 (4.90), 734 (4.86). FT-IR: ν_{max}/cm^{-1}: 2952, 1614, 1507, 1482, 1391, 1362, 1318, 1256, 1197, 1153, 1082, 929, 870, 826, 744, 689, 668, 516.

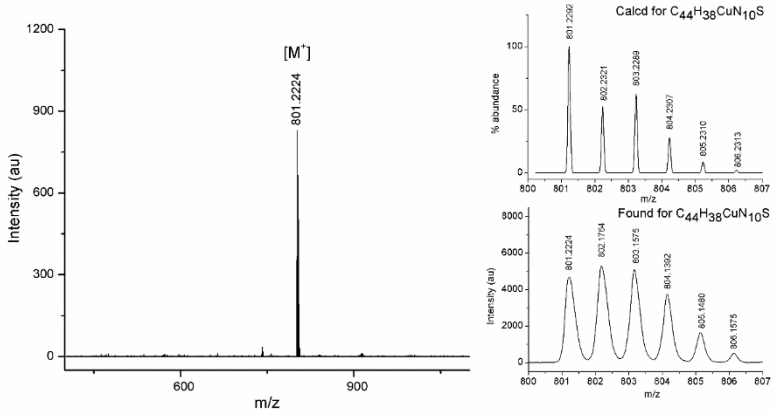

***Figure S10**. HR-MALDI-TOF spectrum of CuPcTDZ.*

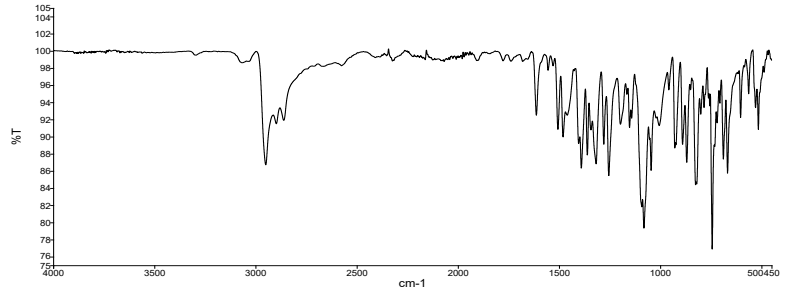

***Figure S11**. FT-IR spectrum of CuPcTDZ.*

1.2 Synthesis of CuPcAE

1.2.1 CuPcAE-Boc:

770 mg (4.2 mmol) of 4-*tert*-butylphthalonitrile **3**, 400 mg (1.4 mmol) of 4-(2-*tert*-butoxycarbonylaminoethoxy)phthalonitrile **4** and 374 mg (2.78 mmol) of $CuCl_2$ in 2 mL of DMAE and 4 drops of DBN under inert atmosphere were stirred at 136ºC for 7 hours. The blue mixture of different phthalocyanines was cooled at room temperature, concentrated under vacuum and purified by sonication/centrifugation in toluene to remove a brown residue, and column chromatography (Toluene/AcOEt; 100:6) with previously deactivated silica gel (Hexane/Et_3N; 95:5) yielding 60 mg (5%) of CuPcAE-Boc. HR-MALDI-TOF (dithranol): *m/z* for $C_{51}H_{53}CuN_9O_3$: calcd. 902.3562 [M+]; found, 902.3544. UV-vis (DMSO) λ_{max}/nm (log ε): 350 (4.64), 610 (4.38), 648 (4.37), 678 (5.11). IR: ν_{max}/cm^{-1}: 2952, 2896, 2861, 1717, 1611, 1506, 1483, 1391, 1363, 1091, 825, 746, 686, 670.

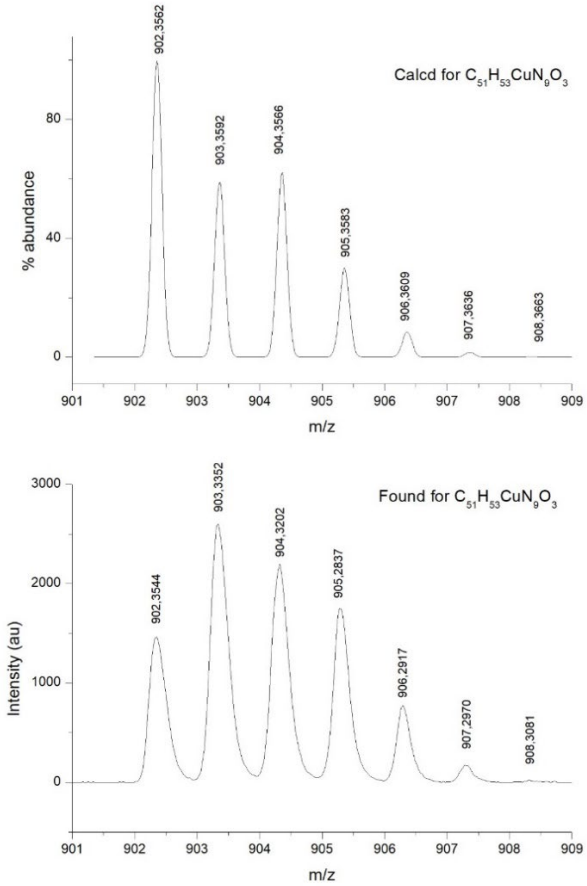

***Figure S12**. HR-MALDI-TOF spectrum of CuPcAE-Boc.*

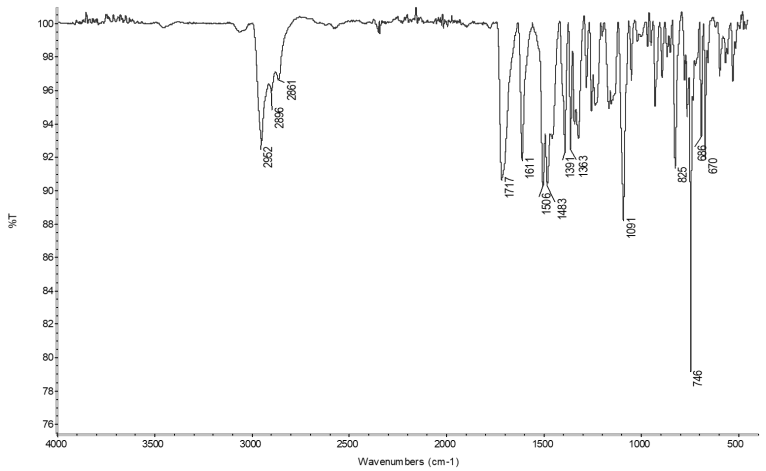

Figure S13. *FT-IR spectrum of CuPcAE-Boc.*

1.2.2 CuPcAE

50 mg (0.06 mmol) of CuPcAE-Boc in 2 ml DCM and 2 ml TFA were stirred at 0ºC for 2 hours. The blue mixture was heated at room temperature, concentrated under vacuum, treated with $NaHCO_3$, extracted with DCM, washed with water, dried with Na_2SO_4, filtered, and concentrated with a nitrogen flow in a warm bath yielding 39 mg (88%) of CuPcAE. HR-MALDI-TOF (dithranol): *m/z* for $C_{46}H_{45}CuN_9O$: calcd. 802.3038 [M^+]; found, 802.3063. UV-vis (DMF) λ_{max}/nm (log ε): 345 (4.73), 609 (4.48), 677 (5.13). FT-IR: ν_{max}/cm^{-1}: 3357, 2955, 1612, 1507, 1481, 1392, 1257, 1089, 1049, 1013, 789, 746.

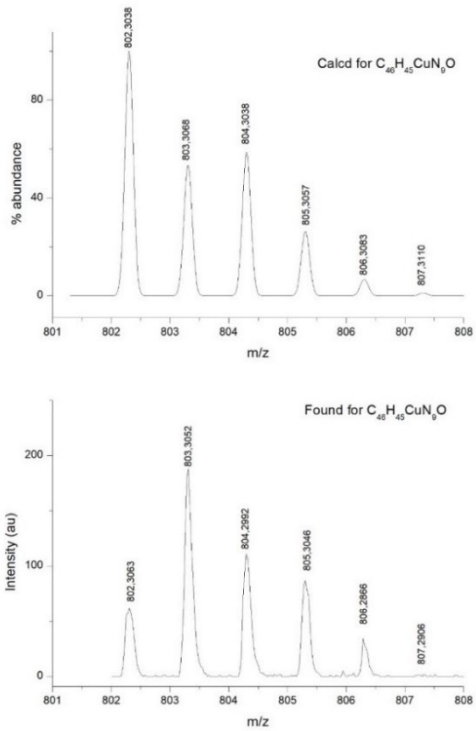

Figure S14*. HR-MALDI-TOF spectrum of CuPcAE.*

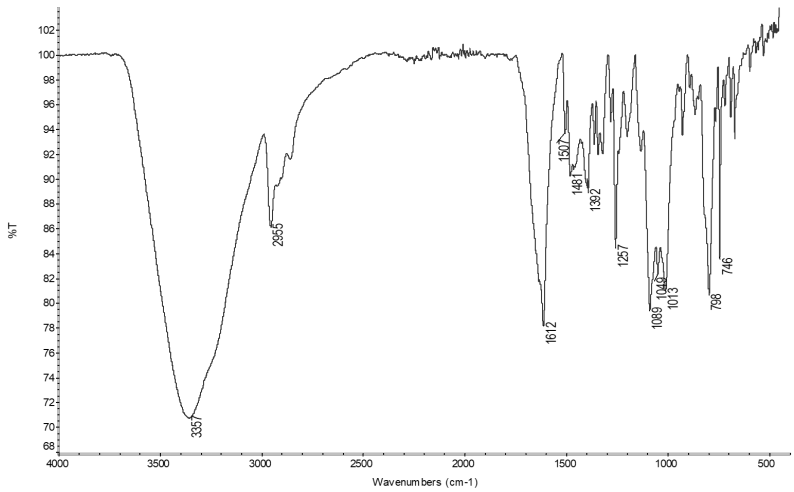

***Figure S15**. FT-IR spectrum of CuPcAE.*

1.3 Synthesis of ZnPcTTPA and CuPcTTPA

1.3.1 ZnPcTTPA

215 mg (1.2 mmol) of 4-*tert*-butylphthalonitrile 3, 150 mg (0.3 mmol) of phthalonitrile 5[11] and 107 mg (0.6 mmol) of $Zn(OAc)_2$ in 0.5 ml of DMAE and 2 drops of DBN under inert atmosphere were stirred at 128ºC for 16 hours. The green mixture was cooled at room temperature, concentrated under vacuum and purified by column chromatography (Hexane/AcOEt 75:25) yielding 60 mg (18%). ^{1}H-NMR (300 MHz, THF-d_8): δ = 1.82 (s, 27H), 3.80 (s, 6H), 6.91 (d, J = 8.9, 4H), 7.00 (d, J = 8.6, 2H), 7.12 (d, J = 8.8, 4H), 7.50 (d, J = 4.1, 1H), 7.65 (d, J = 8.3, 2H), 7.95 (br, 1H), 8.32 (d, J = 8.3, 3H), 8.45 (br, 1H), 9.28-9.47 (m, 4H), 9.55 (s, 3H), 9.67 (br, 1H). HR-MALDI-TOF (dithranol): *m/z* for $C_{68}H_{59}N_9O_2SZn$: calcd. 1129.3738 [M^+]; found, 1129.3698. UV-vis (DMF) λ_{max}/nm (log ε): 358 (4.86), 619 (4.50), 693 (5.21). FT-IR: ν_{max}/cm^{-1}: 3064, 3035, 2946, 2917, 1601, 1503, 1487, 1237, 1087, 1034, 284, 761, 744, 694, 668.

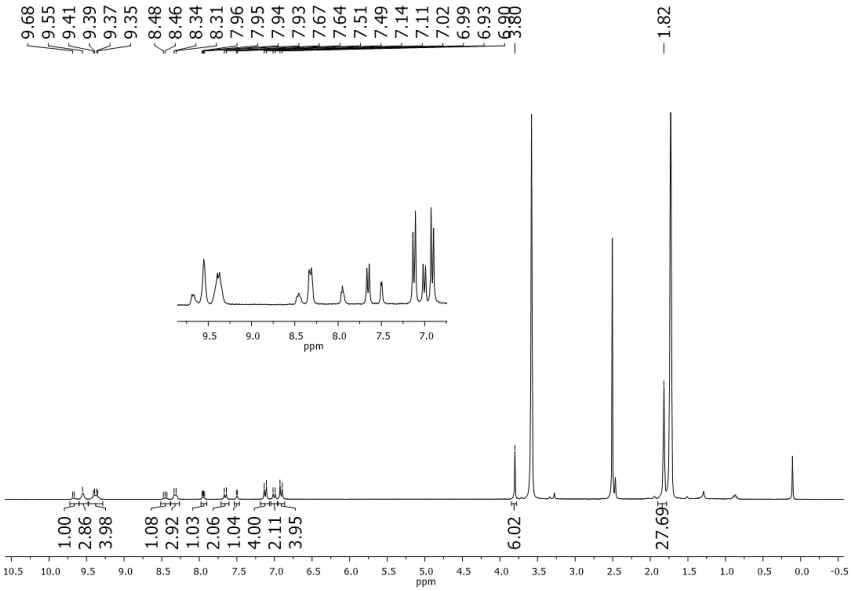

***Figure S16**. ^{1}H-NMR spectrum of ZnPcTTPA in THF-d_8.*

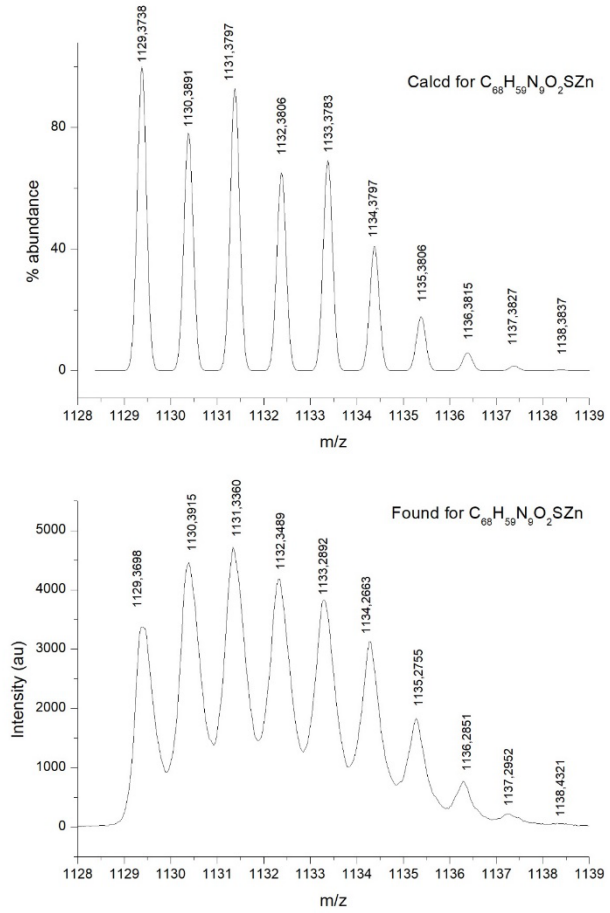

***Figure S17**. HR-MALDI-TOF spectrum of ZnPcTTPA.*

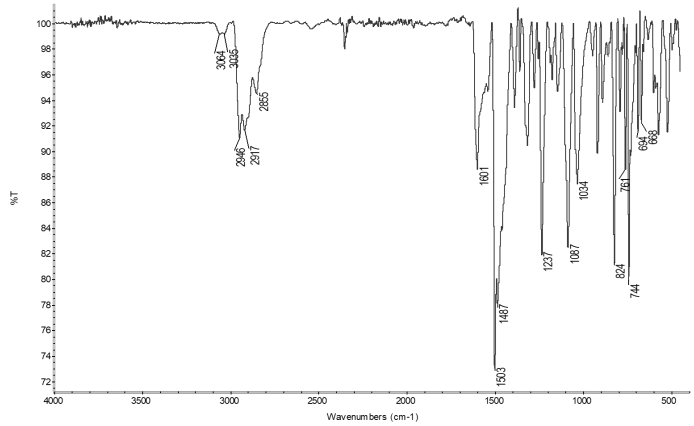

***Figure S18**. FT-IR spectrum of ZnPcTTPA.*

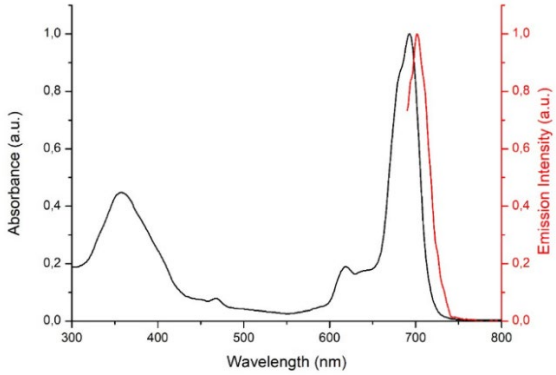

***Figure S19**. Normalized UV-Vis absorption and fluorescence spectra of ZnPcTTPA in DMF.*

1.3.2 CuPcTTPA

215 mg (1.2 mmol) of 4-*tert*-butylphthalonitrile **3**, 150 mg (0.3 mmol) of phthalonitrile 5 and 78 mg (0.6 mmol) of $CuCl_2$ in 0.5 ml of DMAE and 2 drops of DBN under inert atmosphere were stirred at 128ºC for 16 hours. The green mixture was cooled at room temperature, concentrated under vacuum and purified by column chromatography (Hexane/Toluene; 10:90) with previously deactivated silica gel (Hexane/Et_3N; 95:5) yielding 38 mg (12%). HR-MALDI-TOF (dithranol): *m/z* for $C_{68}H_{59}CuN_9O_2S$: calcd. 1128.3803 [M^+]; found, 1128.3702. UV-vis (DMF) λ_{max}/nm (log ε): 349 (4.69), 620 (4.30), 693 (4.97). FT-IR: ν_{max}/cm^{-1}: 3063, 3037, 2951, 2864, 1731, 1602, 1503, 1479, 1238, 1090, 1034, 824, 794, 746, 692, 670.

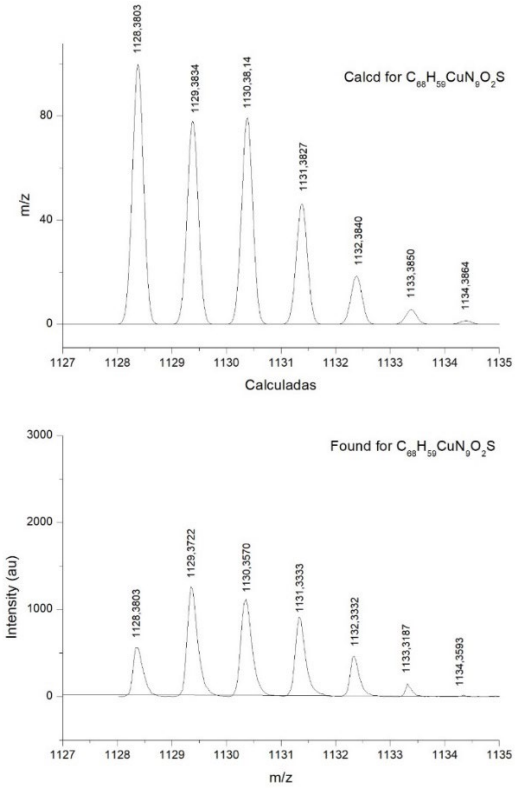

***Figure S20**. HR-MALDI-TOF spectrum of CuPcTTPA.*

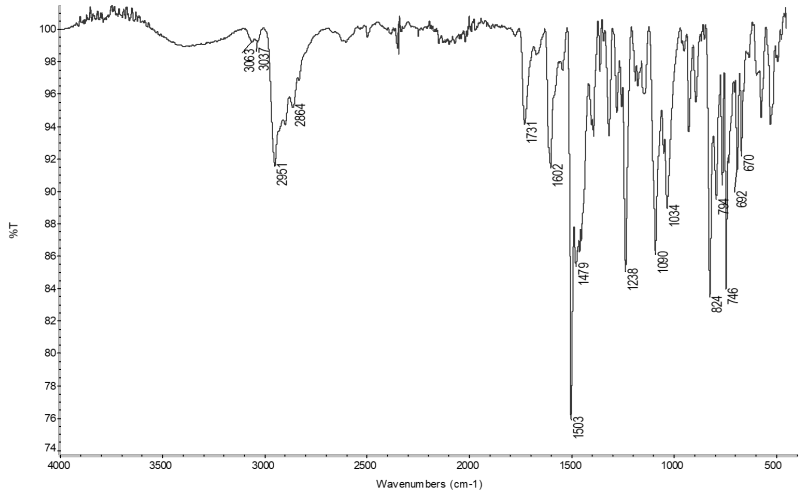

Figure S21. *FT-IR spectrum of CuPcTTPA.*

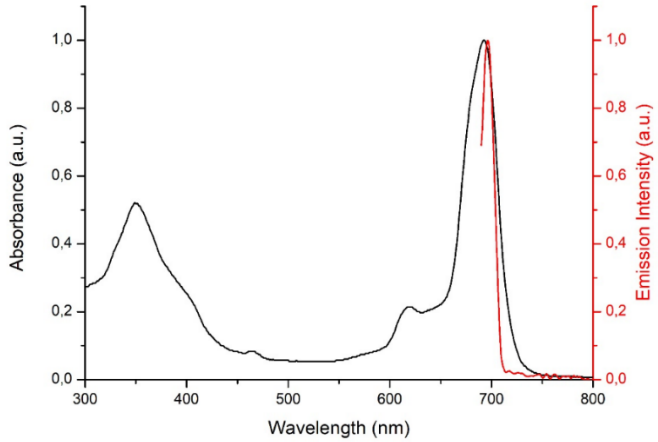

Figure S22. *Normalized UV-Vis absorption and fluorescence spectra of CuPcTTPA in DMF.*

Electrochemistry

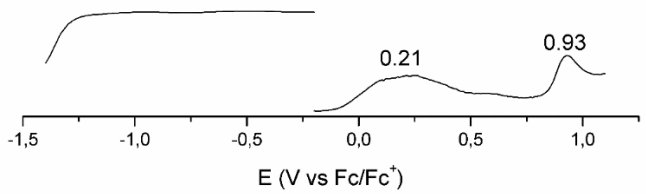

Figure S23. *Differential pulse voltammetry of CuPcTB4 in deaerated PhCN solution containing $TBAPF_6$ (0.1 M) obtained at 298 K.*

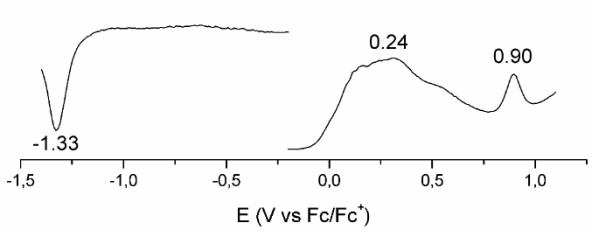

Figure S24. *Differential pulse voltammetry of CuPcTDZ in deaerated PhCN solution containing $TBAPF_6$ (0.1 M) obtained at 298 K.*

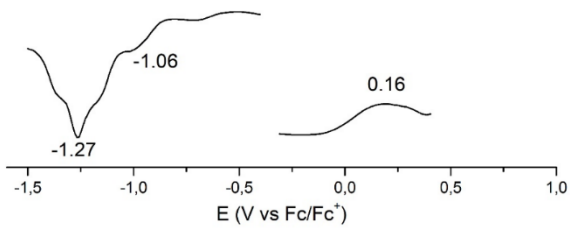

Figure S25. *Differential pulse voltammetry of CuPcAE in deaerated DMF solution containing $TBAPF_6$ (0.1 M) was obtained at 298 K.*

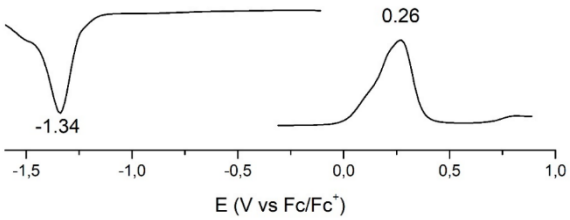

Figure S26. *Differential pulse voltammetry of ZnPcTTPA in deaerated DMF solution containing $TBAPF_6$ (0.1 M) obtained at 298 K.*

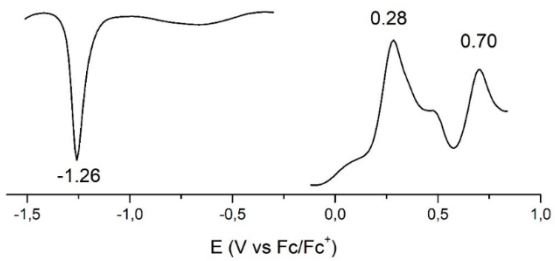

***Figure S27**. Differential pulse voltammetry of CuPcTTPA in deaerated DMF solution containing $TBAPF_6$ (0.1 M) was obtained at 298 K.*

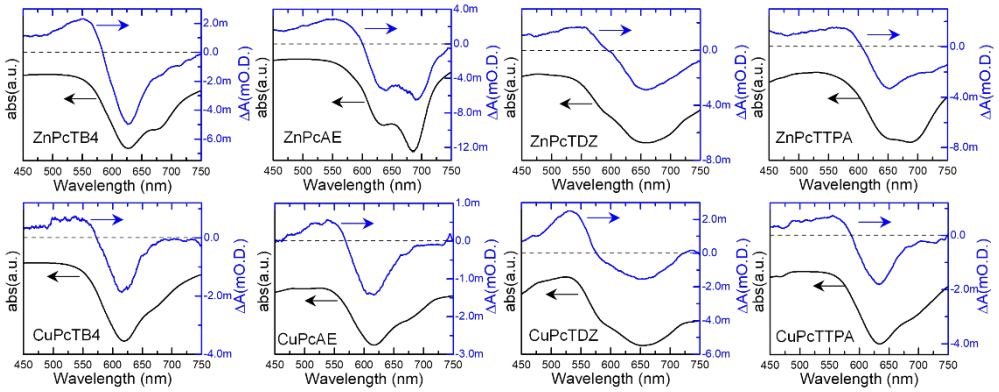

Figure S28. Comparison of transient absorption and UV-vis static absorption spectra of MPcs. The TAS spectra were choosing at 1.4 ps when the signal reached the maximum.

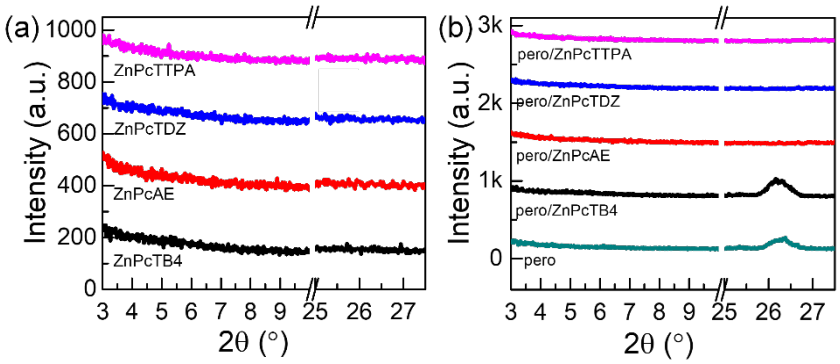

Figure S29. GIXRD patterns of ZnPcs deposited on (a) and (b) perovskite films, perovskite is referred to as "pero". In Figure S29b, the pero/ZnPcTB4 have a similar peak at 26.3º with bare perovskite samples, possibly due to the poor coverage of ZnPcTB4 film on top of perovskite.

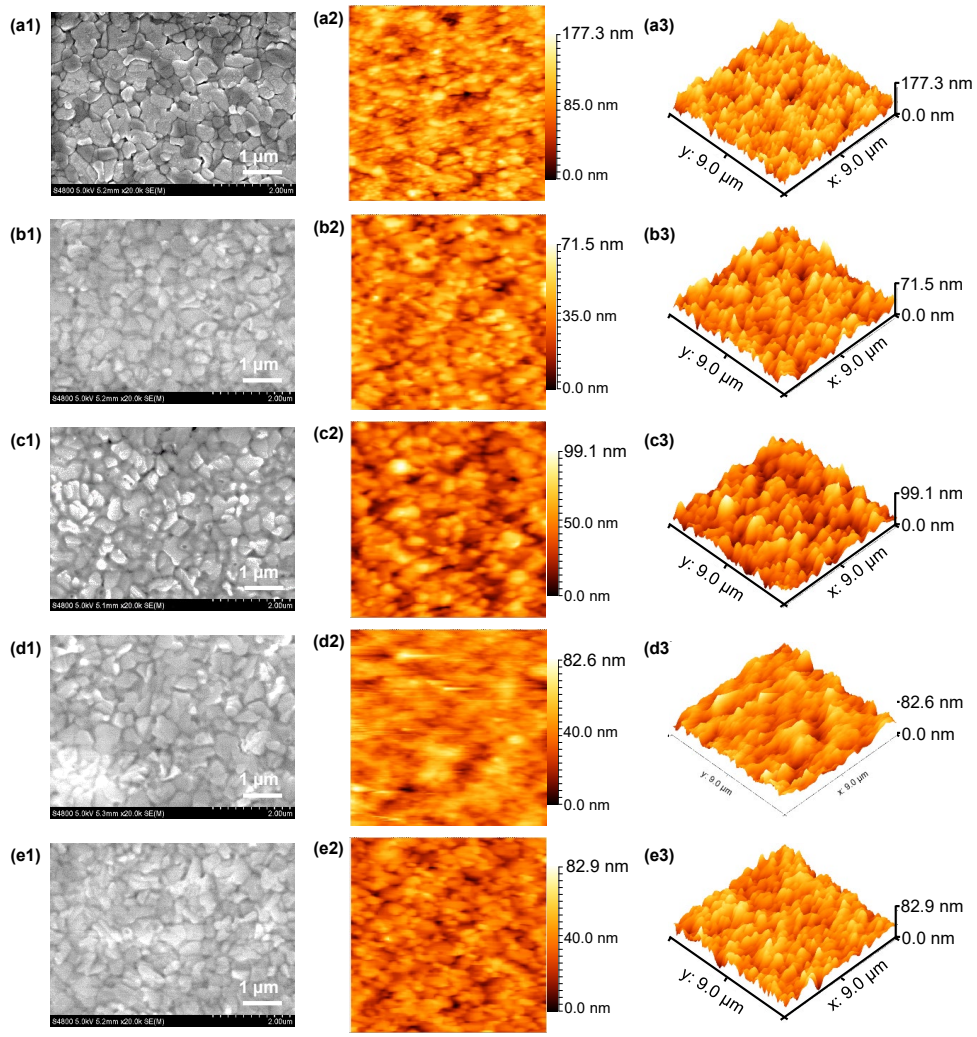

Figure S30. Morphology analyses of perovskite with different ZnPcs . Top-view SEM images of (a1) bare perovskite, (b1) pero/ZnPcTB4, (c1) pero/ZnPcAE, (d1) pero/ZnPcTDZ, and (e1) pero/ZnPcTTPA, respectively. The AFM height images and corresponding 3D images of the (a2, a3) bare perovskite, (b2, b3) pero/ZnPcTB4, (c2, c3) pero/ZnPcAE, (d2, d3) pero/ZnPcTDZ, and (e2, e3) pero/ZnPcTTPA, respectively.

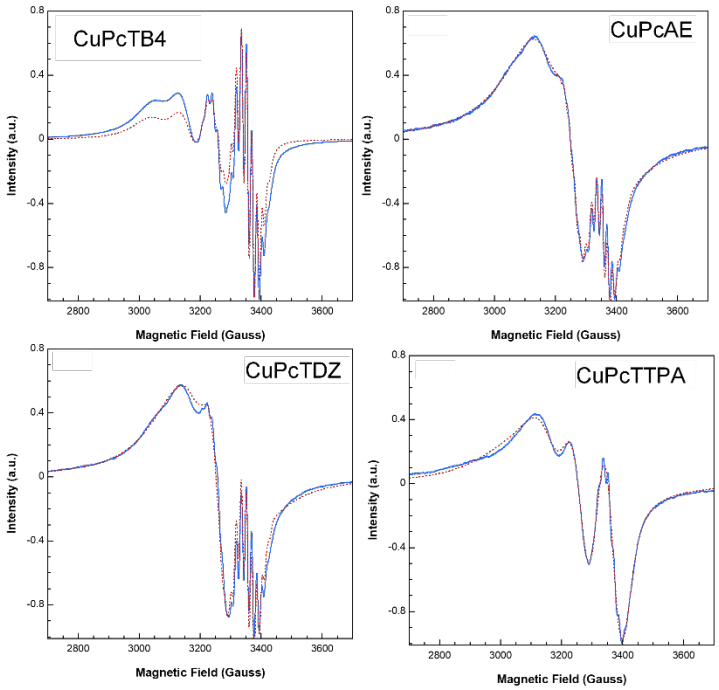

Figure S31. Experimental and simulated (dotted lines) X-band EPR room temperature spectra of toluene solutions of the CuPc complexes.

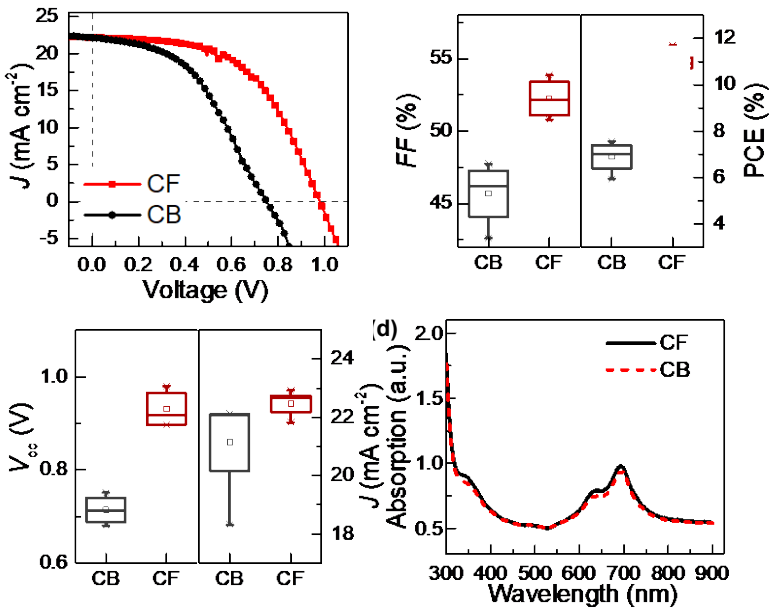

Figure S32. (a) The *J-V* curves of the device with CuPcAE are deposited in different solvents. (b) and (c) The statistical PV parameters of the device with CuPcAE HTM deposited by different solvents. (d) The CuPcAE film on quartz was deposited in different solvents. (CF and CB present chloroform and chlorobenzene, respectively)

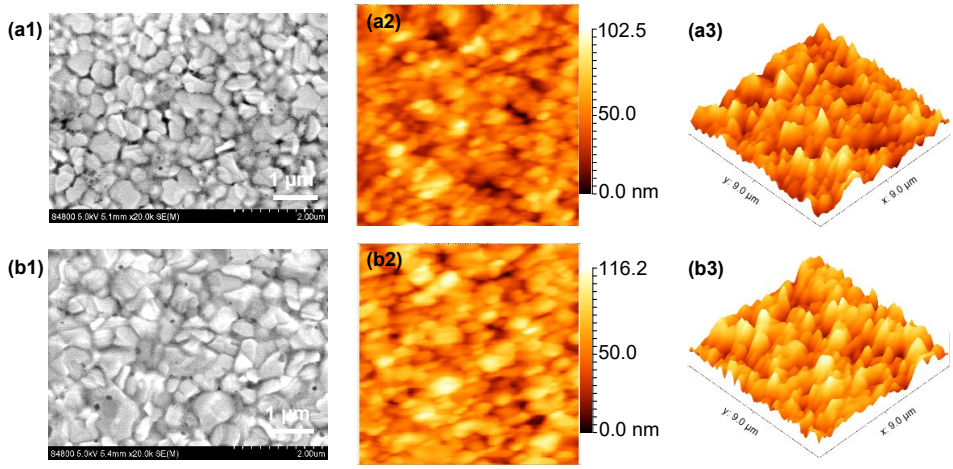

Figure S33. Morphology analyses of perovskite with CuPcAE deposited by different solvents. Top-view SEM images of (a1) pero/CuPcAE(CF) and (b1) pero/CuPcAE(CB). The AFM height images and corresponding 3D images of the (a2, a3) pero/CuPcAE(CF) and (b2, b3) pero/CuPcAE(CB).

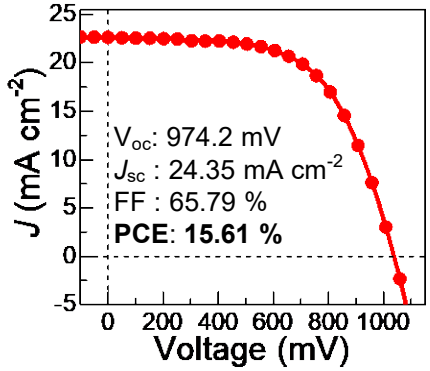

Figure S34. *J-V* curves of the champion device with ZnPcAE as an HTM and *b*-TiO_2/SnO_2 QD as an ETM.

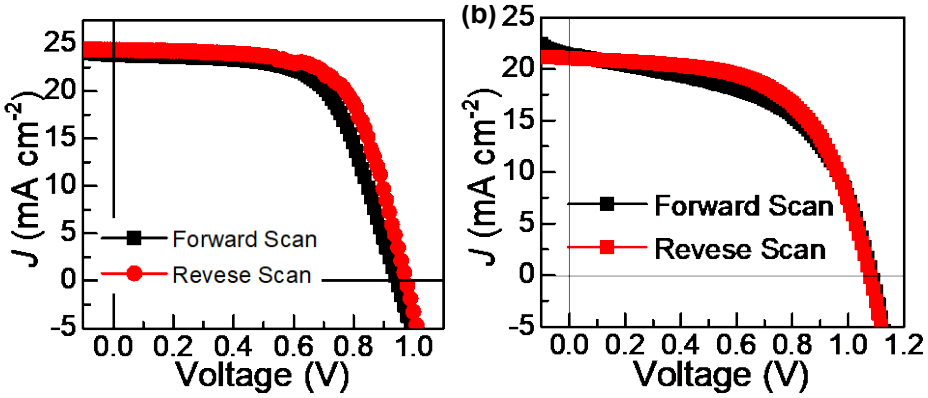

Figure S35. *J*−*V* curves of forward and reverse scans under simulated AM 1.5G illumination for the devices with ZnPcAE (a) and ZnPcTDZ (b) as HTM.

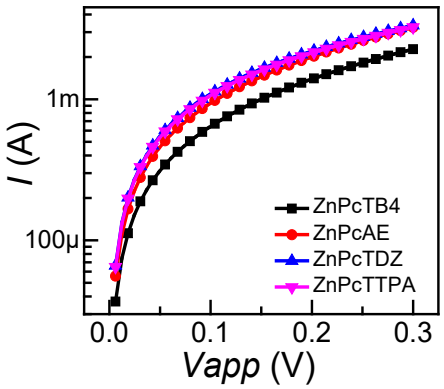

Figure S36. *I-V* curves measuring the device with the structure of FTO/HTM/Ag.

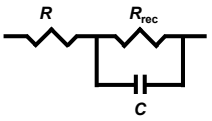

Figure S37. Equivalent circuits are used for fitting the EIS data from ZnPcs-based devices.

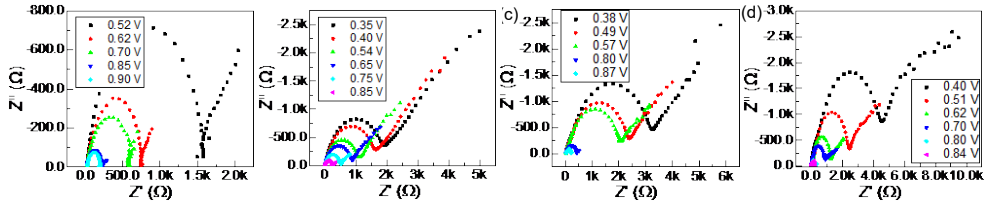

Figure S38. Typical Nyquist (Z′–Z′′) of impedance spectroscopy of devices based on (a) ZnPcTB4, (b) ZnPcAE, (c) ZnPcTDZ, (d) ZnPcTTPA respectively. Different voltages at open circuit conditions were obtained at different illumination intensities.

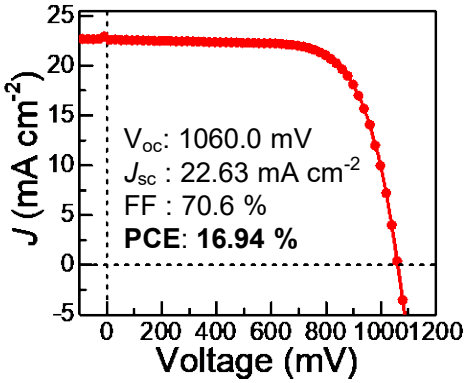

Figure S39 *J-V* curves of the control device with Spiro-OMeTAD as an HTM and *b&mp*-TiO_2 as an ETM.

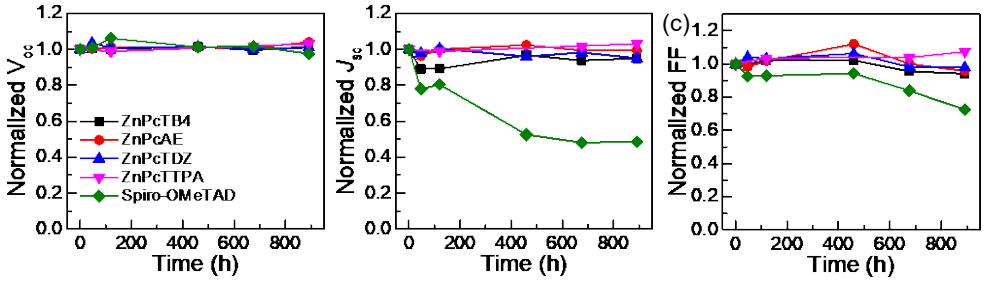

Figure S40. Plots of normalized (a) V_{oc}, (b) J_{sc}, and (c) FF of PSCs based on different ZnPcs and Spiro-OMeTAD (control) HTMs under 30-70% RH condition.

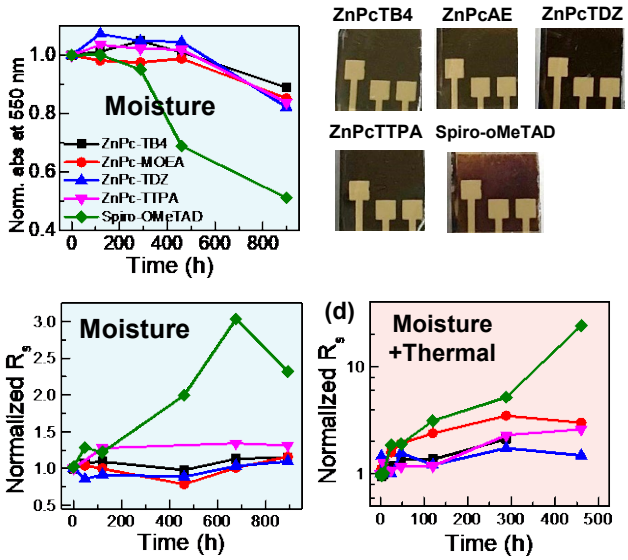

Figure S41. (a) absorbance values of the perovskite layers with different ZnPcs and Spiro-OMeTAD at 550 nm exposed to 30-70% RH with time, (b) photographs of the perovskite films with different HTMs after aging around 900 h under 30-70% RH. (c) the extracted series resistance (Rs) from J-V curves of the device with different HTMs exposed to 30-70% RH with time, (d) the extracted series resistance (Rs) from J-V curves of the device with different HTMs under humidity and heat conditions.

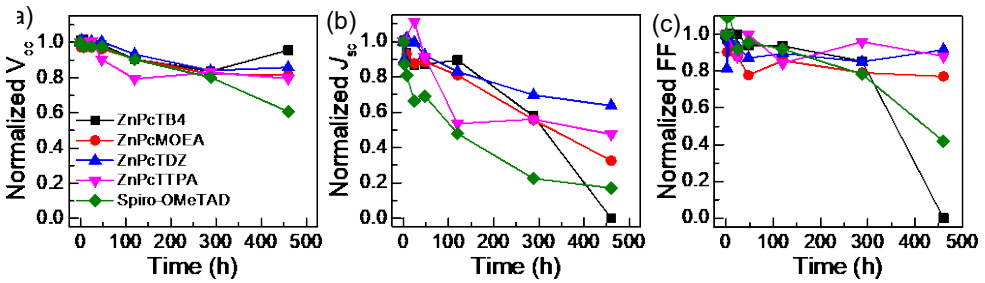

Figure S42. Plots of normalized (a) V_{oc}, (b) J_{sc}, and (c) FF of PSCs based on different ZnPc and Spiro-OMeTAD (control) HTMs under 30-70% RH and heat condition.

Table S1. *Redox potentials in V (vs Fc/Fc^{+}).*

Compound	E_{ox1}	E_{ox2}	E_{red1}	E_{red2}
CuPcTB4	0.21	0.93		
CuPcTDZ	0.24	0.90	-1.33	
CuPcAE	0.16		-1.27	
ZnPcTPPA	0.26		-1.34	
CuPcTTPA	0.28	0.70	-1.26	

Table S2. *Relative amplitude, the time constant of excited state relaxation dynamics of different ZnPcs.*

HTM	α_1	τ_1	α_2	τ_2	α_3	τ_3	$\tau_{ave.}$[a]
ZnPcTB4	0.21	1.3	0.62	92.9	0.17	2825.8	2535.7
ZnPcAE	0.65	1.2	0.24	92.9	0.11	2552.8	2380.0
ZnPcTDZ	0.12	2.2	0.71	73.3	0.16	2239.5	1963.2
ZnPcTTPA	0.16	2.9	0.67	69.6	0.17	2250.7	2005.1

[a] $\tau_{ave} = \sum\alpha_i \tau_i^2 / \sum\alpha_i \tau_i$ (i=3)

Table S3. Spin Hamiltonian parameters were obtained from the EPR spectral simulations of CuPcTB4, CuPcTDZ, CuPcAE, CuPcTTPA.

	CuPcTB4	CuPcTDZ	CuPcAE	CuPcTTPA
g_{iso} (X-band; RT; solid)	2.067	2.066	2.068	2.066
ΔH_{pp} / Gauss	88	103	112	134
$g_{\parallel}$ (Q-band; RT; solid)	2.151	2.149	2.148	2.148
$g_{\perp}$ (Q-band; RT; solid)	2.049	2.050	2.051	2.051
G	3.082	3.010	2.874	2.902
g_{iso} (RT; toluene)	2.082	2.080	2.078	2.082
A_{Cu} / Gauss	91.0	88.0	87.3	89.5
A_N / Gauss	16.7	16.5	16.7	16.2

Table S4. Spin Hamiltonian parameters derived from the EPR spectral simulations of CuPcTB4.

$g_{\parallel}$ (100 K, toluene)	$g_{\perp}$ (100 K, toluene)	$A_{\parallel}$ (^{63}Cu) / Gauss	$A_{\perp}$ (^{63}Cu) / Gauss	$A_{\parallel}$ (^{65}Cu) / Gauss	$A_{\perp}$ (^{65}Cu) / Gauss	$A_{\parallel}$ (^{14}N) / Gauss	$A_{\perp}$ (^{14}N) / Gauss
2.161	2.042	212	18	223	20.8	15.5	17

Table S5 the average photovoltaic parameters of the PSCs based on different MPcs.

HTM	V_{oc} (mV)	J_{sc} (mA cm^{-2})	FF (%)	PCE (%)
ZnPcTB4	1034.8±12.9	17.31±1.15	53.0±4.2	9.47±0.79
ZnPcAE	1038.5±17.1	21.08±0.99	57.9±3.6	12.68±1.14
ZnPcTDZ	1045.9±12.6	18.80±1.44	51.1±5.6	10.11±1.80
ZnPcTTPA	1021.4±28.1	17.27±1.83	50.2±5.1	8.77±0.58
ZnPcAE[a]	959.9±16.5	23.42±0.93	61.31±4.87	13.81±1.50
CuPcTB4	1037.0±9.9	19.34±1.21	65.7±1.7	13.16±0.81
CuPcAE	971.4±25.8	21.00±1.23	53.1±3.4	10.83±0.87
CuPcTDZ	760.7±195.4	18.46±2.58	39.1±9.5	5.95±2.82
CuPcTTPA	1030.6±9.2	20.92±0.61	64.0±1.7	13.81±0.77

[a] PSC based on SnO_2 as ETM, the rest are with *b&mp*-TiO_2 as ETM. The data for the ZnPc-based PSCs was obtained from 10 devices, and for CuPc-based PSCs from 6 devices.

Table S6. The PV parameters of device with ZnPcAE and ZnPcTDZ HTM measured under forward and reverse scan direction.

Direction	HTM	V_{oc} (V)	J_{sc} (mA cm^{-2})	FF (%)	PCE (%)
FS	ZnPcAE	0.943	23.83	63.35	14.23
RS	ZnPcAE	0.974	24.35	65.79	15.61
FS	ZnPcTDZ	1.084	21.47	53.28	12.40
RS	ZnPcTDZ	1.076	21.02	58.79	13.30

Table S7. The value n and J_0 calculating from dark *J-V* curves.

HTM	*n*	J_0 (mA cm^{-2})
ZnPcTB4	2.9	5.5×10^{-6}
ZnPcAE	2.3	1.4×10^{-7}
ZnPcTDZ	2.6	2.2×10^{-6}
ZnPcTTPA	2.4	2.4×10^{-6}

Fluorinated- and non-fluorinated-diarylamine-Zn(II) and Cu(II) Phthalocyanines as Symmetrical vs Asymmetrical Hole Selective Materials

Cite this: DOI: 10.1039/d3tc00254c

Adrián Hernández[a†], Naveen Harindu Hemasiri[b†], Samrana Kazim[b,c], Javier Ortiz[a], Shahzada Ahmad[b,c]* and Ángela Sastre-Santos[a]*

Received 20th January 2023,
Accepted 25th March 2023

DOI: 10.1039/d3tc00254c

rsc.li/materials-c

Four symmetrically substituted and four asymmetrically substituted fluorinated and non-fluorinated-diarylamine CuPcs and ZnPcs have been designed and utilized as hole transporting materials in perovskite solar in a planar *n-i-p* structure. We established the correlation between electronic structure, charge mobility parameters, core metal, and substitutions in metal phthalocyanines. The fluorinated asymmetrically substituted undoped ZnPc-6 yielded the best power conversion efficiency of 15.40 % with an open-circuit voltage (V_{oc}) of 1016.1 mV, a short-circuit current density (J_{sc}) of 21.27 mAcm^{-2}, and a fill factor (FF) of 71.25%, followed by the non- fluorinated asymmetrically substituted ZnPc-5 with 14.36 %. In the case of symmetrical CuPcs, the best performance was measured using non-fluorinated CuPc-3 and fluorinated CuPc-4 gave 11.53% and 10.90% of PCEs, respectively. Importantly, the devices with MPcs showed improved stability under multi-stress conditions.

1. Introduction

The preliminary work of perovskite solar cells (PSCs) can be traced back to Miyasaka *et al*, of using perovskite as a dye in dye-sensitized solar cells measuring 3.8% efficiency.[1] Today, the improvement is remarkable with a 25.7% efficiency.[2] This development is due to the unmatched properties of halide perovskites such as a broad absorption spectral range, a long carrier diffusion length, ambipolar charge transport, and solution processability.[3,4,5] These properties, along with ease of fabrication and low cost due to less material usage[6], make PSCs a promising technology on the way to decreasing carbon emissions.

On the other hand, the development of low-cost, efficient, and stable hole transport materials (HTMs) is a prerequisite for the commercialization of PSCs. The HTM provides electron blocking and charge extraction at the perovskite/HTM interface, as well as transporting the hole to the electrode. Furthermore, in an n-i-p configuration, the HTM can increase the stability of the device by protecting the perovskite layer against humidity and oxygen.[7]
2,2′,7,7′-*tetrakis*-(*N*,*N*-di-*p*-methoxyphenylamine)-9,9′-spirobifluorene (Spiro-OMeTAD) is the HTM used par excellence in n-i-p type PSCs, which possesses low hole mobility in its pristine form.[8,9] To improve its electrical properties, the use of dopants and additives such as lithium bis(trifluoromethanesulfonyl)imide (Li-TFSI), cobalt complex, and 4-*tert*-butylpyridine (*t*-BP) have been commonly used. However, doping also accelerates the degradation of the perovskite layers due to the hygroscopic nature of the dopant and additives that decrease the long-term stability of PSCs.[10,11] It is of high research interest to develop dopant-free HTMs that can overcome the limitations of doped HTMs and are UV stable.[12]

a. Área de Química Orgánica, Instituto de Bioingeniería, Universidad Miguel Hernández, Avda. Universidad S/N, 03202, Elche, Spain. Email: asastre@umh.es
b. BCMaterials, Basque Center for Materials, Applications, and Nanostructures, UPV/EHU Science Park, 48940, Leioa, Spain
Email: shahzada.ahmad@bcmaterials.net.
c. IKERBASQUE, Basque Foundation for Science, Bilbao, 48009, Spain
† Equal contribution
Electronic Supplementary Information (ESI) available: See DOI: 10.1039/d3tc00254c

Phthalocyanines are synthetic analogs of porphyrins that stand out for their effective photochemical and electrochemical stability.[13] Metal phthalocyanines (MPcs) have recently been used as HTMs in PSCs.[14,15] Earlier, we reported ZnPc dimers as HTM, which gave good performance and stability without the addition of dopants, owing to their extended electron delocalization and high charge mobility.[16,17,18] On the other hand, the use of various metals, along with different peripheral and nonperipheral substituents, can modify the optical and electrical properties of MPcs and improve their solubility in conventional solvents.[19] Recently, NiPc substituted with four methoxyethoxy groups has been reported and the devices also exhibited good moisture, thermal, and light stabilities.[20]

On the other hand, arylamine groups, particularly triphenylamine (TPA) or diphenylamine (DPA) based compounds, have been extensively utilized as small-molecule HTMs in the PSCs due to their excellent hole-transporting properties, electron-donor ability, high stability, and solubility.[21] Reports on employing these groups as substituents for MPcs as HTMs are scarce and not well exploited. Nazeeruddin and co-workers reported PSCs with PCE of 11.75% using doped DPA-substituted ZnPc.[22] Similarly, a ZnPc having four peripheral TPA substituents in PSCs achieved a PCE of 5.6%.[23] The photovoltaic performance of PSCs fabricated with doped OMe-DPA-CuPc (16.73%) and OMe-TPA-CuPc (19.67%), was compared, featuring four bis-(4-methoxyphenyl)amino substituents and four *N,N*-bis(4-methoxyphenyl)benzenamino substituents, respectively.[24] Zn(II) and Cu(II) Pcs with arylamine groups having different alkoxy chains were compared and PCE of 20.18% for their best-doped MPc was measured.[25] Our group studied arylamine-based substituents in MPcs such as ZnTTPc,[26] ZnPcTTPA, and CuPcTTPA[27] as undoped HTMs in PSCs. Recently, it was found that the presence of fluorine atoms in phthalocyanines can up-shift the energy level of the HOMO and LUMO orbitals, and enhances interfacial charge transfer, this also improves the stability of the device due to the increased hydrophobic character that prevents the entry of moisture.[28] Moreover, efforts to establish a direct relationship between the nature of the metal ion and the phthalocyanine substituents with the electronic properties to optimize photovoltaic devices have not been reported. Moreover, In comparison, asymmetric structures tend to have excellent solubility, and thermal stability and hold potential for application as HTMs. Yet, asymmetric HTMs have been relatively less studied to date compared to their symmetric counterparts.[29]

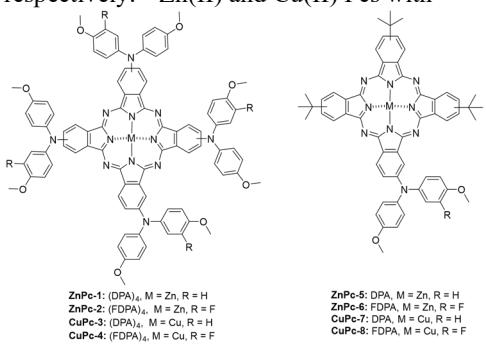

Figure 1. Molecular structure of ZnPc-1, ZnPc-2, CuPc-3, CuPc-4, ZnPc-5, ZnPc-6, CuPc-7, and CuPc-8.

In this work, we designed symmetrical and unsymmetrical substituted phthalocyanines to study the effect of the inclusion of fluorine atoms in the arylamino substituents and the variation of the central metal ion on the conductivity, and hole mobility and their integration as HTM in the PSCs.

Symmetrical phthalocyanines, ZnPc-1, and CuPc-3 have four diphenylamine (DPA), while ZnPc-2, and CuPc 4, consist of four fluorinated diphenylamine (FDPA) substituents respectively. In the case of asymmetric ones, ZnPc-5, and CuPc-7 contain one DPA unit and three *tert*-butyl groups while ZnPc-6, and CuPc-8, are substituted with one fluorinated DPA unit and three *tert*-butyl groups, which have worked well in previous PSC studies. In both families, we have prepared the zinc and copper analogs. (Figure 1).

2. Results and Discussions

Synthesis of MPCs

Phthalonitriles **1** and **2** were synthesized by a high-yield palladium-catalyzed substitution of 4-iodophthalonitrile with the corresponding secondary amine. (Figure 2). Phthalonitriles **1**

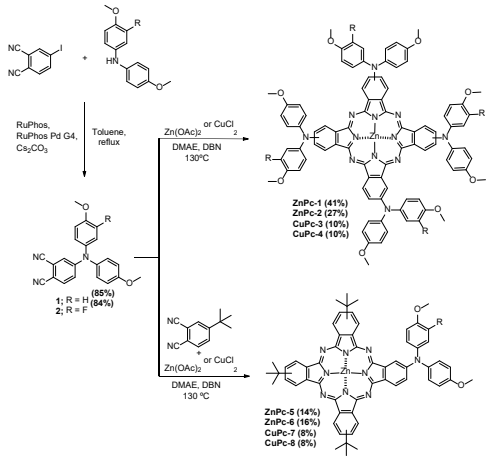

Figure 2. Synthetic route of phthalonitriles and the MPcs.

and **2** were characterized by ^{1}H-NMR and ^{13}C-NMR spectroscopies. Synthesis of symmetrical MPcs was carried out by cyclotetramerization of the corresponding phthalonitrile (**1** or **2**) and $Zn(OAc)_2$ or $CuCl_2$ using DMAE as a solvent and DBN as the catalyst. After purification by silica gel column chromatography, **ZnPc-1**, **ZnPc-2**, **CuPc-3**, and **CuPc-4** were obtained with a yield of 41%, 27%, 10%, and 10%, respectively. For the synthesis of asymmetrical MPcs a statistical cyclotetramerization between 4-*tert*-butylphthalonitrile and the appropriate phthalonitrile (**1** or **2**) and zinc acetate or Cu(II) chloride was performed. After careful purification by silica gel column chromatography, **ZnPc-5**, **ZnPc-6**, **CuPc-7**, and **CuPc-8** were obtained with 14%, 16%, 8%, and 8% yield, respectively. All MPcs were obtained as mixtures of regioisomers. (Figure 2). The yields obtained for copper phthalocyanines are lower because their purification is more difficult, in addition to the fact that copper exerts a worse template effect than zinc in the cyclotetramerization reaction. Asymmetrical MPcs yields are the lowest because all the possible statistical phthalocyanines are formed in the reaction and they must be carefully separated. All the new MPcs are highly soluble in organic solvents such as $CHCl_3$, and THF however they are not soluble in MeOH and hexane. The synthesized MPcs are quite stable and have melting temperatures typically above 300 ºC without decomposition.

The ^{1}H-NMR spectra of ZnPcs in THF-d_8 showed well-defined aromatic and aliphatic signals. **The ZnPc-1** spectrum shows six signals from the isoindole units between 9.2−8.6 and 7.6 ppm; regarding the aromatic chain, we can appreciate two multiplets from the phenyl groups between 7.4−7.0 ppm and a singlet from the methoxy groups at 3.86 ppm. **The ZnPc-2** spectrum is not as well resolved as the other ZnPcs but we can still appreciate the peaks from the isoindole units a little shifted downfield compared with **ZnPc-1**. Furthermore, we observe a new peak at 7.2 ppm due to the loss of symmetry on the phenyl group by the fluorine atom. (Figure 3 and SI). From the **ZnPc-5** spectrum, the three isoindole units with the *tert*-butyl groups show three new signals between 9.5-9.2 and 8.3 ppm, a signal at 1.8 ppm from the *tert*-butyl group, and the peaks from the fourth isoindole unit are shifted downfield compared with **ZnPc-1**. **ZnPc-6** spectrum is equal to the one of **ZnPc-5**, except for the loss of symmetry on the phenyl group by the fluorine atom with a new peak at 7.2 ppm as occurs with **ZnPc-2.** (Figure 3 and SI). Characterization by NMR experiments could not be achieved for CuPcs due to the paramagnetic character of copper (II). Nevertheless, all MPcs were characterized by Fourier transform infrared spectroscopy (FT-IR), high-resolution-matrix-assisted laser desorption ionization time-of-flight mass

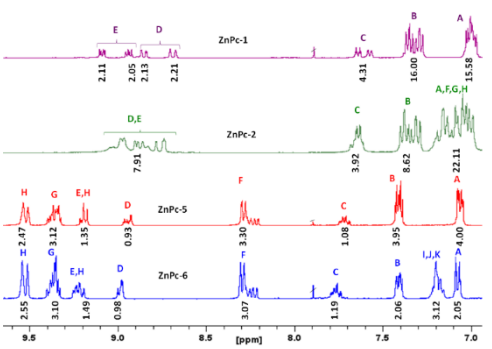

Figure 3. 1H-NMR spectra of ZnPcs in THF-d8.

spectrometry (HR-MALDI-TOF), and UV−vis absorption spectroscopy measurements.

We performed the FT-IR spectra using a KBr pellet (Supporting info). From the different signals of the Pcs, highlight the peaks at 1263, 1256, 1263, and 1258 cm^{-1} of **ZnPc-2**, **ZnPc-6**, **CuPc-4,** and **CuPc-8** respectively, corresponding with the C-F stretching of the fluorine atoms.

Electro-Optical and Physical Properties

The UV-vis absorption spectra measured in DMF solvent show the commonly known Soret and Q bands, from around 350 nm and 600-780 nm, respectively. In addition, we can observe a charge transfer band at 500 nm for the symmetrical MPcs.

The Q bands of the MPcs are shown in Table 1. An increase in the molar extinction coefficient and a small hypsochromic shift are observed in phthalocyanines substituted with fluorinated arylamines. While, in the case of asymmetric Pcs, a large hypsochromic shift and a minor increase in the molar extinction coefficient can be seen as compared to their symmetric counterparts. Furthermore, we noted a decrease in the molar extinction coefficient when the metal ion is changed from Zn(II) to Cu(II) as well as a hypsochromic shift, which is higher in the symmetrical Pcs. (Figures 4a and 4b).

The electrochemical characterization was performed by cyclic voltammetry in dry DMF solvent and ferrocene was used as an external standard. The highest occupied molecular orbital energy levels (E_{HOMO}) were calculated from the equation: $E_{HOMO} = -4.8 - E_{Ox1}$, where E_{Ox1} is the first oxidation potential. The LUMO energy level (E_{LUMO}) was calculated by adding the optical band gap to the E_{HOMO} value. CuPcs showed lower E_{HOMO} levels compared to ZnPcs. A similar effect can be observed in the asymmetrically substituted Pcs, and with the addition of fluorine atoms to the Pcs. Symmetrical Pcs presented a smaller band gap. Nevertheless, they showed adequate E_{HOMO} energy values for hole extraction from the perovskite.

In a similar fashion E_{LUMO} energy is appropriate to prevent the flow of the photogenerated electron and will avoid recombination at the perovskite-HTM interface.

In the absorbance spectra of the phthalocyanines deposited as a thin film, a general broadening of the bands and the splitting of the Q-band can be appreciated, phenomena attributable to the formation of aggregates. The shorter wavelength peak is due to aggregate species and face-to-face stacking of the molecules, while the peak at longer wavelengths is due to monomeric species. This phenomenon can be noted in the case of the phthalocyanines **CuPc-4**, **ZnPc-5**, and **ZnPc-6** (Figure 5a). In the perovskite/HTM absorption spectra deposited as a thin film, the contribution of the phthalocyanines to the absorption is observed, as expected, at wavelengths between 700 and 800 nm (Figure 5b).

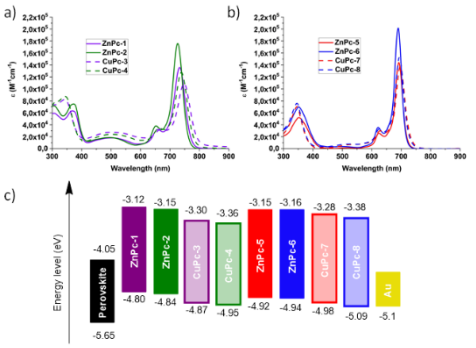

Figure 4. UV-vis absorption spectra of MPcs in solution, a) symmetric MPcs, b) asymmetric MPcs, and c) energy level diagram for the MPcs.

Table 1. Electro-Optical properties of the different MPcs.

MPc	Q band	$E_{g\ optical}$	E_{Ox1}	E_{Ox2}	E_{HOMO}	E_{LUMO}
ZnPc-1	733	1.68	0.00	0.33	-4.80	-3.12
ZnPc-2	726	1.69	0.04	0.40	-4.84	-3.15
CuPc-3	749	1.57	0.07	0.49	-4.87	-3.30
CuPc-4	740	1.59	0.15	0.56	-4.95	-3.36
ZnPc-5	692	1.77	0.12	0.48	-4.92	-3.15
ZnPc-6	690	1.78	0.14	0.56	-4.94	-3.16
CuPc-7	697	1.70	0.18	0.51	-4.98	-3.28
CuPc-8	694	1.71	0.29	0.61	-5.09	-3.38

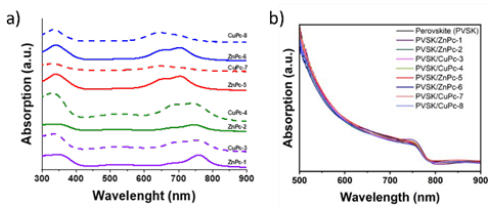

Figure 5. UV-vis absorption spectra in thin films of a) MPcs, b) perovskite with MPcs.

Photovoltaic performance of PSCs with MPcs as HTMs

PSCs were fabricated with a planar *n-i-p* structure of fluorine-doped tin oxide (FTO)/bl-TiO_2/SnO_2/perovskite/MPc/Au using different MPcs as HTM to investigate the effect of core metal and different substitutions on their photovoltaic performance (Figure 6a). Owing to the superior optical absorption and higher stability, a triple-cation perovskite, with the chemical formula of $Cs_{0.1}(FA_{0.9}MA_{0.1})_{0.9}Pb(I_{0.9}Br_{0.1})_3$ was deposited by antisolvent-assisted one step method.[30] The concentration of each HTM was maintained at 10 mM for device fabrication. All layers in the device were deposited by the solution process except the gold anode, which is thermally evaporated. The current density-voltage (*J-V*) curves measured under the reverse scan of the PSCs based on symmetric (Figure 6b) and asymmetric (Figure 6c) MPcs are presented. The corresponding photovoltaic parameters derived from the graph are summarized in Table 2.

The reference device using undoped PTAA as HTM gave a PCE of 15.53% (Figure S44). Notably, among all the MPc-HTMs investigated here, the best PV performances were measured from Zn-based asymmetric Pcs, which are on par with the PTAA-based devices. In particular, the **ZnPc-6** HTM yielded the maximum PCE of 15.40 % with an open-circuit voltage (V_{oc}) of 1016.11 mV, a short-circuit current density (J_{sc}) of 21.27 $mAcm^{-2}$, and a fill factor (FF) of 71.25%, followed by **ZnPc-5** with 14.36% PCE. To note here, the measured FF from these fluorinated substituted asymmetrical Pcs is highest compared to other Pcs. Similarly, from the symmetrical Pc category, ZnPc-2 gave a PCE of 12.66 % with a V_{oc} of 930.72 mV, 20.58 J_{sc} of 20.6 mA/cm^2, and a FF of 66.06%. Different from the case of Cu-based Pc HTMs, the best efficiencies were noted from the symmetrical Pcs, in which CuPc-3 and CuPc-4 gave 11.53% and 10.90% of PCEs, respectively. A similar trend can be found from the statistical distribution of the PCE of different MPc-HTM (Figure 6d and Table S1). Moreover, the measured J_{sc} from the *J-V* curve decreases when the coordination metal Zn(II) is switched out for Cu(II). In general, the deeper HOMO state of the HTM relative to the perovskite's valence band maximum (VBM) (-5.7 eV) would enable a rational energy alignment, this in turn will facilitate charge extraction, subsequently, the smaller the energy barrier between the perovskite and the HTL, the lower the recombination, and minimum voltage (V_{oc}) deficit will be.[31,32] This behavior can be deduced from ZnPcs, where the deeper LUMO level associated with ZnPc-5 and ZnPc-6 close to the VBM of the triple-cation perovskite facilitate a higher V_{oc} when compared with shallow HOMO level associated with ZnPc-1 and ZnPc-2. However, the V_{oc} variation cannot be correlated to the HOMO state position of the Cu-based Pc series. This is per similar behavior of V_{oc} variation from Zn and Cu-based MPcs irrespective of their HOMO state position.[33] Arguably, our finding suggests that the PCE not only depends on the symmetrical nature of the side chain of the MPc but also the metal

Table 2. Performance summary of devices with different MPcs as HTMs.

HTM	Scan	V_{OC} (mV)	J_{sc} ($mAcm^{-2}$)	FF (%)	PCE (%)	R_s (Ω)	R_{sh} (kΩ)
ZnPc-1	RS	954.9	19.48	55.57	10.34	136.89	7.9
	FS	871.4	19.29	30.37	5.11	240.89	0.6
ZnPc-2	RS	930.7	20.58	66.06	12.66	72.10	15.5
	FS	932.2	20.48	61.36	11.71	100.42	12.0
CuPc-3	RS	953.5	19.08	63.35	11.53	109.29	17.6
	FS	946.4	19.12	47.52	8.59	141.87	1.1
CuPc-4	RS	935.5	16.54	70.46	10.90	55.18	9.7
	FS	917.4	16.49	61.35	9.28	127.73	2.8
ZnPc-5	RS	1000.9	20.33	70.59	14.36	57.93	20.7
	FS	999.6	20.21	67.15	13.57	72.79	19.7
ZnPc-6	RS	1016.1	21.27	71.25	15.40	53.50	24.0
	FS	1013.3	21.18	68.77	14.76	63.43	20.1
CuPc-7	RS	884.9	15.49	55.82	7.65	122.75	4.1
	FS	848.9	14.69	39.59	4.94	190.09	0.3
CuPc-8	RS	982.8	16.96	58.17	9.69	124.34	6.7
	FS	955.3	16.28	57.48	8.94	129.19	3.2
PTAA	RS	1031.7	20.55	73.28	15.53	52.15	17.3
	FS	1023.0	20.47	73.90	15.48	53.60	10.0

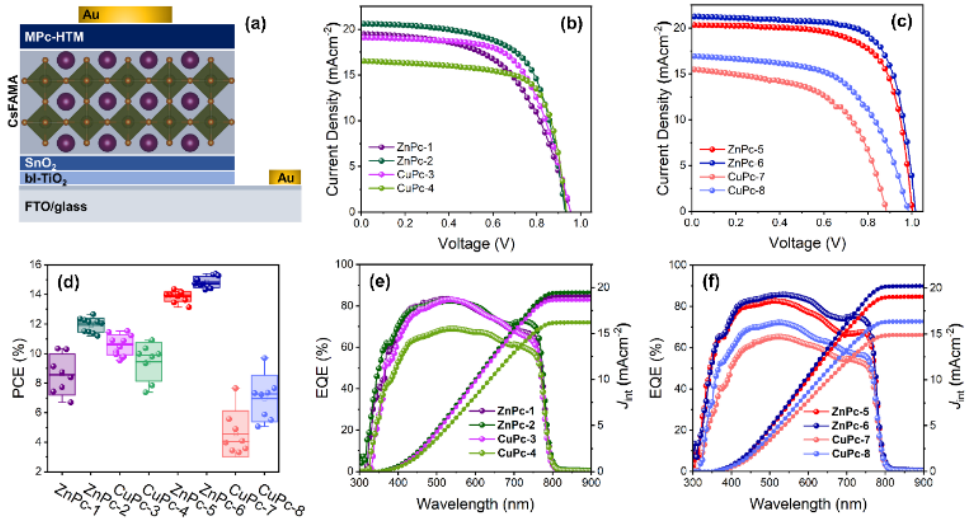

Figure 6. Proposed device architecture: fluorine-doped tin oxide (FTO)/bl-TiO2/SnO2/perovskite/MPc/Au (a), J-V curves of the device using (b) symmetric MPcs and (c) asymmetric MPcs, (d) statistical PCE of PSCs with different MPc-HTMs, corresponding IPCE and integrated current density (Jint) of the device with (e) symmetric MPcs and, (f) asymmetric MPcs.

species attached to it.

All MPc-HTMs exhibit a significant reduction in EQE at wavelengths over 600 nm, which is following the strong absorption band of MPcs in the range of 600-800 nm. The amount of current produced by the second pass of reflected light from the gold electrode can be dramatically reduced by this absorption corresponding to MPcs. Although all MPcs have B-band absorption in a lower wavelength region below 400nm, the aforementioned effect cannot be seen for high-energy photons since the perovskite layer has a higher absorption coefficient at a shorter wavelength.

The reverse and forward scan *J-V* profiles were recorded to uncover the hysteresis behavior of each MPc-HTM (Figure S45 and S46) and the hysteresis indices (HIs) are summarized in Table S1. We noted reduced hysteresis from the PSCs incorporating ZnPc-5 and ZnPc-6, though the high efficiencies were noted from ZnPc-2 and CuPc-3 in the symmetric MPc group they also feature considerable hysteresis. Table 2 summarized the series resistance (R_s) and shunt resistance (R_{sh}), which were extracted from the slop at V_{oc} and J_{sc}, respectively from the corresponding *J-V* curve. The device made with the ZnPc-5 and ZnPc-6 exhibit a lower R_s and a higher R_{sh}, both of which boost the FF and V_{oc} of the PSC by reducing interfacial charge losses and non-radiative charge recombination in the device.[30] Additionally, the stabilized J_{sc} (Figure 7a) was measured for the initial 300 s for PSCs with ZnPc-2, CuPc-3, ZnPc-5, and ZnPc-6 as HTM at their maximum power point (MPP) under ambient conditions (40-60% at 28 °C), which is in agreement with the J_{sc} measured from their *J-V* curves. Overall, the best PV performances were observed from ZnPc-6 > ZnPc-5 > ZnPc-2. We also studied the potential of these MPcs as HTL in inverted (*p-i-n*) PSC with an architect of FTO/MPc/perovskite/$PC_{60}BM$/BCP/Ag. The p-i-n device based on ZnPc-2 as HTL measured a PCE of 9.06 % owing to the V_{oc} of 901.87 mV, J_{sc} of 16.85 $mAcm^{-2}$, and FF of 59.59% followed by ZnPc-6 with a 5.53% of PCE (Figure S50 and Table S2). However, the ZnPc-5 in the p-i-n configuration yielded only a mere PCE of 3.88 %. The observed low J_{sc} values from *p-i-n* devices could be attributed to

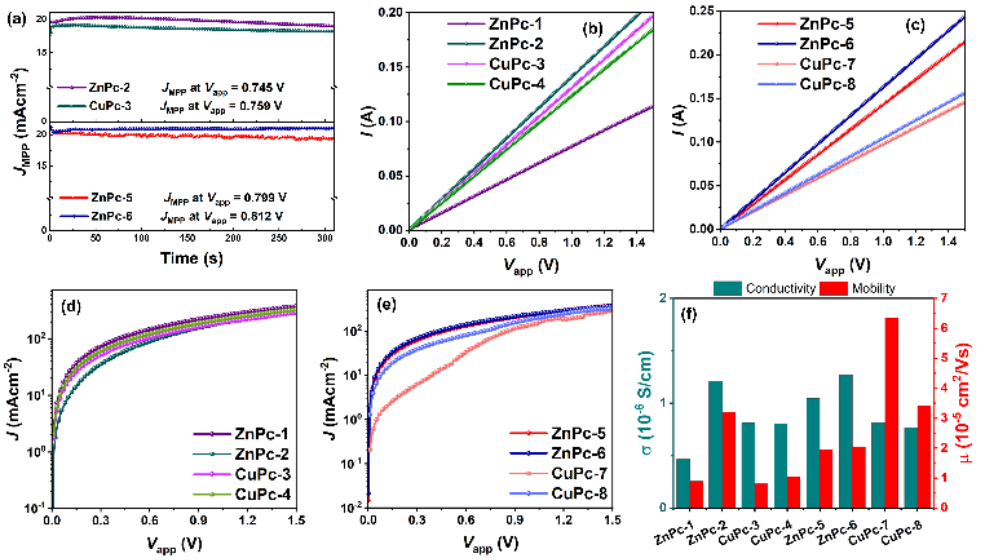

Figure 7. (a) Steady-state photocurrent density for the continuous illumination at the maximum power point (MPP) for the devices in symmetric and asymmetric MPcs as HTL, I-V curves for the conductivity measurement in the configuration of FTO/MPc/Ag for (b) symmetric MPcs and, (c) asymmetric MPcs, J-V curves for the hole mobility measurements in the configuration of FTO/PEDOT: PSS/MPc/Ag for (d) symmetric MPcs, and (e) asymmetric MPcs and (f) conductivity and mobility of each MPc summary.

the higher optical absorption in the whole visible range of these MPCs before the light reaching to the active perovskite layer, hindering the generation of photo-charges in the perovskite layer.

The charge transport abilities of each MPc were investigated by measuring their conductivity and mobility values. The electrical conductivity (σ) was extracted from the *I-V* (current-voltage) curve (Figure 7b, c) of the device with the configuration of FTO/MPc/Ag along with the relation, σ=(I/VA)d, where d is the thickness of the HTM (avg. thickness of each MPc from the cross-sectional image of the hole-only device as shown in Figure S51) and A is the active area of the devices.[34] The space-charge-limited-current (SCLC) measurements were performed to evaluate the hole mobility (μ) of MPcs from semi-logarithmic $J_{0.5}$-V curves (Figure 7d, e) of the hole-only device (FTO/PEDOT: PSS/MPc/Ag) along with the Mott-Gurney equation.[35]

$$J = 9\varepsilon\varepsilon_0\mu V_{app}^2/8L^3$$

The obtained values are summarized in Table S3. The highest conductivity was noted for symmetric ZnPc-6 with 1.268 × 10^{-6} S/cm, which also exhibited the best PCE of PSCs. This was followed by ZnPc-2 with a conductivity value of 1.21 × 10^{-6} S/cm followed by ZnPc-5 with 1.05 × 10^{-6} S/cm, however, their PCE values are not correlated. Even though CuPc-7 and CuPc-8 show the highest mobility, they featured the lowest PCE. It is interesting to note that the conductivity and mobility values obtained from MPcs do not follow a similar trend of PCEs, suggesting that there is another reason apart from the symmetrical nature and the coordination metal in the MPc influences the PV performances. The lower values obtained in our synthetized MPcs compared with the already published diphenylamino substituted metallophthalocyanines[36] could be attributed the the effect of the alkoxy side chains influenced the molecular packing in the solid state of the HTMs, in a way that determined their ability to conduct charges and in the interaction with the perovskite layer.

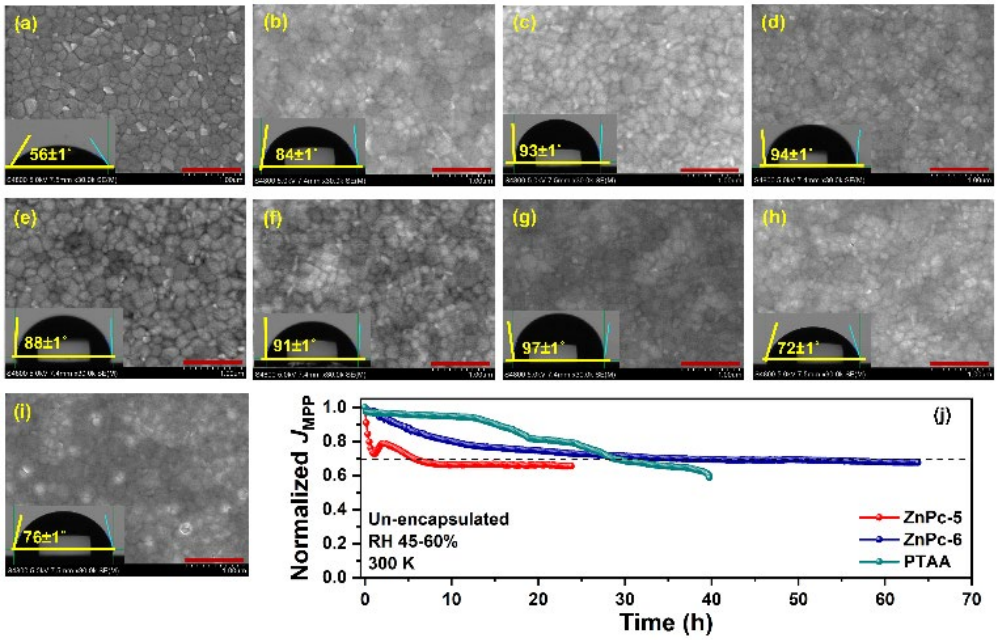

Figure 8. Surface SEM image of (a) perovskite, (b) ZnPc-1, (c) ZnPc-2, (d) CuPc-3, (e) CuPc-4, (f) ZnPc-5, (g) ZnPc-6, (h) CuPc-7, and (i) CuPc-8 deposited on perovskite. Inset: corresponding water contact angle. The red lines represent the 1 µm scale bar, and (j) the normalized current density of continuous maximum power point (MPP) tracking for unencapsulated PSCs based on ZnPc-5, ZnPc-6, and pristine PTAA as HTMs under atmospheric conditions (RH 45-65 %, 300 K).

To further understand photo-induced charge recombination in PSCs, we performed electrochemical impedance spectroscopy (EIS) under dark conditions for the PSCs with both symmetrical (ZnPc-2 and CuPc-3) and asymmetrical (ZnPc-5 and ZnPc-6) categories. The Nyquist plot (Figure S52) at different bias voltages from 0.85 − 1.05 V, is fitted with the equivalent circuit of R_s+R_{rec}/CPE (dots and continuous lines represent raw and fitted curves, respectively), where R_s is the series resistance coming from the external circuit and R_{rec} is the recombination resistance of the PSC. A constant phase element related to carrier diffusion in selective layers and perovskite is assigned as CPE. At a given potential bias, the ZnPc-6-based PSC features a much higher R_{rec} (Figure S53), indicating that ZnPc-6 leads to lower charge recombination and mitigated charge annihilation at the perovskite/HTL interface, which is consistent with the observed reduced V_{oc} losses in the PSC based on ZnPc-6.

The film-forming ability of any HTM is an important criterion to produce high-performance PSCs apart from the band alignment of the transport layer with the perovskite and their charge transportability. It is well known that non-covalent interactions between two or more phthalocyanine (Pcs) molecules cause their derivatives to aggregate, leading to their low solubility in the majority of solvents.[37,38] We observed that Cu-based Pcs give poor solubility and make clusters with time in chlorobenzene, a solvent used for device fabrication. Thus, the likely cause of the PV underperformance seen in some MPcs could be attributed to a lesser degree of solubility and the molecular accumulation that prevent the efficient energetic coupling and introduce recombination centers, thus responsible for the lower PCE measured for PSCs. The film-forming ability and the uniformity of MPcs on the perovskite were examined using scanning electron microscopy (SEM) and the surface image (Figure 8a-i) and the corresponding water contact angle of different HTMs deposited on the perovskite layer are

presented. The best performance featured from the ZnPc-6 is ascribed to their uniform film-forming ability on the perovskite without any visible defects and pinholes, and this is further supported by a maximum water contact angle of 97±1º. Further, ZnPc-5, CuPc-3, and ZnPc-2 show uniform film coverage on the perovskite with the water contact angles of 91±1º, 94±1º, and 93±1º, respectively. Different from this, an inhomogeneous surface with pinholes and aggregated molecular clusters could be observed from CuPc-7 and CuPc-8 samples, which also results in a lower water contact angle owing to the higher wettability of the defective surfaces. Even though, CuPc-7 and CuPc-8 produce significantly higher mobility, their reduced homogeneity on the perovskite layer induces a possible shunting pathway as indicated by their lower shunt resistance value and non-radiative charge recombination at the perovskite/HTM interface. This might be the plausible reason for the low PV performance noted from PSCs based on these two MPcs.

We also studied the long-term operational stability of the un-capsulated devices (ZnPc-5 and ZnPc-6) from the MPc series with reference PTAA device at their maximum power point (MPP) under ambient conditions (relative humidity of 45-60% and 300 K) under white LED light (Figure 8j). While the PSCs based on ZnPc-5 showed stabilized current density just below 70% of its initial value after rapid performance degradation at the early stage of the experiment, ZnPc-6 performed better and showed a nearly linear response, holding around 70% of its initial current density for around 60 h. Particularly, the reference device based on pristine PTAA featured 70% of its original performance up to 30 h and speedy performance lost thereafter.

3. Experimental

Synthesis of phthalocyanines

All chemicals and solvents were purchased from Sigma Aldrich (Merck) and TCI and were used without further purification unless otherwise stated.

Lead Iodide (PbI_2, 99.9%) was procured from Tokyo Chemical Industry (TCI). Other chemicals for perovskite were purchased from Greatcell Solar and employed without further purification. PTAA (M_n = 5000-15000 by GPC) was obtained from Xi'an Polymer Light Technology Corp. [60]PCBM >99.5 % and Bathocuproine (BCP) were purchased from Solenne BV and TCI, respectively. Tin (IV) oxide, 15% in H_2O colloidal dispersion was obtained from Alfa Aesar. Chlorobenzene (CB, 99 %), isopropanol (IPA, 99.9 %), ethanol (EtOH, 99 %), anhydrous dimethyl sulfoxide (DMSO, 99.8 %), and *N, N*-dimethylformamide (DMF, 99.8 %) were purchased from Acros Organics.

NMR spectra were recorded on a BRUKER AVANCE NEO 400 spectrometer. UV-vis were recorded with a Perkin Elmer Lambda 365 spectrophotometer. Fluorescence spectra were recorded with a HORIBA scientific SAS spectrophotometer. High-resolution mass spectra were obtained from a Bruker Microflex LRF20 matrix-assisted laser desorption/ionization-time of flight (MALDI-TOF) using dithranol as a matrix. IR spectra were recorded with Nicolet Impact 400D spectrophotometer. Cyclic voltammetry was measured in a conventional three-electrode cell using a μ-AUTOLAB type III potentiostat/galvanostat at 298 K over DMF and deaerated sample solutions containing 0.10 M tetrabutylammonium hexafluorophosphate ($TBAPF_6$) as supporting electrolyte. Platinum as the working electrode, $Ag/AgNO_3$ (0.01 M in benzonitrile) as the reference electrode, and platinum as the wire counter electrode was employed. Ferrocene/Ferrocenium redox couple was used as an internal standard for all measurements.

Synthesis of phthalonitrile 1: 200 mg (0.79 mmol) of 4-iodophthalonitrile, 270.8 mg (1.18 mmol) of 4,4'-dimethoxydiphenylamine, 33.8 mg (0.04 mmol) of RuPhos Pd G4, 18.6 mg (0.04 mmol) of RuPhos and 518.2 mg (1.59 mmol) of Cs_2CO_3 were dissolved in 10 mL of deaerated toluene and heated to reflux in argon atmosphere for 24 hours. After cooling down to room temperature, H_2O was added to the

crude product and it was extracted with DCM two times, dried with Na_2SO_4, filtered, and concentrated. It was purified by column chromatography (Hexane:AcOEt/8:2) obtaining 238 mg (85%) as a yellow powder. ^{1}H-NMR (400 MHz, $CDCl_3$): δ = 3.83 (s, 6H), 6.91 - 6.94 (m, 5H), 7.00 -7.01 (d, *J* = 2.5 Hz, 1H), 7.09 - 7.13 (m, 4H), 7.41 - 7.43 (d, *J* = 8.9 Hz, 1H). ^{13}C-NMR (100 MHz, $CDCl_3$): δ = 55.7, 102.7, 115.7, 116.0, 116.7, 116.8, 119.2, 120.2, 128.2, 134.4, 137.1, 152.3, 158.3.

Synthesis of phthalonitrile 2: 200 mg (0.79 mmol) of 4-iodophthalonitrile, 292 mg (1.18 mmol) of 3-Fluoro-4-methoxy-*N*-(4-methoxyphenyl)aniline, 33.8 mg (0.04 mmol) of RuPhos Pd G4, 18.6 mg (0.04 mmol) of RuPhos and 518.2 mg (1.59 mmol) of Cs_2CO_3 were dissolved in 10 mL of deaerated toluene and heated to reflux in argon atmosphere for 24 hours. After cooling to room temperature, water was added and it was extracted two times with DCM, dried with Na_2SO_4, filtered, and concentrated under a vacuum. After purification by column chromatography (Hexane:AcOEt/75:25), 247 mg (84%) of **2** were obtained as a yellow powder. ^{1}H-NMR (400 MHz, $CDCl_3$): δ =3.83 (s, 3H), 3.91 (s, 3H), 6.90 - 6.95 (m, 6H), 7.04 (d, *J* = 2.5 Hz, 1H), 7.08 - 7.11 (d, *J* = 8.9 Hz, 2H), 7.44 - 7.46 (d, *J* = 8.8 Hz, 1H). ^{13}C-NMR (100 MHz, $CDCl_3$): δ = 55.7, 56.7, 103.6, 114.5, 114.6, 115.0, 115.2, 115.9, 115.9, 116.6, 117.0, 119.8, 120.8, 122.5, 122.5, 128.3, 134.5, 136.8, 137.3, 137.4, 146.6, 146.7, 151.7, 152.0, 154.2, 158.6.

Synthesis of ZnPc-1: 35 mg (0.10 mmol) of **1** and 9 mg (0.05 mmol) of $Zn(OAc)_2$ in 200 µL of DMAE and one drop of DBN under an inert atmosphere were stirred at 130ºC for 16 hours. The purple mixture was cooled at room temperature, concentrated under vacuum, and purified by column chromatography (Hx:Dioxane/55:45) yielding 15 mg of **ZnPc-1** (43%) as a purple solid. ^{1}H-NMR (400 MHz, THF-*d*$_8$): (mixture of regioisomers), δ = 3.86 (d, *J* = 6.5 Hz, 24H), 7.03-6.97 (m, 16H), 7.37-7.28 (m, 16H), 7.60 – 7.54 (dd, *J* = 8.5, 1.8 Hz, 2H), 7.67 – 7.62 (dt, *J* = 8.4, 2.2 H, 2H), 8.70-8.67 (d, *J* = 12.5 Hz, 2H), 8.87-8.84 (dd, *J* = 11.0, 2.1 Hz 2H), 8.96-8.92 (dd, *J* = 8.4, 5.3 Hz, 2H), 9.10-9.07 (dd, *J* = 8.4, 3.4 Hz, 2H). HR-MALDI-TOF (dithranol): *m/z* for $C_{88}H_{68}N_{12}O_8Zn$: calcd. 1484.4569 [M^+]; found, 1484.4632. UV-vis (DMF) λ_{max}/nm (log ε): 371 (4.77), 511 (4.14), 659 (4.47), 733 (5.13). FT-IR: ν_{max}/cm^{-1}: 3038, 2995, 2950, 2907, 2833, 1604, 1507, 1487, 1440, 1396, 1332, 1272, 1242, 1180, 1089, 1036, 883, 826, 756, 667, 585, 524, 434. Mp> 300 ºC.

Synthesis of ZnPc-2: 50 mg (0.13 mmol) of **2** and 12.28 mg (0.07 mmol) of $Zn(OAc)_2$ in 500 µL of DMAE and one drop of DBN under an inert atmosphere were stirred at 130ºC for 16 hours. The purple mixture was cooled at room temperature, concentrated under vacuum, and purified by column chromatography (Hx:Dioxane/55:45) yielding 14 mg of **ZnPc-2** (27%) as a purple solid. ^{1}H-NMR (400 MHz, THF-*d*$_8$): (mixture of regioisomers), δ = 3.86 (s, 12H), 3.92 (s, 12H), 7.40-6.9 (m, 32H), 7.65-7.62 (m, 4H), 9.05-8.74 (m, 8H). HR-MALDI-TOF (dithranol): *m/z* for $C_{88}H_{64}F_4N_{12}O_8Zn$: calcd. 1556.4192 [$M^+$]; found, 1556.4285. UV-vis (DMF) λ_{max}/nm (log ε): 372 (4.87), 495 (4.24), 653 (4.58), 726 (5.25). FT-IR: ν_{max}/cm^{-1}: 3058, 2999, 2952, 2908, 2835, 1606, 1507, 1488, 1398, 1333, 1263, 1243, 1181, 1089, 1032, 985, 828, 756, 664, 629, 584, 523, 437. Mp> 300 ºC.

Synthesis of CuPc-3¡Error! Marcador no definido.**:** 200 mg (0.56 mmol) of **1** and 38 mg (0.28 mmol) of $CuCl_2$ in 500 µL of DMAE and one drop of DBN under an inert atmosphere were stirred at 130ºC for 16 hours. The purple mixture was cooled at room temperature, concentrated under vacuum, and purified by column chromatography (Hx:Dioxane/55:45) and washed with MeOH, yielding 20 mg of CuPc-3 (10%) as a purple solid. HR-MALDI-TOF (dithranol): *m/z* for $C_{88}H_{68}CuN_{12}O_8$: calcd. 1483.4573 [M^+]; found, 1483.4652. UV-vis (DMF) λ_{max}/nm (log ε): 343 (4.88), 501 (4.35), 671 (4.49), 749 (5.02). FT-IR: ν_{max}/cm^{-}

[1]: 3059, 2995, 2929, 2832, 1605, 1506, 1404, 1338, 1272, 1241, 1179, 1094, 1035, 892, 826, 758, 589, 525, 424. Mp> 300 ºC.

Synthesis of CuPc-4: 100 mg (0.27 mmol) of **2** and 18 mg (0.13 mmol) of $CuCl_2$ in 500 µL of DMAE and one drop of DBN under an inert atmosphere were stirred at 130ºC for 16 hours. The purple mixture was cooled at room temperature, concentrated under vacuum, and purified by column chromatography ($CHCl_3$:MeOH/99:1) and washed with MeOH, yielding 10 mg of CuPc-4 (10%) as a purple solid. HR-MALDI-TOF (dithranol): *m/z* for $C_{88}H_{64}CuF_4N_{12}O_8$: calcd. 1555.4197 [$M^+$]; found, 1555.4241. UV-vis (DMF) λ_{max}/nm (log ε): 346 (4.92), 498 (4.36), 666 (4.52), 740 (5.10). FT-IR: ν_{max}/cm^{-1}: 3059, 2998, 2932, 2834, 1607, 1506, 1404, 1339, 1263, 1243, 1181, 1093, 1032, 826, 758, 629, 524, 436. Mp> 300 ºC.

Synthesis of ZnPc-5: 90 mg (0.25 mmol) of **1** 186.63 mg (1.01mmol) of 4-*tert*-butylphthalonitrile and 92.92 mg (0.51 mmol) of $Zn(OAc)_2$ in 750 µL of DMAE and two drops of DBN under inert atmosphere were stirred at 130ºC for 16 hours. The blue mixture was cooled at room temperature, concentrated under vacuum, and purified by column chromatography (Hx:Dioxane/75:25) yielding 34 mg of **ZnPc-5** (14%) as a blue solid. ^{1}H-NMR (400 MHz, THF-*d*$_8$): (mixture of regioisomers), δ = 1.80-1.77 (m, 27H) 3.89 (s, 6H), 7.08-7.04 (m, 4H), 7.43-7.39 (m, 4H), 7.73-7.71 (m, 1H), 8.30-8.20 (m, 3H), 8.96-8.92 (m, 1H), 9.21-9.27 (m, 1.5H), 9.40-9.32 (m, 3H), 9.54-9.50 (m, 2.5H). HR-MALDI-TOF (dithranol): *m/z* for $C_{58}H_{53}N_9O_2Zn$: calcd. 971.3608 [M^+]; found, 971.3896. UV-vis (DMF) λ_{max}/nm (log ε): 353 (4.71), 624 (4.41), 692 (5.14). FT-IR: ν_{max}/cm^{-1}: 3066, 2955, 2903, 2865, 2834, 1610, 1506, 1489, 1441, 1393, 1329, 1281, 1242, 1181, 1090, 1047, 922, 889, 829, 747, 693, 603, 576, 527, 445. Mp> 300 ºC.

Synthesis of ZnPc-6: 90 mg (0.24 mmol) of **2** 137.67 mg (0.75 mmol) of 4-*tert*-butylphthalonitrile and 88.45 mg (0.48 mmol) of $Zn(OAc)_2$ in 750 µL of DMAE and two drops of DBN under inert atmosphere were stirred at 130ºC for 16 hours. The blue mixture was cooled at room temperature, concentrated under vacuum, and purified by column chromatography (Hx:Dioxane/75:25) yielding 38 mg of ZnPc-6 (16%) as a blue solid. ^{1}H-NMR (400 MHz, THF-*d*$_8$): (mixture of regioisomers), δ = 1.80-1.77 (m, 27H) 3.89 (br, 3H), 3.95 (br, 3H), 7.09-7.06 (m, 2H), 7.20-7.17 (m, 3H), 7.43-7.39 (m, 2H), 7.79-7.74 (m, 1H), 8.31-8.21 (m, 3H), 9.00-9.87 (m, 1H), 9.25-9.19 (m, 1.5H), 9.40-9.33 (m, 3H), 9.55-9.51 (m, 2.5H). HR-MALDI-TOF (dithranol): *m/z* for $C_{58}H_{52}FN_9O_2Zn$: calcd. 989.3514 [M^+]; found, 989.3613. UV-vis (DMF) λ_{max}/nm (log ε): 352 (4.90), 622 (4.60), 690(5.35). FT-IR: ν_{max}/cm^{-1}: 3069, 2955, 2904, 2865, 1608, 1506, 1489, 1441, 1392, 1330, 1282, 1256, 1243, 1181, 1090, 1047, 921, 894, 828, 746, 692, 604, 526, 444. Mp> 300 ºC.

Synthesis of CuPc-7: 100 mg (0.28 mmol) of **1,** 181.44 mg (0.99 mmol) of 4-*tert*-butylphthalonitrile and 75.66 mg (0.56 mmol) of $CuCl_2$ in 750 µL of DMAE and one drop of DBN under inert atmosphere were stirred at 130ºC for 16 hours. The blue mixture was cooled at room temperature, concentrated under vacuum, and purified by column chromatography ($CHCl_3$:THF/99.5:0.5) and washed with MeOH, yielding 21 mg of CuPc-7 (8%) as a blue solid. HR-MALDI-TOF (dithranol): *m/z* for $C_{58}H_{53}CuN_9O_2$: calcd. 970.3613 [M^+]; found, 970.3705. UV-vis (DMF) λ_{max}/nm (log ε): 345 (4.86), 628 (4.49), 697 (5.14). FT-IR: ν_{max}/cm^{-1}: 3060, 2954, 2902, 2833, 1614, 1506, 1406, 1325, 1282, 1241, 1181, 1092, 1038, 930, 827, 749, 671, 575, 530. Mp> 300 ºC.

Synthesis of CuPc-8: 100 mg (0.27 mmol) of **2,** 173 mg (0.94 mmol) of 4-*tert*-butylphthalonitrile and 72 mg (0.54 mmol) of $CuCl_2$ in 750 µL of DMAE and one drop of

DBN under inert atmosphere were stirred at 130ºC for 16 hours. The blue mixture was cooled at room temperature, concentrated under vacuum and purified by column chromatography ($CHCl_3$:MeOH/99.5:0.5), and washed with MeOH, yielding 22 mg of CuPc-8 (8%) as a blue solid. HR-MALDI-TOF (dithranol): *m/z* for $C_{58}H_{52}CuFN_9O_2$: calcd. 988.3519 [M^+]; found, 988.3596. UV-vis (DMF) λ_{max}/nm (log ε): 346 (4.89), 626 (4.52), 694 (5.19). FT-IR: ν_{max}/cm^{-1}: 3068, 2956, 2903, 2866, 1611, 1507, 1407, 1326, 1258, 1243, 1153, 1092, 1034, 930, 829, 749, 694, 530, 435. Mp> 300 ºC.

Device fabrication

n-i-p device: Following successive sonication with Hellmanex II (2 vol.% in deionized water), deionized water, ethanol, acetone, and isopropanol, the laser-etched FTO-coated glass substrates (TEC15) were dried using compressed airflow. Before usage, the substrates underwent further treatment with UV-ozone for 30 minutes. Spray pyrolysis at 500 °C with 1/19 mL of titanium (IV) diisopropoxide bis(acetylacetonate) precursor solution (75% in 2-propanol) in pure ethanol was used to produce a compact TiO_2 blocking layer onto FTO substrates. The electron transport layer (ETL) was fabricated using colloidal SnO_2 2.67% water solution via spin coating at 5000 rpm for 30 s, followed by annealing at 180 °C for 1 h in air. Once cooled down to room temperature the samples were transferred to the Argon-filled glovebox (H_2O level: <1 ppm and O_2 level: <10 ppm). $Cs_{0.1}(FA_{0.9}MA_{0.1})_{0.9}Pb(I_{0.9}Br_{0.1})_3$ perovskite precursor solution was prepared according to the previous report.[29] The perovskite precursor solution was spin-coated on the as-prepared SnO_2 ETL in an antisolvent-assisted two-step spin-coating program set at 1000 rpm and 6000 rpm for 10 and 30 s followed by annealing at 100 ºC for 1 h to induce perovskite crystallization. 10 mM of each MPc-HTM in chlorobenzene was spin-coated on perovskite at 4000 rpm for 20 s at room temperature. Pristine PTAA (10 mg/ml in toluene) was spin-coated at 3000 rpm for 35 s to construct the reference device. ~ 70 nm gold electrode was evaporated (<1 Å/s) by thermal evaporation under low vacuum conditions below 10^{-6} Torr as a final electrode.

p-i-n device: The device was fabricated according to the previous report with modification noted herein.[39] 2 mM of each MPc-HTM in chlorobenzene was spin-coated atop the cleaned FTO substrates at 3000 rpm for 30 s. $Cs_{0.1}(FA_{0.9}MA_{0.1})_{0.9}Pb(I_{0.9}Br_{0.1})_3$ perovskite film was achieved as described previously. The PCBM solution of 15 mg/ml in chlorobenzene was spin-coated at room temperature on perovskite film at 1000 rpm (500 rpm/s) for 20 s followed by annealing at 90 °C for 10 min. A thin layer of BCP (0.5 mg/mL in IPA) was deposited atop PCBM by spin coating at 5000 rpm for 40 s. The device fabrication was completed by evaporating Ag (100 nm, <1 Å/s) in a thermal evaporator under low vacuum conditions (below 10^{-6} Torr).

Thin-film characterization and Device Characterization

To quantify absorption spectra, a Varian Cary 50 UV-vis spectrophotometer was used. We utilized field emission scanning electron microscopy to assess the surface microstructure (Hitachi S-4800). The current-density (*J-V*) curves were recorded using Keithley 2400 source meter with a solar simulator (Newport, ORIEL AAA solar simulator) under irradiation of 100 mW/cm^2 (AM1.5),). An NREL-certified calibrated monocrystalline silicon solar cell was used for the calibration. The generated photocurrent was recorded at a scan rate of 100 mV/s (pre-sweep delay: 10 s) and a 0.09 cm^2 black metal mask was used as an active area of the devices. The external quantum efficiency (EQE) spectra were carried out using a 150 W Xenon lamp along with a Bentham PVE300 motorized 1/4 m monochromator as the light source. Electrochemical impedance spectroscopy (EIS) was performed using a BioLogic SP-300 impedance analyser in the frequency range of 2 MHz-1 Hz under the ac signal in a faradaic chamber, and the resulting data were fitted with EC-Lab software.

4. Conclusions

We synthesized eight different arylamino MPcs, to provide a molecular guideline for the designing of MPcs as hole-selective materials for the fabrication of perovskite solar cells. We unravel the influence of the number of aryl amino groups, the presence of fluorine atom, the central metal, and the symmetry of the molecule on photovoltaic performance. The incorporation of the fluorine atom in arylamino-substituted MPcs is an effective strategy for the performance and stability enhancement in perovskite solar cells. We noted that the PCE not only depends on the symmetrical nature of the side chain of the MPc but also the metal species attached to it. The higher conductivity is found for asymmetric fluorinated ZnPc-6 which also translates into high PV performance. Suggesting the variation in the energy level of the perovskite impacts the PV performances apart from the symmetrical nature and the coordination metal in the MPc.

Author Contributions

A.H. and J. O. carried out the synthesis and characterization of all the compounds. N. H. H and A.H. S.K. performed the experiments, fabricated the devices, and analysed the data. A.H., J. O., and N. H. H prepared the initial draft. S. K., J.O., S.A., and A.S.S. supervised, drafted, and directed the research. All authors contributed to the draft and prepared the final version.

Conflicts of interest

There are no conflicts to declare.

Acknowledgements

This work received funding from the European Union H2020 Programme under a European Research Council Consolidator grant [MOLEMAT, 726360]. Support from the Spanish Ministry of Science and Innovation (PID2019-111774RB-100/AEI/10.13039/501100011033 and INTERACTION {PID2021-129085OB-I00}) is also acknowledged. We want to thank the European Regional Development Fund "A way to make Europe" and the Spanish Ministerio de Ciencia e Innovación/Agencia Estatal de Investigación (PID2020-117855 RB-I00 to Á.S.-S) and the Generalitat Valenciana (CIPROM/2021/059 and MFA/2022/028 to Á. S.-S.) for funding.

References

1. A. Kojima, K. Teshima, Y. Shirai, T. Miyasaka, *J. Am. Chem. Soc.,* 2009, **131**, 6050–6051; L. Calió, S. Kazim, M. Grätzel, S. Ahmad, *Angew. Chem. Int. Ed.* 2016, **55**, 14522-14545.
2. https://www.nrel.gov/pv/cell-efficiency.html (accessed 12/03/2023)
3. C. S. Ponseca, T. J. Savenije, M. Abdellah, K. Zheng, A. Yartsev, T. Pascher, T. Harlang, P. Chabera, T. Pullerits, A. Stepanov, J.-P. Wolf, V. Sundström, *J. Am. Chem. Soc.* 2014, **136**, 5189−5192.
4. S. D. Stranks, G. E. Eperon, G. Grancini, C. Menelaou, M. J. P. Alcocer, T. Leijtens, L. M. Herz, A. Petrozza, H. J. Snaith, *Science*, 2013, **342**, 341−344.
5. W.-J. Yin, T. Shi, Y. Yan, *Adv. Mater*. 2014, **26**, 4653.
6. M. Cai, Y. Wu, H. Chen, X. Yang, Y. Qiang, L. Han, *Adv. Sci*., **2017**, *4*, 1600269.
7. G.-W. Kim, H. Choi, M. Kim, J. Lee, S. Y. Son, T. Park, *Adv. Energy Mater*. 2020, **10**, 1903403.
8. A. Krishna, A.C. Grimsdale, *J. Mater. Chem. A,* 2017, **5**, 16446.
9. G. Ren, W. Han, Y. Deng,W. Wu, Z. Li, J. Guo, H. Bao, C. Liu, W. Guo, *J. Mater. Chem. A*, 2021, **9**, 4589−4625.
10. H. D. Pham, T. C.-J. Yang, S. M. Jain, G. J. Wilson, P. Sonar, *Adv. Energy Mater*, 2020, **10**, 1903326.
11. E. Kasparavicius, A. Magomedov, T. Malinauskas, V. Getautis, *Chem. - Eur. J.,* 2018, **24**, 9910.
12. X. Yin, Z. Song, Z. Li, W. Tang, *Energy Environ. Sci*. 2020, **13**, 4057−4086.
13. G. Bottari, G. de la Torre, D. M. Guldi, T. Torres, *Coord. Chem. Reviews,* 2021, **428**, 213605.
14. (a) D. Molina, J. F. Berna and A. Sastre-Santos, J. Mater. Chem. C, 2023, 10.1039/D2TC04441B. (b) M. Urbani, G. de

la Torre, M. K. Nazeeruddin, T. Torres, *Chemical Society Reviews,* 2019, **48**, 2738-2766.
15. A. M. Schmidt, M.J.F. Calvete, *Molecules*, 2021, **26**, 1.
16. D. Molina, M. A. Ruiz-Preciado, F. Sadegh, M. J. Álvaro-Martins, M. Grätzel, A. Hagfeld, Á. Sastre-Santos, *Journal of Prophyrins and Phthalocyanines,* 2019, **23**, 546-553.
17. D. Molina, M. A. Ruiz-Preciado, B. Carlsen, F. T. Eickemeyer, B. Yang, N. Flores-Díaz, M. J. Álvaro-Martins, K. Nonomura, A. Hagfeldt, Á. Sastre-Santos, *ChemPhotoChem*, 2020, **4**, 307-314.
18. M. Pegu, D. Molina, M. J. Álvaro-Martins, M. Castillo, L. Ferrer, P. Huang, S. Kazim, Á. Sastre-Santos, S. Ahmad, *J. Mater. Chem. C,* 2022, **10**, 11975-11982.
19. L. Caliò, J. Follana-Berná, S. Kazim, M. Madsen, H.G. Rubahn, Á. Sastre-Santos, S. Ahmad, *Sustain. Energy Fuels,* 2017, **1**, 2071-2077.
20. Z. Yu, L. Wang, X. Mu, C. C. Chen, Y. Wu, J. Cao, Y. Tang, *Angew. Chem., Int. Ed.* 2021, **60**, 6294.
21. M.M.H. Desoky, M. Bonomo, R. Buscaino, A. Fin, G. Viscardi, C. Barolo, P. Quagliotto, *Energies*, 2021, **14**, 2279.
22. K. T. Cho, K. Rakstys, M. Cavazzini, S. Orlandi, G. Pozzi, M. K. Nazeeruddin, *Nano Energy*, 2016, **30**, 853.
23. G. Sfyri, N. Vamshikrishna, C.V. Kumar, L. Giribabu, P. Lianos, *Sol. Energy*, 2016, **140**, 60.
24. Y. Feng, Q. Hu, E. Rezaee, M. Li, Z.X. Xu, A. Lorenzoni, F. Mercuri, M. Muccini, *Adv. Energy Mater*., 2019, **9**, 1.
25. N. Klipfel, J. Xia, P. Čulík, S. Orlandi, M. Cavazzini, N. Shibayama, H. Kanda, C. Igci, W. Li, Y.-B. Cheng, V. Jankauskas, K. Genevicius, A. M. Asiri, C. Momblona, K. Rakstys, G. Pozzi, M. K. Nazeeruddin, *Materials Today Energy*, 2022, **29**, 101110.
26. P. Huang, A. Hernández, S. Kazim, J. Ortiz, Á. Sastre-Santos, S. Ahmad, S. *Sustain. Energy Fuels ,* 2020, **4**, 6188−6195.
27. P. Huang, A. Hernández, S. Kazim, J. Follana-Berná, J. Ortiz, L. Lezama, Á. Sastre-Santos, S. Ahmad, *ACS Appl. Energy Mater*. 2021, 4, **9**, 10124–10135.
28. E. Oleiki, S. Javaid, G. Lee, *Nanoscale Adv.,* 2022, **4**, 5070-5076.
29. .(a) J. Zhang, H. Lu, Y. Xu, C. Zhong, K. Chen,. R. Tang,.P. Zhang,.F. Wu,. L. Zhu, *J. Mater. Chem. C,* 2022, **10**, 14668-14674; (b) Tian Qin, F. Wu, D. Ma, Y. Mu, X. Chen, Z. Yang, L. Zhu, Y. Zhang, J.Zhao, Z. Chi, *ACS Materials Lett.* 2020, **2**, 1093–1100.
30. N. H. Hemasiri, S. Kazim, S. Ahmad, *J. Mater. Chem. C*, 2021, **9**, 9865–9873.
31. I. Gelmetti, N. F. Montcada, A. P. Rodríguez, E. Barrena, C.Ocal, I. G. Benito, A. M. Ontoria, N. Martín, A. V. Ferran, E. Palomares, *Energy Environ. Sci.*, 2019, **12**, 1309–1316.
32. C. M. Wolff, F. Zu, A. Paulke, L. P. Toro, N. Koch, D. Neher, *Adv. Mater*., 2017, **29**, 1700159.
33. N. Klipfel, J. Xia, P. Culík, S. Orlandi, M. Cavazzini, N. Shibayama, H. Kanda, C. Igci, W. Li, Y. B. Cheng, V. Jankauskas, K. Genevicius, A. M. Asiri, C. Momblona, K. Rakstys, G. Pozzi, M. K. Nazeeruddin, *Mater*, 2022, **29**, 101110.
34. Y. Cao, Y. Li, T. Morrissey, B. Lam, B. O. Patrick, D. J. Dvorak, Z. Xia, T. L. Kelly, C. P. Berlinguette, *Energy Environ. Sci*., 2019, **12**, 3502–3507.
35. (a) T. Niu, W. Zhu, Y. Zhang, Q. Xue, X. Jiao, Z. Wang, Y. M. Xie, P. Li, R. Chen, F. Huang, Y. Li, H. L. Yip, Y. Cao, *Joule*, 2021, **5**, 249–269; (b) N. H. Hemasiri, L. Caliò, M. Pegu, S. Kazim, S. Ahmad, *Solar RRL*, 2022, **6**, 2100793.
36. N. Klipfel, J. Xia, P. Culı́k, S. Orlandi, M. Cavazzini, N. Shibayama, H. Kanda, C. Igci, W. Li, Y.-B. Cheng, V. Jankauskas, K. Genevicius, A. M. Asiri, C. Momblona, K. Rakstys, G. Pozzi and M. K. Nazeeruddin, *Mater. Today Energy*, 2022, **29**, 101110.
37. D. Erzunov, T. Tikhomirova, A. Botnar, S. Znoyko, I. Abramov, V. Mayzlish, Y. Marfin, A. Vashurin, *J. Therm. Anal. Calorim*., 2020, **142**, 1807–1816.
38. A. W. Snow, The porphyrin handbook, 2003, 129–176.
39. H. Dhifaoui, N. H. Hemasiri, W. Aloui, A. Bouazizi, S. Kazim, S. Ahmad, Adv. Mater. Interfaces, 2021, **8**, 2101002.

Supporting information for

Fluorinated- and non-fluorinated-diarylamine-Zn(II) and Cu(II) Phthalocyanines as Symmetrical vs Asymmetrical Hole Selective Materials

Adrián Hernández[a], *Naveen Harindu Hemasiri[b], Samrana Kazim[b,c]*, Javier Ortiz[a], Shahzada Ahmad[b,c]* and Ángela Sastre-Santos[a]*

[a.] *Área de Química Orgánica, Instituto de Bioingeniería, Universidad Miguel Hernández, Avda. Universidad S/N, 03202, Elche, Spain.*

[b.] *BCMaterials, Basque Center for Materials, Applications, and Nanostructures, UPV/EHU Science Park, 48940, Leioa, Spain. Email: shahzada.ahmad@bcmaterials.net*

[c.] *IKERBASQUE, Basque Foundation for Science, Bilbao, 48009, Spain*

Characterization of phthalonitrile 1

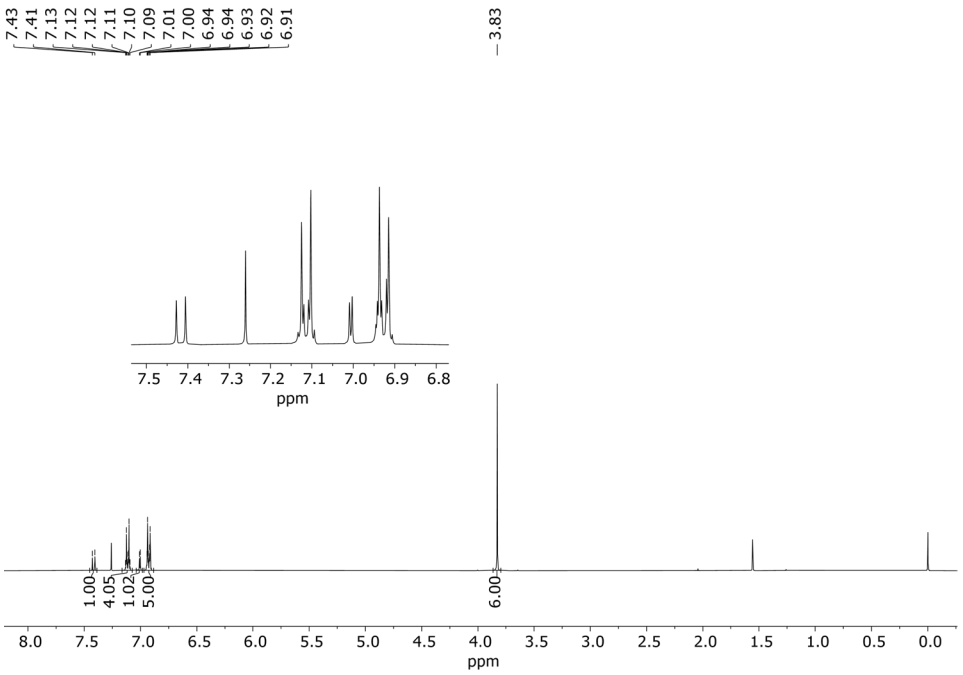

*Figure S1. [1]H-NMR of **1** in $CDCl_3$.*

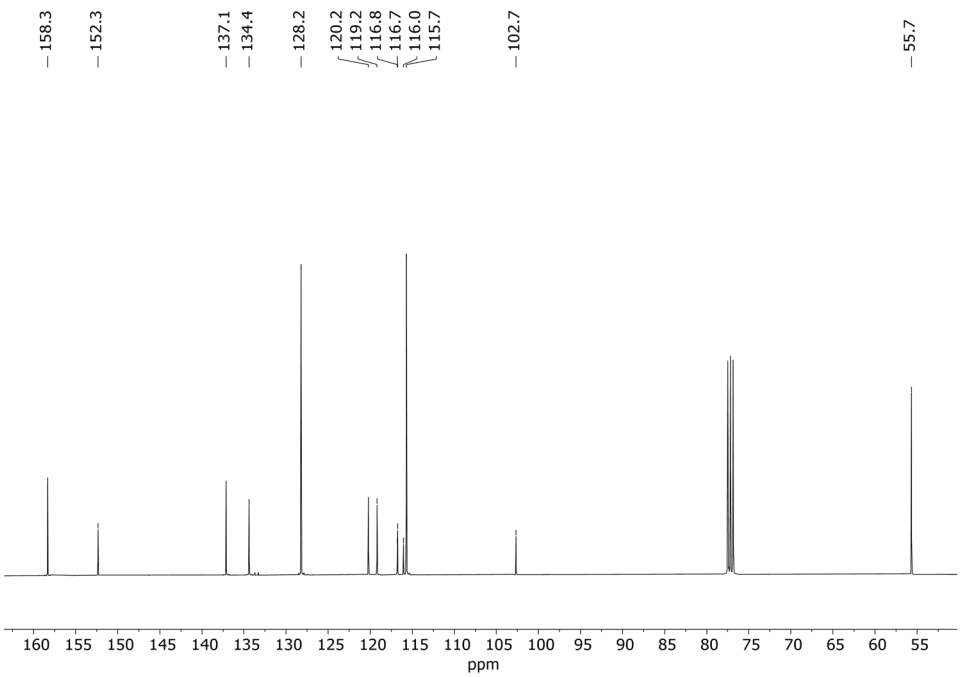

*Figure S2. [13]C-NMR of **1** in $CDCl_3$.*

Characterization of phthalonitrile 2

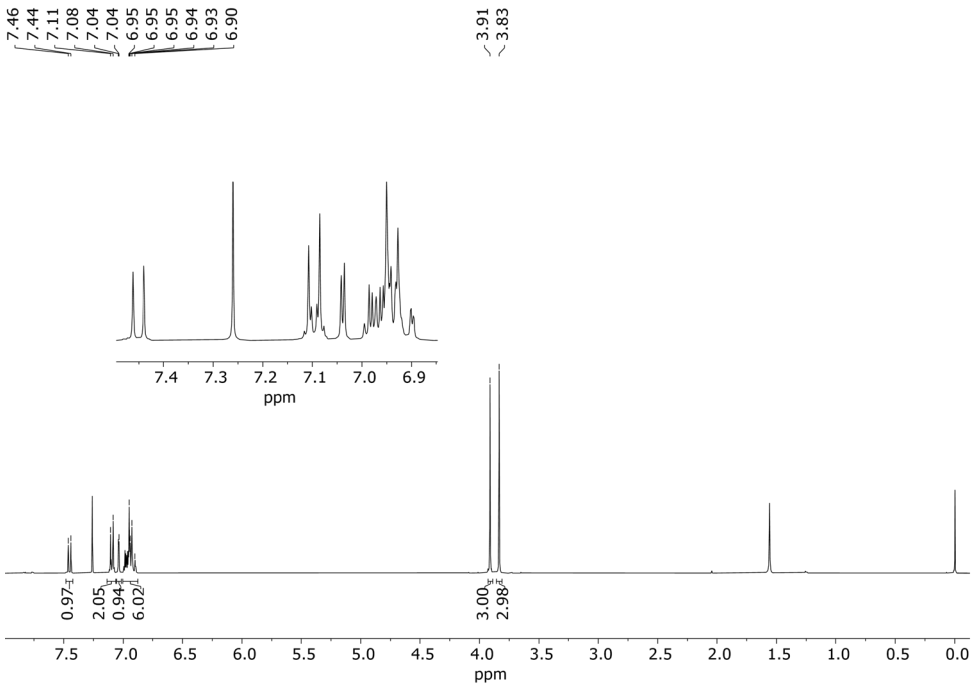

*Figure S3. [1]H-NMR of **2** in $CDCl_3$.*

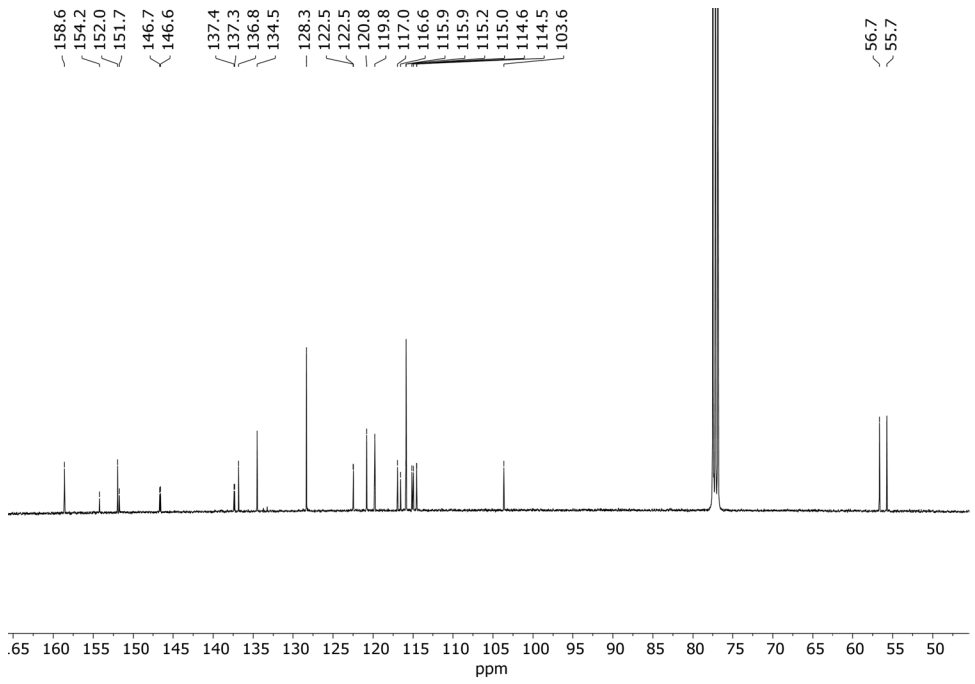

*Figure S4. [13]C-NMR of **2** in $CDCl_3$.*

Characterization of ZnPc-1

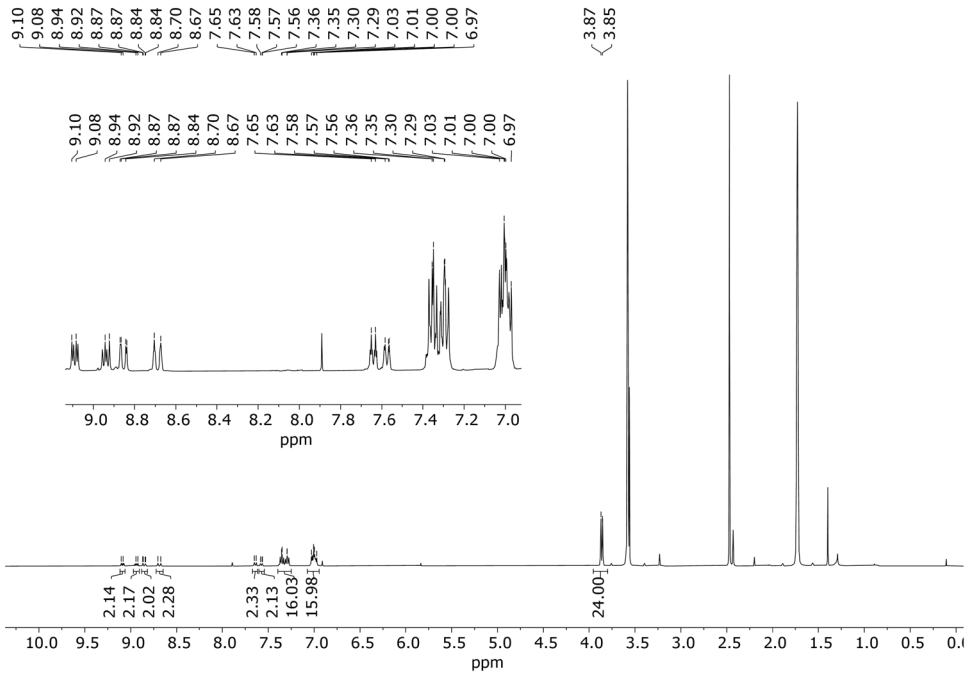

*Figure S5. [1]H-NMR of **ZnPc-1** in THF-d8.*

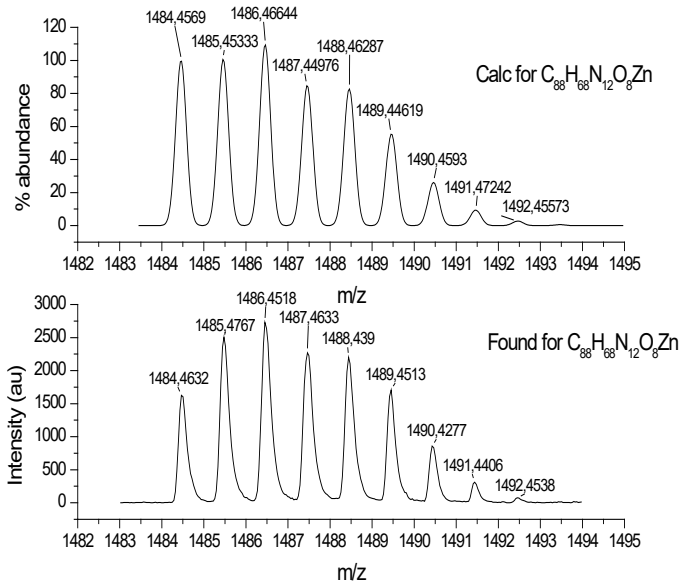

*Figure S6. HR-MALDI-TOF spectrum of **ZnPc-1**.*

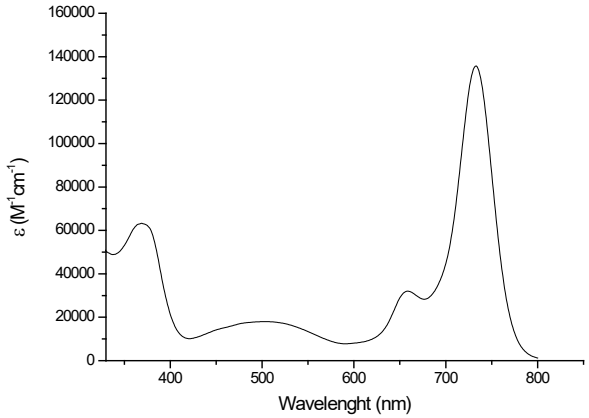

*Figure S7. Uv-vis absorption spectra of **ZnPc-1** in DMF.*

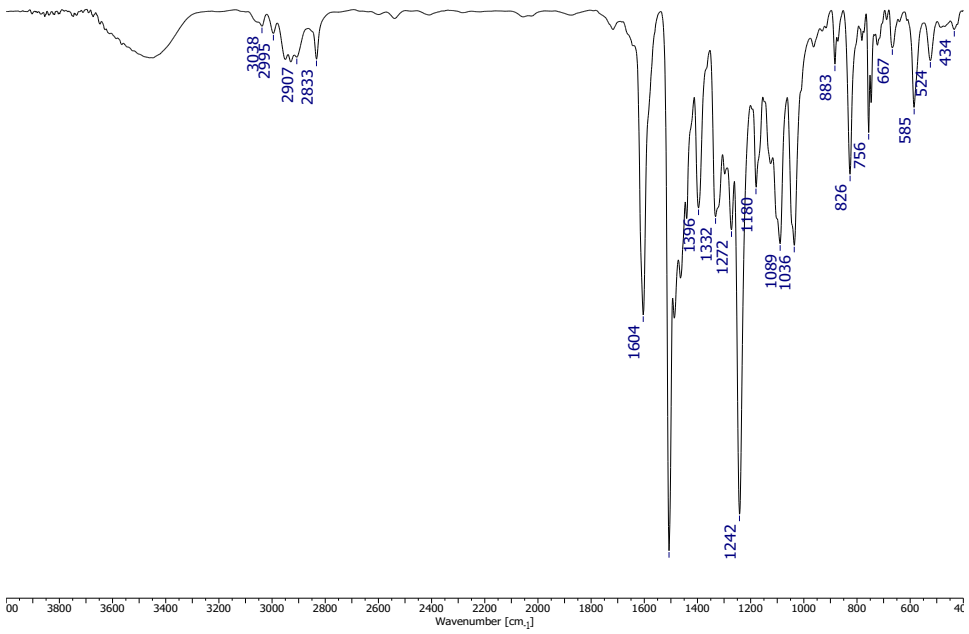

*Figure S8. FT-IR of **ZnPc-1**.*

Characterization of ZnPc-2

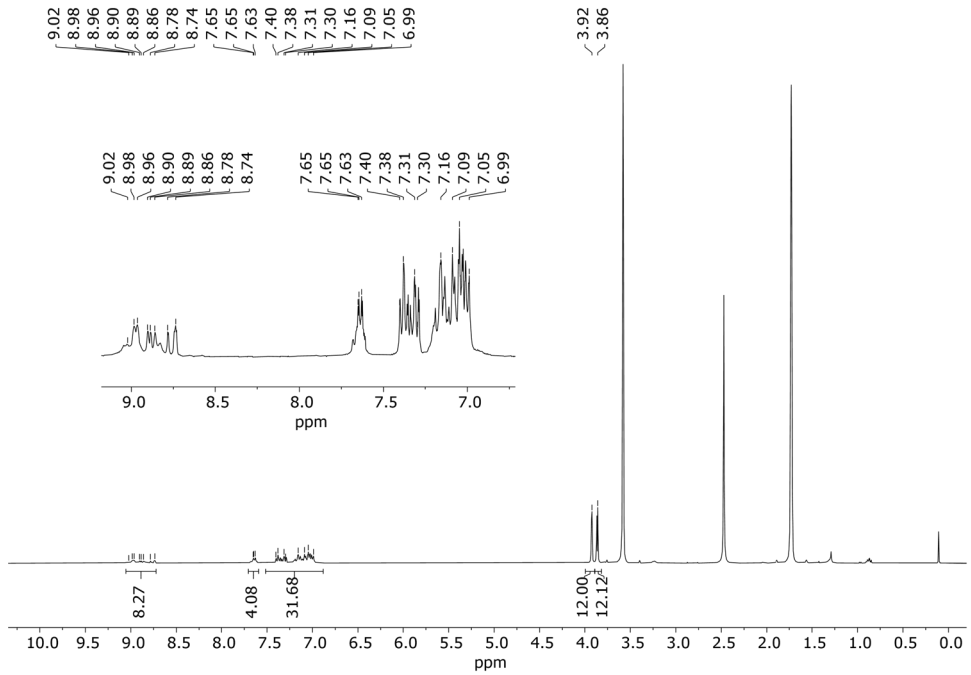

*Figure S9. [1]H-NMR of **ZnPc-2** in THF-d8.*

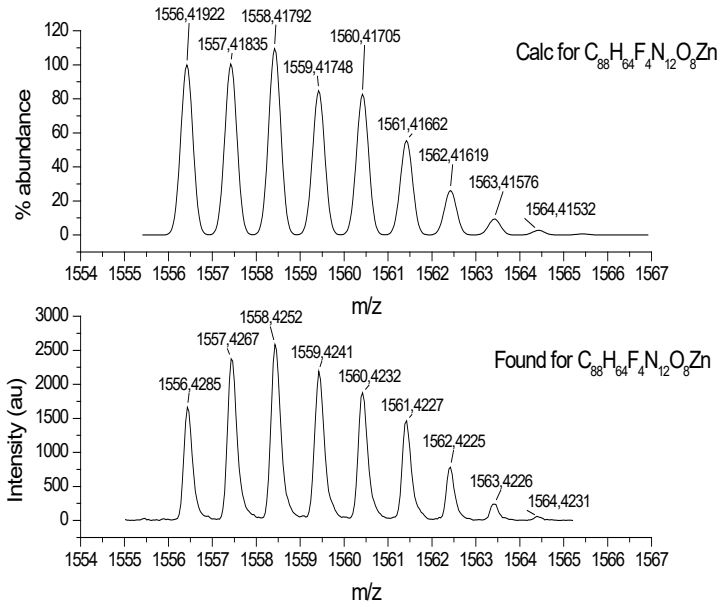

*Figure S10. HR-MALDI-TOF spectrum of **ZnPc-2**.*

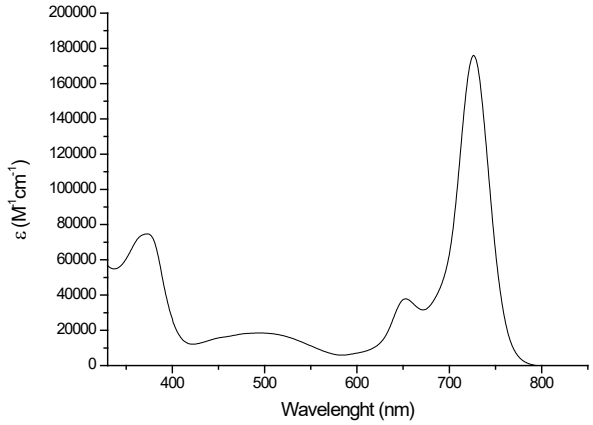

*Figure S11. UV-vis absorption spectra of **ZnPc-2** in DMF.*

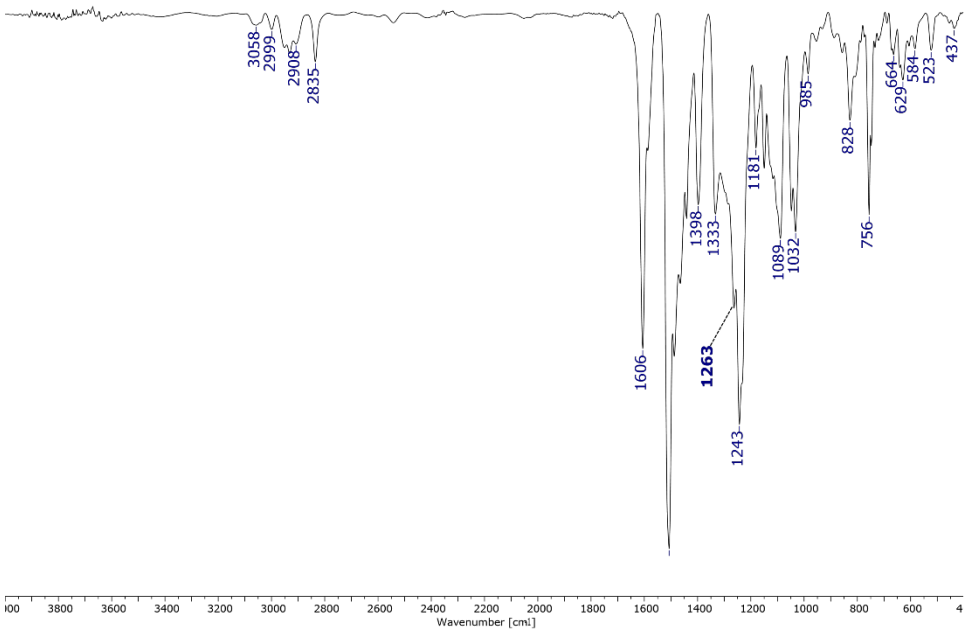

*Figure S12. FT-IR of **ZnPc-2**.*

Characterization of CuPc-3

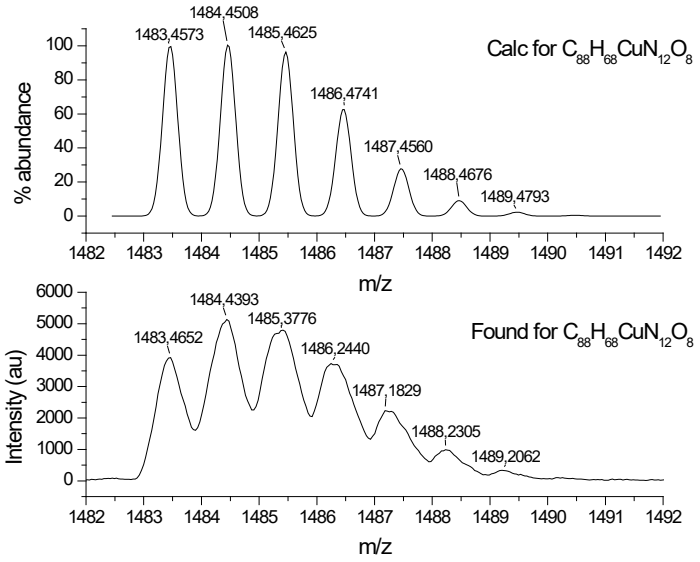

*Figure S13. HR-MALDI-TOF spectrum of **CuPc-3**.*

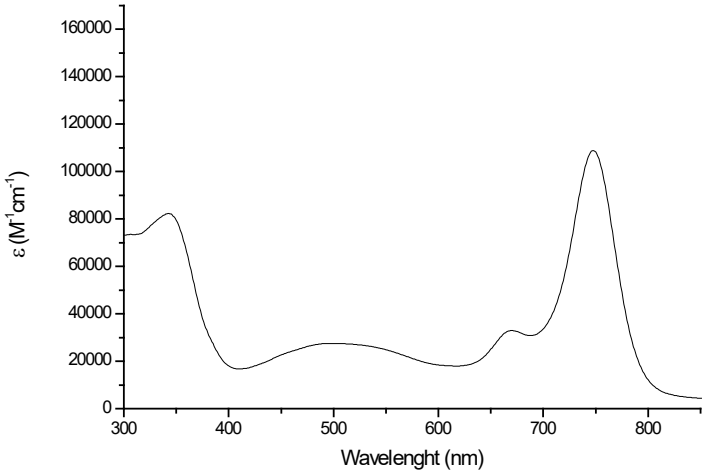

*Figure S14. Uv-vis absorption spectra of **CuPc-3** in DMF.*

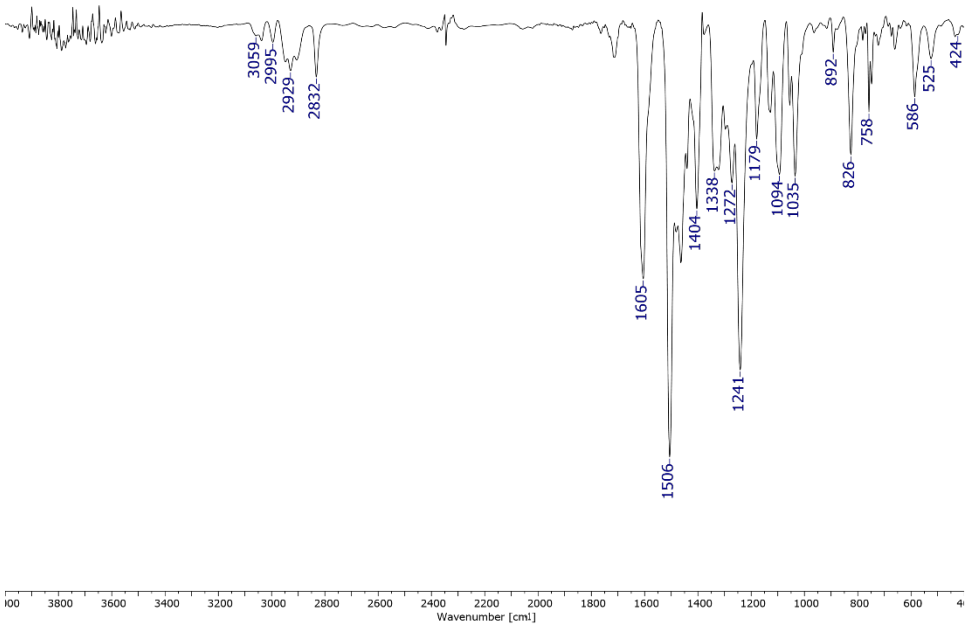

Figure S15. FT-IR of ***CuPc-3.***

Characterization of CuPc-4

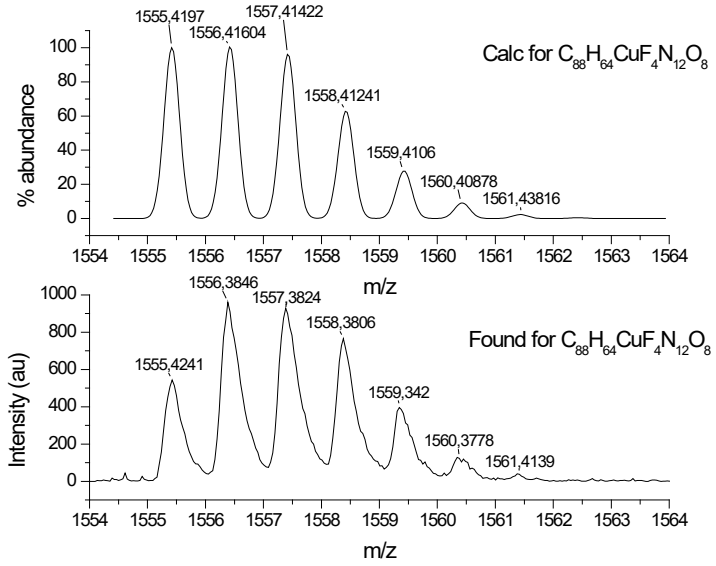

Figure S16. HR-MALDI-TOF spectrum of ***CuPc-4.***

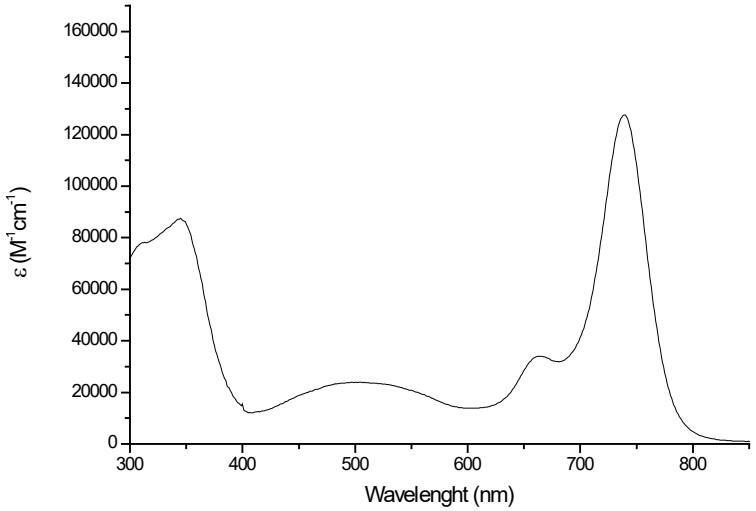

*Figure S17. UV-vis absorption spectra of **CuPc-4** in DMF.*

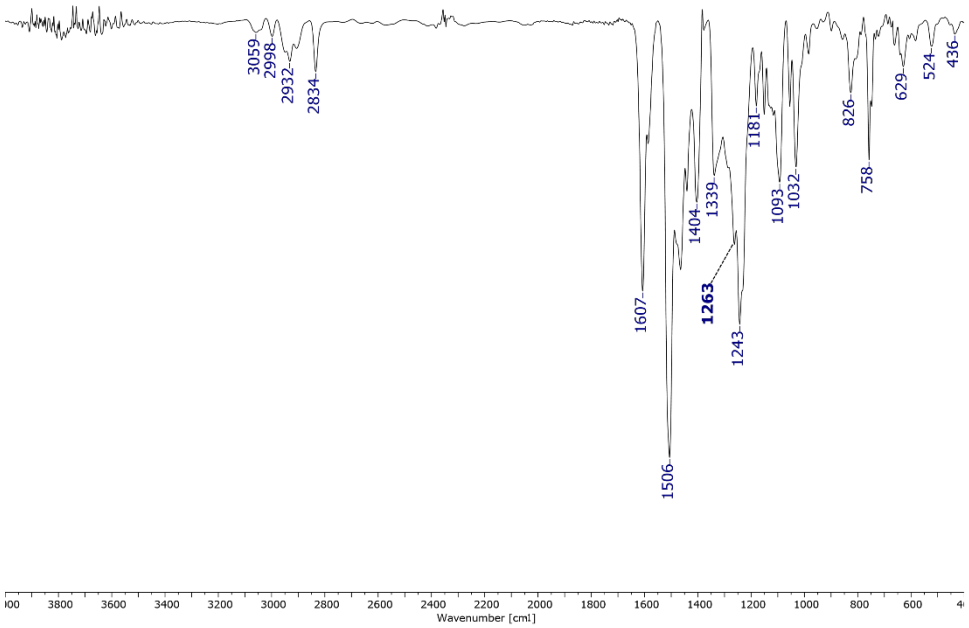

*Figure S18. FT-IR of **CuPc-4**.*

Characterization of ZnPc-5

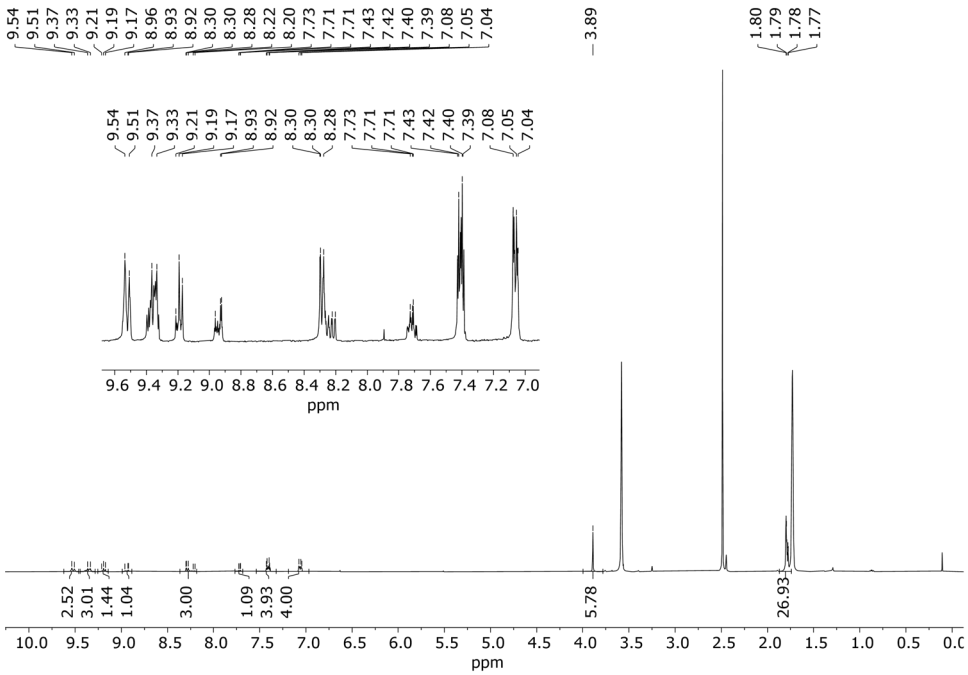

*Figure S19. [1]H-NMR of **ZnPc-5** in THF-d_8.*

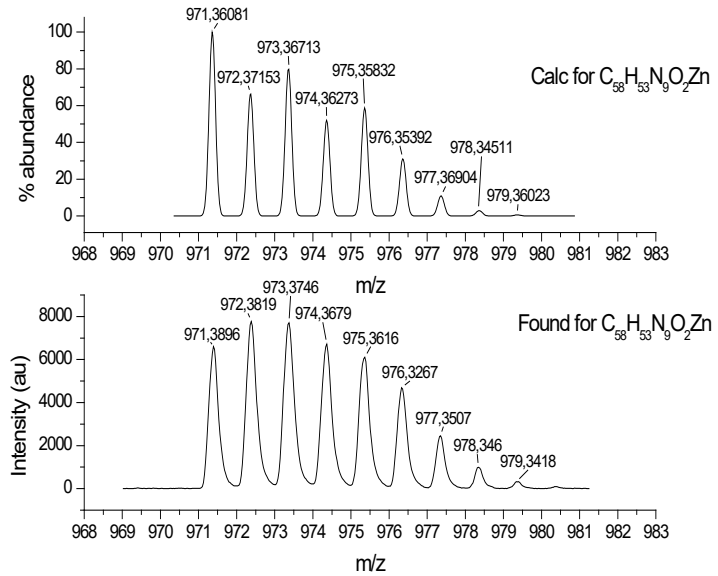

*Figure S20. HR-MALDI-TOF spectrum of **ZnPc-5**.*

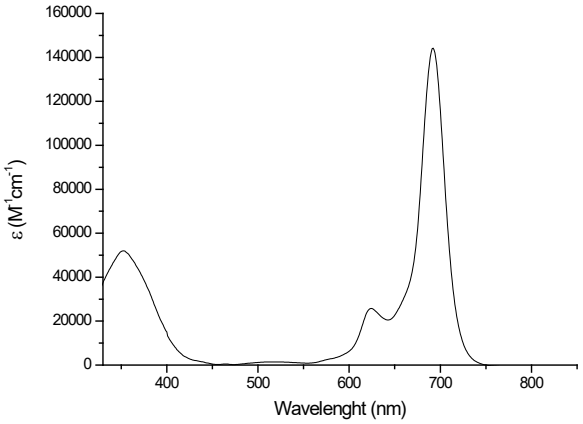

*Figure S21. UV-vis absorption spectra of **ZnPc-5** in DMF.*

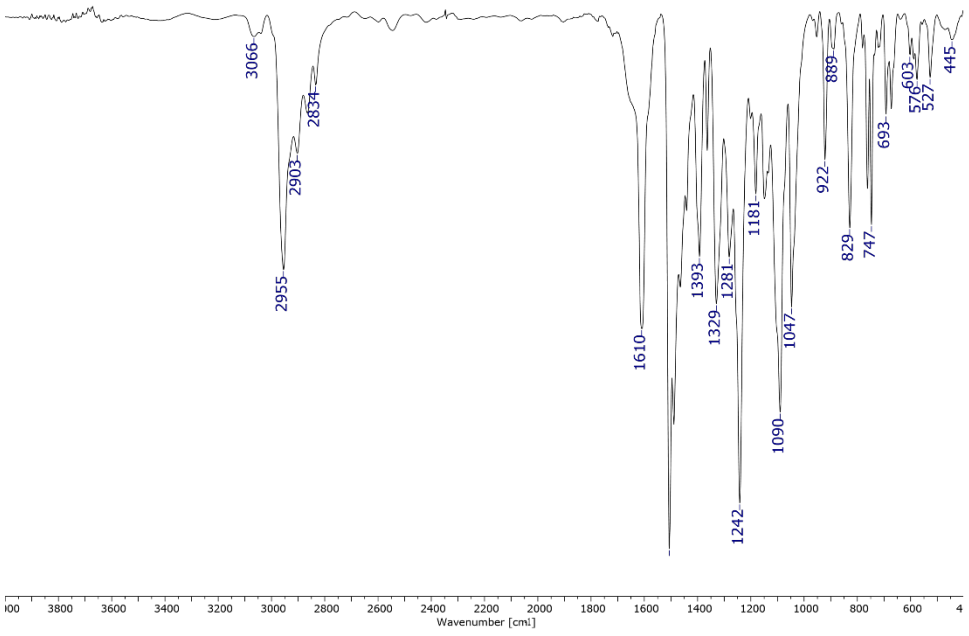

*Figure S22. FT-IR of **ZnPc-5**.*

Characterization of ZnPc-6

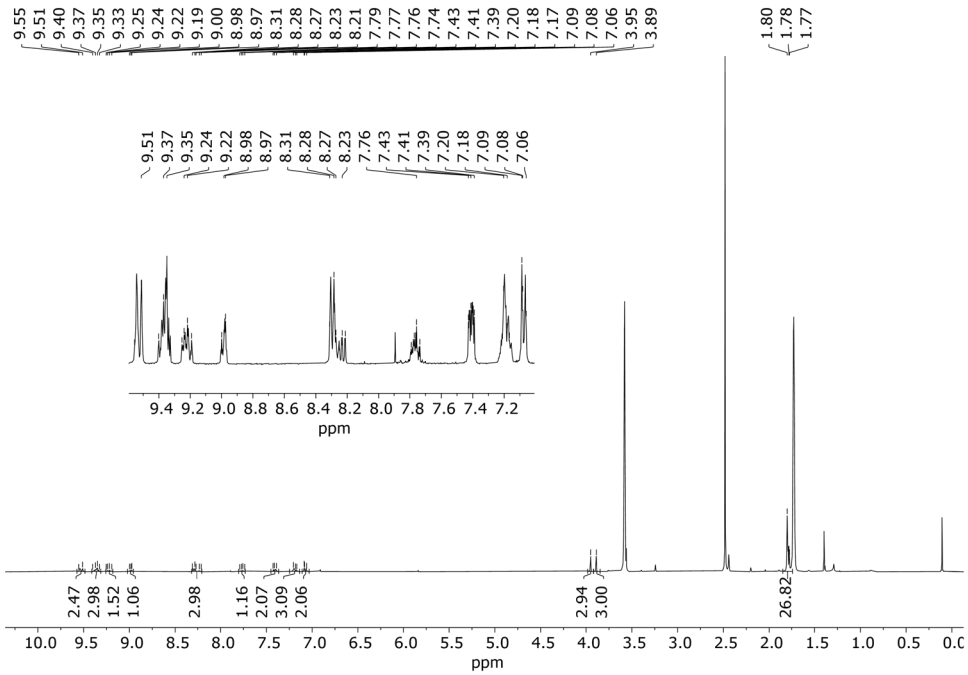

*Figure S23. [1]H-NMR of **ZnPc-6** in THF-d_8.*

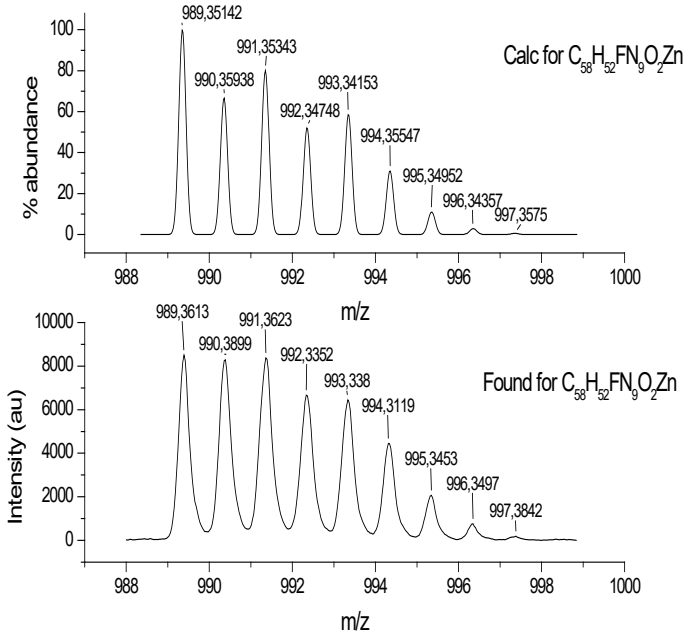

*Figure S24. HR-MALDI-TOF spectrum of **ZnPc-6**.*

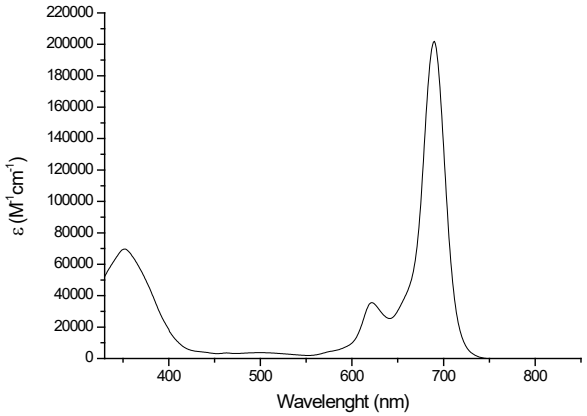

*Figure S25. UV-vis absorption spectra of **ZnPc-6** in DMF.*

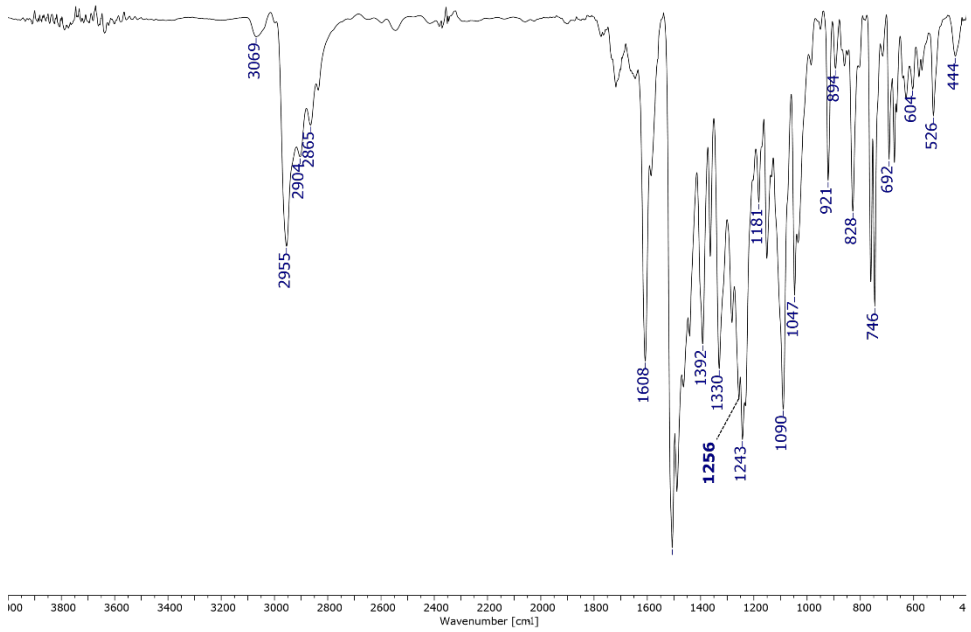

*Figure S26. FT-IR of **ZnPc-6**.*

Characterization of CuPc-7

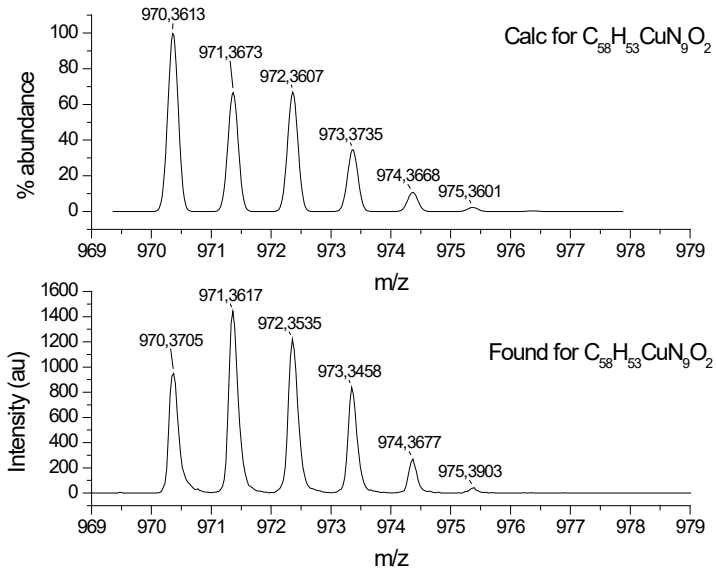

*Figure S27. HR-MALDI-TOF spectrum of **CuPc-7**.*

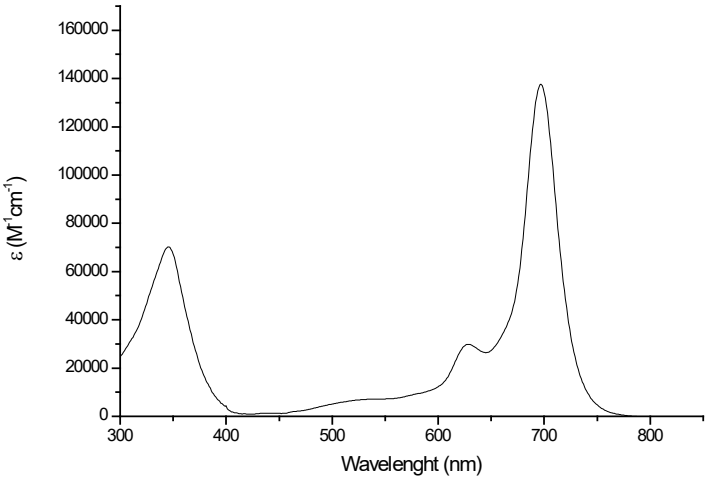

*Figure S28. UV-vis absorption spectra of **CuPc-7** in DMF.*

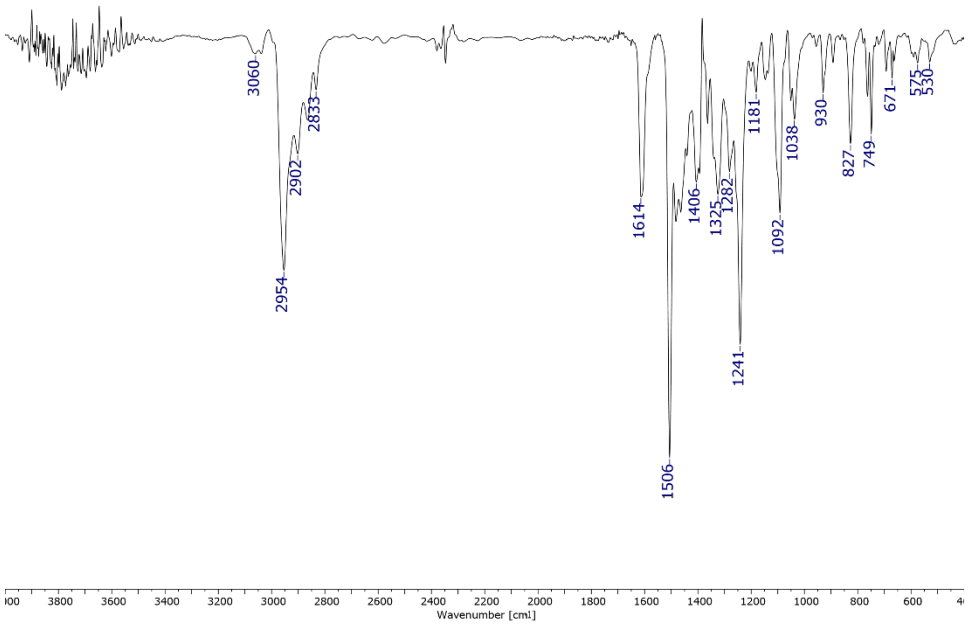

*Figure S29. FT-IR of **CuPc-7**.*

Characterization of CuPc-8

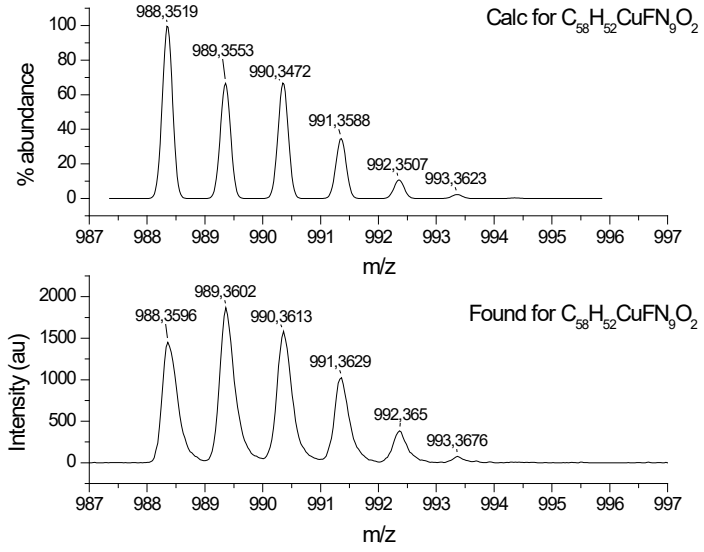

*Figure S30. HR-MALDI-TOF spectrum of **CuPc-8**.*

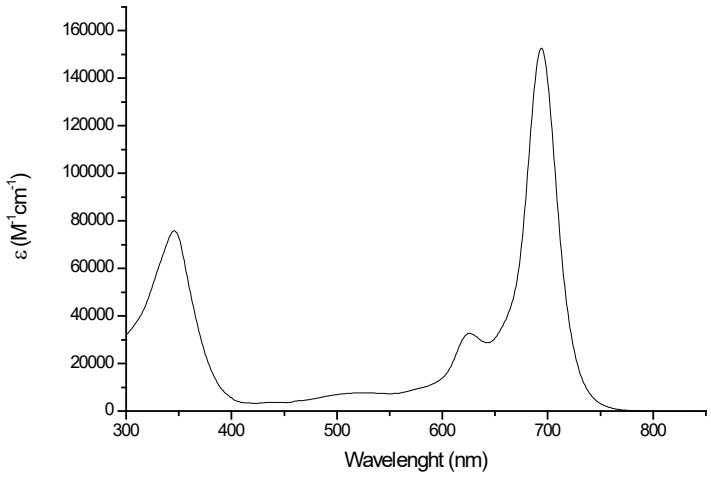

*Figure S31. UV-vis absorption spectra of **CuPc-8** in DMF.*

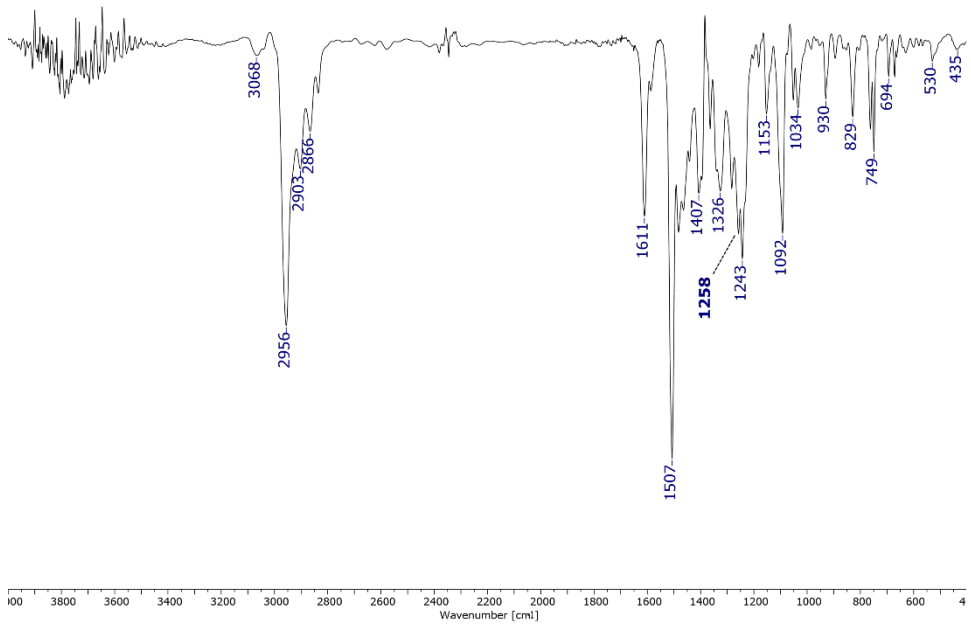

*Figure S32. FT-IR of **CuPc-8**.*

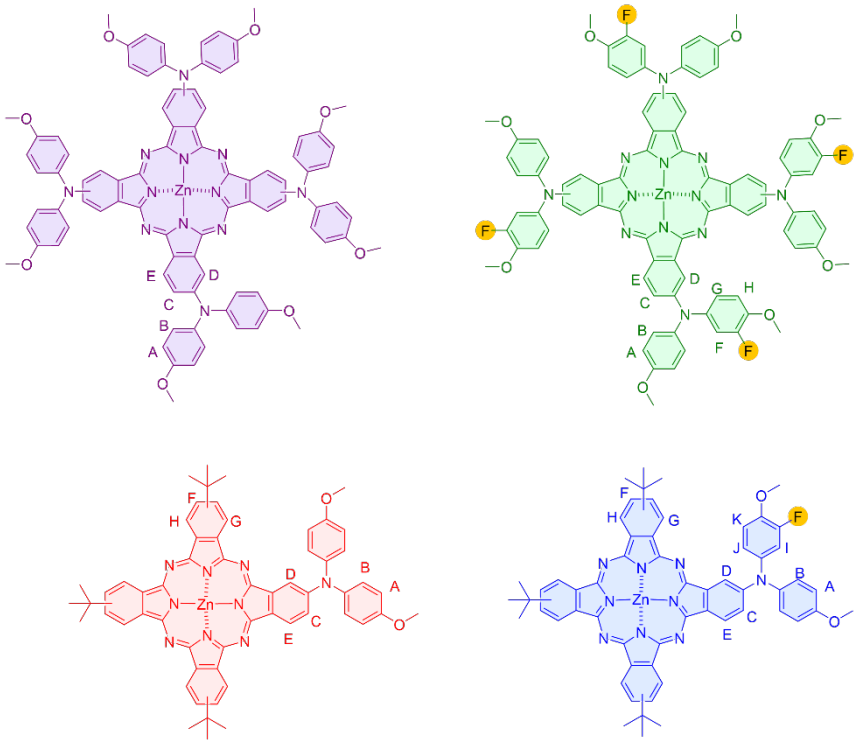

*Figure S33. [1]H-NMR assignation of protons for **ZnPc -1** (purple), **-2** (green), **-5** (red), and **-6** (blue).*

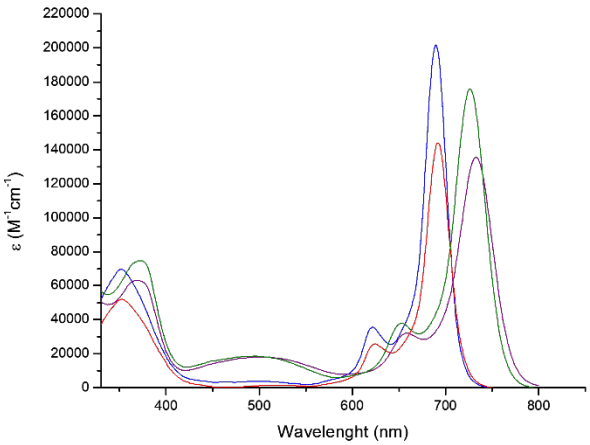

*Figure S34. UV-vis absorption spectra of **ZnPc -1** (purple), **-2** (green), **-5** (red), and **-6** (blue).*

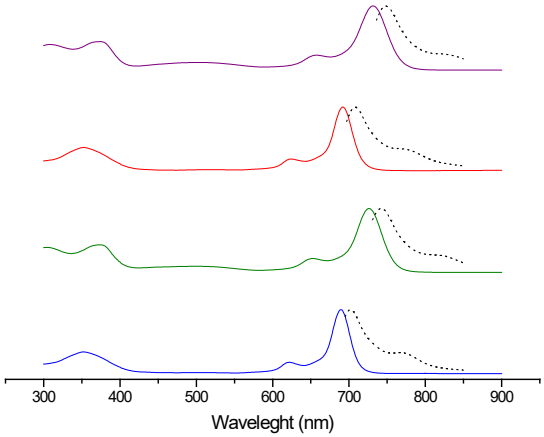

*Figure S35. Normalized UV-vis absorption (solid line) and fluorescence (dotted line) spectra of **ZnPc -1** (purple), **-2** (green), **-5** (red), and **-6** (blue).*

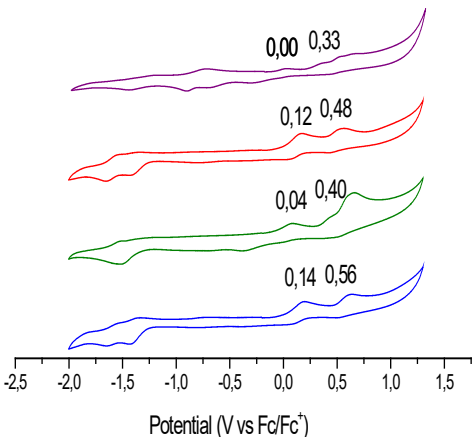

*Figure S36. Cyclic voltammogram of **ZnPc -1** (purple), **-2** (green), **-5** (red), and **-6** (blue).*

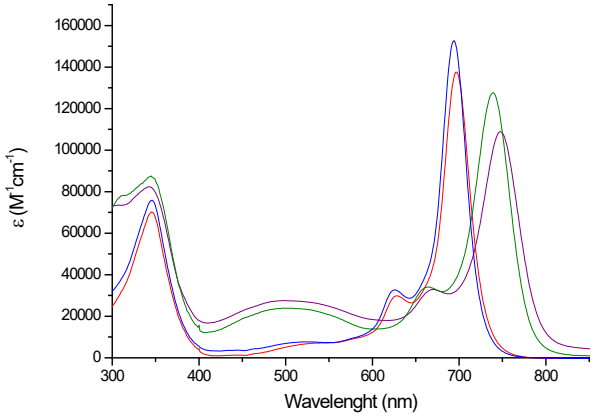

Figure S37. UV-vis absorption spectra of CuPc ***-3*** *(purple),* ***-4*** *(green),* ***-7*** *(red), and* ***-8*** *(blue).*

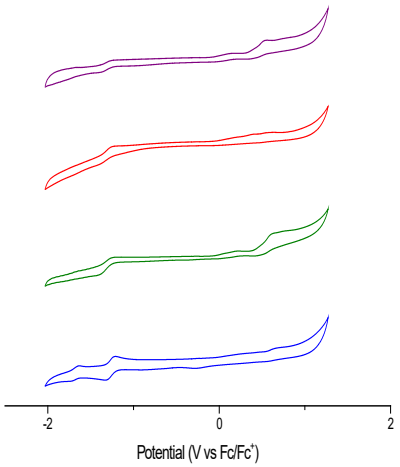

Figure S38. Cyclic voltammogram of CuPc ***-3*** *(purple),* ***-4*** *(green),* ***-7*** *(red), and* ***-8*** *(blue).*

Electrochemistry

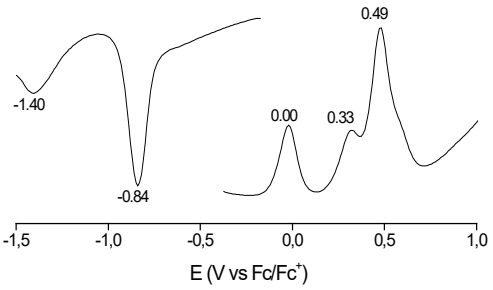

Figure S39. Differential pulse voltammetry of ZnPc-1 in deaerated DMF solution containing $TBAPF_6$ (0.1 M) obtained at 298 K.

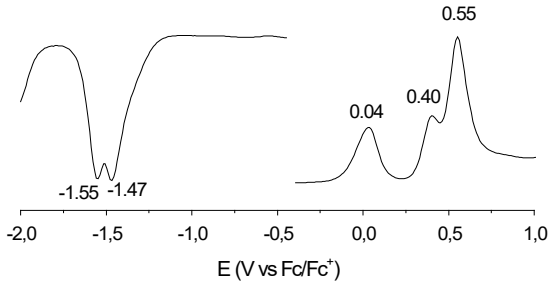

Figure S40. Differential pulse voltammetry of ZnPc-2 in deaerated DMF solution containing TBAPF6 (0.1 M) obtained at 298 K.

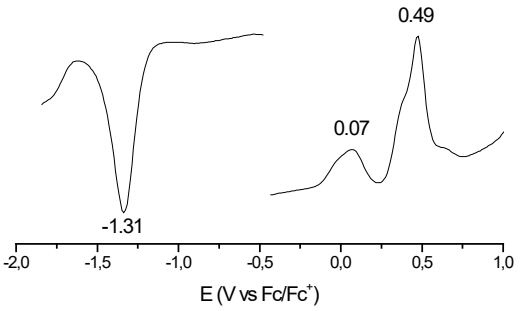

Figure S41. Differential pulse voltammetry of CuPc-3 in deaerated DMF solution containing TBAPF6 (0.1 M) obtained at 298 K.

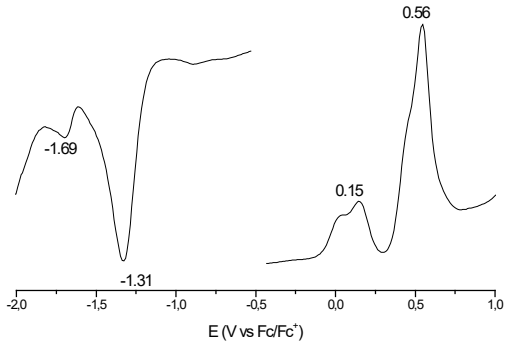

Figure S42. Differential pulse voltammetry of CuPc-4 in deaerated DMF solution containing TBAPF6 (0.1 M) obtained at 298 K.

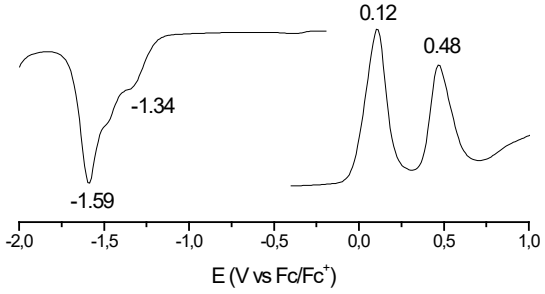

Figure S43. Differential pulse voltammetry of ZnPc-5 in deaerated DMF solution containing TBAPF6 (0.1 M) obtained at 298 K.

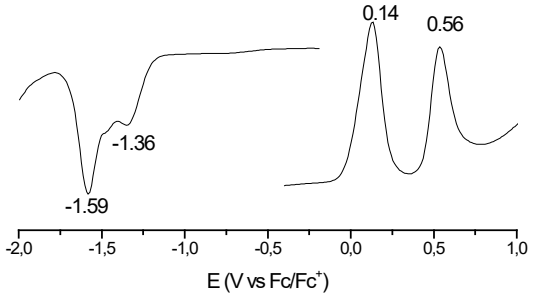

Figure S44. Differential pulse voltammetry of ZnPc-6 in deaerated DMF solution containing TBAPF6 (0.1 M) obtained at 298 K.

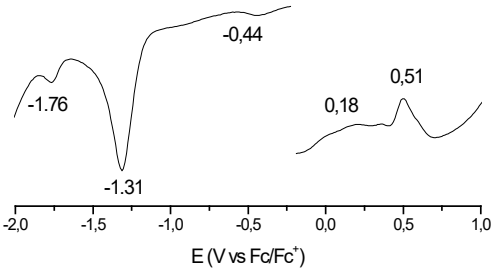

Figure S45. Differential pulse voltammetry of CuPc-7 in deaerated DMF solution containing TBAPF6 (0.1 M) obtained at 298 K.

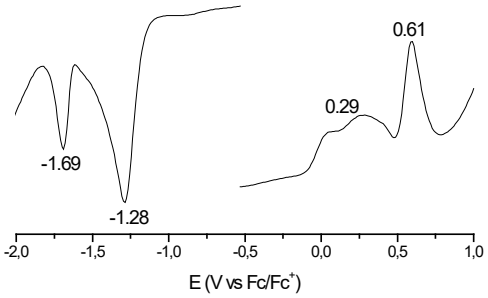

Figure S46. Differential pulse voltammetry of CuPc-8 in deaerated DMF solution containing TBAPF6 (0.1 M) obtained at 298 K.

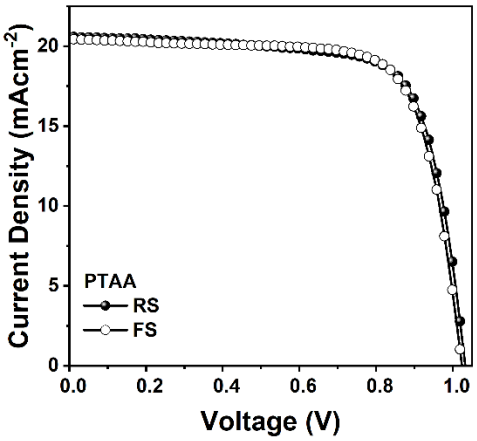

Figure S47. Reverse and forward scan J-V curves for PSC based on pristine PTAA as HTM.

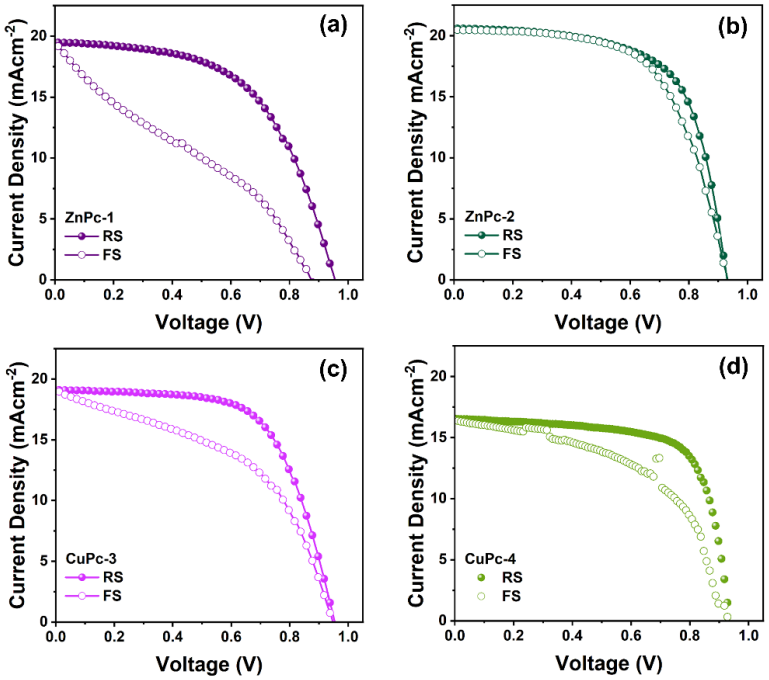

Figure S48. Reverse and forward scan J-V curves for PSCs based on symmetrical MPcs, (a) ZnPc-1, (b) ZnPc-2, (3) CuPc-3, and (4) CuPc-4.

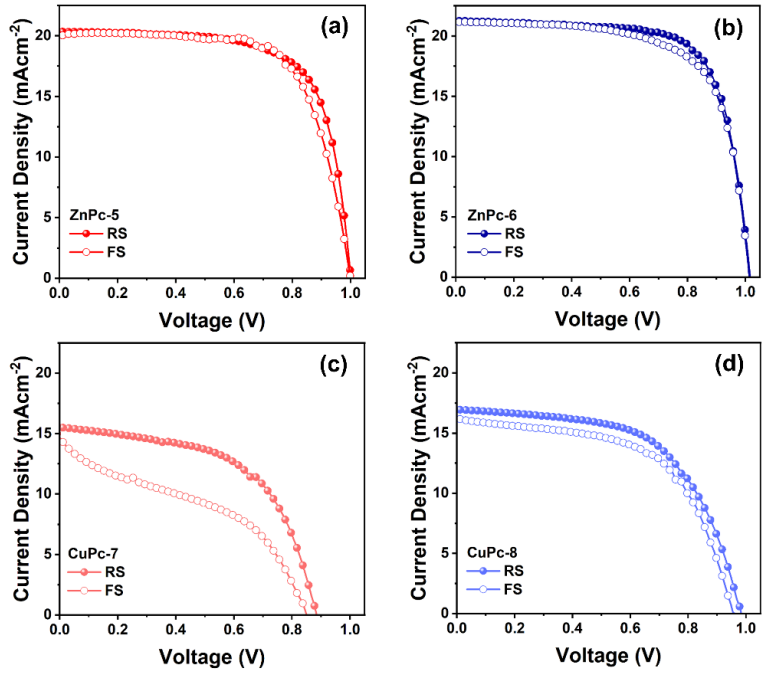

Figure S49. Reverse and forward scan J-V curves for PSCs based on symmetrical MPcs, (a) ZnPc-5, (b) ZnPc-6, (3) CuPc-7, and (4) CuPc-8.

Table S1. Statistical data of J-V parameters of champion devices based on n-i-p configuration.

HTM	V_{oc} (mV)	J_{sc} (mAcm^{-2})	FF (%)	PCE (%)	*HI
ZnPc-1	890.54±48.83	17.89±1.08	54.21±8.31	8.59±1.22	0.5058
ZnPc-2	936.01±7.43	20.08±0.29	63.39±1.81	11.92±0.47	0.0750
CuPc-3	962.83±17.17	17.36±1.18	63.38±2.75	10.58±0.68	0.2549
CuPc-4	930.26±15.24	16.66±0.60	60.99±7.36	9.45±1.15	0.1486
ZnPc-5	995.24±5.77	20.01±0.26	69.55±0.89	13.85±0.34	0.0550
ZnPc-6	1011.98±4.04	20.94±0.18	70.03±1.16	14.84±0.37	0.0415
CuPc-7	833.46±58.74	10.98±2.84	50.39±7.59	4.56±1.37	0.3542
CuPc-8	881.8±48.27	15.10±1.58	52.36±8.47	6.96±1.38	0.0773

*HI = [PCE_{RS} − PCE_{FS}]/PCE_{RS}, where PCE_{RS} and PCE_{FS} represent the PCE from reverse and forward scans, respectively. Statistical distribution was calculated from 8 devices of each ZnPc-1, CuPc-4, CuPc-7, CuPc-8, and 10 devices of each ZnPc-2, CuPc-3, ZnPc-5, ZnPc-6.

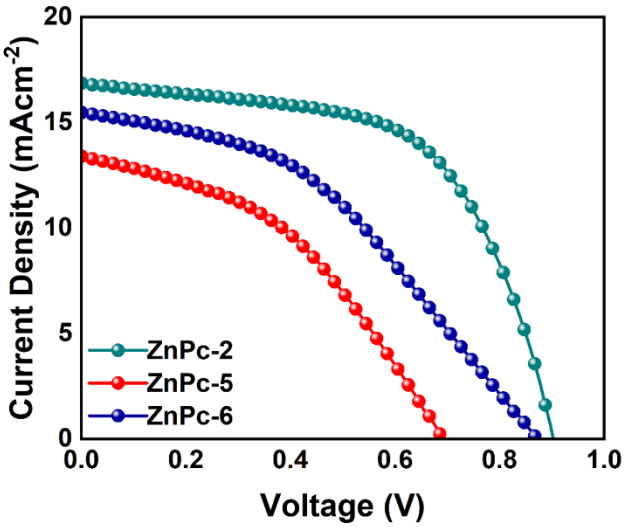

Figure S50. J-V curves in the reverse scan for p-i-n devices based on ZnPc-2, ZnPc-5, and ZnPc-6.

Table S2. Performance summary of devices based on p-i-n configuration with ZnPc-2, ZnPc-5, and ZnPc-6.

HTM	V_{oc} (mV)	J_{sc} (mAcm^{-2})	FF ((%)	PCE (%)	R_s (Ω)	R_{sh} (kΩ)
ZnPc-2	901.87	16.85	59.59	9.06	98.86	4.379
ZnPc-5	693.94	13.41	41.74	3.88	300.88	1.880
ZnPc-6	865.26	15.48	41.28	5.53	311.79	2.604

Table S3. Performance summary of devices based on p-i-n configuration with ZnPc-2, ZnPc-5, and ZnPc-6.

HTM	Conductivity (S/cm)	Mobility (cm^2/Vs)
ZnPc-1	4.660×10^{-7}	8.994×10^{-6}
ZnPc-2	1.210×10^{-6}	3.199×10^{-5}
CuPc-3	8.121×10^{-7}	8.150×10^{-6}
CuPc-4	8.024×10^{-7}	1.051×10^{-5}
ZnPc-5	1.045×10^{-6}	1.949×10^{-5}
ZnPc-6	1.268×10^{-6}	2.039×10^{-5}
CuPc-7	8.142×10^{-7}	6.335×10^{-5}
CuPc-8	7.688×10^{-7}	3.434×10^{-5}

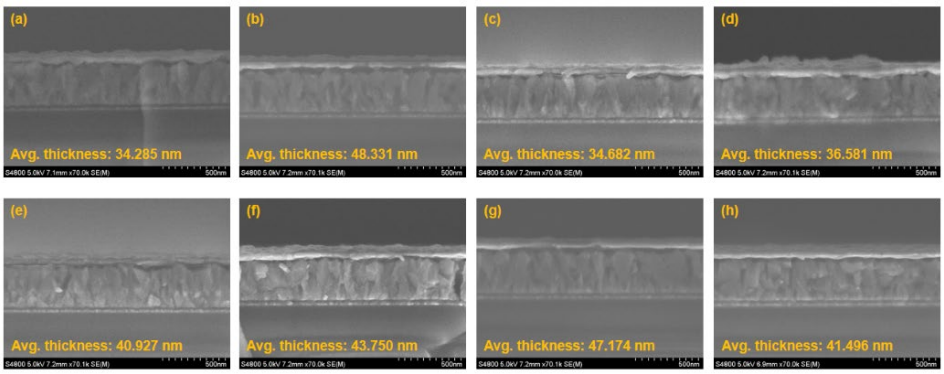

Figure S51. Cross-sectional SEM images of FTO/MPc/Ag devices and average thickness of each MPc.

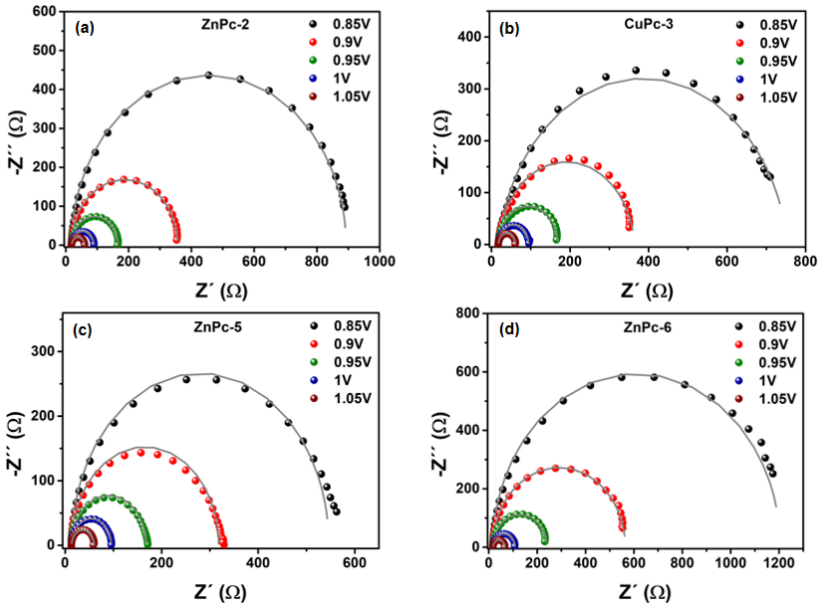

Figure S52. Electrochemical impedance spectra (EIS) of PSCs based on ZnPc-2, CuPc-3, ZnPc-5, and ZnPc-6 measured at different bias voltages from 0.85−1.05 V under dark conditions (raw and fitted data).

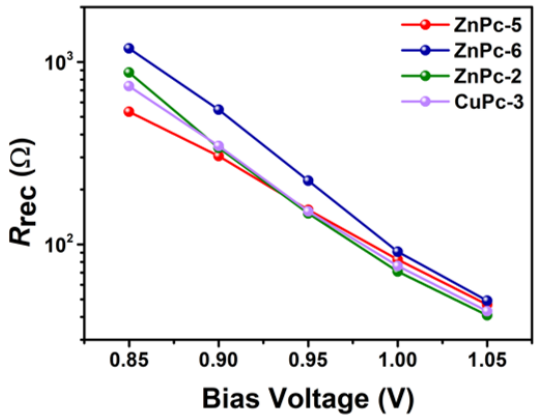

Figure S53. The bias voltage-dependent interfacial charge recombination resistance extracted from Nyquist plots under dark conditions.

2.4 Discusión y conclusiones

En este capítulo se han sintetizado trece ftalocianinas con diferente ion metálico (cinc o cobre) en su cavidad central y tetrasustituidas con grupos *terc*-butilo, arilamino o 2-aminoetoxilo en las posiciones periféricas. Se han utilizado como material transportador de huecos en células solares de perovskita.

2.4.1 Resumen artículo 1

La síntesis de **ZnTPPc 1** (ZnTPPc en el artículo 1), comenzó a partir del 4-yodoftalonitrilo, obtenido de acuerdo con la bibliografía.[107] A continuación se llevó a cabo una reacción de Suzuki-Miyaura con el éster de pinacol de ácido tiofeno-2-borónico catalizada por paladio dando lugar al ftalonitrilo **4**. En este caso particular el rendimiento de la reacción mejoraba utilizando acetato de paladio en lugar de los catalizadores convencionales como $Pd_2(dba)_3$, facilitando además la síntesis al ser menos sensible al aire que estos.[108] Mediante la bromación de **4** con N-bromosuccinimida en medio ácido se obtuvo el derivado bromado **3**.[109] Seguidamente, a partir de otra reacción de Suzuki entre **3** y el arilboronato correspondiente catalizada por $Pd_2(dba)_3$ se obtuvo el ftalonitrilo **2** como un sólido rojo. Los ftalonitrilos **2**, **3**, y **4**, se caracterizaron por ^{1}H-NMR y ^{13}C-NMR, espectros que pueden verse en la información suplementaria del artículo. Finalmente se obtuvo **ZnTPPc 1** como una mezcla de regioisómeros, mediante la autocondensación del ftalonitrilo **2** en presencia de acetato de cinc y una gota de DBN como catalizador, con un rendimiento del 52% tras su purificación en columna cromatográfica (**Esquema 2.2**).

El producto final **ZnTPPc 1** se caracterizó mediante espectroscopía de ^{1}H-RMN, espectrometría de masas HR-MALDI-TOF, absorción UV-vis y espectros de fluorescencia. El espectro de ^{1}H-RMN en DMSO-d_6 de **ZnTPPc 1** no muestra señales bien definidas, posiblemente por apilamiento y la presencia de cuatro regioisómeros diferentes (**Figura S7** en el artículo, pg. 56). El espectro de absorción de **ZnTPPc 1** en DMF, presenta las bandas Soret ubicada en la región ultravioleta alrededor de 390 nm y la banda Q con intensas absorciones a 647 nm y 719 nm. Además, muestra un pico de fluorescencia a 768 nm y un *gap* óptico de 1.65 eV, estimado de la intersección entre la absorción y la fluorescencia (**Figura 2.23a**). De la caracterización electroquímica (**Figura 2.23b**) se obtuvieron los picos de oxidación necesarios para determinar los niveles de energía HOMO y LUMO. Una vez obtenidos se representaron junto al resto de componentes de la PSC (**Figura 2.23c**) y se observó que están bien posicionados tanto para la extracción de huecos como para bloquear eficientemente los electrones fotogenerados y evitar la recombinación en la interfaz de perovskita/HTM.

[107] S.M. Marcuccio, P.I. Svirskaya, S. Greenberg, A. B. P. Lever, C.C. Leznoff, K.B. Tomer, *Can. J. Chem*., **1985**, *63*, 3057-3069
[108] a) S. Cogal, S. Erten-Ela, K. Ocakoglu, A.U. Oksuz, *Dyes and Pigments*, **2015**, *113*, 747-480. b) W, Li, D.P. Nelson, M.S. Jensen, R.S. Hoerrner, D. Cai, R.D. Larsen, *Org. Synth*. **2005**, *81*, 89.
[109] X. Yan, H. Fan, H. Gu, J. Zhang, X. Huang, R. Zhang, X. Zhan, Dyes and Pigments, 2015, 114, 124-128

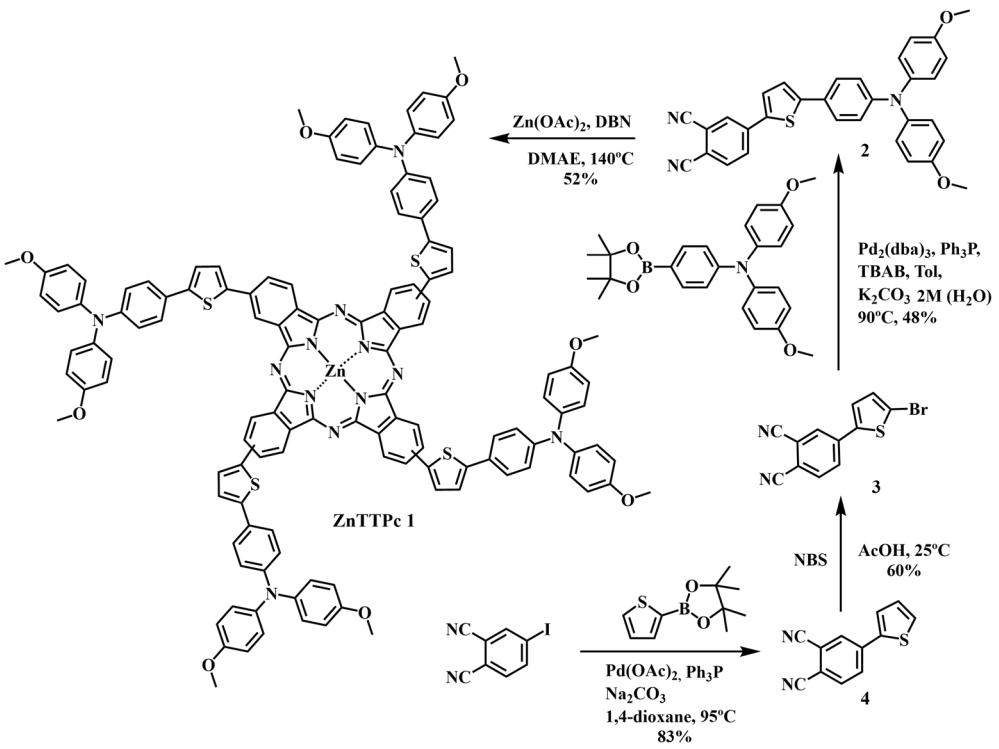

Esquema 2.2. Síntesis de ZnTPPc 1 y sus precursores.

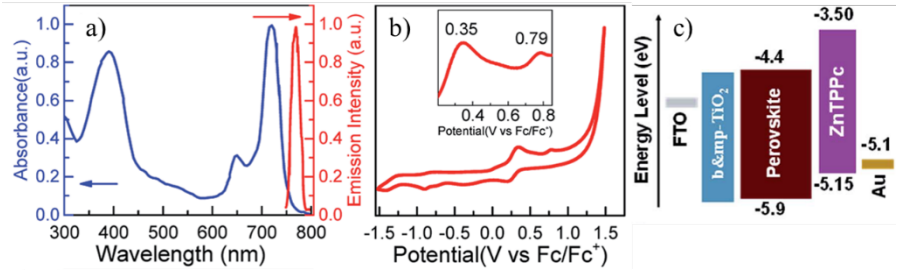

*Figura 2.**23**. a) Espectros de absorción UV-visible y fluorescencia de **ZnTTPc 1** en DMF, b) voltamograma cíclico de **ZnTTPc 1** en DMF, c) diagrama de los niveles de energía de la PSC.*

Se fabricaron los dispositivos con la arquitectura FTO/b&mp-TiO_2/perovskita/**ZnTPPc 1**/Au sin dopar, y se utilizaron spiro-OMeTAD prístino y dopado como HTMs de referencia. Los resultados experimentales de los dispositivos se muestran en la **Figura 2.24** y los parametros obtenidos se resumen en la **Tabla 2.1**. Se puede comprobar que la eficiencia del dispositivo con **ZnTPPc 1** prístina es tres veces mayor que spiro prístino y algo inferior al spiro dopado.

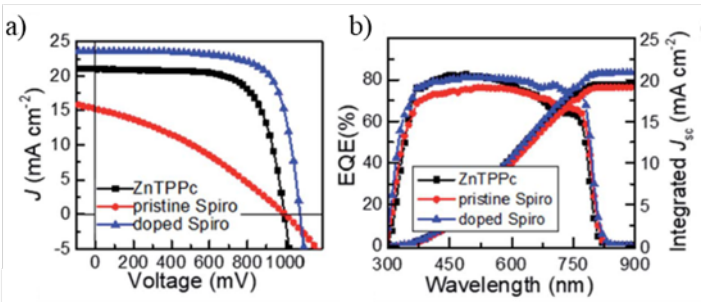

*Figura 2.**24**. a) Curvas J-V de los dispositivos con diferentes HTMs, b) EQE y J_{sc} integrada de los dispositivos campeones de cada HTM.*

Tabla 2.1. Parámetros fotovoltaicos de las PSCs con diferentes HTMs.

HTM	V_{oc} (mV)	J_{sc} (mA cm^{-2})	FF(%)	PCE (%)	R_s (Ω)	R_{sh} (kΩ)
ZnTPPc	**994.3**	**21.00**	**69.42**	**14.50**	**58**	**19.2**
Spiro	**993.9**	**15.25**	**33.92**	**5.14**	**424**	**1.7**
Spiro dopado	**1075.9**	**23.62**	**72.69**	**18.47**	**44**	**5.6**
ZnTPPc (Estadística)	**1011.4 ± 21**	**19.92 ± 0.81**	**58.42 ± 5.6**	**11.80 ± 1.51**		

La estabilidad a largo plazo de los dispositivos es otro parámetro importante de los HTM. En condiciones de humedad relativa del 40-50% y temperatura ambiente el dispositivo con **ZnTPPc 1** aumentó ligeramente la eficiencia inicial a las 432 horas y seguía manteniendo el 88% de la eficiencia inicial después de más de 3000 h (**Figura 2.25a**). Por el contrario, la eficiencia del dispositivo con spiro-OMeTAD dopado se redujo aproximadamente un 10% en tan solo 120 h, posiblemente esto sea debido a la mayor hidrofobicidad de **ZnTTPc 1** (**Figura 2.25b**).

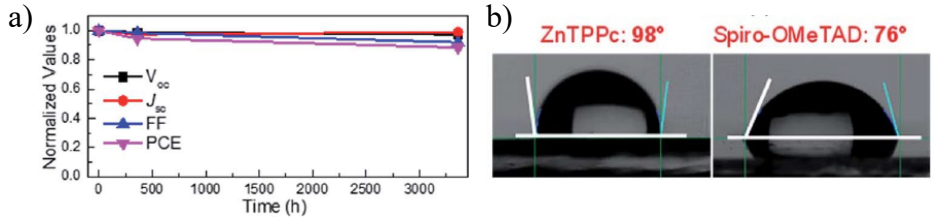

*Figura 2.**25**. a) Valores normalizados de los dispositivos con **ZnTTPc 1** durante el envejecimiento y b) ángulo de contacto de la perovskita con diferentes HTMs.*

En resumen, se ha sintetizado una ftalocianina simétrica tetrasustituida con grupos aromáticos conjugados de trifenilaminotienilo (**ZnTPPc 1**), con propiedades eléctricas superiores a las del material spiro-OMeTAD prístino, incluyendo una conductividad y movilidad relativamente altas, así como la capacidad de prevenir la formación de estados trampa en la superficie de la perovskita. Utilizando **ZnTPPc 1** como material transportador de huecos en células solares de perovskita hemos logrado una eficiencia de conversión de energía altamente competitiva superior al 14.5%, sin necesidad de utilizar dopantes ni aditivos.

2.4.2 Resumen artículo 2

En el artículo 2, se comparan las ftalocianinas objetivo con las ftalocianinas tetrasustituidas con grupos *terc*-butilo (**MPcTB4**) y sustituida con un grupo tiadiazol de cinc y de cobre (**MPcTDZ**) sintetizadas por el Dr. Jorge Follana.

La ftalocianina **ZnPcAE 5** (ZnPcAE en el artículo) se sintetizó de acuerdo con la literatura. [110] Para sintetizar **CuPcAE 6** (CuPcAE en el artículo), se siguió un protocolo similar. Primero se sintetizó **CuPcAEBoc 8** (CuPcAEBoc en el artículo) por ciclotetramerización estadística del 4-*terc*-butilftalonitrilo y 4-Boc-aminoetoxiftalonitrilo en presencia de $CuCl_2$. Seguidamente, por medio de su desprotección en medio ácido se obtuvo **CuPcAE 6**. Las ftalocianinas asimétricas **ZnPcTTPA 9** y **CuPcTTPA 10** (ZnPcTTPA y CuPcTTPA en el artículo) se prepararon mediante la ciclotetramerización estadística del 4-*terc*-butilftalonitrilo, y el ftalonitrilo **2** con la correspondiente sal metálica de cinc o cobre (**Esquema 2.3**).

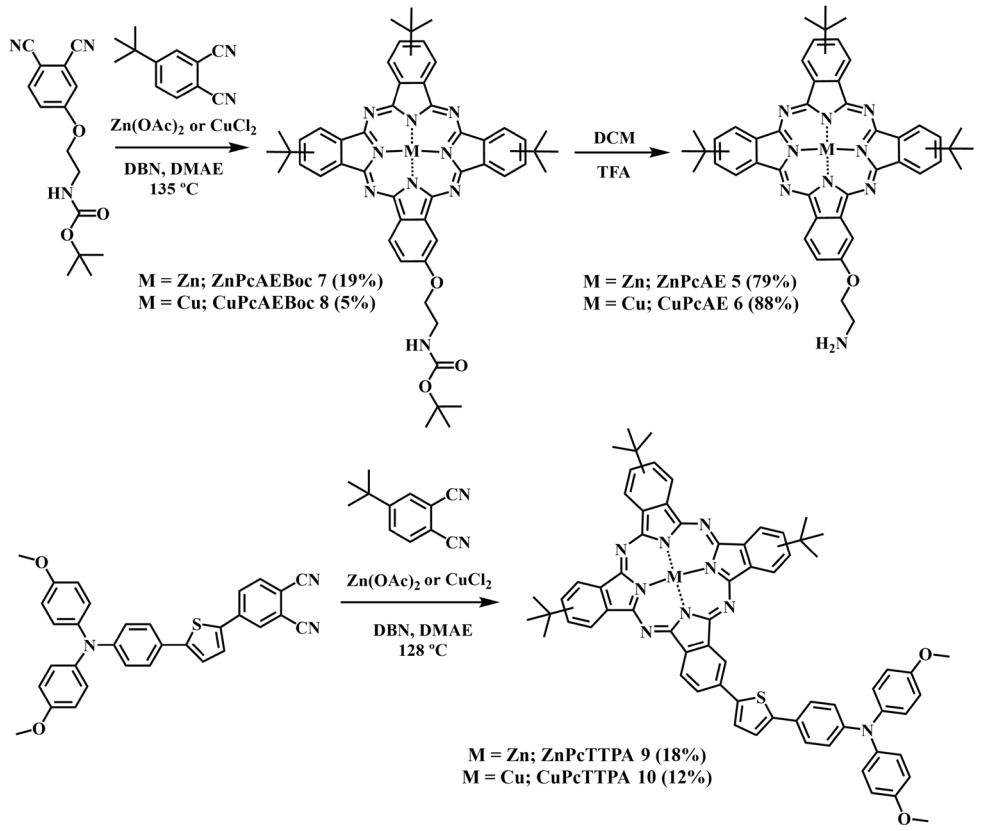

Esquema 2.3. Síntesis de ZnPcAE 5, CuPcAE 6, ZnPcTTPA 9 y CuPcTTPA 10.

El espectro de ^{1}H-RMN de **ZnPcTTPA 9** en THF-d_8 muestra señales aromáticas y alifáticas bien definidas (**Figura S16** en el artículo, pg. 86). En los espectros de absorción en DMF pueden verse la Banda Soret entre 300-400 nm y la Banda Q entre 600-700 nm típicas

[110] S. Fukuzumi, K. Ohkubo, J. Ortiz, A.M. Gutiérrez, F. Fernández-Lázaro, Á. Sastre-Santos, *J. Phys. Chem. A*, **2008**, *112*, 10744− 10752.

de las ftalocianinas (**Figura 2.26a**). La absorbancia como láminas delgadas sufre un ensanchamiento de las bandas, probablemente debido a la agregación (**Figura 2.26b**). Se caracterizaron las MPcs electroquímicamente mediante voltametría de pulso diferencial (**Figuras S25-S27** en el artículo, pgs 90 y 91) para calcular los valores de energía HOMO y LUMO. Parece que las ftalocianinas con sustitución similar pero diferentes metales centrales presentan E_{HOMO} y E_{LUMO} similares, mientras que diferentes sustituciones influyen en las propiedades semiconductoras. Además, puede verse que los niveles de energía de las MPcs están bien posicionados para la extracción de huecos y para impedir el paso del electrón fotogenerado (**Figura 2.26c**).

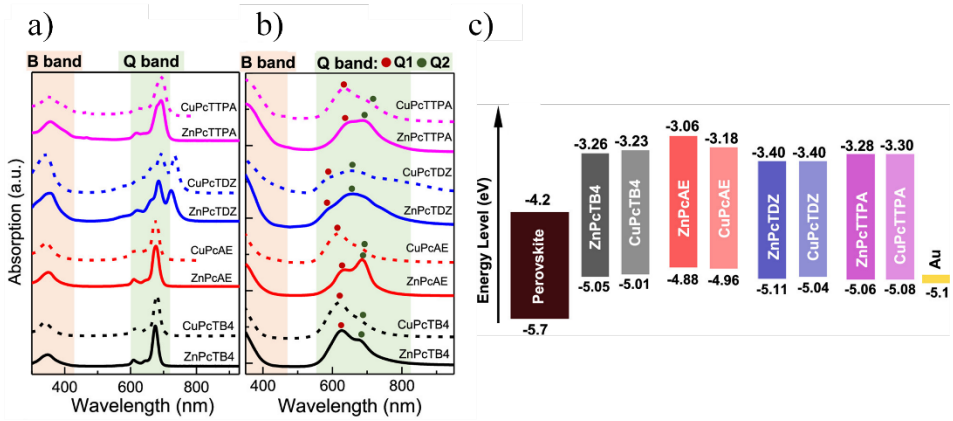

*Figura 2.**26**. Espectros de absorción UV-visible de las MPcs en a) disolución y b) lámina delgada, c) diagrama de los niveles de energía de las MPcs.*

Se fabricaron los dispositivos con las MPcs siguiendo la arquitectura FTO/b&mp-TiO_2/perovskita/MPcs/Au sin dopar, los resultados experimentales se muestran en la **Figura 2.27** y se resumen en la **Tabla 2.2**. La tendencia indica que las ftalocianinas de cobre tienden a obtener mayor eficiencia que sus análogas de cinc. La baja solubilidad de **CuPcAE 6** no permitió depositarla como lámina delgada uniforme, por lo que los resultados pueden no correlacionarse con sus verdaderas propiedades electrónicas. Además, se probó una arquitectura distinta con **ZnPcAE 5**, utilizando b-TiO_2/ SnO_2 en lugar de b&mp-TiO_2 como ETM, obteniendo aún mejores resultados de PCE llegando al 15.61%. Por lo que, no solo las propiedades electrónicas de las moléculas son importantes, sino también el resto de sus propiedades, como la solubilidad para facilitar el proceso de fabricación del dispositivo, así como la propia arquitectura del dispositivo final.

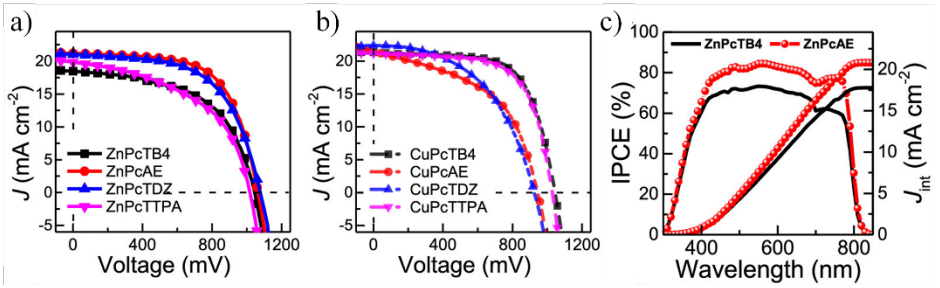

*Figura 2.**27**. Curvas J-V de los dispositivos campeones con a) ZnPcs y b) CuPcs como HTMs, c) IPCE y J_{int} integrada de los dispositivos **ZnPcTB4** y **ZnPcAE 5**.*

Tabla 2.2. Parámetros fotovoltaicos campeones de las PSCs con diferentes HTMs.

HTM	V_{oc} (mV)	J_{sc} (mA cm^{-2})	FF(%)	PCE (%)
ZnPcAE 5	**1063.5**	**21.19**	**63.2**	**14.25**
ZnPcAE 5[a]	**974.3**	**24.35**	**65.8**	**15.61**
CuPcAE 6	**915.7**	**22.66**	**59.2**	**12.29**
ZnPcTTPA 9	**1016.6**	**19.83**	**49.5**	**9.97**
CuPcTTPA 10	**1028.8**	**21.14**	**66.0**	**14.35**

[a]Dispositivos con b-TiO_2/SnO_2 como ETM, el resto con b&mp-TiO_2

Como se ha comentado anteriormente, la estabilidad a largo plazo es una característica fundamental. Para estudiarla se realizaron diferentes experimentos como medir el ángulo de contacto de una gota de agua, así como someter a los dispositivos a diferentes condiciones de estrés (**Figura 2.28**). Puede verse que en condiciones de humedad (30-70%) los dispositivos con ftalocianinas mantenían alrededor del 90 % de la eficiencia inicial tras 900h, mientras que el control con spiro-OMeTAD había perdido el 70% de eficiencia. Incluso en condiciones de estrés combinadas como humedad y calor o humedad y luz puede verse como los dispositivos con MPcs están mejor protegidos ante las condiciones adversas que los dispositivos control.

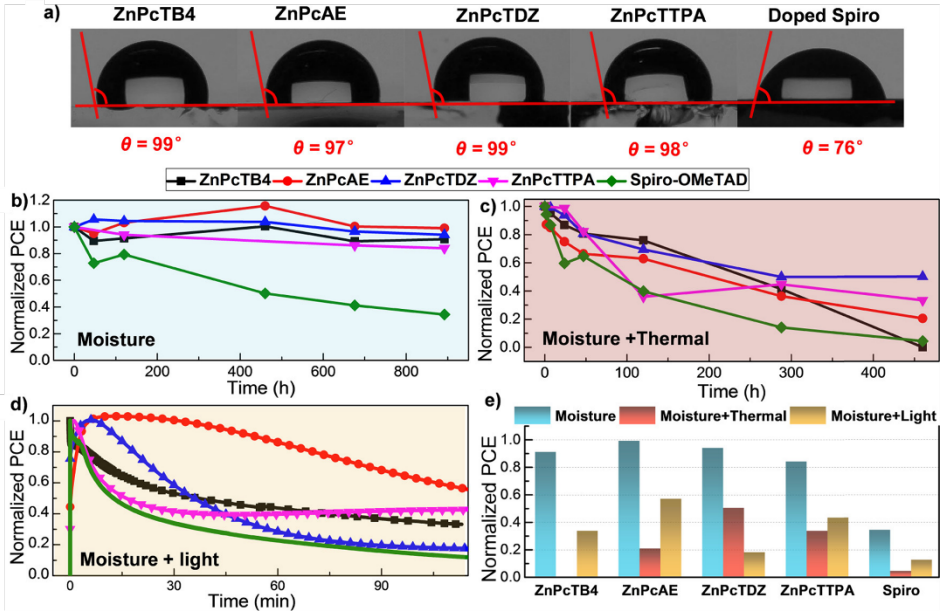

*Figura 2.**28**. a) Ángulo de contacto de la perovskita con los diferentes HTM. Gráficas de PCE de PSCs con diferentes ZnPcs y Spiro- OMeTAD envejecidas en b) condiciones ambientales (30-70% HR) durante unas 900 horas y c) condiciones de humedad y calor; d) seguimiento del punto de máxima potencia bajo condiciones de humedad e iluminación de 1 sol del dispositivo sin encapsular con diferentes HTMs, y (e) PCE normalizado obtenido tras las condiciones de envejecimiento.*

Como resumen de este artículo indicar que se ha llevado a cabo la síntesis de cuatro ftalocianinas asimétricas de cinc y cobre funcionalizadas con grupos aromáticos conjugados de trifenilaminotienilo o 2-aminoetoxilo y se han empleado como material transportador de huecos en células solares de perovskita sin utilizar dopantes. Los resultados obtenidos indican que **ZnPcAE 5** ha sido la ftalocianina que ha logrado la mayor eficiencia con un valor de 15.61%, seguida de **CuPCTTPA 10** con un 14.35% de PCE. Estos hallazgos sugieren que el diseño de las MPcs no puede ser guiado por un solo parámetro, tal como el metal central, ya que, para diferentes sustituyentes, el metal que proporciona las mejores eficiencias no ha sido siempre el mismo.

2.4.3 Resumen artículo 3

Antes de proceder con el resumen del tercer artículo, es importante destacar que la elaboración de los dispositivos con las diversas ftalocianinas como HTM, así como los ensayos subsecuentes, fueron posibles gracias a una estancia predoctoral de un mes en el grupo de investigación del Profesor Shahzada Ahmad en el Basque Center for Materials, Applications, and Nanostructures (BCMaterials) de la Universidad del País Vasco.

Los ftalonitrilos **19** y **20** se sintetizaron mediante una reacción de acoplamiento cruzado de Buchwald-Hartwig entre 4-yodoftalonitrilo y la amina secundaria correspondiente, catalizada por RuPhos Pd siguiendo las condiciones descritas por Nazeeruddin y colaboradores para un grupo de moléculas similares.[111] Gracias al uso de RuPhos Pd en lugar de $Pd_2(dba)_3$ se consiguió mejorar el rendimiento de la reacción del 43% al 85%. La síntesis de las ftalocianinas simétricas se llevó a cabo mediante la autocondensación del ftalonitrilo indicado (**19** o **20**) y $Zn(OAc)_2$ o $CuCl_2$ utilizando como disolvente DMAE y como catalizador DBN. Se obtuvieron **ZnPc-11**, **ZnPc-12**, **CuPc-13** y **CuPc-14** (ZnPc-1, ZnPc-2, CuPc-3 y CuPc-4 en el artículo) con rendimientos de 41%, 27%, 10% y 10%, respectivamente. Para las MPcs asimétricas se realizó una ciclotetramerización estadística entre 4-*terc*-butilftalonitrilo y el ftalonitrilo **19** o **20**, con la sal de zinc o cobre correspondiente, obteniéndose **ZnPc-15**, **ZnPc-16**, **CuPc-17** y **CuPc-18** (ZnPc-5, ZnPc-6, CuPc-7 y CuPc-8 en el artículo) con rendimientos del 14%, 16%, 8% y 8%, respectivamente (**Esquema 2.4**).

Los espectros ^{1}H-RMN de las ZnPcs en THF-d_8 mostraron señales aromáticas y alifáticas bien definidas (**Figuras S5**, **S9**, **S19**, **S23** en el artículo, pgs 118, 120, 125 y 127). Los espectros de absorción UV-vis medidos en DMF muestran las comúnmente conocidas bandas Soret y Q alrededor de 350 nm y 600-780 nm, respectivamente. Además, podemos observar una banda de transferencia de carga a 500 nm para las MPcs simétricas (**Figura 2.29a** y **b**). Se observa un aumento en el coeficiente de extinción molar y un pequeño cambio hipsocrómico en las ftalocianinas sustituidas por arilaminas fluoradas. Mientras que, en el caso de las MPcs asimétricas, se puede ver un gran desplazamiento hipsocrómico y un aumento menor en el coeficiente de extinción molar en comparación con sus contrapartes simétricas. Además, notamos una disminución en el coeficiente de extinción molar cuando el ion metálico se cambia de Zn (II) a Cu (II), así como un desplazamiento hipsocrómico, que es mayor en las Pcs simétricas. A partir de la caracterización electroquímica se obtuvieron los potenciales de oxidación y los valores de energía HOMO y LUMO (**Figura 2.29c** y **Tabla 1** en el artículo, pg 102). Las CuPcs mostraron niveles de E_{HOMO} más bajos en comparación con las ZnPcs. Se

[111] K.T. Cho, K. Rakstys, M. Cavazzini, S. Orlandi, G. Pozzi, M.K. Nazeerudin, *Nano Energy*, **2016**, *30*, 853-857.

puede observar un efecto similar en las Pcs sustituidas asimétricamente, y con la adición de átomos de flúor a las Pcs.

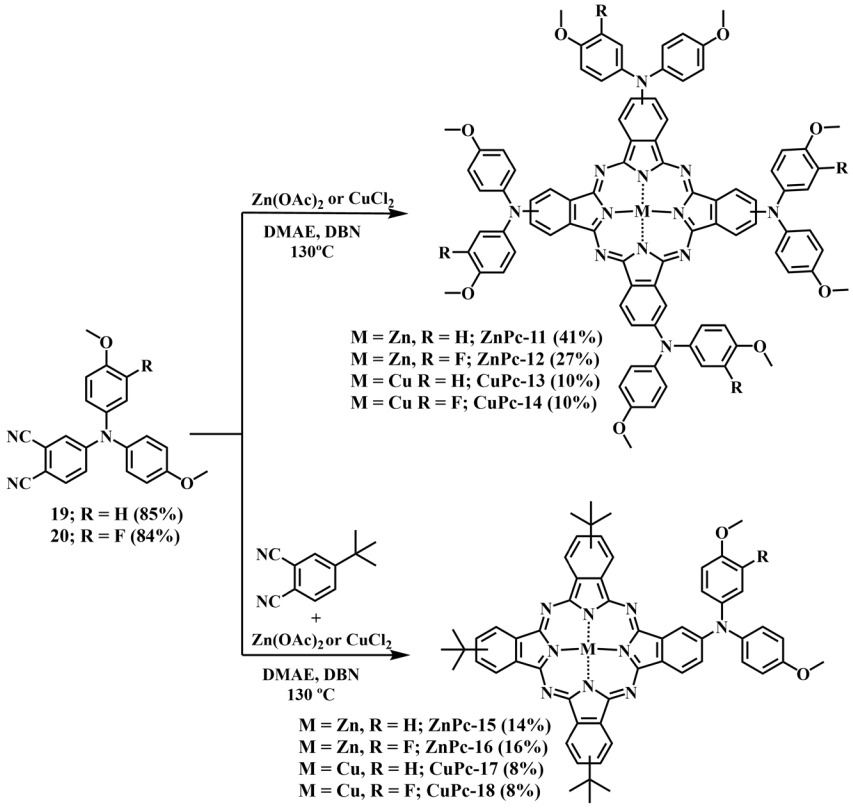

Esquema 2.4. Síntesis de ZnPc 11, ZnPc 12, CuPc 13, CuPc 14, ZnPc 15, ZnPc 16, CuPc 17 y CuPc 18.

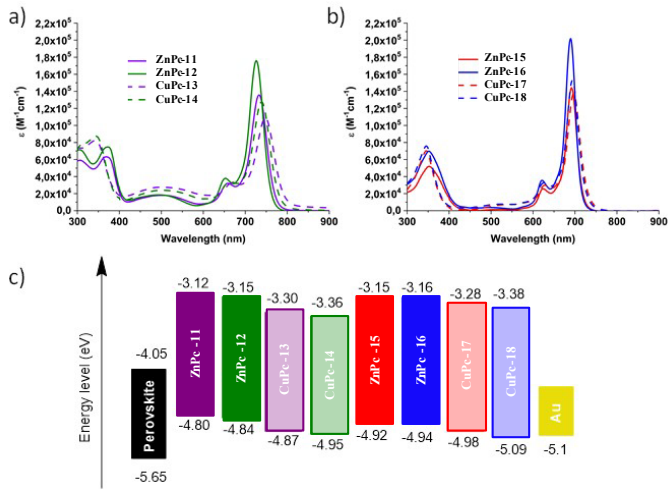

*Figura 2.**29**. Espectros de absorción UV-visible de las MPcs en disolución, a) MPcs simétricas, b) MPcs asimétricas, c) diagrama de los niveles de energía de las MPcs.*

Las PSCs se fabricaron con una estructura plana *n-i-p* de FTO/bl-TiO_2/ SnO_2/perovskita/MPc/Au, siendo la perovskita de triple catión, con la fórmula química de $Cs_{0.1}(FA_{0.9}MA_{0.1})_{0.9}Pb(I_{0.9}Br_{0.1})_3$ y no utilizando dopantes. Los resultados experimentales se representan en la **Figura 2.30** y resumen en la **Tabla 2.3**. Entre todas las MPcs, los mejores rendimientos fotovoltaicos se midieron a partir de Pcs asimétricas de Zn, que están a la par con los dispositivos basados en PTAA. En particular, el dispositivo con **ZnPc-16** con tres *terc*-butilos y un átomo de flúor produjo la máxima PCE un 15.40 %. En el caso de las CuPcs, las mejores eficiencias se observaron en las Pcs simétricas **CuPc-13** y **CuPc-14**, sin flúor y con flúor, respectivamente. Una causa probable del bajo rendimiento fotovoltaico observado en algunas MPcs podría atribuirse a un menor grado de solubilidad, factor clave para la formación de una capa homogénea.

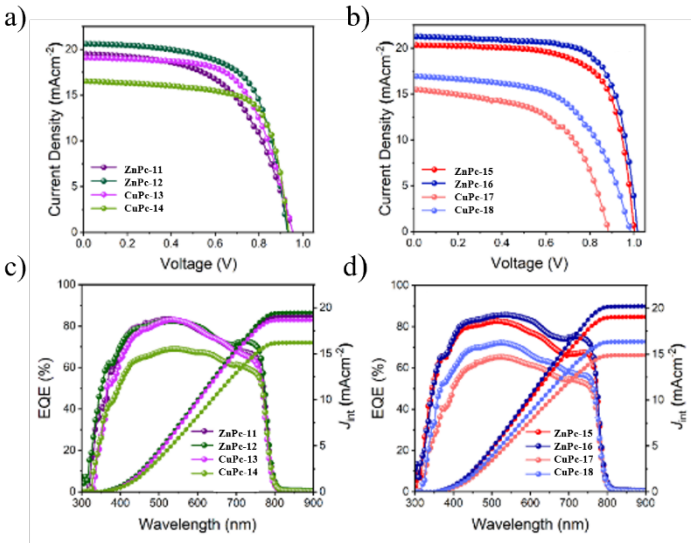

*Figura 2.**30**. Curvas J-V de los dispositivos con a) MPcs simétricas y b) MPcs asimétricas, EQE y J_{sc} integrada de los dispositivos con c) MPcs simétricas y d) MPcs asimétricas.*

Tabla 2.3. Parámetros fotovoltaicos de las PSCs con diferentes MPcs como HTM.

HTM	Scan	V_{OC} (mV)	J_{sc} (mAcm^{-2})	FF (%)	PCE (%)	Rs (Ω)	Rsh (kΩ)
ZnPc-11	**RS**	**954.9**	**19.48**	**55.57**	**10.34**	**136.89**	**7.9**
ZnPc-12	**RS**	**930.7**	**20.58**	**66.06**	**12.66**	**72.10**	**15.5**
CuPc-13	**RS**	**953.5**	**19.08**	**63.35**	**11.53**	**109.29**	**17.6**
CuPc-14	**RS**	**935.5**	**16.54**	**70.46**	**10.90**	**55.18**	**9.7**
ZnPc-15	**RS**	**1000.9**	**20.33**	**70.59**	**14.36**	**57.93**	**20.7**
ZnPc-16	**RS**	**1016.1**	**21.27**	**71.25**	**15.40**	**53.50**	**24.0**
CuPc-17	**RS**	**884.9**	**15.49**	**55.82**	**7.65**	**122.75**	**4.1**
CuPc-18	**RS**	**982.8**	**16.96**	**58.17**	**9.69**	**124.34**	**6.7**
PTAA	**RS**	**1031.7**	**20.55**	**73.28**	**15.53**	**52.15**	**17.3**

Se estudió la estabilidad operativa a largo plazo de los dispositivos con **ZnPc-15** y **ZnPc-16** no encapsulados y del dispositivo con PTAA de referencia en el punto de máxima

potencia (MPP) en condiciones ambientales (humedad relativa de 45-60% y 300 K) bajo luz LED blanca (**Figura 2.31**). Una vez más, **ZnPc-16** fue la que mejor funcionó mostrando una respuesta casi lineal manteniendo alrededor del 70% de su densidad de corriente inicial durante más de 60 h. Mientras que el dispositivo de referencia con PTAA prístino conservaba el 70% de su rendimiento original hasta 30 h, seguido de una rápida pérdida de rendimiento a partir de entonces.

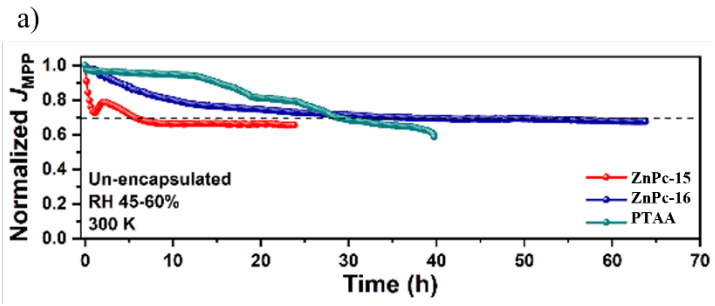

*Figura 2.**31**. Densidad de corriente normalizada del seguimiento continuo del punto de máxima potencia (MPP) para PSCs no encapsulados con ZnPc-15, ZnPc-16, y PTAA prístino como HTMs bajo condiciones atmosféricas.*

Se han sintetizado ocho ftalocianinas, cuatro simétricas y cuatro asimétricas, de cobre y cinc. Las ftalocianinas contenían grupos funcionales de difenilamina con y sin flúor, y se utilizaron como HTM en células solares de perovskita en ausencia de dopantes. La ftalocianina asimétrica **ZnPc-16** mostró la mayor eficiencia de conversión del 15.40%, seguida de la ftalocianina asimétrica **ZnPc-15** con una eficiencia del 14.36%. En el caso de las ftalocianinas de cobre, las ftalocianinas simétricas **CuPc-13** y **CuPc-14** mostraron las eficiencias de conversión más altas del 11.53% y 10.90%, respectivamente. Los resultados obtenidos respaldan las conclusiones aportadas en el resumen del artículo anterior, todos los parámetros sintéticos influyen en la eficiencia final de los dispositivos. En este caso concreto, se observó que los dispositivos que utilizan ftalocianinas de cinc obtuvieron mejores resultados de eficiencia, especialmente los que tienen una estructura asimétrica. Por otro lado, los dispositivos con ftalocianinas de cobre tuvieron mejores resultados utilizando ftalocianinas simétricas.

2.4.4 Conclusión general

Los resultados obtenidos en este capítulo de tesis reafirman la idea de que las ftalocianinas son buenas candidatas para actuar como material transportador de huecos en células solares de perovskita. Algunos de los compuestos sintetizados (**ZnPc-16 y ZnPcAE 5**) consiguen valores de eficiencia muy próximos a los referentes actuales (spiro-OMeTAD y PTAA) y todos ellos muestran mayor estabilidad frente a condiciones adversas. Es necesario recalcar que el diseño molecular de las ftalocianinas a sintetizar es de suma importancia, teniendo en cuenta no solo las propiedades electrónicas, como la presencia de buenos grupos conductores, sino también el resto de sus características, como la solubilidad para la facilidad de procesado y la correcta distribución de la capa, o la hidrofobicidad para mejorar la estabilidad.

En este capítulo hemos observado patrones para tener en cuenta de cara a la síntesis de futuras moléculas, como son:

Se esperaba que la extensión de la conjugación de la cadena en los sustituyentes de las Pcs, en este caso mediante anillos de tiofeno conjugados, supusiera una mejora en las propiedades electrónicas finales de estas moléculas y por lo tanto se viese reflejado en las eficiencias de los dispositivos finales. No obstante, se ha comprobado que no ha sido así.

Los grupos amino terminales son capaces de interaccionar con la capa de perovskita mejorando los resultados, esto se debe posiblemente a la pasivación de defectos mediante interacciones con los iones parcialmente expuestos de la capa de perovskita. Sin embargo, el aumento del número de grupos amino terminales disminuye la solubilidad en disolventes orgánicos dificultando su aplicación.

De la misma forma, se había observado una tendencia que parecía indicar que las ftalocianinas portadoras de cobre en su cavidad central, mostrarían mejores propiedades electrónicas que sus análogas de cinc. A pesar de ello, lo que hemos comprobado es que las CuPcs poseen peor solubilidad, por lo que las capas formadas son menos homogéneas, presentando defectos y proporcionando un peor resultado final.

Otro factor que hemos observado es que la adición de átomos de flúor en sustituyentes formados por grupos arilamino en MPcs tanto simétricas como asimétricas, parece disminuir los niveles de energía HOMO y LUMO de las ftalocianinas y, sobre todo, mejorar la eficiencia de los dispositivos fabricados con ellas.

Finalmente, se ha comprobado que el uso de ftalocianinas como material transportador de huecos sin dopar en células solares de perovskita ofrece prestaciones de eficiencia competitivas y de estabilidad excelentes.

Capítulo 3

Derivados de Ftalocianina y su aplicación como Agentes de Reconocimiento de Cuadruplejos

3 Ftalocianinas para reconocimiento de cuadruplejos

3.1 Introducción

El ácido desoxirribonucleico, más conocido por sus siglas ADN, es el conjunto de moléculas encargadas de contener la información genética, así como de transmitirla. Se descubrió en el año 1868 por Miescher que aisló un precipitado del núcleo celular con alto contenido en fosfatos al que nombró "nucleína", se trataba del ácido desoxirribonucleico.[112] No fue hasta 1953 cuando James Watson y Francis Crick[113] elucidaron la estructura de doble hélice del ADN ayudados por los patrones de rayos X de Franklin[114] y Wilkins[115] (**Figura 3.1**).

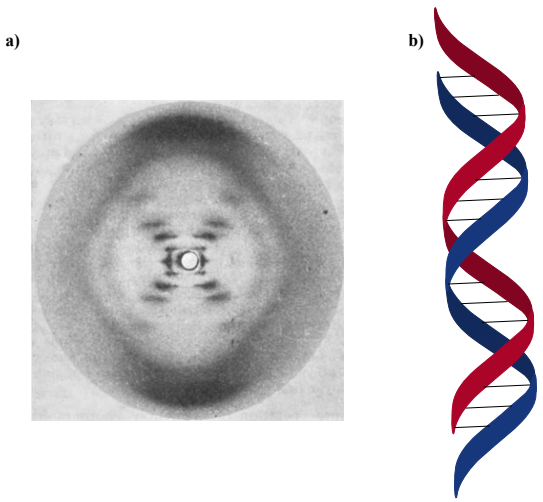

*Figura 3.**1**. a) Patrón de difracción de rayos X[114] y b) diagrama de la estructura tridimensional de la doble helice.*

El ADN está compuesto por nucleótidos, que a su vez están formados por una 2'-desoxirribosa, una base nitrogenada y un grupo fosfato. Contiene cuatro bases nitrogenadas, dos púricas (adenina y guanina) y dos pirimidínicas (la citosina y la timina). Los nucleótidos se unen formando una cadena mediante enlaces fosfodiéster entre los fosfatos 5' de uno y los OH- 3' de la desoxirribosa del siguiente (**Figura 3.2a**). Dos cadenas antiparalelas y complementarias pueden hibridarse formando la doble hélice. La estabilidad de esta estructura es muy elevada gracias a los enlaces de hidrogeno que forman las bases complementarias (**Figura 3.2b**) y por interacciones tipo π ente las bases consecutivas.

[112] R. Dahm, *Hum. Genet*., **2008**, *122*, 565-581.
[113] J.D. Watson, F.H.C. Crick, *Nature*, **1953**, *171*, 737-738.
[114] R.E. Franklin, R.G. Gosling, *Nature*, **1953**, *171*, 740-741.
[115] M.H.F. Wilkins, A.R. Stokes, H.R. Wilson, *Nature*, **1953**, *171*, 738-740.

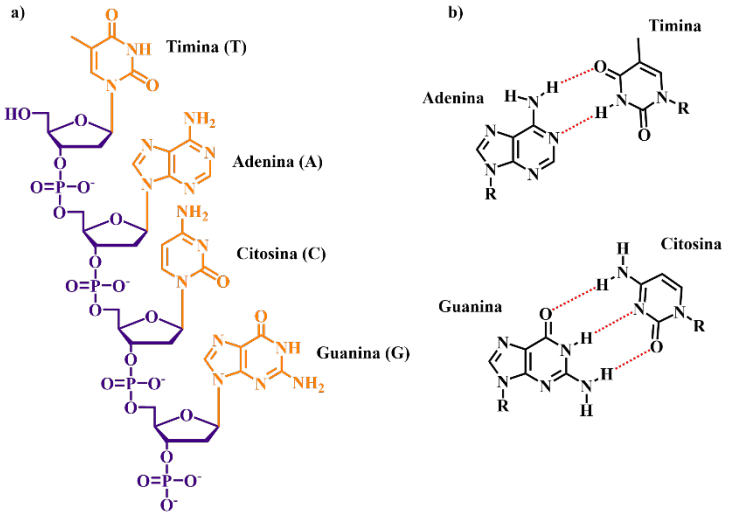

*Figura 3.**2**. a) Composición de la hebra de ADN, en morado el esqueleto de fósfato y la 2'-desoxirribosa, y en naranja las distintas bases. b) Pares de bases unidos mediante enlaces de hidrógeno en la configuración Watson-Crick.*

3.1.1 Descubrimiento

Los ácidos nucleicos son biomoléculas capaces de plegarse en diversas estructuras además de la generalmente conocida doble hélice descubierta por James Watson y Francis Crick en 1953.[113] De esta forma se amplía la visión de los procesos en los que están involucrados los ácidos nucleicos además de contener y transmitir la información genética. De hecho, solo el 3% del genoma humano se expresa en forma de proteínas, mientras que la gran mayoría (80%) está involucrado en la regulación de procesos bioquímicos.[116] Una de las formas no canónicas de los ácidos nucleicos son los cuadruplejos de guanina (G4s). La estructura de los G4s se descubrió en 1962,[117] casi una década después del modelo de doble hélice, Davies y colaboradores propusieron una estructura que se basaba en la asociación de cuatro guaninas en el mismo plano (**Figura 3.3**). Aunque para ello era necesario asumir que los enlaces de hidrogeno no seguían el modelo de Watson-Crick. Sin embargo, la primera observación de la formación de esta estructura fue en 1910 en disoluciones de ácidos nucleicos ricos en guanina que obtenían propiedades físicas similares a las de un gel.[118] Los G4s se pueden formar en condiciones fisiológicas por regiones de ADN y ARN ricas en guaninas. Su estructura principal, llamada tétrada o cuartete de guaninas, consiste en la disposición plana cuadrada de cuatro guaninas estabilizadas por enlaces de hidrógeno tipo Hoogsteen.[119] Otro factor que ayuda a la estabilización de esta estructura son las interacciones π-π entre las guaninas de tétradas contiguas.

[116] I. Dunham, A. Kundaje, S.F. Aldred, P.J. Collins, C.A. Davis, F. Doyle, C. Epstein, S. BSFrietze, J. Harrow, R. Kaul, et al., *Nature*, **2012**, *489*, 57–74.
[117] M. Gellert, M. Lipsett, D. Davies, *Proc. Natl. Acad Sci. USA*, **1962**, *48*, 2013–2018.
[118] I. Bang, *Biochem. Z.*, **1910**, *26*, 293–311.
[119] J. Carvalho, J.-L. Mergny, G.F. Salgado, J.A. Queiroz, C. Cruz, *Trends Mol. Med.*, **2020**, *26*, 848–861.

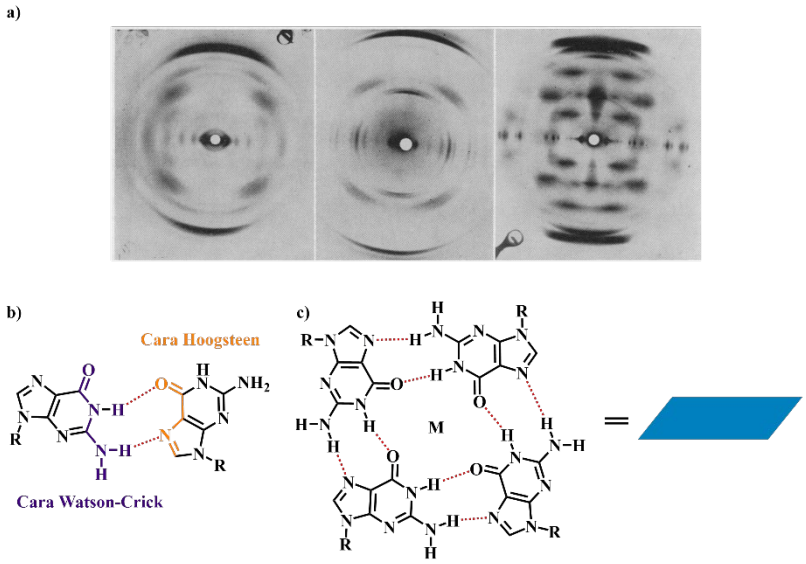

Figura 3.3. a) Patrones de difracción de G4s. b) Enlaces de hidrogeno entre las caras Watson-Crick y Hoogsteen. c) Estructura de una tétrada formada por 4 guaninas.

Las tétradas pueden estabilizarse con cationes como el potasio y el sodio, que se coordinan con el canal central electronegativo formado por los grupos carbonilos.[119] Los G4s formados con K^+ tienen mayor relevancia debido a la mayor concentración intracelular (alrededor de 140 mM) y a que por tamaño se sitúa en la cavidad formada por dos tétradas estabilizándose con 8 oxígenos, en lugar de 4 como pasa en el caso del Na^+, que se sitúa en el interior de una tétrada.[120] Los G4s pueden presentar una amplia variedad de topologías dependiendo de la secuencia de nucleótidos, el tamaño del bucle, la estequiometría de la cadena (intra o intermolecular), la polaridad y orientación de las cadenas (paralela o antiparalela) y el catión presente.[121]

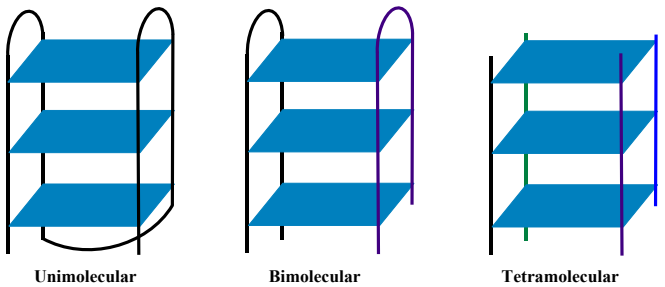

Figura 3.4. Diagrama de la estructura de G4s unimoleculares, bimoleculares y tetramoleculares.

En cuanto a la estequiometría de la cadena, se pueden distinguir G4s unimoleculares, bimoleculares y tetramoleculares, según si están formados por una, dos o cuatro moléculas de ácidos nucleicos (**Figura 3.4**). Ordenamientos de tres cadenas también son posibles.[122] Como

[120] C. Reina, V. Cavalieri, *Int. J. Mol. Sci.*, **2020**, *21*, 4172-4191.
[121] J. Spiegel, S. Adhikari, S. Balasubramanian, *Trends Chem.*, **2020**, *2*, 123–136.
[122] A. Singh, S. Kukreti, *J. Biomol. Struct. Dyn.*, **2017**, *36*, 2773–2786

norma general, secuencias ricas en guaninas con capacidad de formar G4s unimoleculares están compuestas por cuatro regiones de guaninas, separadas por tres regiones bucle de diferentes longitudes y secuencias. Las bimoleculares por secuencias que contienen dos o tres regiones de guaninas y las tetramoleculares por secuencias que contienen una única región de guaninas. [123] Las G4 biológicamente más relevantes presentan estructuras intramoleculares con tres tétradas de guanina siendo la más común. Las guaninas de cada tétrada pueden adoptar conformaciones *anti* y *syn* (**Figura 3.5**), lo que define la topología del G4.[119] Las G4s paralelos tienen todas las guaninas en conformación *anti*, estando las cadenas en la misma dirección relativa, mientras que los antiparalelos tienen ambas conformaciones y las cadenas de sentidos opuestos. Existe también una topología híbrida en la cual tres cadenas tienen el mismo sentido y la cuarta el contrario. [124] La topología y estabilidad del G4 también dependen en gran medida del catión. Por ejemplo, la misma secuencia puede adquirir diferentes conformaciones con K^+ y Na^+ como sucede en secuencias de ADN teloméricas. [125] En cuanto a los G4s de ARN, existe menor diversidad en cuanto a la topología que pueden presentar. Esto es debido a que solo pueden adoptar una conformación paralela por el grupo 2'-hidroxilo de la ribosa, que bloquea las guaninas en posición *anti*. [126]

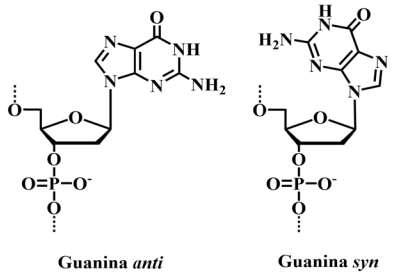

Figura 3.5. Conformación anti y sin de las guaninas.

Disponer de la secuencia completa del genoma humano ha permitido buscar regiones ricas en guanina capaces de formar G4s. Multitud de análisis computacionales realizados por diferentes grupos han encontrado más de 700.000 secuencias potenciales a lo largo del genoma humano. [127, 128] Un detalle importante proveniente de estos estudios es que estas secuencias propensas a formar G4s están ampliamente distribuidas a lo largo del genoma, pero no de forma aleatoria. Están dispuestas de forma prevalente en los telómeros, regiones promotoras de oncogenes y en regiones 5' sin traducir.[128] Las secuencias ricas en guaninas se encuentran en regiones que influyen en procesos del metabolismo de los genes, así como procesos biológicos clave como la replicación y recombinación del ADN, la transcripción y la traducción de genes. Estas observaciones han impulsado la investigación tanto en la posible función de los G4s en enfermedades como el cáncer, como en el desarrollo de moléculas pequeñas como ligandos para utilizarse como potenciales agentes terapéuticos.

[123] S. Kolesnikova, E.A. Curtis, *Molecules*, **2019**, *24*, 3074-3093.
[124] S. Zhang, Y. Wu, W. Zhang, *ChemMedChem*, **2014**, *9*, 899–911.
[125] A. Ambrus, D. Chen, J. Dai, T. Bialis, R.A. Jones, D. Yang, *Nucleic Acids Res.*, **2006**, *34*, 2723–2735.
[126] J. Song, J.-P. Perreault, I. Topisirovic, S. Richard, *Translation*, **2016**, *4*, e1244031-e1244046.
[127] A. Bedrat, L. Lacroix, J.-L. Mergny, *Nucleic Acids Res*., **2016**, *44*, 1746–1759.
[128] V.S. Chambers, G. Marsico, J.M. Boutell, G.P. Smith, M. Di Antonio, S. Balasubramanian, *Nat Biotechnol*, **2015**, *33*, 877-881.

3.1.2 Dianas de G4s en células cancerosas

Telomerasa y mantenimiento de los telómeros

Los telómeros son regiones de ADN no codificante situadas en los extremos de los cromosomas. Se trata de secuencias altamente repetitivas encargadas de estabilizar los cromosomas e intervienen en el envejecimiento celular. En la división de células somáticas, cada vez que el material genético se replica, los telómeros se acortan hasta el punto en el que la célula alcanza la senescencia, momento en el cual deja de dividirse y entra en un estado de apoptosis. El ADN telomérico humano está compuesto por 5-10 kb de longitud de doble cadena con repeticiones en tándem de d[TTAGGG] seguida de una cadena simple de 30-600 bases en el extremo 3'.[129] La primera observación de la formación de G4s biológicamente relevantes se dio en este extremo monocatenario rico en guaninas.[130] La longitud de la doble cadena disminuye cada vez que se produce la división celular en células somáticas debido al efecto del final de la replicación. Por otro lado, el extremo monocatenario puede alargarse por la telomerasa, una enzima con actividad transcriptasa inversa. En células cancerosas, la telomerasa está sobreexpresada, manteniendo la longitud de los telómeros y actuando como promotor tumoral ayudando a las células a evitar la apoptosis y conseguir la inmortalidad celular.[131] Por lo tanto, el desarrollo de moléculas que se unan y estabilicen G4s teloméricos, inhibiendo la actividad de la telomerasa, es una prometedora estrategia terapéutica contra el cáncer (**Figura 3.6**).[132]

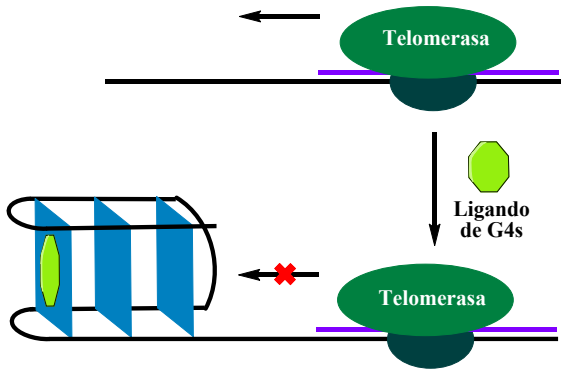

Figura 3.6. Diagrama de la inhibición de la telomerasa por la estabilización del G4.

La estructura de los G4s teloméricos es muy polimórfica, por lo que se han propuesto diversos modelos.[133] El primer modelo se propuso en 1992 para la secuencia única repetida d[TTAGGGT], la cual formaba un G4 de cadenas paralelas en una disolución con K^+.[134] Éste junto con otros estudios avalaban la posibilidad de formación de G4s en los telómeros y el potencial de las moléculas pequeñas para estabilizarlos.[135] Esta idea se demostró por primera

[129] A. Wojtyla, M, Gladych, B. Rubis, *Mol. Biol. Rep.*, **2010**, *38*, 3339–3349
[130] C. Lin, D. Yang, In *Telomeres and Telomerase: Methods in Molecular Biology*; Z. Songyang, Ed.; Humana Press: New York, NY, USA, **2017**, *1587*, 171–196.
[131] J.W. Shay, W.E Wright, *Nat. Rev. Genet.*, **2019**, *20*, 299–309.
[132] S. Neidle, *J. Med. Chem.*, **2016**, *59*, 5987–6011.
[133] S. Neidle, *Therapeutic Applications of Quadruplex Nucleic Acids*, 1st ed.; Academic Press Inc.: Amsterdam, The Netherlands, **2012**.
[134] Y. Wang, D.J. Patel, *Biochemistry*, **1992**, *31*, 8112–8119.
[135] N. Zhang, A.T. Phan, D.J. Patel, *J. Am. Chem. Soc.*, **2005**, *127*, 17277–17285

vez con el compuesto 2,6-diamidodiantraquinona, que podía inhibir la actividad de la telomerasa estabilizando las estructuras de los G4s. [136]

Promotores

En genómica, se entiende por promotor a una región situada relativamente próxima al inicio de transcripción de un gen, donde se pueden unir proteínas relevantes (como la ARN polimerasa o factores de transcripción) que promueven o inhiben la transcripción de dicho gen. La primera vez que se observó la aparición de conformaciones inusuales de ADN en promotores de genes fue en un elemento hipersensible a nucleasas (NHE) dentro del promotor del gen *c-myc*. [137] El gen *c-myc* interviene en el crecimiento celular y en procesos de apoptosis, por lo que su sobreexpresión produce un aumento de la proliferación celular e inhibición de la diferenciación, y está asociado con gran variedad de cánceres humanos como colon, mama, pulmón, osteosarcoma, glioblastoma y leucemia mieloide. [138] La primera evidencia de que los G4s podían actuar como represores transcripcionales vino del uso de la porfirina catiónica TMPyP4, que inhibió la transcripción de *c-myc* estabilizando la estructura G4 en su promotor (**Figura 3.7**). [139]

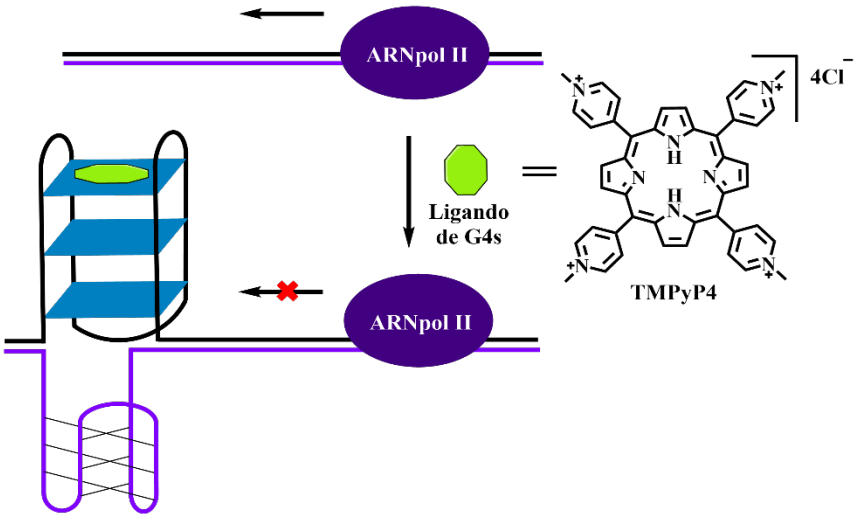

Figura 3.7. Diagrama de la inhibición de la transcripción por la estabilización del G4 en la región promotora.

Desde entonces, se han encontrado más secuencias capaces de formar G4s en regiones promotoras de otros oncogenes como *c-Fos, c-kit*, *KRAS*, *VEGF*, *PDGF-A*, *Rb*, *RET*, *Hif-1α*, bcl2 y *hTERT*. [140] Estos protooncogenes están involucrados con el crecimiento y la proliferación, y sus regiones promotoras contienen varias regiones ricas en G y C. Se cree que la formación de G4s en estas regiones modula la actividad transcripcional de los genes. Además, estos genes son importantes en la señalización y diferenciación celular, la regulación

[136] D. Sun, B. Thompson, B.E. Cathers, M. Salazar, S. Kerwin, J.O. Trent, T.C. Jenkins, S. Neidle, L.H. Hurley, *J. Med. Chem*., **1997**, *40*, 2113–2116.
[137] S. Basu, E. Wickstrom, *Nucleic Acids Res*., **1997**, *25*, 1327–1332.
[138] B.-J. Chen, Y.-L. Wu, Y. Tanaka, W. Zhang, *Int. J. Biol. Sci*., **2014**, *10*, 1084–1096.
[139] A. Siddiqui-Jain, C.L. Grand, D.J. Bearss, L.H. Hurley, *Proc. Natl. Acad. Sci. USA*, **2002**, *99*, 11593–11598.
[140] R. Rigo, M. Palumbo, C. Sissi, *Biochim. Biophys. Acta (BBA) Gen. Subj*., **2017**, *1861*, 1399–1413.

metabólica y la progresión del cáncer. Se han desarrollado varios ligandos con la capacidad de regular la expresión génica a nivel de G4s.[140]

ARN

Como se ha comentado anteriormente la formación de G4s en ácidos nucleicos de ARN también es común, además son más estables termodinámicamente, compactos y menos hidratados que los de ADN.[126] En el año 2008 se demostró por primera vez que el transcrito de ADN telomérico TERRA, compuesto por motivos UUAGGG repetidos en tándem era capaz de formar G4s estables.[141] También se pueden encontrar en ARNm no codificante y en mi-ARN. Se ha demostrado en diversos estudios que los G4s de ARN intervienen en procesos como transcripción, regulación de la traducción, procesado de ARNm y empalme alternativo.[142] Por ello es interesante la búsqueda de ligandos que puedan estabilizar o desestabilizar estas estructuras para conseguir la inhibición de la traducción o recuperar la regulación de niveles alterados de moléculas de ARN en diferentes patologías. Por ejemplo, carboxipiridostatina que presenta una alta especificidad por los G4s de ARN frente a los de ADN.[143]

Control de la formación y relajación de G4s

Las helicasas son motores moleculares capaces de separar las cadenas del ADN bicatenario. Están implicadas en la replicación, reparación, recombinación y transcripción del ADN, además del mantenimiento de los telómeros.[144] Los G4s se pueden formar cuando actúa la helicasa. La correcta formación y desplegamiento de los G4s es esencial para el funcionamiento adecuado de los procesos biológicos implicados. Son proteínas con actividad helicasa las que regulan específicamente la formación de los G4s (WRN, BLM, DHX36, FANCJ, and ScPif).[145] Las helicasas de G4s actúan durante el mantenimiento de telómeros, la replicación de ADN y la transcripción génica. Sin estas proteínas la acumulación de G4s genera defectos en estos procesos.[146] La actividad de las helicasas podría modularse en presencia de ligandos de G4s con finalidad farmacológica (**Figura 3.8**).

[141] Y. Xu, K. Kaminaga, M. Komiyama, *Nucleic Acids Symp. Ser*. **2008**, *52*, 175–176.
[142] M. Malgowska, K. Czajczynska, D. Gudanis, A. Tworak, Z. Gdaniec, *Acta Biochim. Pol*., **2017**, *63*, 609–621.
[143] M. Di Antonio, G. Biffi, A. Mariani, E.-A. Raiber, R. Rodriguez, S. Balasubramanian, *Angew. Chem. Int. Ed.*, **2012**, *51*, 11073–11078.
[144] O. Mendoza, A. Bourdoncle, J.-B. Boulé, R.M. Brosh, J.-L. Mergny, *Nucleic Acids Res*., **2016**, *44*, 1989–2006
[145] M. Sauer, K. Paeschke, *Biochem. Soc. Trans*., **2017**, *45*, 1173–1182.
[146] a) L. Crabbe, R.E. Verdun, C.I. Haggblom, J. Karlseder, *Science*, **2004**, *306*, 1951–1953. b) P. Prorok, M. Artufel, A. Aze, P. Coulombe, I. Peiffer, L. Lacroix, A. Guédin, J.-L. Mergny, J. Damaschke, A. Schepers, et al., *Nat. Commun*., **2019**, *10*, 1–16. c) L.T. Gray, A.C. Vallur, J. Eddy, N. Maizels, *Nat. Chem. Biol*., **2014**, *10*, 313–318.

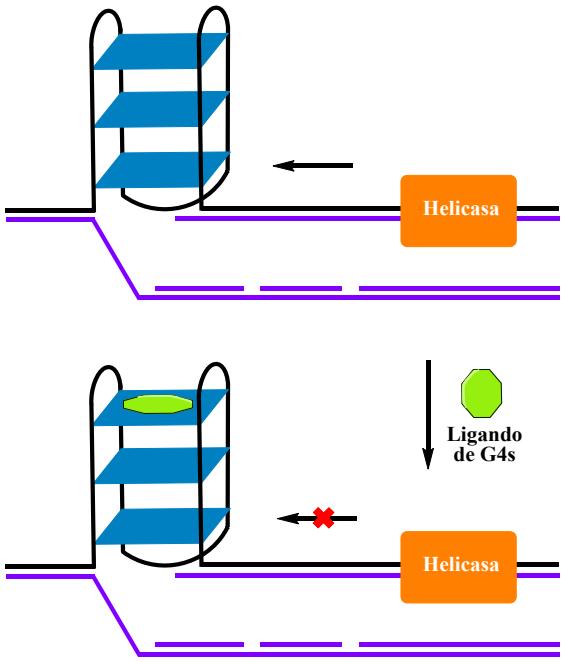

Figura 3.8. Diagrama de la inhibición de la actividad helicasa por la estabilización del G4.

La existencia de proteínas naturales que reconocen e interaccionan con G4s *in vivo* refuerza la idea de que las estructuras G4 provenientes de secuencias ricas en guaninas son de gran relevancia biológica. Estas proteínas se unen, favorecen o desestabilizan los G4s, se han encontrado más de 30 capaces de unirse a estructuras G4 en regiones teloméricas, regiones de promotores y a G4s de ARN. [147]

3.1.3 Relevancia terapéutica de los G4s

Los G4s están relacionados con los mecanismos que controlan los telómeros, la regulación transcripcional de genes relacionados con cáncer, la replicación y la inestabilidad genómica. Además, se ha visto experimentalmente que existe un mayor número de G4s en células cancerosas que en células normales, lo que puede facilitar estas estructuras como dianas contra el cáncer. [148] La formación de G4s de ADN depende en gran medida de la estructura de la cromatina y se encuentra con frecuencia en regiones reguladoras sin nucleosomas en las proximidades de sitios de inicio de la transcripción de genes que experimentan una transcripción elevada. [149] Además, los G4s de ARN influyen en la traducción y en las proteínas de unión asociadas al empalme, regulando el empalme alternativo de multitud de genes importantes en la carcinogénesis. Las diferentes topologías de los G4s permiten el reconocimiento selectivo de sus estructuras mediante pequeños ligandos. Diversos ligandos

[147] a) D.J. Patel, A.T. Phan, V. Kuryavyi, *Nucleic Acids Res*., **2007**, *35*, 7429–7455. b) V. Brázda, L. Hároníková, J.C.C. Liao, M. Fojta, *Int. J. Mol. Sci*., **2014**, *15*, 17493–17517. c) S. Ray, J.N. Bandaria, M.H. Qureshi, A. Yildiz, H. Balci, *Proc. Natl. Acad. Sci. USA*, **2014**, *111*, 2990–2995. d) V.A. Soldatenkov, A.A. Vetcher, T. Duka, S. Ladame, *ACS Chem. Biol*., **2008**, *3*, 214–219.
[148] V.S. Chambers, G. Marsico, J.M. Boutell, M. Di Antonio, G.P. Smith, S. Balasubramanian, *Nat. Biotechnol.*, **2015**, *33*, 877–881.
[149] R. Haensel-Hertsch, D. Beraldi, S.V. Lensing, G. Marsico, K. Zyner, A. Parry, M. Di Antonio, J. Pike, H. Kimura, M. Narita, et al., *Nat. Genet*., **2016**, *48*, 1267–1272.

han sido evaluados por su potencial terapéutico y han mostrado actividad antitumoral *in vitro* y en modelos de xenoinjertos. [150] Algunos incluso están en ensayos clínicos. Por ejemplo, CX-5461 [151] para pacientes con cáncer de mama con tumores deficientes en BRCA, o CX-3543 [152] contra diferentes tumores, aunque debido a su alta unión a la albumina no pasó de fase III. Es natural asumir que muchos de estos ligandos podrían unirse a diferentes G4s y por lo tanto regular la expresión de genes indeseados, por ello sería necesario realizar un perfil transcripcional de los sistemas cancerosos tratados con ligandos de G4s para identificar las rutas afectadas.

3.1.4 Complejos metálicos en el diseño de ligandos de G4s

Los complejos metálicos tienen un amplio espectro de propiedades estructurales y electrónicas que pueden aplicarse al diseño de ligandos de G4s con gran afinidad de unión y selectividad. El metal central puede jugar un papel importante en la organización estructural de los ligandos con geometrías y orientaciones específicas para la unión. Se pueden establecer diferentes geometrías de coordinación modificando el metal central y los ligandos. Además, los metales al tener la capacidad de retirar electrones permiten la formación de sistemas pobres en electrones lo que permite interacciones π más fuertes con las tétradas. En principio, el metal electropositivo podría situarse en el interior de las tétradas, sustituyendo el catión que normalmente ocuparía este lugar y aumentando así la estabilización electrostática. Todas estas características hacen a los complejos metálicos muy buenos candidatos para establecer uniones especificas con G4s. Por ello, se han estudiado multitud de compuestos metalados capaces de unirse a G4s, [153, 154] entre ellos, han tomado mayor importancia los complejos con metales divalentes como Zn(II), Cu(II), o Pt(II) capaces de adoptar la conformación plana cuadrada.

La mayor parte de los estudios se han centrado en moléculas planas con sistemas π deslocalizados que pueden interaccionar mediante apilamiento π con las tétradas. También se ha visto que pueden interaccionar con el esqueleto de fosfato negativamente cargado en los bucles de ADN si poseen sustituyentes con carga positiva. [155] Los complejos metálicos podrían interaccionar también mediante coordinación directa con las bases o el esqueleto de fosfato.

Los complejos metálicos fluorescentes que reconozcan específicamente estructuras de G4s pueden ser útiles también como sonda/marcadores para la detección y visualización de estas estructuras en las células. Otra ventaja de los complejos metálicos es que su fluorescencia puede ser sensible a cambios, por lo que puede utilizarse como sonda de unión si su fluorescencia aumenta o disminuye al unirse al G4.

---

[150] R. Rodriguez, K.M. Miller, J. Forment, C. Bradshaw, M. Nikan, S. Britton, T. Oelschlaegel, B. Xhemalce, S. Balasubramanian, S.P. Jackson, *Nat. Chem. Biol.*, **2012**, *8*, 301–310.

[151] H. Xu, M. Di Antonio, S. McKinney, V. Mathew, B. Ho, N.J. O'Neil, N. Dos Santos, J. Silvester, V. Wei, J. Garcia, et al., *Nat. Commun*., **2017**, *8*, 14432-14449.

[152] D. Drygin, A. Siddiqui-Jain, S. O'Brien, M. Schwaebe, A. Lin, J. Bliesath, C.B. Ho, C. Proffitt, K. Trent, J.P. Whitten, et al., *Cancer Res*., **2009**, *69*, 7653–7661.

[153] a) T. Kench, R. Vilar, In *Annual Reports in Medicinal Chemistry*; S. Neidle, Ed.; Academic Press Inc.: Cambridge, MA, USA, **2020**; *54*, 485–515. b) S. N. Georgiades, N.H.A. Karim, K. Suntharalingam, R. Vilar, *Angew. Chem. Int. Ed*., **2010**, *49*, 4020–4034. c) R. Vilar, In *Advances in Inorganic Chemistry*; P.J. Sadler, R. van Eldik, Eds.; Academic Press Inc.: Cambridge, MA, USA, **2020**; *75*, 425–445.

[154] a) Q. Cao, Y. Li, E. Freisinger, P.Z. Qin, R.K.O. Sigel, Z.-W. Mao, *Inorg. Chem. Front*. **2016**, *4*, 10–32. b) A. Erxleben, *Chim. Int. J. Chem*., **2017**, *71*, 102–111.

[155] a) J.E. Reed, S. Neidle, R. Vilar, *Chem. Commun*., **2007**, 4366–4368. b) J.E. Reed, A. Arola-Arnal, S. Neidle, R. Vilar, *J. Am. Chem. Soc*. **2006**, *128*, 5992–5993. c) S. Gama, I. Rodrigues, F. Mendes, I.C. Santos, E. Gabano, B. Klejevskaja, J. Gonzalez-Garcia, M. Ravera, R. Vilar, A. Paulo, *J. Inorg. Biochem*. **2016**, *160*, 275–286.

Los ligandos metálicos pueden combinar propiedades fluorescentes y anticancerígenas, confiriéndoles capacidad de imagen/diagnosis. Esta combinación puede aprovecharse para el uso teragnóstico, que incluye la terapia y el diagnostico al mismo tiempo. Aunque presenta limitaciones debido a la corta penetración de la luz y fotones del infrarrojo cercano en tejidos biológicos, lo que limita su utilidad para aplicaciones *in vivo* de cuerpo entero, como el caso de enfermedad metastática ampliamente distribuida. A pesar de que este problema podría solucionarse con las técnicas de imagen nuclear, aún no se han estudiado complejos radiometalados como ligandos de G4s.

3.1.5 Antecedentes

Las metaloporfirinas han sido ampliamente estudiadas como ligandos de G4s debido a que poseen el tamaño, simetría y geometría ideales para apilarse con las tétradas mediante interacciones π-π. La primera porfirina utilizada para el reconocimiento de G4s fue **TMPyP4**, sin embargo, se unía a G4s con el doble de afinidad que la doble cadena (**Figura 3.9a**).[156] Otro ejemplo es **Pd-TEGPy**, que actúa como sonda fluorescente al unirse selectivamente a G4s, siendo un compuesto prometedor para la detección de estas estructuras *in vitro* (**Figura 3.9b**).[157] El grupo de Bhattacharyya estudió dos porfirinas catiónicas de cobalto (**Tetrakis**) y paladio (**Octacetyl**) como ligandos para estabilizar G4s de KRAS (**Figura 3.9c**). Los dos complejos presentaron una citotoxicidad importante y bloquearon la metástasis inhibiendo la transición epitelial a mesenquimal. Además, la expresión del gen KRAS se redujo drásticamente tanto a nivel de proteína como de ARN. En los estudios *in vivo* en modelos de ratón, se observó que eran efectivas contra los tumores sólidos de EAC (Adenocarcinoma de esófago) junto con una toxicidad sistémica significativamente baja.[158]

[156] N.V. Anantha, M. Azam, R.D. Sheardy, *Biochemistry*, **1998**, *37*, 2709-2714.
[157] P.D Diabate, A. Laguerre, M. Pirrotta, N. Desbois, J. Boudon, C.P. Gros, D. Monchaud, *New J. Chem*., **2016**, *40*, 5683–5689.
[158] R. Pattanayak, A. Barua, A. Das, T. Chatterjee, A. Pathak, P. Choudhury, S. Sen, P. Saha, M. Bhattacharyya, *Eur. J. Pharm. Sci*., **2018**, *125*, 39–53.

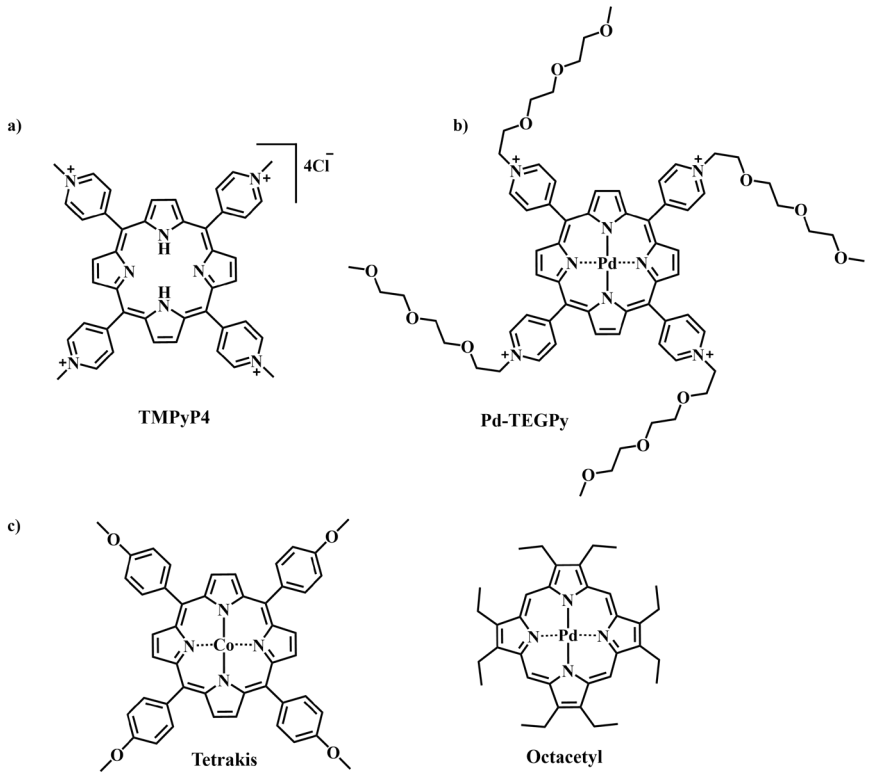

Figura 3.9. Estructura de diferentes porfirinas utilizadas como ligandos de G4s.

Otra amplia familia de macrociclos metálicos estudiada como ligandos de G4s son las ftalocianinas metálicas. Un importante ejemplo es la ftalocianina **Zn-DIGP**, sustituida con diisopropilguanidinas, descrita por Luedtke (**Figura 3.10a**). [159] Se observó experimentalmente que podía actuar como sonda para G4s de *c-myc*, además de reducir su expresión. También se demostró que podía estabilizar los G4s formados en la región promotora de KRAS y de regular potencialmente su expresión. Entre las ventajas de esta MPc se encuentra su solubilidad en agua, capacidad de entrar en las células y su afinidad por ARN/ADN. Los resultados apuntan a que las MPcs catiónicas son candidatas adecuadas para el desarrollo de terapias luminiscentes que pueden dirigirse específicamente a oncogenes.

En otro estudio de Luedtke se sintetizaron seis ftalocianinas de cinc en las que se modificaba la longitud de la cadena lateral o su grupo funcional (**Figura 3.10b**). [160] Las seis ZnPcs mostraron excelente afinidad y estabilidad hacia G4s de ADN de *c-myc*, c-kit y promotores de H-Telo, además presentaban una afinidad entre 100 y 1000 veces mayor por los G4s que por el ADN bicatenario y monocatenario. Se observó que para las que tenían cadenas más largas entre el núcleo de la Pc y los grupos amonio, aumentaba considerablemente su florescencia por la unión con G4s.

[159] a) J. Alzeer, B. Vummidi, P. Roth, N.W. Luedtke, N. *Angew. Chem. Int. Ed*., **2009**, *48*, 9362–9365. b) A. Membrino, M. Paramasivam, S. Cogoi, J. Alzeer, N.W. Luedtke, L. Xodo, *Chem. Commun*., **2010**, *46*, 625–627.
[160] J. Alzeer, N.W. Luedtke, *Biochemistry*, **2010**, *49*, 4339–4348.

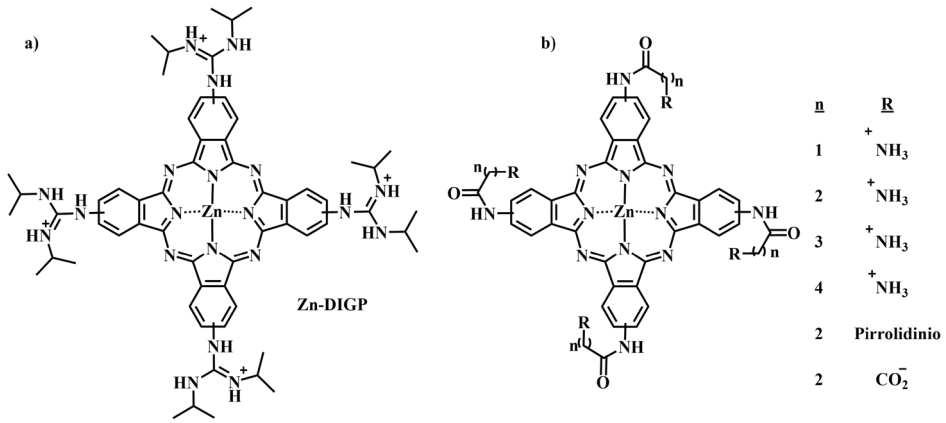

Figura 3.10. Estructura de diferentes ZnPcs utilizadas como ligandos de G4s.

Neves y colaboradores sintetizaron cuatro ZnPcs con cuatro u ocho cargas positivas en diferentes posiciones para utilizarlas como ligandos de G4s (**Figura 3.11**).[161] Basándose en esta familia de MPcs, los autores establecieron una relación estructura-actividad para definir tanto la importancia del número de cargas como su posición en la afinidad y selectividad de G4s. Entre ellas, la Pc con 4 cargas positivas más expuestas [**ZnPcH$_{12}$(SPyMe)$_4$**] y la de 8 cargas positivas menos expuestas [**ZnPcH$_8$(NPyOMe)$_8$**] fueron las que mejor selectividad y afinidad mostraron por los G4s. Además, se estudió su localización en células cancerosas por microscopia de fluorescencia y experimentos de teñido, observándose una intensa emisión en el núcleo de las células cancerosas para ambos.

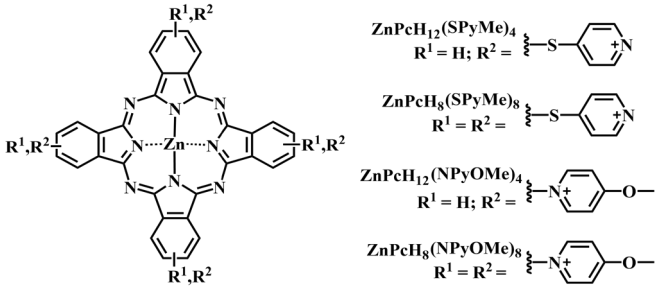

Figura 3.11. Estructura de diferentes ZnPcs con 4 u 8 cargas positivas utilizadas como ligandos de G4s.

Yamamoto y colaboradores sintetizaron dos MPcs con grupos piridinio una con cloruro de galio (III) y otra con Zn (II) como núcleos metálicos (**Figura 3.12**).[162] Comprobaron que la fotogeneración de especies reactivas de oxígeno de las MPcs en presencia de un G4 de cadena paralela, se suprime para la **GaPc**, mientras que la de **ZnPc** mejora con la adición del ADN. La pérdida de la capacidad de generar ROS en **GaPc** se debía a la transferencia de electrones desde el estado fundamental de la base de guanina del ADN al estado fotoexcitado

[161] C.I.CV Ramos, S.P. Almeida, L.M.O. Lourenço, P.M.R. Pereira, R. Fernandes, M.A.F. Faustino, J.P.C. Tomé, J. Carvalho, C. Cruz, M.G.P.M.S. Neves, *Molecules*, **2019**, *24*, 733-755.
[162] M. Uchiyama, A. Momotake, T. Ikeue, Y. Yamamoto, *Bull. Chem. Soc. Jpn*., **2020**, *93*, 1504-1508.

de **GaPc**. Por otro lado, la mejora de **ZnPc** al unirse al G4 posiblemente se deba a la disociación de su agregado no fluorescente al interaccionar con el ADN.

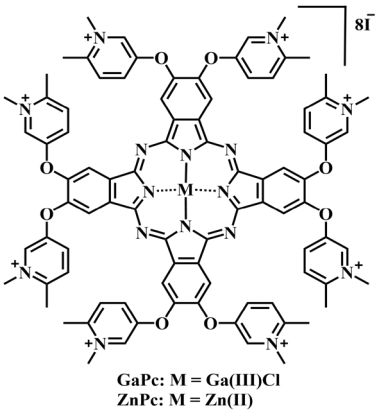

Figura 3.12. Estructura de diferentes MPcs utilizadas como ligandos de G4s.

El grupo de Durmuş realizó estudios con unas ftalocianinas similares a las anteriores con 4 y 8 sustituyentes (**Figura 3.13**).[163] En ellos se comprobó que ambas MPcs interaccionaban tanto con ADNct como con G4s y lo hacen de distintas formas, **OGaPc** se une intercalándose con el ctDNA, mientras que **TGaPc** se une a ctDNA a través de unión a surco y / o interacciones electrostáticas. También se observó que **TGaPc** muestra afinidad selectiva por AS1411 y puede usarse como una sonda selectiva para AS1411.

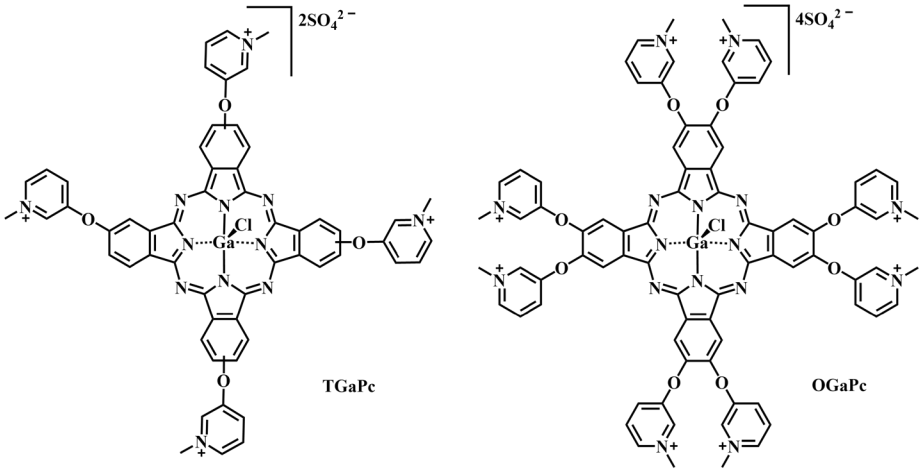

Figura 3.13. Estructura de diferentes GaPcs utilizadas como ligandos de G4s.

En otro estudio de Durmuş, se sintetizaron dos MPcs muy parecidas a **OGaPc**, pero sustituyendo el átomo de oxígeno por uno de azufre y utilizando diferentes metales centrales. En ellos se confirmaron las interacciones entre ambas Pcs y los G4s a nivel molecular. [164]

[163] H.E. Yilmaz, E. Bağda, E. Bağda, M. Durmuş, *Polyhedron*, **2021**, *208*, 115404-115412.
[164] F. Aydin, E. Bağda, E. Bağda, M. Durmuş, *Polyhedron*, **2023**, *238*, 116413-116423.

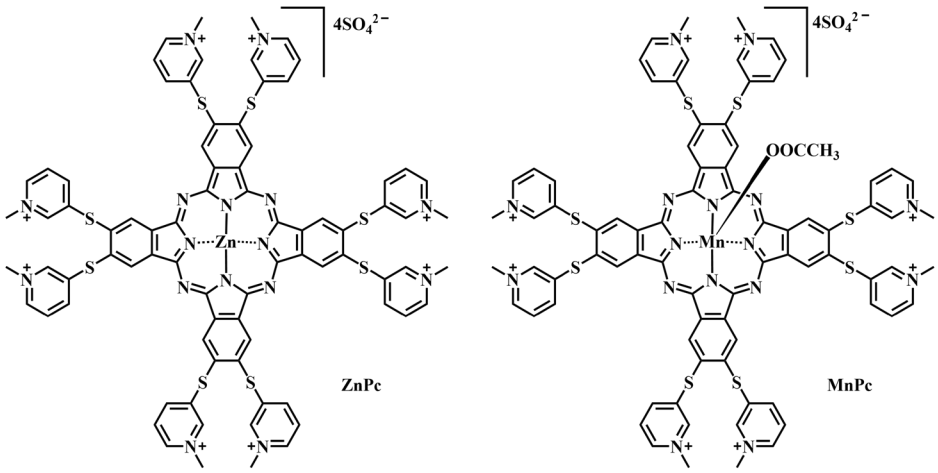

Figura 3.14. Estructura de diferentes MPcs utilizadas como ligandos de G4s

En el grupo de Kabay se sintetizaron ftalocianinas de cinc con grupos antraquinona como sustituyentes periféricos y no periféricos (**Figura 3.15**).[165] En los estudios *in silico* muestran una eficiente y especifica capacidad de unión al ADN, sobre todo ***p*-ZnPc**, que presenta la mayor afinidad por los G4s y la menor por el ADN bicatenario. Sin embargo, como los propios autores comentan, aún son necesarios estudios para comprobar sus propiedades anticancerígenas.

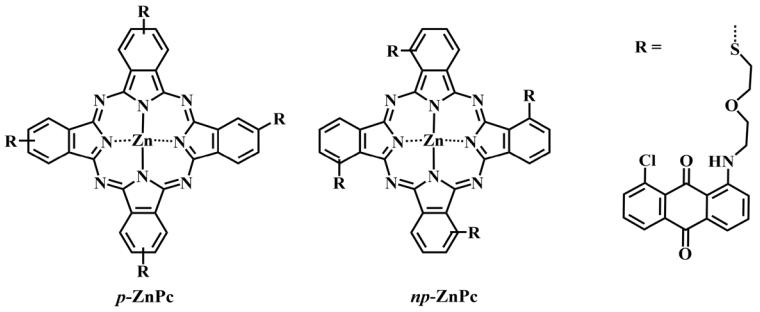

Figura 3.15. Estructura de diferentes ZnPcs con antraquinonas utilizadas como ligandos de G4s.

Gök y colaboradores sintetizaron una ftalocianina de cinc con sustituyentes periféricos cíclicos con triazoles (**Figura 3.16**).[166] Se estudiaron sus propiedades fotoquímicas y se comprobó la producción de oxígeno singlete con un rendimiento cuántico (φ_Δ) de 0.47. También se comprobó que era capaz de unirse de forma eficiente y especifica a G4s y que producía un efecto antiproliferativo *in vitro* sobre líneas celulares de carcinoma de pulmón.

[165] M. Koç, N. Kabay, *J. Porphyrins Phthalocyanines*, **2022**, 19–30.
[166] Y. Baygu, N. Kabay, B. Kabay, B. Yıldız, İ. Ömeroğlu, M. Durmuş, E.R. Karagür, H. Akça, Ç. Ergin, Y. Gök, *Journal of Molecular Structure*, **2023**, *1271*, 134010-134017.

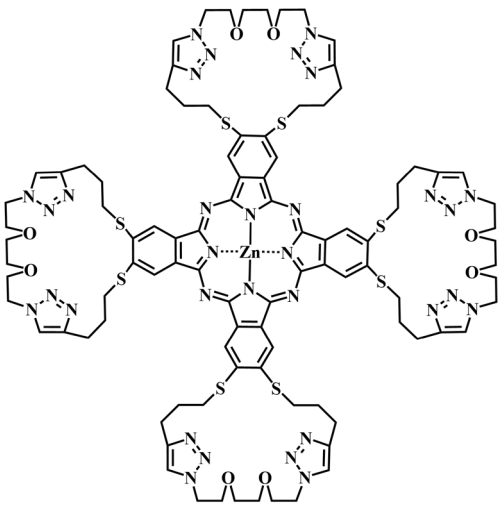

Figura 3.16. Estructura de una ZnPc con sustituyentes cíclicos utilizada como ligando de G4s.

3.2 Objetivos

3.2.1 Síntesis y caracterización de ftalocianinas de cinc y níquel sustituidas con grupos 2-aminoetoxilo

Nuestro objetivo ha sido sintetizar dos ftalocianinas con grupos amonio cuyas cargas positivas pudiesen facilitar la estabilización del G4 mediante interacciones electrostáticas y enlaces de hidrógeno con su esqueleto fosfato. Además, se pretende estudiar la influencia del ion metálico central en esta interacción con los G4s. Por ello se han sintetizado las ftalocianinas de cinc **ZnPc 21** y de níquel **NiPc 22** (**Esquema 3.1**).

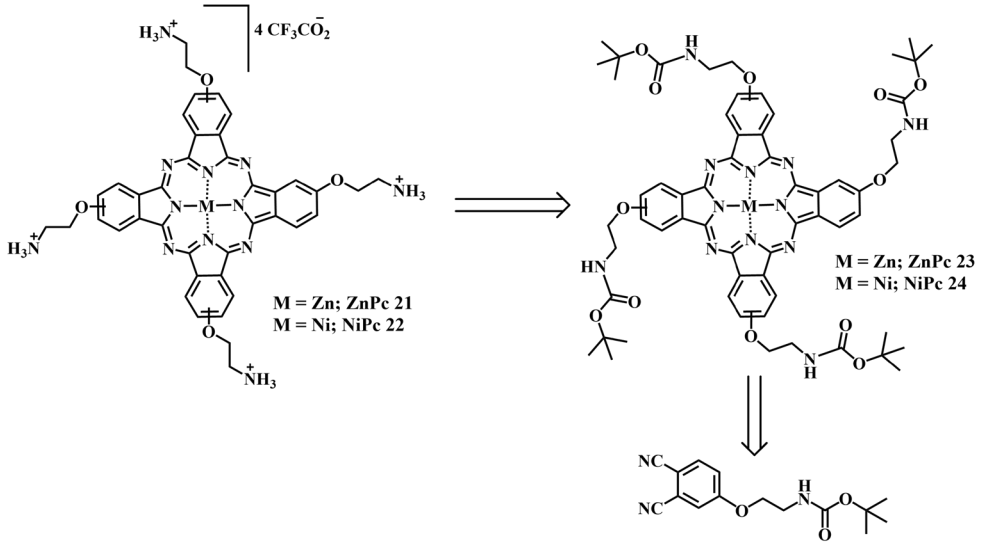

Esquema 3.1. Síntesis de ZnPc 21 y NiPc 22.

3.2.2 Interacción con G4s y capacidad de generar especies reactivas de oxigeno

El objetivo final de la síntesis de estas dos MPcs es comprobar su afinidad y especificidad por los G4s frente a la doble hélice de ADN, así como evaluar su capacidad para generar ROS. Finalmente, el estudio de la localización celular y fototoxicidad de ambos compuestos para su posible desarrollo como agente teragnóstico, pudiendo tanto reconocer la estructura de G4s como actuar sobre ellos. Los ensayos se realizarán por el grupo del Prof. Enrique García España en el Instituto de Ciencia Molecular (ICMol) y departamento de Química Orgánica de la Universidad de Valencia.

3.3 Resultados:

Los resultados obtenidos en este capítulo se recogen en la siguiente publicación

A. Gil-Martínez, A. Hernández, C. Galiana-Roselló, S. López-Molina, J. Ortiz, Á. Sastre-Santos, E. García-España, J. González-García, Development and Application of Metallo-Phthalocyanines as Potent G-quadruplex DNA Binders and Photosensitizers, *J Biol Inorg Chem*, **2023**, DOI:

Development and Application of Metallo-Phthalocyanines as Potent G-quadruplex DNA Binders and Photosensitizers

Ariadna Gil-Martínez,[a] Adrián Hernández,[b] Cristina Galiana-Roselló,[a] Sònia López-Molina,[a] Javier Ortiz,[b] Ángela Sastre-Santos,[b] Enrique García-España,[a]* Jorge González-García[a]**

[a]Institute of Molecular Science (ICMol) and Department of Inorganic Chemistry, University of Valencia, C./ Jose Beltran 2, 46980 Paterna, Spain

[b]Área de Química Orgánica, Instituto de Bioingeniería, Universidad Miguel Hernández, Avda. de la Universidad s/n, 03202 Elche, Spain

ORCIDs
Ariadna Gil Martínez (0000-0003-1086-6660); Cristina Galiana Roselló (0000-0003-1365-1323); Sonia López Molina (0000-0001-7897-6888); Javier Ortiz (0000-0003-3480-6793); Ángela Sastre Santos (0000-0002-8835-2486); Enrique García-España (0000-0002-4601-6505); Jorge Gonzalez Garcia (0000-0001-8994-1779)

KEYWORDS
G-quadruplex DNA; nickel phthalocyanine; photosensitizer; zinc phthalocyanine; metallo-phthalocyanines.

ABSTRACT

Metallo-phthalocyanines (**MPc**) are common photosensitizers with ideal photophysical and photochemical properties. Also, these molecules have shown to interact with non-canonical nucleic acid structures, such as G-quadruplexes, and modulate oncogenic expression in cancer cells. Herein, we report the synthesis and characterization of two metallo-phthalocyanines containing either zinc (**ZnPc**) or nickel (**NiPc**) in the central aromatic core and four alkyl ammonium lateral chains. The interaction of both molecules with G-quadruplex DNA was assessed by UV-Vis, fluorescence and FRET melting experiments. Both molecules bind strongly to G-quadruplexes and stabilize these structures, being **NiPc** the most notable G-quadruplex stabilizer. In addition, the photosensitizing ability of both metal complexes was explored by the evaluation of the singlet oxygen generation and their photoactivation in cells. Only **ZnPc** showed a high singlet oxygen generation either by direct observation or by indirect evaluation using a DPBF dye. The cellular evaluation showed mainly cytoplasmatic localization of **ZnPc** and a decrease of the IC_{50} values of the cell viability of **ZnPc** upon light activation of two orders of magnitude.

INTRODUCTION

Modern medicinal chemistry covers the discovery and targeting of novel disease modulators such as histone modifications, nucleosome remodelers, modified DNA/RNA bases and a variety of non-coding mediating elements.[1] One of the most attractive non-coding targets in cancer and neurodegenerative disorders are G-quadruplex (G4s) nucleic acid structures.[2-4] G4s are non-canonical DNA or RNA structures formed by guanine-rich sequences, which form planar rearrangements of four guanine bases termed as G-quartets.[5-6] These guanine quads result from the hydrogen bonding association between the Hoogsteen and Watson-Crick faces of the guanines and the metal coordination of potassium and sodium to the guanine oxygens.[5-6] Next generation sequencing and bioinformatic analysis have located putative G4s forming sequences in telomeres, oncogene-promoter regions, replication initiation sites and untranslated regions in human genomes.[7] Of outmost importance is the evidence of G4s formation under physiological conditions in cells and its key role in regulating biological processes such as oncogene expression, telomere maintenance and chromosome stability,[8] which highlight the potential of using G4s as anticancer targets by small molecules.[9-19] In this regard, G4 binders Quarfloxin and CX-5461 have reached clinical trial stages for the treatment of cancers, and other drugs, allegedly targeting G4s, are currently under the preclinical scope.[20-21] Quarfloxin inhibits the RNA polymerase through the interaction with ribosomal G4s in the nucleolus, resulting in a reduction of the tumor volume in pancreatic cancer xenograft models but advanced clinical studies have withdrawn it due to bioavailability issues.[22] CX-5461 has a complex mechanism involving the stabilization of the promoters of *cMyc, cKit* proto-oncogenes and telomere G4s in addition to the blockage of the replication forks, which results in the induction of DNA damage and inhibition of ribosomal RNA biogenesis.[23] Currently, it is evaluated in phase I clinical trials for patients with BRCA1/2 deficient tumors.[24]

Recently, an interesting approach to tackle cancer has emerged combining G4 binding and the photosensitization of the G4 ligand, which can then generate reactive oxygen species (ROS) and the resulting breakage of the G4DNA/RNA structures and other nearby biomolecules. In this line, a family of porphyrins was photosensitized to cleave G4 RNAs from the Rat sarcoma virus (*ras*) oncogenes, which then reduced the tumor growth in pancreatic xenograft models.[25] In most of the works, porphyrins have been selected as G4 ligands with photosensitizing properties[26-29] but the large efforts in the last years to apply photodynamic therapy into the clinics have generated novel molecules which overcome the limitations of traditional photosensitizers (poor aqueous solubility, poor photostability…).[30-35] The main attention has focused on the incorporation of a metal ion into an aromatic core. In this regard, metallo-phthalocyanines are a promising family scarcely explored as dual G4 binders / photosensitizers. MPcs harbor the large π-planar structure able to interact *via* π-π stacking with the external tetrads of G4s and the appropriate photophysical properties to act as photosensitizer in photodynamic therapy (i.e. Q-band in the visible range for irradiation, high quantum yield and lifetime…).[36-37] Their capacities for G4 binding and photosensitizing strongly depend on the coordination metal since diamagnetic metal ions promote photosensitivity although adopt a non-planar metal coordination that hampers G4 interaction in contrast to paramagnetic metal ions showing low photoactivation together with square

planar structures more idoneous for G-tetrad stacking.[38-39] Several important G4 ligands are described by Luedtke *et al.* based on guanidinium and amide-modified zinc phthalocyanines.[40-42]. Among them, the zinc phthalocyanine Zn-DIGP, substituted with isopropylguanidines showed excellent affinity and stabilization effect towards G4 DNAs from *c-myc*, *c-kit, KRAS* and *HTelo* with high selectivity for G4s over double- and single-stranded DNA. Strikingly, Zn-DIGP exhibited both turn-on luminescence upon G4 binding and down-regulation of *c-myc* and *KRAS* expression in cancer cell lines, suggesting a G4-mediated promoter inhibition.[40-41] Several nickel and zinc metallo-phthalocyanines containing eight quaternary ammonium groups have shown large HTelo G4 stabilization effect and potent inhibition of the telomerase.[43-44] Other phthalocyanines containing copper or gallium have demonstrated the G4 binding[45-46] with a concomitant suppression of the photogeneration of ROS.[47] Miyoshi group evaluated the G4 binding and the photo-irradiation consequences of several metallo-phthalocyanines, suggesting that the down-regulation of *ras* expression is due to the G4 binding in the oncogene promoter with the concomitant selective photocleavage.[48]

Herein, we report the preparation of two metallo-phthalocyanines incorporating zinc (**ZnPc**) and nickel (**NiPc**) within the aromatic core and containing four ethylammonium trifluoroacetate (TFA) substituents in the non-peripheral positions (Figure 1). The presence of a flexible ethoxy ammonium linker would increase the possibilities of interactions with the G4s as well as the cationic nature of the substitutions. ZnPc and NiPc are mixtures of 4 different regioisomers with C_{4h}, C_{2v}, C_s, and D_{2h} symmetry, and we study the interaction of all these isomers with the ligand. The photophysical properties and the aggregation behavior of these molecules were studied by UV-Vis/fluorescence emission experiments. Their interaction with G4s and duplex DNAs were assessed using FRET melting assays and UV-Vis and fluorescence emission spectroscopies. Then, the singlet oxygen generation has been studied *in vitro* by means of different biophysical methods. Lastly, the viability in several cell lines has been evaluated in the dark and using red light.

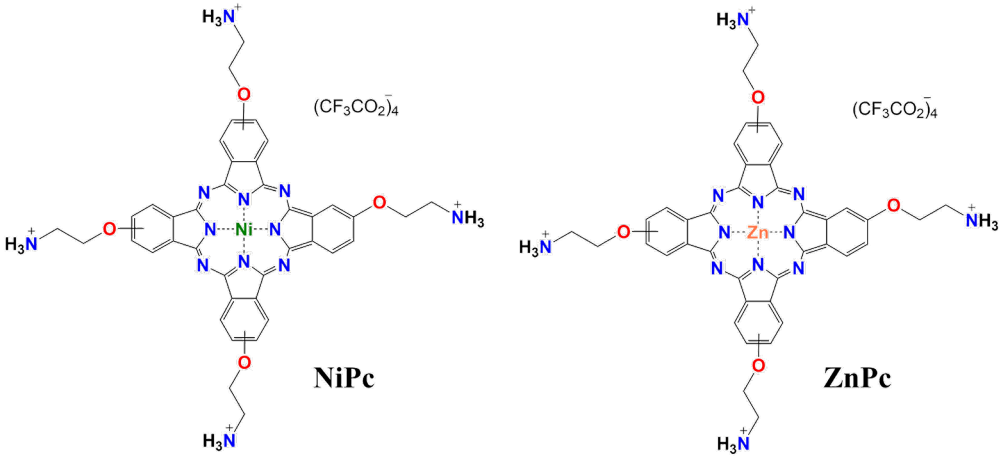

Figure 1.- Metallo-phthalocyanines studied in this work.

EXPERIMENTAL METHODS

All solvents and reagents were purchased from commercial sources and used as received. ^{1}H /^{13}C NMR spectra were recorded with a Bruker Avance 400 spectrometer, using tetramethylsilane as a reference. The solvent for spectroscopic studies was of spectroscopic grade and used as received. UV-Vis spectra were measured with Helios Gamma and Cary 100 UV-Vis spectrophotometers. Fluorescence spectra were recorded with HORIBA scientific SAS and PTI spectrophotometers. High-resolution mass spectra were obtained from a Bruker Microflex LRF20 matrix-assisted laser desorption/ionization time-of-flight (MALDI-TOF). IR spectra were measured with Nicolet Impact 400D spectrophotometer. The unlabeled and labelled DNA oligonucleotides (see Table S1) were purchased from IDT DNA purified in HPLC grade and the labelling dyes were 5'-FAM (FAM: 6-carboxyfluorescein) and 3'-TAMRA (TAMRA: 6-carboxytetramethylrhodamine). All concentrations of oligonucleotides were estimated by UV absorption using the extinction coefficients and expressed in strand molarity. Ligands were dissolved in DMSO to give 5 mM stock solutions. All solutions were stored at -20 ºC and defrosted and diluted immediately before use in the suitable buffer to the appropriate concentrations.

Synthesis of NiPc-Boc. 300 mg (1.04 mmol) of 4-(2-*tert*-butoxycarbonylaminoethoxy)phthalonitrile (**1**, see Scheme 1), 129.91 mg (0.52 mmol) of $Ni(OAc)_2 \cdot 4H_2O$, DBN, 1,5-Diazabicyclo[4.3.0]non-5-ene (DBN, 3 drops) in dimethylaminoethanol (DMAE, 600 µL) were stirred at 135 ºC for 7 h under an inert atmosphere. The blue mixture was cooled at room temperature, concentrated under vacuum and purified by column chromatography (DCM:MeOH 94:6) yielding 50 mg (24%) of **NiPc-Boc**. HR-MALDI-TOF (dithranol): *m/z* for $C_{60}H_{68}N_{12}NiO_{12}$: calcd. 1206.4433 [$M^+$]; found, 1206.4589. UV-Vis (DMF) λ_{max}/nm (log ε): 382 (4.37), 613 (4.53), 674 (4.92). IR (ν_{max}/cm^{-1}): 3370, 2976, 2933, 2877, 1704, 1612, 1531, 1462, 1419, 1393, 1366, 1351, 1272, 1242, 1171, 1129, 1096, 1070, 963, 894, 868, 823, 782, 752, 651, 582.

Synthesis of NiPc. 50 mg (0.04 mmol) of **NiPc-Boc** were dissolved in a mixture of DCM (1 ml) and TFA (1 ml) and stirred for 2 h at 0ºC. The blue mixture was heated at room temperature and concentrated under vacuum, yielding **NiPc** quantitatively. HR-MALDI-TOF (dithranol): *m/z* for $C_{40}H_{36}N_{12}NiO_4$: calcd. 806.2336 [M^+]; found, 806.2322. UV-Vis (H_2O) λ_{max}/nm (log ε): 370 (4.03), 625 (4.40). IR (ν_{max}/cm^{-1}): 3294, 2929, 2879, 1729, 1655, 1608, 1531, 1456, 1394, 1336, 1280, 122, 1123, 1091, 1062, 1014, 960, 837, 749, 700, 622. ^{1}H NMR (TFA-d_1): δ= 4.13 (br s, 8H, CH_2O), 5.04 (br s, 8H, CH_2N), 8.01 (br s, 4H, ArH), 9.11 (br s, 4H, ArH) 9.48 (br s, 4H, ArH).

FRET melting assay. Labelled DNA was dissolved as a 20 µM stock solution in MilliQ water and then a solution of 400 nM concentration was prepared in cacodylate buffer (pH 7.3) supplemented with potassium or sodium. The solutions were annealed at 95 ºC for 10 min, and allowed to cool slowly to room temperature overnight. The buffer used for the antiparallel G4 HTelo was 100 mM NaCl, 10 mM LiCac, while for the rest of G4s and duplex was 100 mM KCl, 10 mM LiCac. Ligand solutions were diluted from stock solutions (see above) to a final concentration of 20 µM in the buffer. Each well of a 96- well plate (Applied Biosystem) was prepared with 60 µl, with a final 200 nM DNA concentration and increasing concentration of tested ligands (0–4 µM). Measurements were performed on a PCR AriaMx (Agilent

Technologies) with excitation at 450–495 nm and detection at 515–545 nm. Readings were taken from 25 ºC to 95 ºC at interval of 0.5 ºC maintaining a constant temperature for 30 seconds before each reading. Each measurement was done in triplicate. The normalized fluorescence signal was plotted against the compound concentration and the ΔT_m values were determined.

Spectrophotometric and spectrofluorimetric titrations. The DNA oligonucleotides were dissolved in Tris buffer (100 mM KCl, 10 mM Tris pH 7.4) and annealed at 95 ºC for 10 min before cooling to room temperature overnight. The concentration of DNA was confirmed using the molar extinction coefficients provided by the manufacturer. Annealing concentrations were approximately 500 μM. Absorption spectra were recorded with a Cary 100 UV-Vis Spectrometer (Agilent) in quartz cells (path length 1 cm) by using scan rates of 300 nm min^{-1}. Fluorescence spectra were recorded with a PTI Spectrofluorimeter in quartz cells with a cross-section of 1×0.5 cm, by using slit widths of 2 nm and an integration time of 0.1 s. The fluorescence emission spectra were recorded between 630 and 900 nm with an excitation wavelength of 620 nm. UV-Vis titrations were conducted with a concentration of **MPc** of 5 μM while fluorescence titrations used 2 μM. The absorption/emission maxima data were analyzed according to the independent-site model by means of a Levenberg – Marquardt fitting routine and equations reported previously by Thordarson.[49]

Singlet oxygen evaluation. *Indirect evaluation:* singlet oxygen generation was evaluated in air using the indirect method with diphenylisobenzofuran (DPBF) acting as a singlet oxygen chemical quencher in DMSO. To avoid chain reactions of the quencher in the presence of singlet oxygen, the concentration of DPBF was kept at ∼3×10^{-5} M. Solutions of the **MPc** with an absorbance of ∼0.5 at the irradiation wavelength were prepared in the dark and irradiated at 730 nm with a LED array lamp in the presence of DPBF. Then, the reactions were followed spectrophotometrically by observing the decrease in the 417 nm absorption peak of DPBF as a function of irradiation time. *Direct evaluation:* the sample was prepared in an air-saturated acetonitrile or deuterated water solution with an absorption of 0.2 at 400 nm. The sample was irradiated at 400 nm with a mounted M450LP1 LED (Thorlabs). To cut off light at wavelengths shorter than 850 nm, a long pass glass filter was placed in front of the monochromator entrance slit. The signal was detected with an EO-817L IR-sensitive liquid-nitrogen cooled germanium diode detector (North Coast Scientific Corp.). The luminescence signal, centered at 1270 nm, was measured from 1100 to 1400 nm.

Cell culture. HeLa Human cervical and A549 lung cancer cells and RAW 264.7 macrophages were grown in low glucose Dulbecco's modified Eagle medium containing 10% fetal bovine serum at 37 °C with 10% CO_2 in humidified air. Cells were kept continuously under confluence before split twice a week and the possibility of contamination was excluded by performing regularly mycoplasma tests.

Cellular imaging. Cells were seeded on chambered coverglass (*ca.* 2×10^4, 300 μl, 0.8 cm^2) for 24 h, then the medium was replaced with fresh phenol red free medium containing **ZnPc** (20 μM, 200 μl) for 2 h. Prior to imaging, the cells were washed with PBS and replaced with fresh growth medium. Cells were imaged using a confocal fluorescence microscope (FV1000, Olympus). Using a 60x magnification microscope objective (water immersion, NA ¼ 1.2) and an excitation wavelength of 620 nm for **MPc**, images of the cells were recorded in both

transmission and fluorescence modes. For the fluorescence images, the detection band was 640–800 nm which covered the emission range of the metal complexes.

Intracellular oxidative stress. The measurement of the broad spectrum of intracellular ROS gave an indicative assessment of the oxidative stress using the specific oxidation-sensitive fluorescent probe 2',7'-dichlorofluorescein diacetate (DCFH-DA). Cells were loaded with DCFH-DA (25 μM) diluted in serum free medium and incubated at 37 ºC for 60 min. Then, they were treated with 10, 50 and 100 μM solutions of **MPc** for 24 h. The fluorescence of the probe was registered in a multi-mode microplate reader with an excitation wavelength of 485 nm and an emission wavelength of 528 nm before and after irradiation at 730 nm during 20 min (5.2 mW cm^{-2}, 3.1 J cm^{-2}) light using an Atlas Photonics LUMOS BIO irradiator.

Phototoxicity on cell cultures. A total of 5×10^3 HeLa, A549 and RAW 264.7 cells were seeded on 96-well plates and allowed to adhere for 24 h. The cells were treated with increasing concentrations of the **MPc** diluted in cell medium achieving a total volume of 200 μl. The cells were incubated with the **MPc** for 24 h and, then the medium was refreshed with phenol red free medium. To study the phototoxic effect of the **MPc**, the cells were exposed to 730 nm (spectral half-width: 20 nm, 10 min, 5.2 mW cm^{-2}, 3.1 J cm^{-2}) light using an Atlas Photonics LUMOS BIO irradiator. To study the dark cytotoxicity of the **MPc**, the cells were not irradiated and the medium exchanged. The cells were grown for an additional 24 h period at 37 °C. After this time, the medium was replaced with fresh medium containing MTT with a final concentration of 0.5 mg mL^{-1}. The cells were incubated for 4 h and the generated formazan crystals were solubilized in 100 μl DMSO. The absorbance was registered with a SpectraMax M2 Microplate Reader (Molecular Devices). The obtained data was analyzed with the GraphPad Prism software.

RESULTS AND DISCUSSION

Design, synthesis and photophysical characterization of the metallo-phthalocyanines

Attending to the two main structural characteristics of potent G4 binders, comprising a planar polycyclic π-deficient core and one or several charged side chains, we prepared two metallo-phthalocyanines differentiated by the metal within the macrocyclic isoindole core, either nickel or zinc. In the nickel phthalocyanine, the metal coordinates four nitrogen atoms of the macrocycle adopting a square planar geometry while zinc generates a pyramidal geometry by coordinating an additional solvent molecule in addition to the nitrogen atoms of the macrocycle. The different arrangement will allegedly impact the binding to G4s through the most common binding mode of π-π stacking on the top of the G-quartets. The metal complexes were also designed with four side chains with pH-dependent protonable groups to enhance the aqueous solubility and hamper the self-aggregation. [43, 50-51] Moreover, these moieties can improve the interaction with DNA by binding to the phosphates and the nucleobases.

ZnPc was synthesized according to the literature, with a minor modification on the procedure to obtain the TFA salt instead of the HCl one.[52] **NiPc-Boc** was obtained upon the cyclotetramerization of the precursor phthalonitrile **1** in the presence of $Ni(OAc)_2$ (see Scheme 1) and further purification by chromatography (*yield:* 24%). The ^1H NMR spectra registered in different deuterated solvents (data not shown) showed no well-defined signals due to aggregation of the phthalocyanine core. Then, **NiPc** was obtained in quantitative yield by

treatment of **NiPc-Boc** with TFA (see Scheme 1). **NiPc** was characterized by ^{1}H NMR and FT-IR spectroscopies and HR-MALDI-TOF spectrometry. The ^{1}H NMR spectrum in TFA-d_1 showed well defined aromatic and aliphatic signals: three signals from the isoindol units can be found at 9.48, 9.11 and 8.01 ppm integrating for 12 hydrogen atoms, and from the aminoethoxy chain two signals can be observed, one at 5.04 corresponding to the 8 protons closer to the amine group and the second one at 4.13 ppm corresponding to the 8 protons closer to the oxygen (Figure S1). Additionally, HR-MALDI-TOF assays, performed at positive mode confirmed the obtention of both, **NiPc-Boc** and **NiPc**, with isotopic distributions that match the simulated isotope patterns. Furthermore, in the FT-IR spectrum of **NiPc** the band at 1704 cm^{-1} corresponding to the carbonyl group (C=O) of the **NiPc-Boc** is missing, as well as the apparition of a broad band of the ammonium groups centered at 3294 cm^{-1} (Figures S3 and S4).

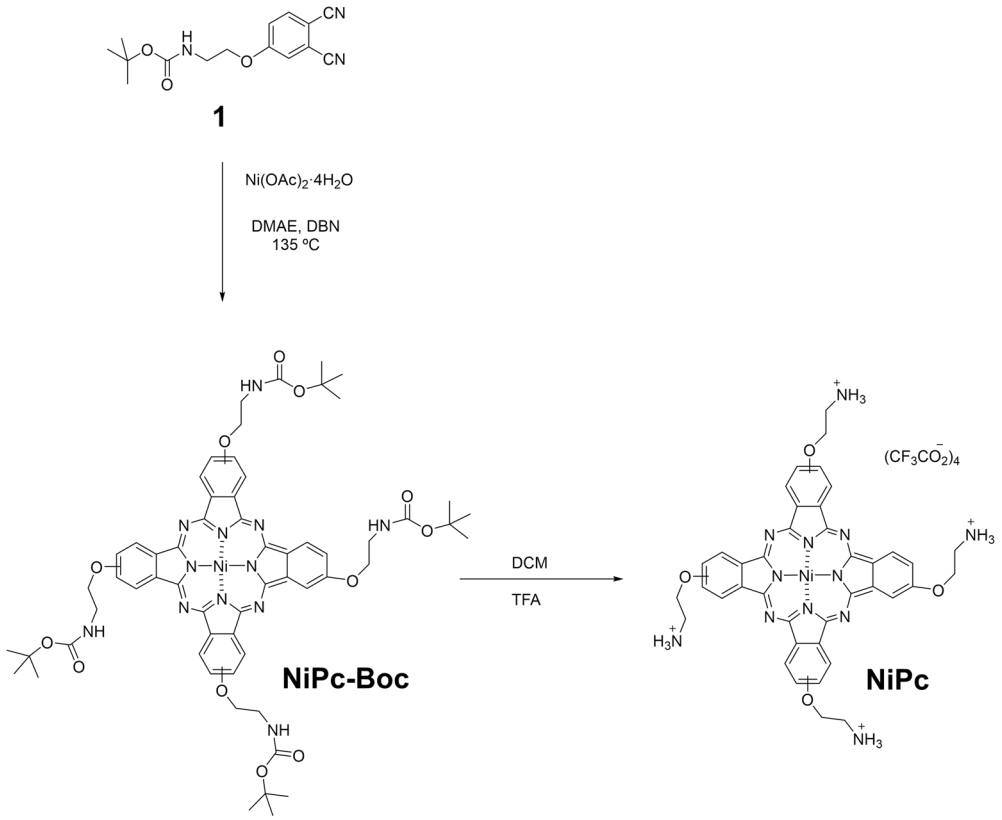

Scheme 1.- Synthetic route of **NiPc**

Both **MPc** show the typical UV-Vis bands of metallo-phthalocyanines with a band at lower wavelength and centered at 350 nm, which is assigned to the Soret band of the phthalocyanine scaffold (see Table 1). A second band located within the visible region and centered at 680 nm is ascribed to the Q band. The linearity of the absorption versus the concentration of the metal complexes indicates the absence of aggregation in aqueous solution up to 100 μM for **ZnPc** and 50 μM for **NiPc** (Figure S5). Similar to other metallo-phthalocyanines, only the zinc phthalocyanine presents a fluorescence emission band at 705 nm in H_2O (see Table 1).

Table 1.- Photophysical data of the two metallo-phthalocyanines (**MPc**) in different solvents.

MPc	Solvent	λ_{abs} (nm)	Ɛ (cm^{-1} M^{-1})	λ_{em} (nm)
NiPc	H_2O	625	25370	
NiPc	CH_3CN	600	21978	
ZnPc	H_2O	637	8083	705
ZnPc	CH_3CN	627	6186	

Interaction of the metallo-phthalocyanines with DNAs

We initially evaluated the stabilization of DNA induced by the ligands by FRET melting experiments. We included G4s of different topology (parallel, antiparallel and mixed/hybrid) and number of G-tetrads (e.g., 2 and 3 tetrads), as well as a duplex model (see Table S1). **NiPc** induced a larger stabilization effect for all G4s than **ZnPc** (i.e., ΔT_m values in F21T-K G4 are 33.1 and 25.7 for **NiPc** and **ZnPc**, respectively at ratio [DNA]:[**MPc**] of 1:10). The larger stabilization produced by **NiPc** can be ascribed to the square-planar geometry of the nickel core, which can stack more efficiently on the top of the external G-tetrads in comparison with the pyramidal geometry of the zinc site with less efficient stacking. Both ligands do not stabilize the duplex model (dark brown bar in Figure 2), indicating a high degree of selectivity for G4 over duplex DNA. The low interaction of the **MPc** towards double stranded DNA structures has already been observed and associated to the large aromatic core, which hampers the base pair intercalation and the groove binding to the double helix. [40-41, 50-51, 53] Strikingly, **NiPc** induces a high stabilization effect on the *bi*tetrad thrombin G4 TBA (light grey bar in Figure 2).

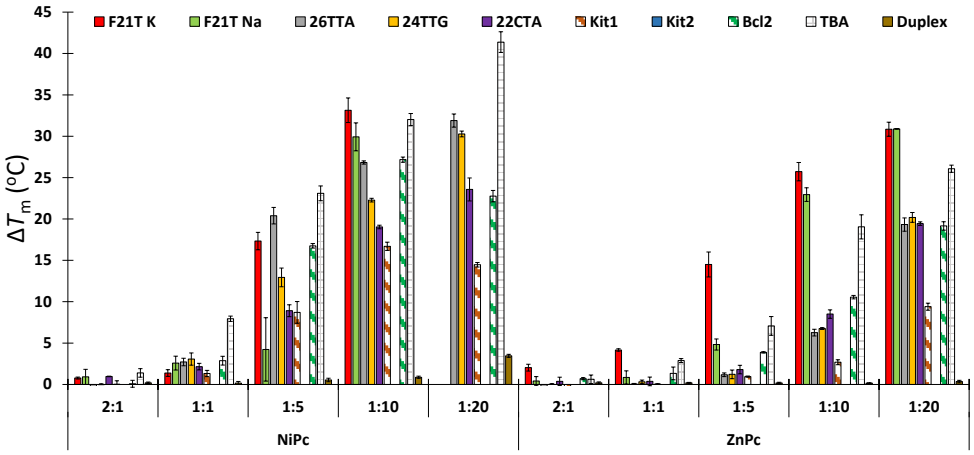

Figure 2.- Representation of ΔT_m values obtained from the FRET melting studies for the interaction of the metallo-phthalocyanines with several G4/duplex DNA structures. The concentration of DNA was 0.2 μM, whereas the concentration of the **MPc** was increased and the [DNA]:[**MPc**] ratios showed in the bottom part (2:1, 1:1, 1:5, 1:10 and 1:20). Errors denote the standard deviations of at least three independent experiments.

Once assessed the stabilization effect, we performed UV-Vis titrations with HTelo G4 (telomeric region), cMyc G4 (oncogene promoter) and a duplex DNA (ds26) to evaluate the affinity for DNAs. **NiPc** and **ZnPc** present in aqueous solution an absorption band at 600 and 625 nm, respectively, assigned to the Q band (Figure 3). Addition of DNA to **ZnPc** yields a decrease in the band and the appearance of a new Vis band at 690 nm (Figures S6-S11). The intensity of this band depends on the structure studied, being G4s the structures that shows the largest enhancement of the intensity. **NiPc** shows a decrease and a red shift of the visible band in addition to the apparition of a new band centered at 720 nm when bound to G4s (Figure 3). UV-Vis titrations with duplex DNA afforded minimal change in these bands, indicating a soft interaction for double stranded DNA in concordance with the FRET melting results. The affinity constants calculated from the titrations are collected in Table 2, which indicate the high affinity for G4s of both **MPc** ($K_a \approx 10^6$ M^{-1}). In contrast, both complexes show low affinity for the duplex DNA ($K_a < 10^3$ M^{-1}), confirming the selectivity observed by the FRET melting assays.

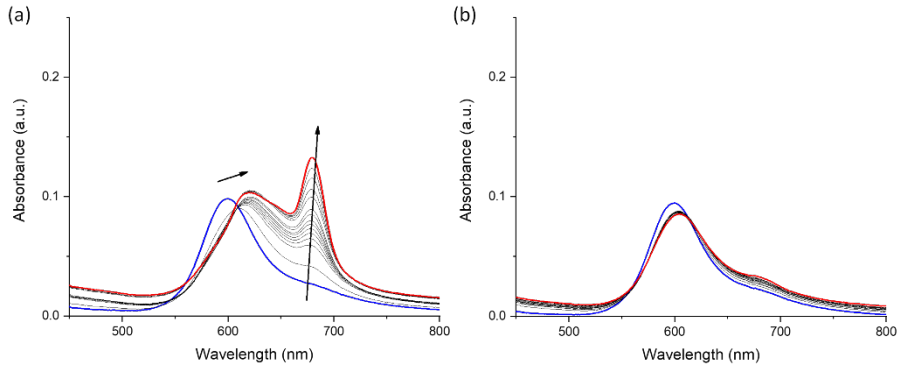

Figure 3.- UV-Vis titrations of **NiPc** with cMyc G4 (a), and ds26 (b). Blue spectrum corresponds to the initial titration and red spectrum to last one.

Table 2.- Binding constants (log K_a) determined from the UV-Vis and fluorescence titration experiments of MPc with G4 and duplex DNAs in Tris buffer (100 mM KCl, 10 mM Tris pH 7.4). n.d.: no determined. 1: Obtained by UV-Vis titrations. 2: Obtained by fluorescence titrations.

MPc	HTelo	cMyc	ds26
NiPc	5.2 (±0.1)[1]	6.3 (±0.2)[1]	n.d.
ZnPc	6.7 (±0.4)[1] 5.2(±0.1)[2]	6.3 (±0.7)[1] 6.3 (±0.2)[2]	n.d. 4.6 (±0.4)[2]

Fluorescence emission titrations were carried out to determine the binding affinity of **ZnPc** for different DNAs. **ZnPc** shows a low fluorescent emission in aqueous buffered conditions and the addition of DNAs yields the apparition of a fluorescent emission band centered at 702 nm (see Figure 4 and S12-S16 in ESI). The intensity changes of the fluorescence emission are different depending on the nucleic acid structure, being larger for G4s (G4-DNA yields a 60-fold increase while duplex-DNA experiences a 20-fold increase, see Figure 4). The binding constants afforded values within the micromolar range for G4s structures (see Table 2) while

the duplex model presents affinity constants of two orders of magnitude lower, which agrees with the UV-Vis and FRET melting experiments.

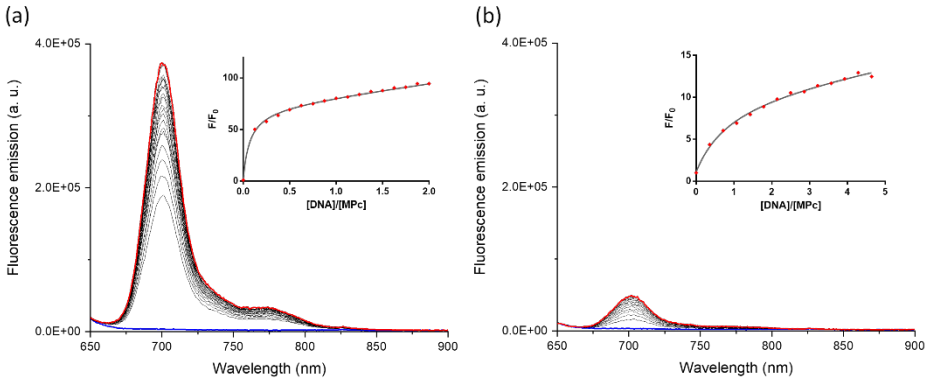

Figure 4.- Fluorescence titrations of **ZnPc** with G4 HTelo (a) and ds26 (b) in Tris 10 mM, KCl 100 mM, pH 7.4, λ_{exc} = 620 nm. Inset: Plot of the F/F_o *vs.* ratio [DNA]/[**MPc**]. Blue spectrum corresponds to the initial titration and red spectrum to last one.

Assessment of the ROS generation

Following our initial hypothesis, the capacity to regulate gene expression of G4 ligands can be tightly associated to the photosensitizing capacity which breaks down the G4 structures upon binding. Therefore, we assessed the capability to induce singlet oxygen under irradiation of both metallo-phthalocyanines and well-known photosensitizers, Zinc 2,9,16,23-tetra-*tert*-butyl-29*H*,31*H*-phthalocyanine (**Zn-PS**) and Rose Bengal (**RB**). We studied the DPBF quenching upon irradiation of the **MPc** at different concentrations and irradiation times. DPBF traps selectively singlet oxygen ($^1O_2$) and arises a decrease in the band at 460 nm, whose intensity is directly associated to the $^1O_2$ generation. As it can be observed in Figure 5, **ZnPc** generates singlet oxygen even at the lowest concentration studied (1 μM), being the generation of $^1O_2$ dependent on the concentration of the metallo-phthalocyanine. In contrast, the **NiPc** barely generates $^1O_2$ species indicating that the metal-core is fundamental for the activation of oxygen radicals upon irradiation. Interestingly, the quenching rates of DPBF are higher for **ZnPc** than for **Zn-PS** (Figure S17) indicating that **ZnPc** is a more efficient photosensitizer than the reference photosensitizer **Zn-PS**.

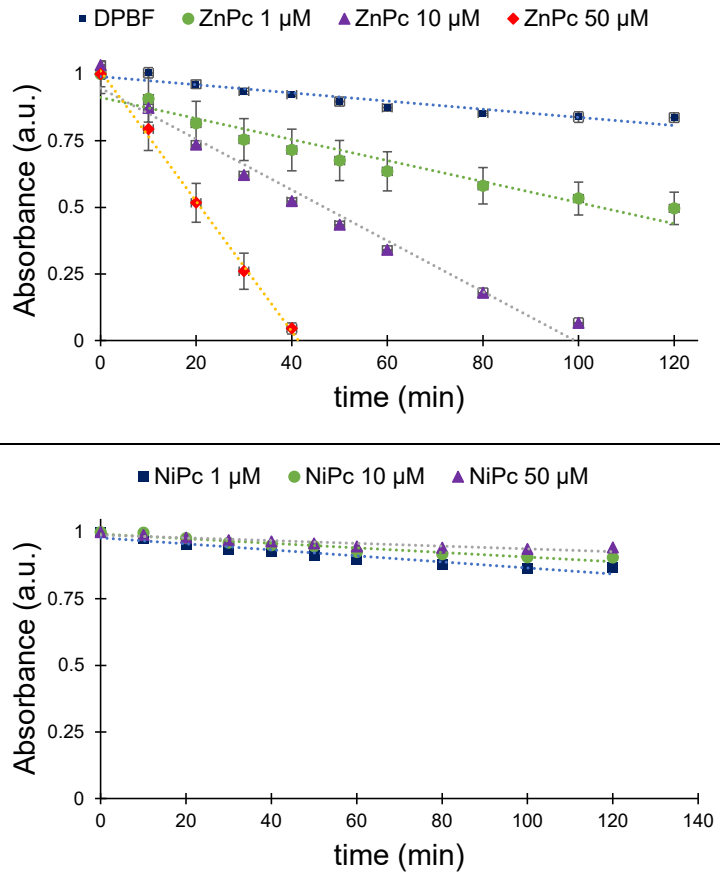

Figure 5.- Comparison of the decay rate of DPBF in DMSO induced by **ZnPc** (top panel) and **NiPc** (bottom panel) under red light irradiation.

An additional assessment was conducted by measuring the phosphorescent spectra of the singlet oxygen generated by the **MPc** and **RB** upon irradiation. We could only observe phosphorescence for **ZnPc** and **RB** in acetonitrile solution (Figure S18), suggesting that they can act as photosensitizers in contrast to **NiPc** which is unable to generate $^1O_2$. The intensity of the spectrum of **ZnPc** is higher than that of **RB**, indicating a qualitative estimation of the higher oxygen sensitizing effect of **ZnPc**.

Cellular experiments using the metallo-phthalocyanines

Initially, we investigated the cell localization of **ZnPc** by confocal fluorescence microscopy using its intrinsic fluorescence emission. The metal-complex was rapidly uptake into human cervical cancer cells (HeLa) as a bright red emission was detected in the cytoplasm of the cells (Figure 6).

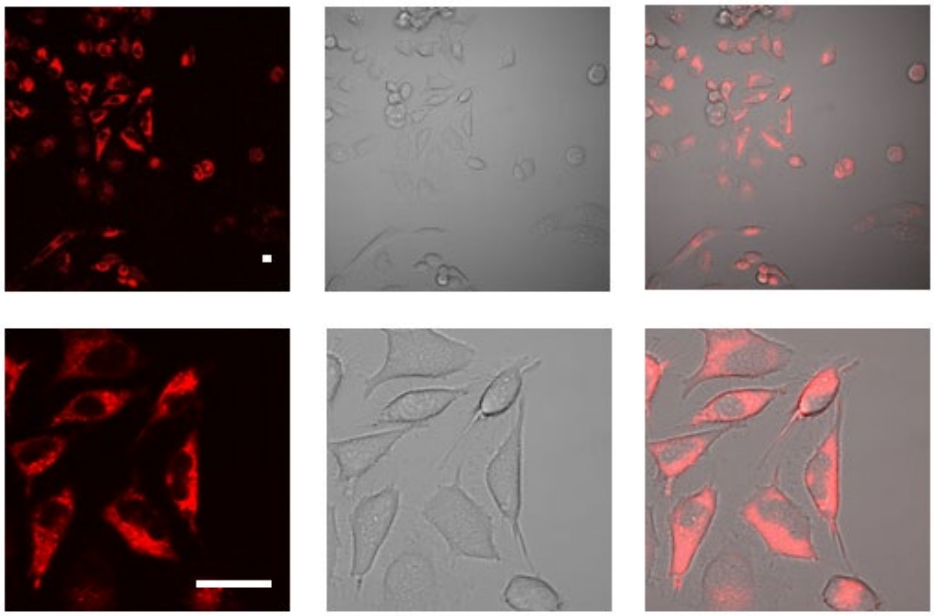

Figure 6.- Confocal fluorescence images of HeLa cells incubated with **ZnPc** (20 μM, 2 h). Left panel is the fluorescence emission of **ZnPc**, central panel is bright field and right panel is the image emerged from the fluorescence and bright field. Scale bar: 20 μm.

Once confirmed that **ZnPc** enters into the cells, we assessed the oxidative stress generated on HeLa, lung cancer cells (A549) and macrophages (Raw 264.7) by both **MPc** in the dark and upon the irradiation at 730 nm. The quantification of the ROS was evaluated by monitoring the cleavage of the intracellular fluorescence probe DCFH-DA (see Experimental Methods). We included the broadly used **Zn-PS** as a positive control of photosensitizer and H_2O_2. The incubation of the **MPc** with cells in the dark has not significant increase of the ROS except for the **ZnPc** at the highest concentration (100 μM, 24h), with an enhancement to 3.5 and 2.2-fold of the initial cellular ROS (Figure 7, top).

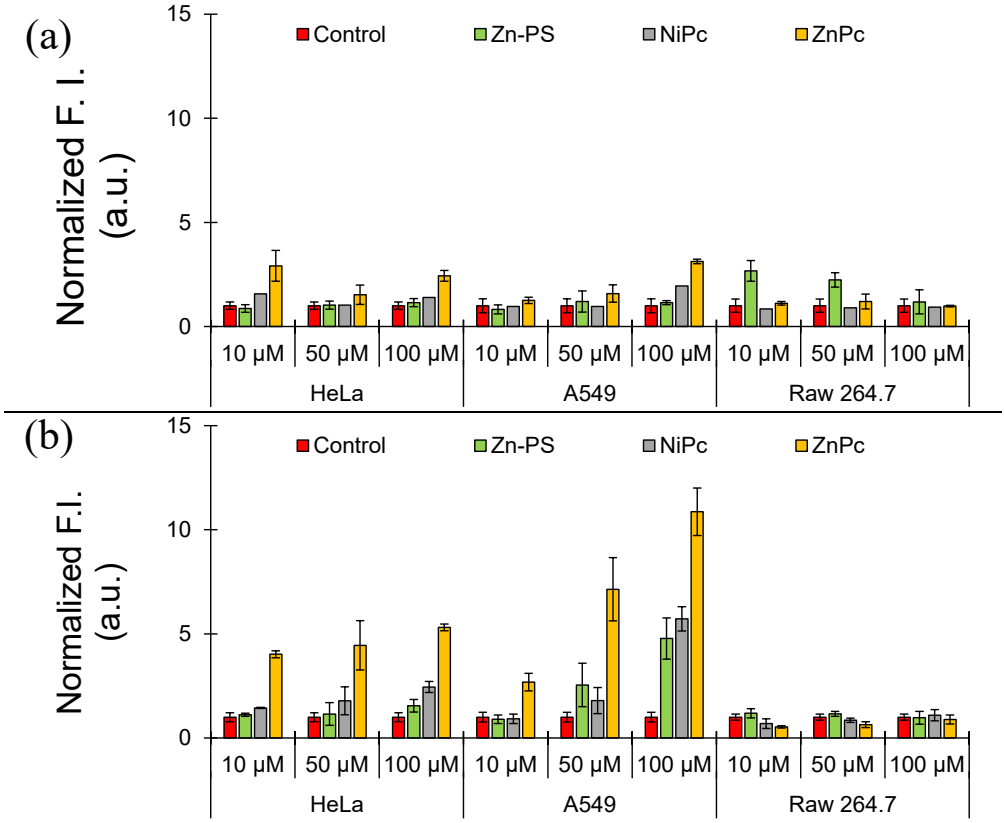

Figure 7.- ROS levels in HeLa, A549 and Raw 264.7 cells treated with **NiPc**, **ZnPc** and **Zn-PS** at different concentrations (10, 50 and 100 µM). Top panel in the dark and bottom panel irradiated at 730 nm.

In contrast, cells treated with both **MPc** and irradiated at 730 nm during 20 min generated a significant amount of ROS. Cells treated with **NiPc** increased up to 2.4 and 5.7-fold ROS depending on the cell line. The zinc phthalocyanine treatment yielded over 2.5-fold increase of ROS for the lowest concentration, reaching to100-fold ROS increase using the largest concentration. PS showed a similar trend than **ZnPc** although with lower quantity of ROS generated, suggesting that **ZnPc** has higher capacity to generate ROS than reference metallo-phthalocyanine photosensitizer.

Then, the photocytotoxic potential of the **MPc** was evaluated on the same cell lines. **Zn-PS** was also included as a control in our experiments. The results are summarized in Table 3 and representative dose–response plots are shown in Figures 8 and S19-S22. The cells were incubated with increasing concentrations of compounds for 24 h, irradiated at 730 nm for 20 min or maintained in the dark and then, incubated for an additional 24 h, before determining the cytotoxicity. As shown in Table 3, very low toxicity (IC_{50} values > 50 µM) was obtained for **NiPc** as well as for **ZnPc** in the dark. In contrast, **ZnPc** shows high toxicity when irradiated with IC_{50} values ranging from 0.04 µM to 0.89 µM depending on the cell line. These results confirm the capacity of **ZnPc** to exert photocytotoxicity under red light irradiation.

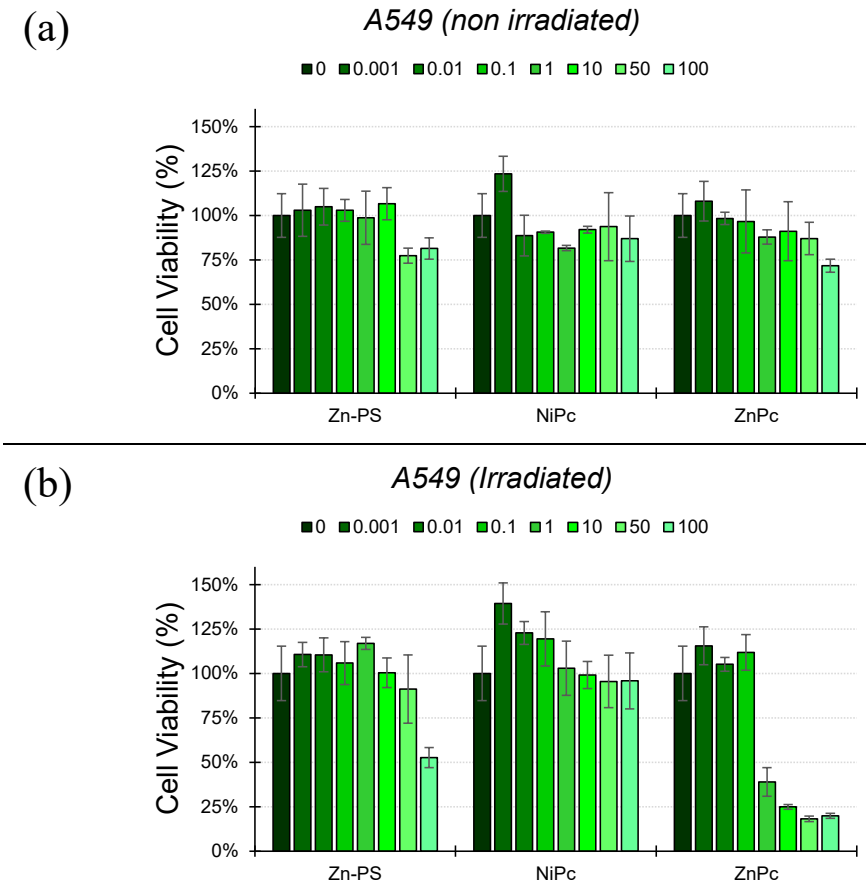

Figure 8. Cell viability on A549 cell line of **Zn-PS**, **NiPc** and **ZnPc** in the dark (a) and under irradiation (b). Colors and numbering in the legend refer to the compound concentrations (μM).

Table 3.- Values of IC_{50} assessed by MTT of the **MPc** in the dark and under irradiation.

Cell line	**NiPc**		**ZnPc**		**Zn-PS**	
	Dark	Irrad	Dark	Irrad	Dark	Irrad
HeLa	> 100	> 100	> 100	**0.039**	> 100	> 100
A549	> 100	> 100	> 100	**0.89**	> 100	> 100
Raw264.7	> 100	> 100	**58.7**	**0.37**	**22.9**	**42.4**

Conclusions

Two metallo-phthalocyanines have been obtained in good yield, which incorporate zinc and nickel within the aromatic core and containing four trifluoroacetate ethylammonium substituents in the non-peripheral positions, termed as **ZnPc** and **NiPc** respectively. The photophysical properties and the aggregation behavior of the molecules show no aggregation of both molecules in water, indicating that the positively charged ammonium groups at physiological pH increase the aqueous solubility and helping to disrupt the molecule inter-

aggregation. Both metallo-phthalocyanines show affinity constants in the micromolar range for G4s by means of UV-Vis and fluorescence emission experiments, whereas the interaction to duplex DNA is lower, *ca.* $K_a = 10^{-3}$ M. In line with photophysical studies, FRET melting assays show a large stabilization effect on G4s of **NiPc** and moderate stabilization effect of **ZnPc**, suggesting that the central metal core is important for G4 binding and that the square planar geometry of nickel has a better π-π overlapping with the G-quartets that the pyramidal geometry of zinc complex. In addition, no one stabilizes the duplex DNA, in agreement with UV-Vis and fluorescence titrations.

As photosensitizers, **ZnPc** exhibits a higher singlet oxygen generation upon red light activation *in vitro* and in cellular assays in contrast to **NiPc** which shows negligible photosensitization. Strikingly, the ROS generation of **ZnPc** is comparable to photosensitizers such as **RB** and **Zn-PS**. Finally, the treatment of the HeLa, A549 and Raw 264.7 cells with **MPc** shows a strong photocytotoxic effect for **ZnPc**, having IC_{50} values five orders of magnitude lower than in the dark. The results herein described give new insights into the development of novel anticancer drugs operating *via* a dual mechanism involving G4 binding and photokilling of the cancer cells.

Corresponding Author

*Institute of Molecular Science (ICMol) and Department of Inorganic Chemistry, University of Valencia, Catedrático José Beltrán 2, 46980, Paterna, Spain. Email: jorge.gonzalez@uv.es

Author Contributions

A.G.-M., S.L-M and J.G.-G. conducted the experimental work with DNAs. C.G.-R. and J.G.-G. conducted the cellular experiments. A.H. and J.O. performed the synthesis and characterization of the molecules. A.S.-S., E.G.-E. and J.G.-G. designed the project, obtained the funding and wrote the manuscript.

Funding Sources

This research was funded by the Spanish Ministry for Science and Innovation, The National Research Agency and FEDER funds from the EU (grants PID2019-110751RB-I00, PID2019-108643GA-I00, PID2020-117855RB-I00, RED2018-102331-T, CEX2019-000919, MFA/2022/014 and MFA/2022/028) and the Conselleria de Innovación, Universidades, Ciencia y Sociedad Digital of the Generalitat Valenciana (CIDEGENT/2018/015). This contribution is also based upon work from COST Action CA18202, NECTAR - Network for Equilibria and Chemical Thermodynamics Advanced Research, supported by COST (European Cooperation in Science and Technology).

Notes

Any additional relevant notes should be placed here.

ABBREVIATIONS

Pc, phthalocyanine; MPc, metallo-phthalocyanine; G4, G-quadruplex; Quad, quadruplet; DBN, 1,5-Diazabicyclo[4.3.0]non-5-ene; DMAE, dimethylaminoethanol; DCFH-DA, 2',7'-dichlorofluorescein diacetate; ROS, Reactive Oxygen Species; Zn-PS, Zinc 2,9,16,23-tetra-tert-butyl-29H,31H-phthalocyanine; RB, Rose Bengal.

REFERENCES

[1]. Kelly T.K.; De Carvalho, D.D.; Jones, P.A. Epigenetic modifications as therapeutic targets. *Nat. Biotechnol.*, **2010**, *28*, 1069–1078.
[2] Neiddle, S. Quadruplex Nucleic Acids as Novel Therapeutic Targets. *J. Med. Chem.*, **2016**, *59*, 5987-6011.
[3] Palma, E.; Carvalho, J.; Cruz, C.; Paulo. A. Metal-Based G-Quadruplex Binders for Cancer Theranostics. *Pharmaceuticals,* **2021**, *14*, 605;
[4] Kosiol, N.; Juranek, S.; Brossart, P.; Heine, A.; Paeschke, K. G-quadruplexes: a promising target for cancer therapy. *Mol. Cancer*, **2021**, ***20***:40.
[5] Neidle, S.; Balasubramanian. S. (Eds.), *Quadruplex Nucleic Acids*, RSC (Cambridge, UK), **2006**.
[6] Spiegel, J.; Adhikari, S.; Balasubramanian, S. The Structure and Function of DNA G-Quadruplexes. *Trends Chem.*, **2020**, *2:2*, 123-136.
[7] Chambers, V. S.; Marsico, G.; Boutell, J. M.; Di Antonio, M.; Smith, G. P.; Balasubramanian, S. High-throughput sequencing of DNA G-quadruplex structures in the human genome. *Nat. Biotechnol.*, **2015**, *33*, 877– 881.
[8] Rhodes, D.; Lipps, H. J. G-quadruplexes and their regulatory roles in biology. *Nucleic Acids Res.,* **2015**, *43*, 8627-8637.
[9] Varshney, D.; Spiegel, J.; Zyner, K.; Tannahill, D.; Balasubramanian, S. The regulation and functions of DNA and RNA G-quadruplexes. *Nat. Rev. Mol. Cell Biol.*, **2020**, *21*, 459–474.
[10] Collie, G. W.; Parkinson, G. N. The application of DNA and RNA G-quadruplexes to therapeutic medicines. *Chem. Soc. Rev.*, **2011**, *40*, 5867– 5892.
[11] Islam, M. K.; Jackson, P. J. M.; Rahman, K. M.; Thurston, D. E. Recent advances in targeting the telomeric G-quadruplex DNA sequence with small molecules as a strategy for anticancer therapies. *Future Med. Chem.*, **2016**, *8(11)*, 1259-1290.
[12] Neidle, S. Quadruplex nucleic acids as targets in cancer drug discovery. *Nat. Rev. Chem.*, **2017**, *1(5)*, 0041.
[13] Carvalho, J.; Mergny, J.-L.; Salgado, G. F.; Queiroz, J. A.; Cruz, C. G-quadruplex, Friend or Foe: The Role of the G-quartet in Anticancer Strategies. *Trends Mol. Med.*, **2020**, *26(9)*, 848-861.
[14] Cao, Q.; Li, Y.; Freisinger, E.; Qin, P. Z.; Sigel, R. K. O.; Mao, Z.-W. G-quadruplex DNA targeted metal complexes acting as potential anticancer drugs. *Inorg. Chem. Front.*, **2017**, *4(1)*, 10-32.
[15] Chaudhuri, R.; Bhattacharya, S.; Dash, J.; Bhattacharya, S. Recent Update on Targeting c-MYC G-Quadruplexes by Small Molecules for Anticancer Therapeutics. *J. Med. Chem.*, **2021**, *64(1)*, 42-70.
[16] Xu, J.; Huang, H.; Zhou, X. G-Quadruplexes in Neurobiology and Virology: Functional Roles and Potential Therapeutic Approaches. *JACS Au*, **2021**, *1(12)*, 2146-2161.
[17] Ruggiero, E.; Richter, S. N. G-quadruplexes and G-quadruplex ligands: targets and tools in antiviral therapy. *Nucleic Acids Res.*, **2018**, *46(7)*, 3270-3283.
[18] Plavec, J. Quadruplex targets in neurodegenerative diseases. *Annu. Rep. Med. Chem.*, **2020**, *54*, 441-483.
[19] Wang, E.; Thombre, R.; Shah, Y.; Latanich, R.; Wang, J. G-Quadruplexes as pathogenic drivers in neurodegenerative disorders. *Nucleic Acids Res*., **2021**, *49(9)*, 4816-4830.

[20] Balaratnam, S.; Schneekloth Jr. J. S. Transcriptional regulation of MYC through G-quadruplex structures. *Annu. Rep. Med. Chem.*, **2020**, *54*, 361-407.
[21] Mendes, E.; Aljnadi, I. M.; Bahls, B.; Victor, B.L.; Paulo, A. Major Achievements in the Design of Quadruplex-Interactive Small Molecules. *Pharmaceuticals*, **2022**, *15(3)*, 300.
[22] Drygin, D.; Siddiqui-Jain, A.; O'Brien, S.; Schwaebe, M.; Lin, A.; Bliesath, J.; Ho, C. B.; Proffitt, C.; Trent, K.; Whitten, J. P.; Lim, J. K. C.; Von Hoff, D.; Anderes, K.; Rice, W. G. Anticancer activity of CX-3543: a direct inhibitor of rRNA biogenesis. *Cancer Res.*, **2009**, *69*, 7653–7661.
[23] Drygin, D.; Lin, A.; Bliesath, J.; Ho, C. B.; O'Brien, S. E.; Proffitt, C.; Omori, M.; Haddach, M.; Schwaebe, M. K.; Siddiqui-Jain, A.; Streiner, N.; Quin, J. E.; Sanij, E.; Bywater, M. J.; Hannan, R. D.; Ryckman, D.; Anderes, K.; Rice, W. G. Targeting RNA polymerase I with an oral small molecule CX-5461 inhibits ribosomal RNA synthesis and solid tumor growth. *Cancer Res.*, **2011**, *71*, 1418–1430.
[24] Xu, H.; Di Antonio, M.; McKinney, S.; Mathew, V.; Ho, B.; O'Neil, N. J.; Santos, N. D.; Silvester, J.; Wei, V.; Garcia, J.; Kabeer, F.; Lai, D.; Soriano, P.; Banath, J.; Chiu, D. S.; Yap, D.; Le, D. D.; Ye, F. B.; Zhang, A.; Thu, K.; Soong, J.; Lin, S.-C.; Tsai, A. H. C.; Osako, T.; Algara, T.; Saunders, D. N.; Wong, J.; Xian, J.; Bally, M. B.; Brenton, J. D.; Brown, G. W.; Shah, S. P.; Cescon, D.; Mak, T. W.; Caldas, C.; Stirling, P. C.; Hieter, P.; Balasubramanian, S.; Aparicio, S. CX-5461 is a DNA G-quadruplex stabilizer with selective lethality in BRCA1/2 deficient tumours. *Nat. Commun.*, **2017**, *8*, 14432.
[25] Ferino, A.; Nicoletto, G.; D'Este, F.; Zorzet, S.; Lago, S.; Richter, S. N.; Tikhomirov, A.; Shchekotikhin, A.; Xodo, L. E. Photodynamic Therapy for ras-Driven Cancers: Targeting G-Quadruplex RNA Structures with Bifunctional Alkyl-Modified Porphyrins. *J. Med. Chem.,* **2020**, *63*(3), 1245–1260.
[26] Cogoi, S.; Xodo, L. E. G-quadruplex formation within the promoter of the KRAS proto-oncogene and its effect on transcription. *Nucleic Acids Res.,* **2006**, *34(9)*, 2536-2549.
[27] Wheelhouse, R. T.; Sun, D. Haiyong; H.; Frank X.; Hurley, L. H. Cationic Porphyrins as Telomerase Inhibitors: the Interaction of Tetra-(N-methyl-4-pyridyl)porphine with Quadruplex DNA. *J. Am. Chem. Soc.*, **1998**, *120(13)*, 3261-3262.
[28] Zheng, X.-H.; Nie, X.; Liu, H.-Y.; Fang, Y.-M.; Zhao, Y.; Xia. L.-X. TMPyP4 promotes cancer cell migration at low doses, but induces cell death at high doses. *Sci. Rep.*, **2016**, *6*, 26592.
[29] Caterinoa, M.; D'Ariaa, F.; Kustov, A. V.; Belykh D. V.; Khudyaeva, I. S.; Starseva, O. M.; Berezin, D. B.; Pylina, Y. I.; Usacheva, T.; Amato, J.; Giancola. C. Selective binding of a bioactive porphyrin-based photosensitizer to the G-quadruplex from the KRAS oncogene promoter. *Int. J. Biol. Macromol.*, **2020**, *145*, 244-251.
[30] McKenzie, L. K.; Bryant, H. E.; Weinstein, J. A. Transition metal complexes as photosensitisers in one- and two-photon photodynamic therapy. *Coord. Chem. Rev.*, **2019**, *379*, 2–29.
[31] Imberti, C.; Zhang, P.; Huang, H.; Sadler, P. J. New Designs for Phototherapeutic Transition Metal Complexes. *Angew. Chem. Int. Ed.*, **2020**, *59*, 61 – 73.
[32] Monro, S.; Colón, K. L.; Yin, H.; Roque, III, J.; Konda, P.; Gujar, S.; Thummel, R. P.; Lilge, L.; Cameron, C. G.; McFarland. S. A. Transition Metal Complexes and Photodynamic

Therapy from a Tumor-Centered Approach: Challenges, Opportunities, and Highlights from the Development of TLD1433. *Chem. Rev.*, **2019**, *119*, 797−828.
[33] McFarland, S. A.; Mandel, A.; Dumoulin-White, R.; Gasser, G. Metal-based photosensitizers for photodynamic therapy: the future of multimodal oncology? *Curr. Op. Chem. Biol*., **2020**, *56*, 23-27.
[34.] Karges, J. Clinical Development of Metal Complexes as Photosensitizers for Photodynamic Therapy of Cancer. *Angew. Chem. Int. Ed.*, **2022**, *61(5)*:e202112236.
[35] Li, X.; Lee, S.; Yoon, J. Supramolecular photosensitizers rejuvenate photodynamic therapy. *Chem. Soc. Rev.*, **2018**, *47(4)*, 1174-1188.
[36] Yaku, H.; Fujimoto, T.; Murashima, T.; Miyoshi, D.; Sugimoto, N. Phthalocyanines: a new class of G-quadruplex-ligands with many potential applications. *Chem. Commun.*, **2012**, *48*, 6203–6216.
[37] Yaku, H.; Murashima, T.; Miyoshi, D.; Sugimoto, N. Specific binding of anionic porphyrin and phthalocyanine to the G-quadruplex with a variety of in vitro and in vivo applications. *Molecules* **2012**, *17*, 10586-10613.
[38] Lo, P.-C.; Rodríguez-Morgade, M. S.; Pandey, R. K.; Ng, D. K. P.; Torres, T.; Dumoulin, F. The unique features and promises of phthalocyanines as advanced photosensitisers for photodynamic therapy of cancer. *Chem. Soc. Rev.*, **2020**, *49(4)*, 1041-1056.
[39] Li, X.; Zheng, B.-D.; Peng, X.-H.; Li, S.-Z.; Ying, J.-W.; Zhao, Y.; Huang, J.-D.; Yoon, J. Phthalocyanines as medicinal photosensitizers: Developments in the last five years. *Coord. Chem. Rev.*, **2019**, *379*, 147-160.
[40] Alzeer, J.; Vummidi, B. R.; Roth, P. J. C.; Luedtke, N. W. Guanidinium-modified phthalocyanines as high-affinity G-quadruplex fluorescent probes and transcriptional regulators. *Angew. Chem. Int. Ed.*, **2009**;*48(49)*, 9362-9365.
[41] Membrino, A.; Paramasivam, M.; Cogoi, S.; Alzeer, J.; Luedtke, N. W.; Xodo, L. E. Cellular uptake and binding of guanidine-modified phthalocyanines to KRAS/HRAS G-quadruplexes. *Chem. Commun*., **2010**, *46(4)*, 625-627.
[42] Alzeer, J.; Luedtke, N. W. pH-Mediated fluorescence and G-quadruplex binding of amido phthalocyanines. *Biochemistry*, **2010**, *49*, 4339-4348.
[43] Ren, L.; Zhang, A.; Huang, J.; Wang, P.; Weng, X.; Zhang, L.; Liang, F.; Zhou, X. Quaternary ammonium zinc phthalocyanine: inhibiting telomerase by stabilizing G quadruplexes and inducing G-quadruplex structure transition and formation. *ChemBioChem*, **2007**, *8*, 775-780.
[44] Zhang, L.; Huang, J.; Ren, L.; Bai, M.; Wu, L.; Zhai, B.; Zhou, X. Synthesis and evaluation of cationic phthalocyanine derivatives as potential inhibitors of telomerase. *Bioorg. Med. Chem.*, **2008**, *16*, 303-312.
[45] Macii, F.; Perez-Arnaiz, C.; Arrico, L.; Busto, N.; Garcia, B.; Biver, T. Alcian blue pyridine variant interaction with DNA and RNA polynucleotides and G-quadruplexes: changes in the binding features for different biosubstrates. *J. Inorg. Biochem.*, **2020**, *212*, 111199
[46] Yılmaz, H. E.; Bagda, E.; Bagda, E.; Durmus¸ M. Interaction of water soluble cationic gallium(III) phthalocyanines with different G-quadruplex DNAs. *Polyhedron*, **2021**, *208*, 115404.

[47] Uchiyama, M.; Momotake, A.; Ikeue, T.; Yamamoto, Y. Photogeneration of Reactive Oxygen Species from Water-Soluble Phthalocyanine Derivatives Bound to a G-Quadruplex DNA. *Bull. Chem. Soc. Jpn.*, **2020**, *93*, 1504– 1508.
[48] Kawauchi, K.; Sugimoto, W.; Yasui, T.; Murata, K.; Itoh, K.; Takagi, K.; Tsuruoka, T.; Akamatsu, K.; Tateishi-Karimata, H.; Sugimoto, N.; Miyoshi, D. An anionic phthalocyanine decreases NRAS expression by breaking down its RNA G-quadruplex. *Nat. Commun.,* **2018**, *9*, 2271.
[49] Thordarson, P. Determining association constants from titration experiments in supramolecular chemistry. *Chem. Soc. Rev.*, **2011**, *40*, 1305–1323.
[50] Ramos, C. I. V.; Almeida, S. P.; Lourenço, L. M. O.; Pereira, P. M. R.; Fernandes, R.; Faustino, M. A. F.; Tomé, J. P. C.; Carvalho, J.; Cruz, C.; Neves, M. G. P. M. S. Multicharged Phthalocyanines as Selective Ligands for G-Quadruplex DNA Structures. *Molecules*, **2019**, *24(4)*, 733
[51] Lopes-Nunes, J.; Carvalho, J.; Figueiredo, J.; Ramos, C. I. V.; Lourenço, L. M. O.; Tomé, J. P. C.; Neves, M. G. P. M. S.; Mergny, J.-M.; Queiroz, J. A.; Salgado, G. F.; Cruz, C. Phthalocyanines for G-quadruplex aptamers binding. *Bioorg. Chem.*, **2020**, *100*, 103920.
[52] Sibrian-Vázquez, M.; Ortiz, J.; Nesterova, I.V.; Fernández-Lázaro, F.; Sastre-Santos, Á.; Soper, S. A.; Vicente, M. G. H. Synthesis and properties of cell-targeted Zn(II)-phthalocyanine-peptide conjugates. *Bioconjugate Chem.*, **2007**, *18(2)*, 410–420.
[53] Yaku, H.; Murashima, T.; Miyoshi, D.; Sugimoto, N. Anionic phthalocyanines targeting G-quadruplexes and inhibiting telomerase activity in the presence of excessive DNA duplexes. *Chem. Commun.*, **2010**, *46*, 5740-5742.

Supporting information for

Development and Application of Metallo-Phthalocyanines as Potent G-quadruplex DNA Binders and Photosensitizers.

Ariadna Gil-Martínez,[a] Adrián Hernández,[b] Cristina Galiana-Roselló,[a] Sònia López-Molina,[a] Javier Ortiz,[b] Angela Sastre-Santos[b,] Enrique García-España,[a] Jorge González-García[a]*

[a]Institute of Molecular Science (ICMol) and Department of Inorganic Chemistry, University of Valencia, C./ Jose Beltran 2, 46680 Paterna, Spain

[b]Área de Química Orgánica, Instituto de Bioingeniería, Universidad Miguel Hernández, Avda. de la Universidad s/n, 03202 Elche, Spain

Table S1. List of DNA sequences used in this work, acronym, localization in the genome

Abreviation	Sequence (5' → 3')	Topology	Localization
HTelo	AGGGTTAGGGTTAGGGTTAGGG	Mixed	telomere
F21T-K	GGGTTAGGGTTAGGGTTAGGG	Mixed	telomere
F21T-Na	GGGTTAGGGTTAGGGTTAGGG	Antiparallel	telomere
CEB25	AAGGGTGGGTGTAAGTGTGGGTGGGT	Parallel	minisatellite loci
Kras	AGGGCGGTGTGGGAATAGGGAA	Parallel	promoter of *ras*
22CTA	AGGGCTAGGGCTAGGGCTAGGG	Antiparallel	telomere
26TTA	TTAGGGTTAGGGTTAGGGTTAGGGTT	Hybrid 2	telomere
24TTG	TTGGGTTAGGGTTAGGGTTAGGGA	Hybrid 1	telomere
Kit1	AGGGAGGGCGCTGGGAGGAGGG	Parallel	promoter of kit
Kit2	CGGGCGGGCGCGAGGGAGGGG	Parallel	promoter of kit
Bcl2	GGGCGCGGGAGGAATTGGGCGGG	Hybrid	promoter of Bcl2
TBA	GGTTGGTGTGGTTGG	Antiparallel	Thrombin binding aptamer
ds26	CAATCGGATCGAATTCGATCCGATTG	B-type duplex	

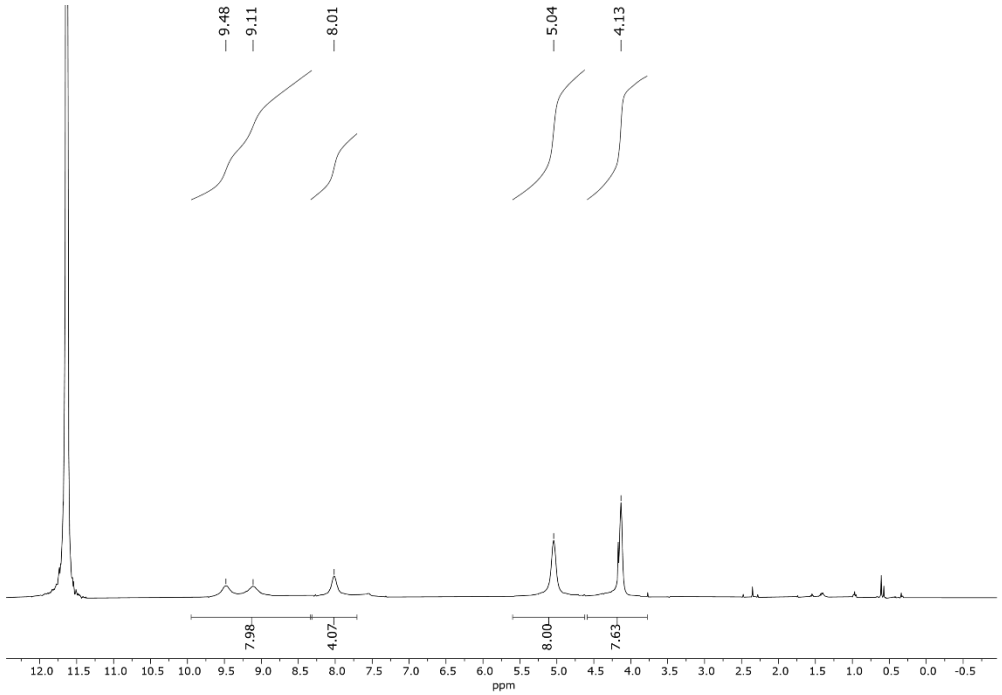

Figure S1.- ^{1}H NMR spectrum of **NiPc** in TFA-*d*

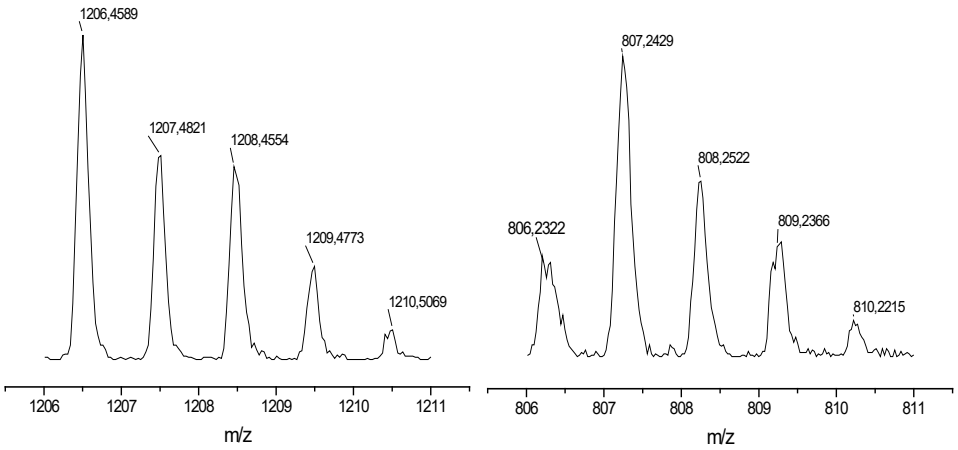

Figure S2. HR-MALDI-TOF spectrum of **NiPc-Boc** (left panel) and **NiPc** (right panel).

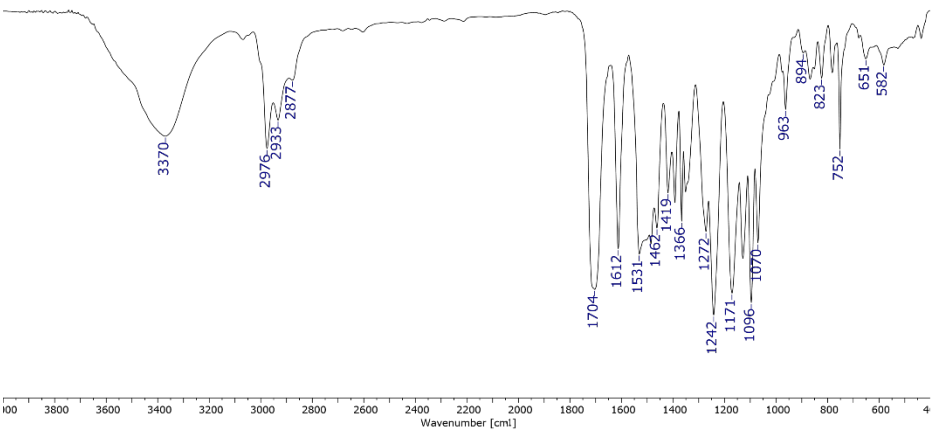

Figure S3. FT-IR spectrum of **NiPc-Boc**

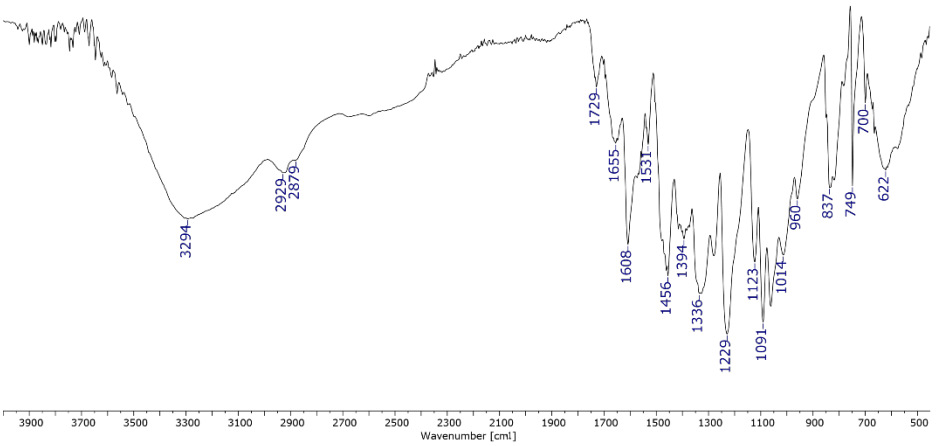

Figure S4. FT-IR spectrum of **NiPc**

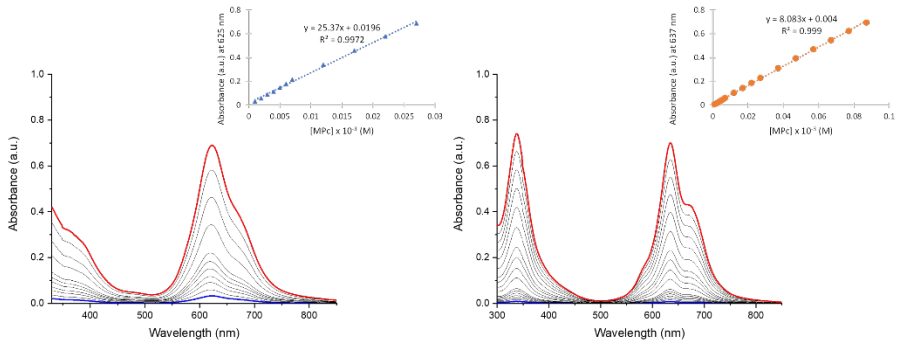

Figure S5.- UV-Vis spectra of **NiPc** (left panel) and **ZnPc** (right panel) at different concentration (1 µM – 100 µM) in H_2O. Insets: Lambert-Beer Plots for MPcs. Blue spectrum corresponds to the initial titration and red spectrum to last one.

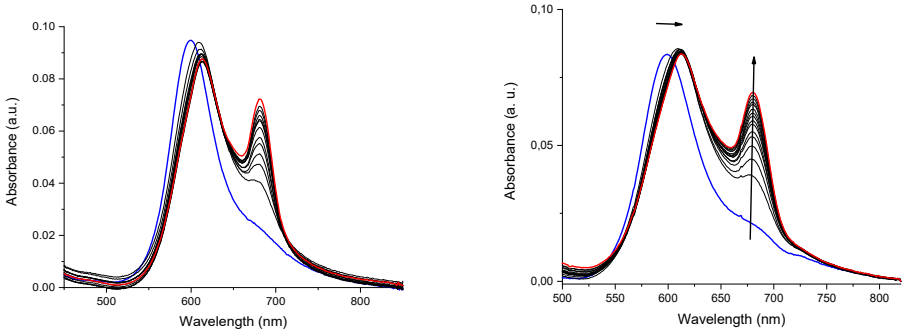

Figure S6. UV-vis titration of **NiPc** (5 µM) with G4 DNA HTelo22 in Tris buffer (Tris 10 mM, KCl 100 mM) at pH= 5 (left panel) and pH 7.4 (right panel). Blue spectrum corresponds to the initial titration and red spectrum to last one.

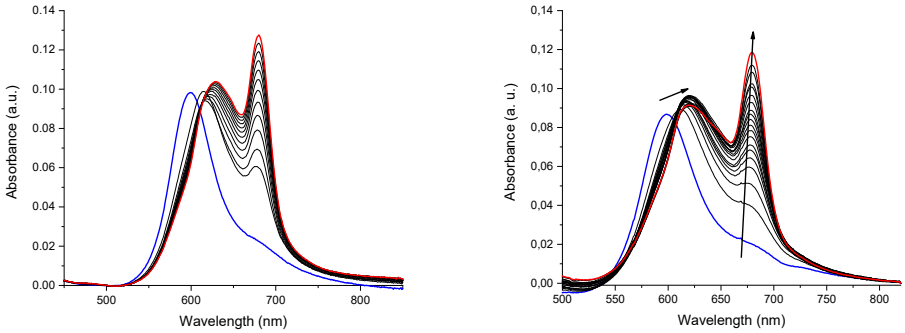

Figure S7. UV-vis titration of **NiPc** (5 µM) with G4 DNA cMyc in Tris buffer (Tris 10 mM, KCl 100 mM) at pH= 5 (left panel) and pH 7.4 (right panel). Blue spectrum corresponds to the initial titration and red spectrum to last one.

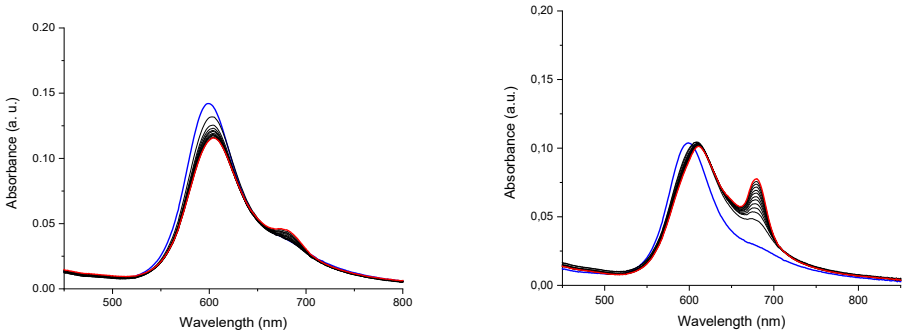

Figure S8. UV-vis titration of **NiPc** (5 µM) with duplex DNA ds26 in Tris buffer (Tris 10 mM, KCl 100 mM) at pH= 5 (left panel) and pH 7.4 (right panel). Blue spectrum corresponds to the initial titration and red spectrum to last one.

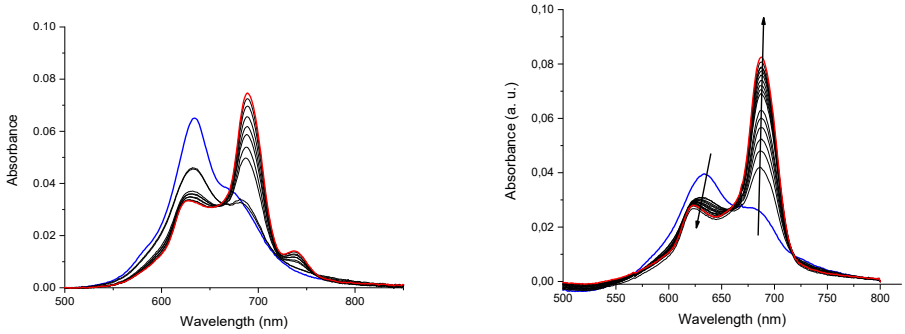

Figure S9. UV-vis titration of **ZnPc** (5 µM) with G4 DNA HTelo22 in Tris buffer (Tris 10 mM, KCl 100 mM) at pH= 5 (left panel) and pH 7.4 (right panel). Blue spectrum corresponds to the initial titration and red spectrum to last one.

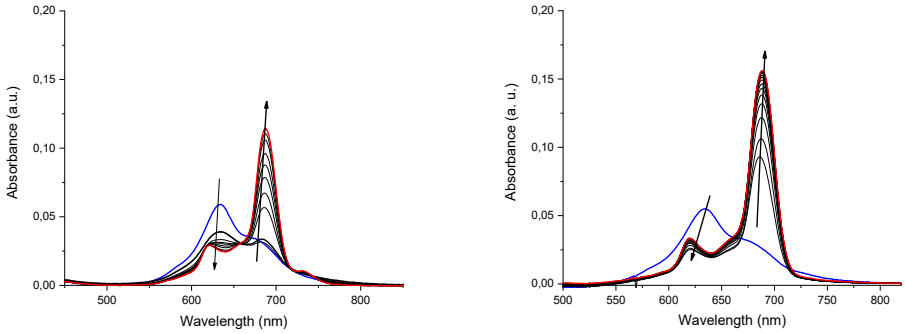

Figure S10. UV-vis titration of **ZnPc** (5 µM) with G4 DNA cMyc in Tris buffer (Tris 10 mM, KCl 100 mM) at pH= 5 (left panel) and pH 7.4 (right panel). Blue spectrum corresponds to the initial titration and red spectrum to last one.

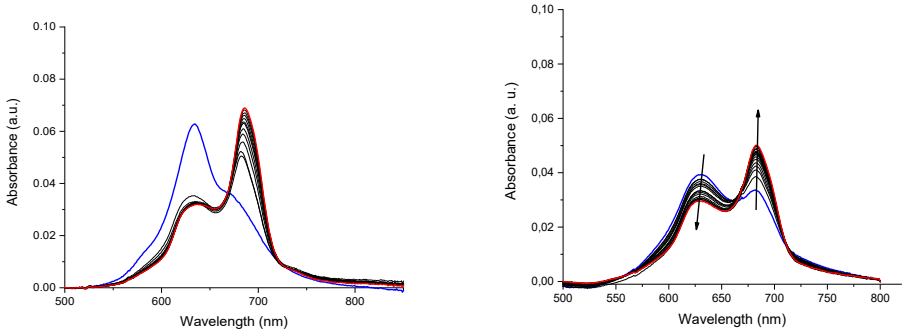

Figure S11. UV-vis titration of **ZnPc** (5 µM) with duplex DNA ds26 in Tris buffer (Tris 10 mM, KCl 100 mM) at pH= 5 (left panel) and pH 7.4 (right panel). Blue spectrum corresponds to the initial titration and red spectrum to last one.

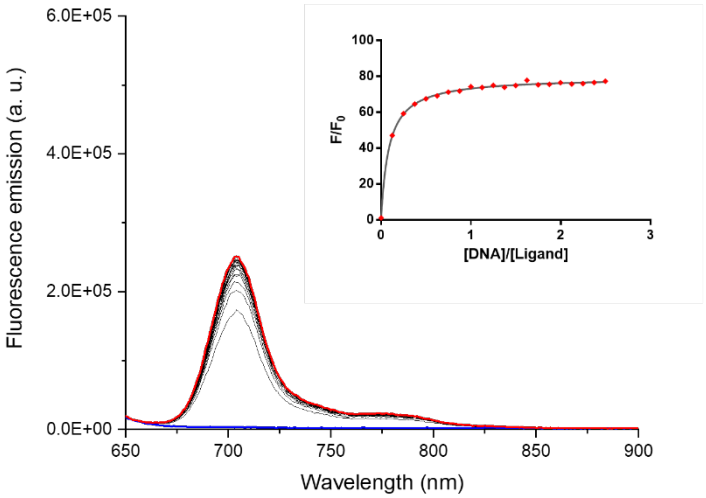

Figure S12. Fluorescence titration of **ZnPc** (2 µM) with G4 DNA HTelo in Tris buffer (Tris 10 mM, KCl 100 mM, pH= 7.4, λ_{exc} = 620 nm). Inset: Plot of the F/Fo vs. ratio [DNA]/[MPc]. Blue spectrum corresponds to the initial titration and red spectrum to last one.

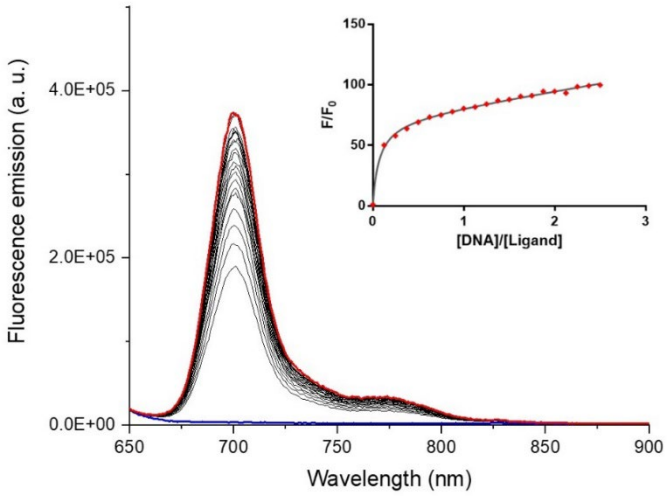

Figure S13. Fluorescence titration of **ZnPc** (2 µM) with G4 DNA cMyc in Tris buffer (Tris 10 mM, KCl 100 mM, pH= 7.4, λ_{exc} = 620 nm). Inset: Plot of the F/Fo vs. ratio [DNA]/[MPc]. Blue spectrum corresponds to the initial titration and red spectrum to last one.

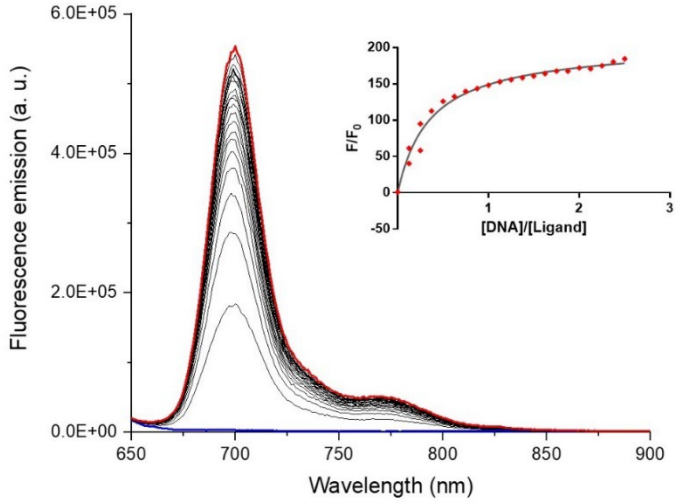

Figure S14. Fluorescence titration of **ZnPc** (2 µM) with G4 DNA CEB25 in Tris buffer (Tris 10 mM, KCl 100 mM, pH= 7.4, λ_{exc} = 620 nm). Inset: Plot of the F/Fo vs. ratio [DNA]/[MPc]. Blue spectrum corresponds to the initial titration and red spectrum to last one.

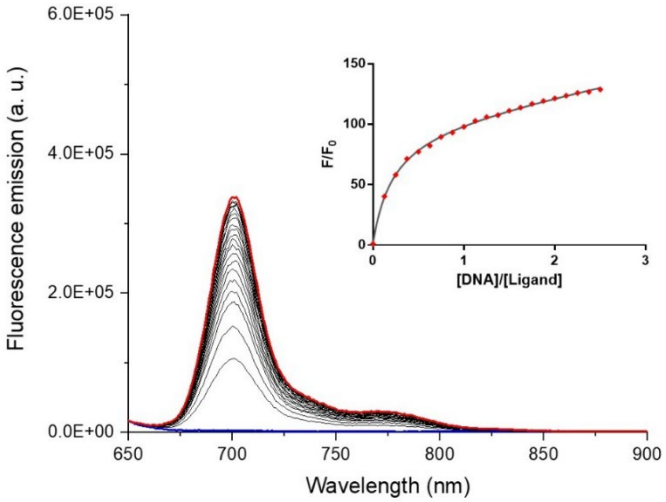

Figure S15. Fluorescence titration of **ZnPc** (2 µM) with G4 DNA Kras in Tris buffer (Tris 10 mM, KCl 100 mM, pH= 7.4, λ_{exc} = 620 nm). Inset: Plot of the F/Fo vs. ratio [DNA]/[MPc]. Blue spectrum corresponds to the initial titration and red spectrum to last one.

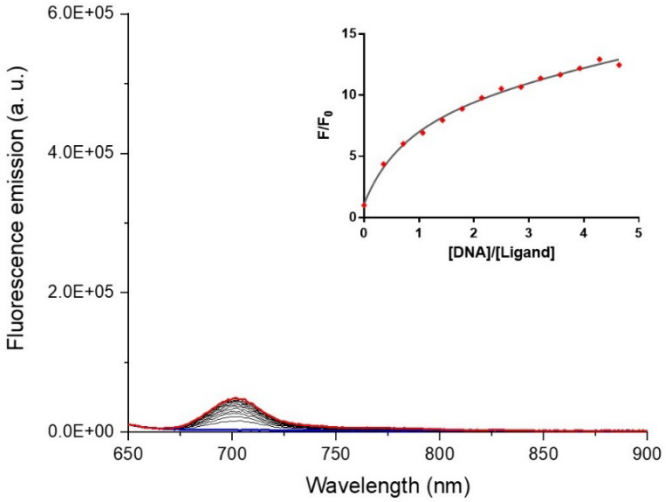

Figure S16. Fluorescence titration of **ZnPc** (2 µM) with duplex DNA ds26 in Tris buffer (Tris 10 mM, KCl 100 mM, pH= 7.4, λ_{exc} = 620 nm). Inset: Plot of the F/Fo vs. ratio [DNA]/[MPc]. Blue spectrum corresponds to the initial titration and red spectrum to last one.

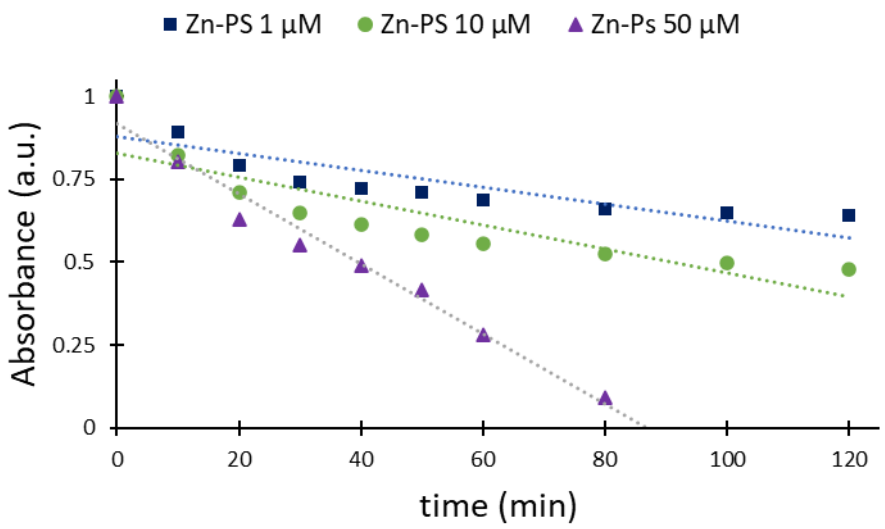

Figure S17. Decay rate of DPBF in DMSO induced by **Zn-PS** under red light irradiation.

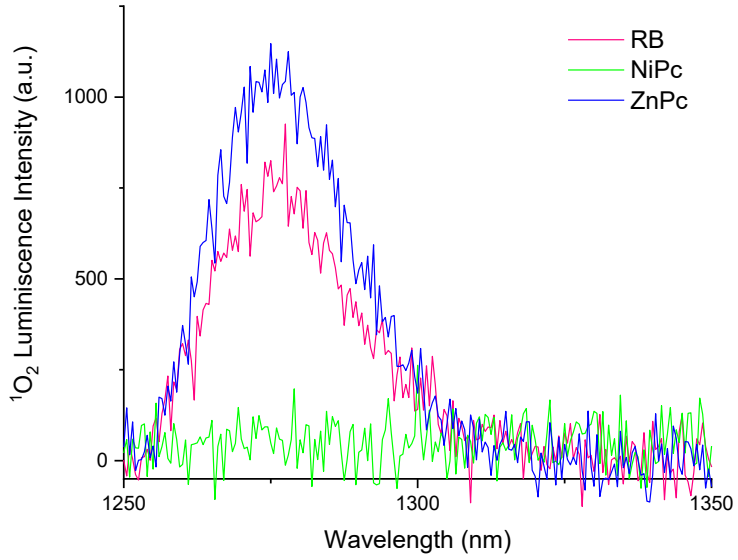

Figure S18. Luminescence of singlet oxygen generated by irradiating of **RB**, **NiPc** and **ZnPc**.

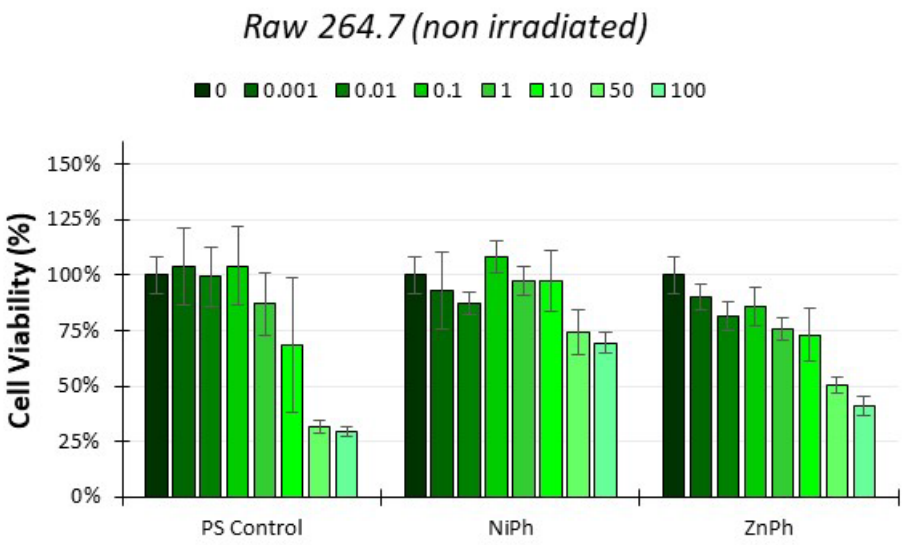

Figure S19. Cell viability on Raw264.7 cell line of **Zn-PS**, **NiPc** and **ZnPc** in the dark. Colors and numbering in the legend refer to the compound concentrations (μM).

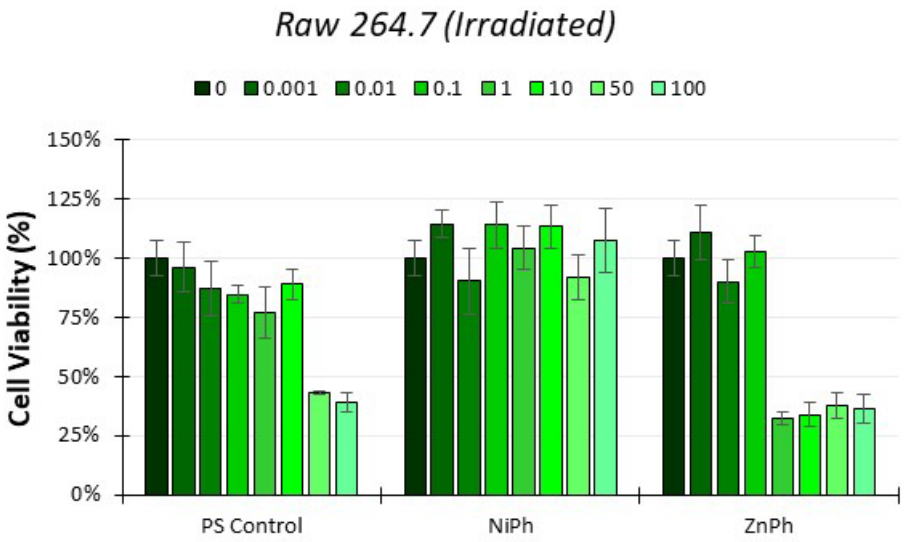

Figure S20. Cell viability on Raw264.7 cell line of **Zn-PS**, **NiPc** and **ZnPc** under irradiation. Colors and numbering in the legend refer to the compound concentrations (μM).

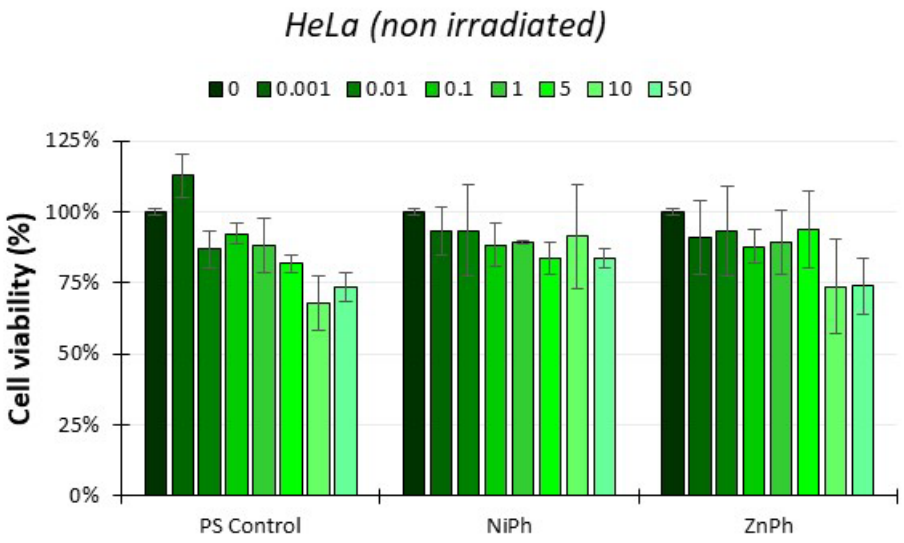

Figure S21. Cell viability on HeLa cell line of **Zn-PS**, **NiPc** and **ZnPc** in the dark. Colors and numbering in the legend refer to the compound concentrations (μM).

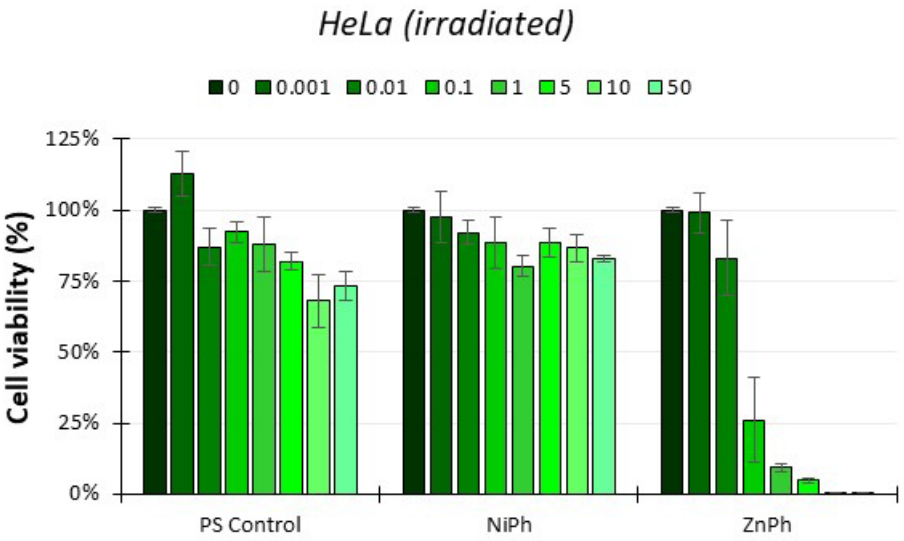

Figure S22. Cell viability on HeLa cell line of **Zn-PS**, **NiPc** and **ZnPc** under irradiation. Colors and numbering in the legend refer to the compound concentrations (μM).

3.4 Discusión y conclusiones

En este capítulo se han sintetizado ftalocianinas de cinc y níquel tetrasustituidas con sustituyentes etoxiamonio que aportan flexibilidad y grupos amonio terminales capaces de interaccionar con el esqueleto de fosfato de los cuadruplejos de ADN a los que dichas MPcs pueden reconocer y unirse.

3.4.1 Resumen artículo 4

La síntesis de **ZnPc 21** y **NiPc 22** se llevó a cabo siguiendo un método similar ya descrito en la literatura. [167] Para ello es necesaria la formación previa de **ZnPc-Boc 23** y **NiPc-Boc 24**, con el grupo Boc (*terc*-butoxicarbonilo) protegiendo la amina. Estas se sintetizaron mediante la autocondensación de 4-Boc-aminoetoxiftalonitrilo en presencia de una sal de $Zn(OAc)_2$ o $Ni(OAc)_2 \cdot H_2O$, en DMAE como disolvente y con DBN como catalizador, dando unos rendimientos de 40% y 24% respectivamente. Una vez obtenidas, se eliminó el grupo protector en medio ácido, obteniéndose los productos finales **ZnPc 21** y **NiPc 22** como derivado tetraamonio tetratrifluoroacetato con rendimientos cuantitativos. (**Esquema 3.2**).

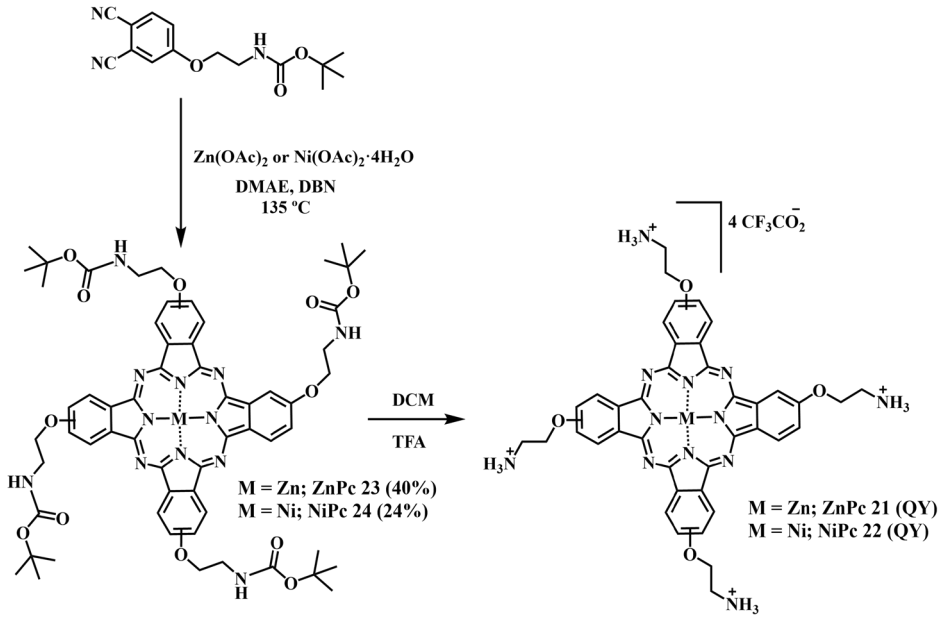

Esquema 3.2. Síntesis de ZnPc 21 y NiPc 22.

ZnPc 21 y **NiPc 22** se caracterizaron por espectroscopía de ^{1}H-RMN, espectrometría de masas HR-MALDI-TOF, absorción UV-vis y espectros de fluorescencia (**Figuras S1-S5** del artículo, pgs. 197-199). En el espectro de ^{1}H-RMN pueden verse señales aromáticas y alifáticas bien definidas de **NiPc 22** en TFA-d_1: tres señales de las unidades de isoindol a 9.48, 9.11 y 8.01 ppms que integran por 12 átomos de hidrogeno, de la cadena de 2-aminoetoxilo se observan dos señales, una a 5.04 ppms correspondiente a los ocho hidrógenos cercanos al nitrógeno, y la otra a 4.13 ppms de los ocho hidrógenos próximos al oxígeno. El espectro FT-

[167] M. Sibrian-Vazquez, J. Ortiz, I.V. Nesterova, F. Fernández-Lázaro, A. Sastre-Santos, S.A. Soper, M.Gr.H. Vicente, *Bioconjugate Chem*., **2007**, *18*, 410–420.

IR de **NiPc 22** muestra la aparición de una banda ancha centrada en 3294 cm^{-1} que corresponde a los grupos amonio y la desaparición de la banda a 1704 cm^{-1} del grupo carbonilo (C=O) en **NiPc-Boc 24**. Ambas MPcs muestran las bandas UV-vis típicas, la banda Soret centrada en 350 nm, y la banda Q centrada en 680 nm. La linealidad de la absorción frente a la concentración de las MPcs indica la ausencia de agregación en solución acuosa hasta 100 µM para **ZnPc 21** y 50 µM para **NiPc 22**. Sólo **ZnPc 21** presenta banda de emisión de fluorescencia a 705 nm en H_2O.

Se realizaron experimentos de fusión FRET para comprobar la estabilización del ADN con las MPcs (**Figura 2** del artículo, pg. 183). Se observó que **NiPc 22** generaba una mayor estabilización de los G4s que **ZnPc 21**, y que ninguna de ellas estabilizaba el ADN de doble hélice, sugiriendo una alta selectividad hacia los G4s. Para comprobar la afinidad de las MPcs hacia el ADN se realizaron valoraciones por UV-Vis (Figura 3.17**a-b** y **Figuras S6-S11** en el artículo). Éstas mostraron constantes de afinidad tres órdenes de magnitud mayor para los G4s que para la doble hélice con ambas MPcs (**Tabla 3.1**). Para **ZnPc 21** también se hicieron valoraciones por fluorescencia (Figura 3.17**c-d** y **Figuras S12-S16** en el artículo) con constantes de afinidad dos órdenes de magnitud mayor para los G4s (**Tabla 3.1**).

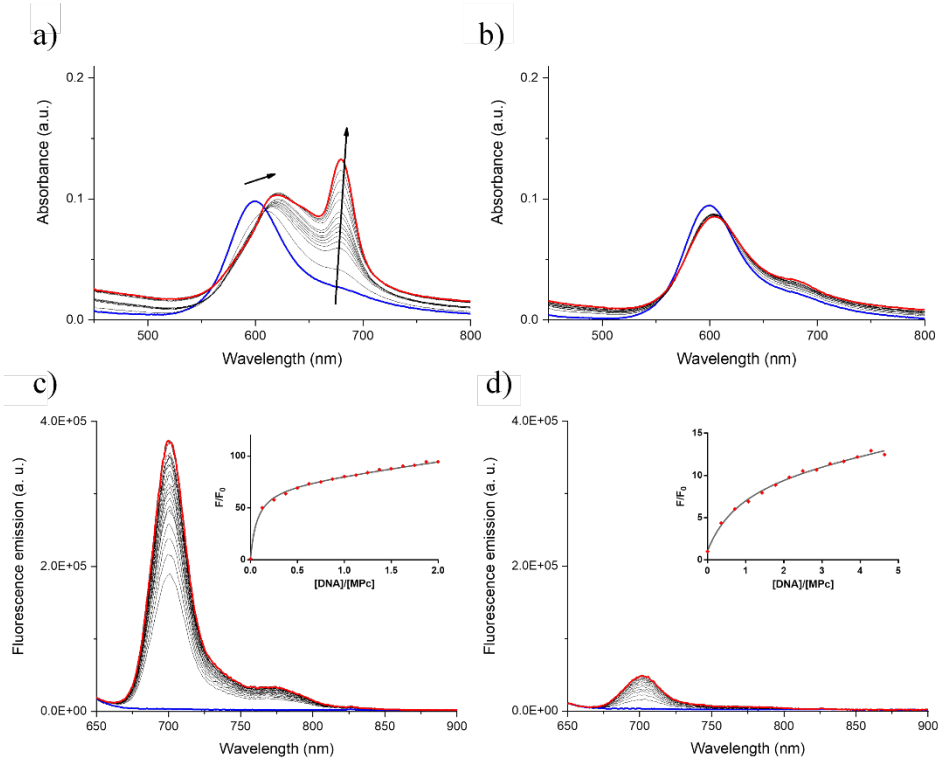

*Figura 3.17. Valoraciones UV-visible de **NiPc 22** con a) cMyc y b) ds26. Valoraciones de fluorescencia de **ZnPc 21** con c) G4 HTelo y b) ds26 en Tris 10 mM, KCl 100 mM, pH 7.4, λ_{exc} = 620 nm. Ampliación: Representación de F/F_o vs [DNA]/[MPc]. El espectro azul corresponde con la valoración inicial y el rojo con la final.*

Tabla 3.1. Constantes de unión (log K_a) determinadas por los experimentos de valoración de las MPcs. 1: obtenidos por UV-vis, 2: obtenido por fluorescencia.

MPc	HTelo	cMyc	ds26
NiPc	**5.2 (±0.1)[1]**	**6.3 (±0.2) [1]**	**n.d.**
ZnPc	**6.7 (±0.4)[1]**	**6.3 (±0.7) [1]**	**n.d.**
	5.2 (±0.1)[2]	**6.3 (±0.2) [2]**	**4.6 (±0.4) [2]**

Se estudió la capacidad de generar oxígeno singlete ($^1O_2$) bajo irradiación de ambas MPcs mediante la variación relativa de la absorbancia del 1,3-difenilisobenzofurano (DPBF), que se produce por su reacción con el $^1O_2$ generado. **ZnPc 21** presenta una alta capacidad para la generación de $^1O_2$ incluso a la mínima concentración estudiada, mientras que **NiPc 22** prácticamente no lo generaba (**Figura 3.18**). Se realizó otro experimento adicional para comprobar la capacidad de generar $^1O_2$, midiendo el espectro de fosforescencia del oxígeno singlete de las MPcs y de Rosa de Bengala (RB) como control positivo en acetonitrilo después de irradiarlos. Se observó fosforescencia con **ZnPc 21** y RB, siendo mayor con **ZnPc 21**, mientras que con **NiPc 22** no se apreciaba fosforescencia, confirmando los resultados obtenidos previamente (**Figura 3.19)**

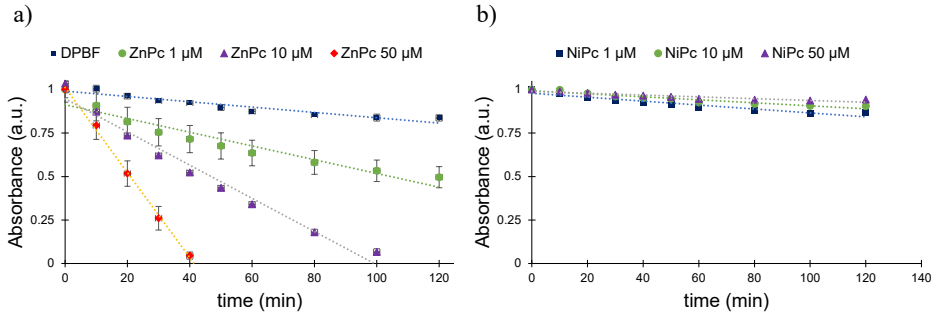

*Figura 3.18. Comparación de la tasa de decaimiento de DPBF en DMSO inducida por a) **ZnPc 21** y b) **NiPc 22** bajo irradiación de luz roja.*

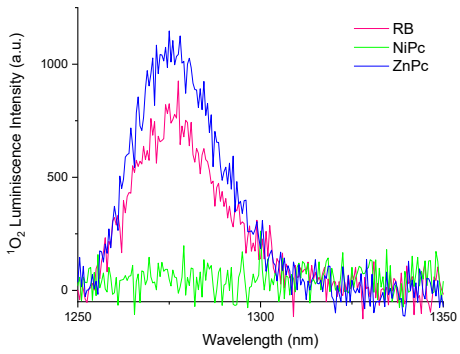

Figura 3.19. Luminiscencia del oxígeno singlete generado por la irradiación de RB, NiPc y ZnPc.

Utilizando la propia fluorescencia intrínseca de **ZnPc 21** se comprobó la localización celular en células de cáncer de cuello de útero (HeLa), situándose en el citoplasma de éstas (**Figura 3.20a**). Una vez confirmada la entrada en las células, el siguiente paso fue evaluar el estrés oxidativo generado tanto en oscuridad como con irradiación a 730 nm (**Figura 3.20b**). Se cuantificó la cantidad de ROS generados mediante el aumento de la fluorescencia debido a la oxidación de diacetato de 2',7'-diclorodihidrofluoresceína (DCFH-DA), incluyendo la ampliamente utilizada (^{t}Bu)$_4$ZnPc (**Zn-PS**) y H_2O_2 como control En oscuridad, las MPcs no muestran un incremento significativo de ROS, no obstante, al irradiarlas generaban una considerable cantidad de ROS. Para **NiPc 22** el incremento de ROS era menor, se situaba en torno a 2.4-5.7 veces mayor dependiendo de la línea celular. En contraste, **ZnPc 21** mostraba un incremento 2.5 mayor para su menor concentración y hasta 100 veces mayor para la concentración más elevada. El aumento con Zn-PS es menor que con **ZnPc 21**, sugiriendo que **ZnPc 21** presenta mayor capacidad para generar ROS que la ftalocianina de referencia.

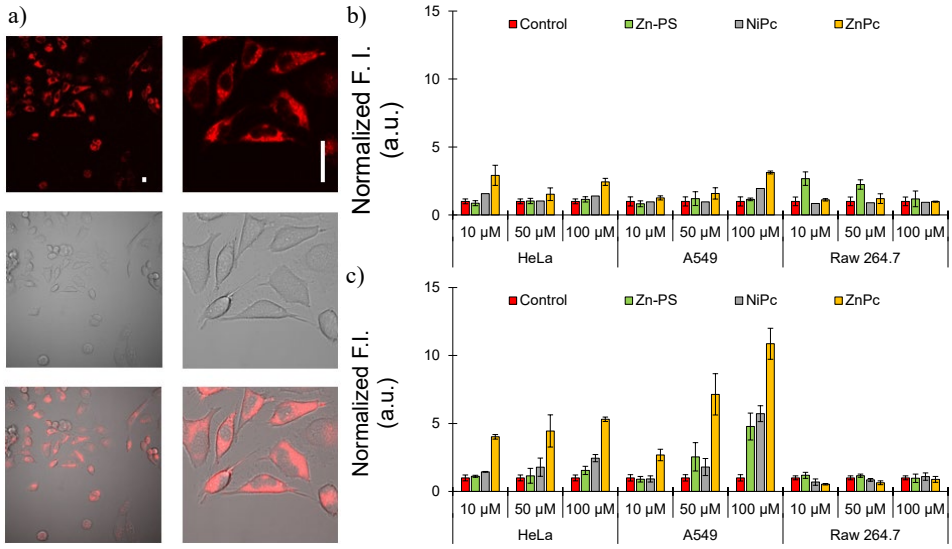

*Figura 3.20. a) Imágenes de fluorescencia confocal de células HeLa incubadas con **ZnPc 21**, el panel superior corresponde con la fluorescencia de **ZnPc 21**, el panel central a campo claro y el panel inferior a la superposición de ambos. Escala:20 µm.; Niveles de ROS en líneas celulares tratadas con las MPcs a diferentes concentraciones b) en oscuridad, c) tras irradiar a 730 nm.*

El potencial fototóxico de las MPcs **ZnPc 21**, **NiPc 22** y **Zn-PS** se evaluó en líneas celulares HeLa, A549 y Raw 264.7. Las células se incubaron 24h con concentraciones crecientes de las MPcs, se irradiaron a 730 nm o mantuvieron en oscuridad, y se incubaron otras 24h antes de comprobar la citotoxicidad (**Figura 3.21** y **Figuras S19-S22** en el artículo, pgs. 206 y 207). Los valores de IC_{50} obtenidos experimental mente se resumen en la **Tabla 3.2**. En el caso en el que las células no se irradiaban, ambas MPcs mostraban muy baja toxicidad. Para las células irradiadas, **NiPc 22** muestra baja toxicidad como era de esperar tras los resultados obtenidos en los estudios de generación de $^1O_2$ y ROS. Por el contrario, **ZnPc 21** muestra elevados niveles de toxicidad al irradiar, con valores de IC_{50} que van desde 0.04 µM a 0.89 µM dependiendo de la línea celular.

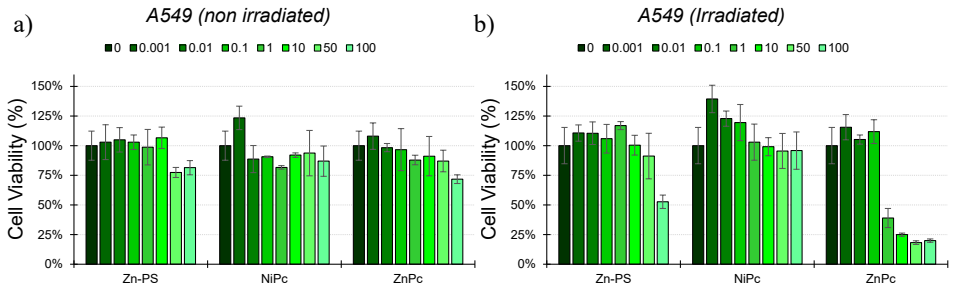

Figura 3.21. Viabilidad celular de la línea A549 con las distintas MPcs en a) oscuridad y b) tras irradiación. Los colores y números de la leyenda corresponden a la concentración de las MPcs (μM).

Tabla 3.2. Valores de IC_{50} obtenidos mediante MTT de las MPcs en oscuridad y bajo irradiación.

Cell line	NiPc 22		ZnPc 21		Zn-PS	
	Dark	Irrad	Dark	Irrad	Dark	Irrad
Hela	**>100**	**>100**	**>100**	**0.039**	**>100**	**>100**
A549	**>100**	**>100**	**>100**	**0.89**	**>100**	**>100**
Raw264.7	**>100**	**>100**	**58.7**	**0.37**	**22.9**	**42.4**

3.4.2 Conclusiones

Se han sintetizado dos ftalocianinas, una de cinc y otra de níquel, con grupos amonio terminales para proporcionarles solubilidad en agua y cadenas alquílicas para aportarles flexibilidad y aumentar la interacción con el esqueleto de fosfato de los nucleótidos.

Se ha observado que ninguna de las Pcs se agrega en agua, posiblemente debido a que los grupos amonio positivamente cargados aumentan la solubilidad en agua y evitan la agregación por repulsión.

Se ha comprobado la alta afinidad de ambas MPcs hacia G4s mediante experimentos de UV-Vis y fluorescencia, además de la capacidad de estabilización de G4s por fusión FRET, siendo mucho mayor para **NiPc 22**. Este hecho indica la importancia del ion metálico para la unión al G4, siendo más sencillo al complejo de níquel que al de cinc. Además, se ha visto que ninguna estabiliza el ADN de doble hélice.

También se ha estudiado la capacidad de ambas MPcs para actuar como fotosensibilizadores, comprobando que sólo **ZnPc 21** es capaz de generar oxígeno singlete y ROS tras irradiar con luz roja, presentando un valor de IC_{50} cinco órdenes de magnitud menor que en oscuridad.

Finalmente, podemos concluir que tanto **ZnPc 21** como **NiPc 22** pueden actuar como ligandos de G4s, ya que ha sido demostrado que ambas presentan alta afinidad por estas estructuras y no por el ADN de doble hélice. Asimismo, se ha visto que ambas presentan una baja toxicidad en oscuridad, pero que **ZnPc 21** es altamente fototóxica cuando se irradia con longitudes de onda de 730 nm, por lo que además de reconocer y unirse a los G4s también puede generar especies reactivas de oxígeno, permitiendo eliminar así las células cancerosas.